UNIVERSITAT DE
BARCELONA

Targeting the TGF-beta pathway of cancer-associated fibroblasts in colorectal cancer metastasis

Jordi Badia Ramentol

ADVERTIMENT. La consulta d'aquesta tesi queda condicionada a l'acceptació de les següents condicions d'ús: La difusió d'aquesta tesi per mitjà del servei TDX (**www.tdx.cat**) i a través del Dipòsit Digital de la UB (**diposit.ub.edu**) ha estat autoritzada pels titulars dels drets de propietat intel·lectual únicament per a usos privats emmarcats en activitats d'investigació i docència. No s'autoritza la seva reproducció amb finalitats de lucre ni la seva difusió i posada a disposició des d'un lloc aliè al servei TDX ni al Dipòsit Digital de la UB. No s'autoritza la presentació del seu contingut en una finestra o marc aliè a TDX o al Dipòsit Digital de la UB (framing). Aquesta reserva de drets afecta tant al resum de presentació de la tesi com als seus continguts. En la utilització o cita de parts de la tesi és obligat indicar el nom de la persona autora.

ADVERTENCIA. La consulta de esta tesis queda condicionada a la aceptación de las siguientes condiciones de uso: La difusión de esta tesis por medio del servicio TDR (**www.tdx.cat**) y a través del Repositorio Digital de la UB (**diposit.ub.edu**) ha sido autorizada por los titulares de los derechos de propiedad intelectual únicamente para usos privados enmarcados en actividades de investigación y docencia. No se autoriza su reproducción con finalidades de lucro ni su difusión y puesta a disposición desde un sitio ajeno al servicio TDR o al Repositorio Digital de la UB. No se autoriza la presentación de su contenido en una ventana o marco ajeno a TDR o al Repositorio Digital de la UB (framing). Esta reserva de derechos afecta tanto al resumen de presentación de la tesis como a sus contenidos. En la utilización o cita de partes de la tesis es obligado indicar el nombre de la persona autora.

WARNING. On having consulted this thesis you're accepting the following use conditions: Spreading this thesis by the TDX (**www.tdx.cat**) service and by the UB Digital Repository (**diposit.ub.edu**) has been authorized by the titular of the intellectual property rights only for private uses placed in investigation and teaching activities. Reproduction with lucrative aims is not authorized nor its spreading and availability from a site foreign to the TDX service or to the UB Digital Repository. Introducing its content in a window or frame foreign to the TDX service or to the UB Digital Repository is not authorized (framing). Those rights affect to the presentation summary of the thesis as well as to its contents. In the using or citation of parts of the thesis it's obliged to indicate the name of the author.

TARGETING THE TGF-β PATHWAY OF CANCER-ASSOCIATED FIBROBLASTS IN COLORECTAL CANCER METASTASIS

JORDI BADIA RAMENTOL
Tesi doctoral
2019

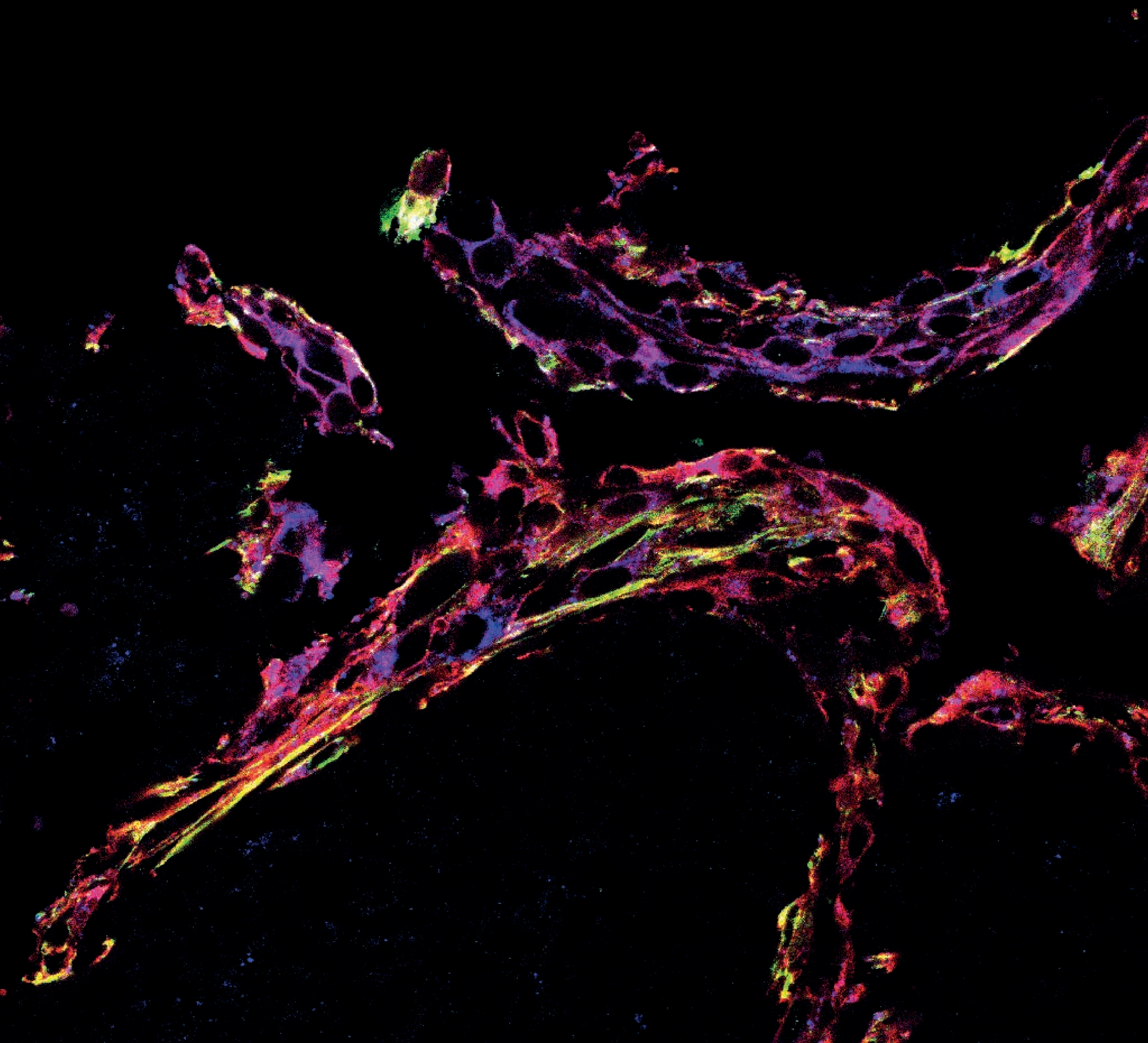

Targeting the TGF-beta pathway of cancer-associated fibroblasts in colorectal cancer metastasis

---

Tesi doctoral - 2019

Jordi Badia Ramentol

Programa de doctorat en genètica

Tesi realitzada a l'Institut de Recerca Biomèdica de Barcelona (IRB Barcelona)

Memòria presentada per Jordi Badia Ramentol per optar al grau de doctor per la Universitat de Barcelona

Director de Tesi:
Eduard Batlle Gómez, PhD

Co-director de Tesi:
Daniele V.F. Tauriello, PhD

Tutora de Tesi:
Montserrat Corominas Guiu, PhD

Doctorand:
Jordi Badia Ramentol

Departament de Genètica
Microbiologia i Estadística

LIBERTAS PERFVNDET
OMNIA LVCE
UNIVERSITAT DE BARCELONA

Laboratori de càncer colorectal
Programa de biologia del càncer

IRB BARCELONA
INSTITUT DE RECERCA BIOMÈDICA

Al Papa, la Mama, el Santi i la Laura,
pel vostre suport diari

“I am I and my circumstance; and, if I do not save it, I do not save myself.”

- José Ortega y Gasset, Meditations on Quixote

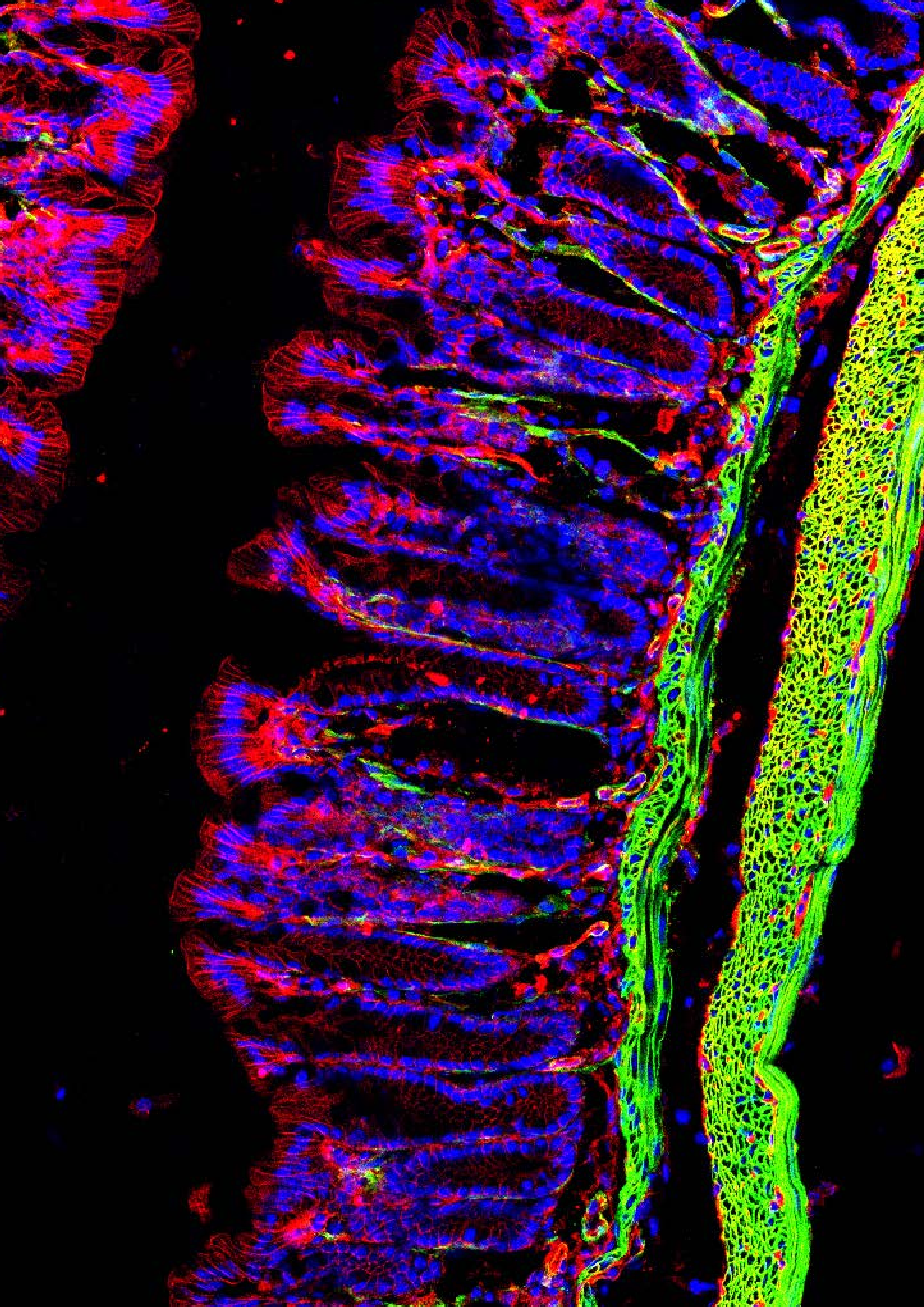

ACKNOWLEDGEMENTS

> *"One, remember to look up at the stars and not down at your feet. Two, never give up work. Work gives you meaning and purpose and life is empty without it. Three, if you are lucky enough to find love, remember it is there and don't throw it away."*
>
> \- Stephen Hawking

Crec recordar haver llegit en els agraïments d'alguna tesi que aquesta secció "és la part més difícil... perquè sou molts els que heu estat aquí i bla bla bla...". Honestament no recordo de qui era i no voldria pas ser controvertit. Els que millor em coneixeu sabeu perfectament que de vegades sóc mordaç, però sempre des de la conya i el respecte. Però sigui qui fos qui ho va dir, i permeteu-me expressar-me lliurement, aquests tòpics avui ens els podem estalviar. Una tesi doctoral és un exercici que posa a prova les capacitats físiques i mentals a nivells extrems. Escriure els agraïments? Facilíssim!! Fàcil, i alhora meravellosa. Els agraïments m'obliguen a pensar i recordar a tots aquells que m'heu fet costat, a tots aquells que no han dubtat en dedicar-me un bon moment, una abraçada, unes paraules d'ànims. Arquímedes va dir: "doneu-me un punt de recolzament i mouré la terra", i tot i que no ho utilitzo en el sentit més literal, vosaltres heu sigut el punt de recolzament que m'ha permès avançar no només els darrers 5 anys, sinó tota la meva vida. Els agraïments em fan recordar que sóc molt afortunat.

Començaré aquesta visita emocional pel laboratori. Edu i Elena, m'heu donat la oportunitat de poder treballar en un laboratori brillant, on he pogut créixer com a científic i com a persona. Sou els primers a qui haig d'agrair dins d'aquesta aventura el laboratori de càncer colorectal. Daniele, you have been mentoring me since I started and even today from your brand new lab. It was not easy at the beginning, but it has been a privilege working side by side with you. I have learnt a lot and I am proud to have you as a co-director of my thesis. Sergio, crec que he perdut el compte de les vegades que m'has salvat el cul. La teva ajuda i empenta constant han fet que pugui seguir endavant amb el projecte. Moltes gràcies també a la Carme, Felipe, Jelena (también por echar un vistazo a mi tesis!), Xavi i Marta, que també he pogut comptar amb vosaltres pel que he necessitat, i pels més recents, Gerhard, Nicola, Ana i Sara, que espero gaudir de vosaltres a l'equip. Mencionar també als antics membres del laboratori, Francisco, Peter, Mark, Alex, Enza i Elisa. Espero que la vida us provi allà on sigueu. Per acabar la ronda del laboratori, voldria fer una menció especial als "Young Batlles", amb qui possiblement he compartit més temps: Gemma, que vam iniciar aquest viatge junts i sempre et tindré carinyo. Clara, eres la més experimentada al laboratori i sempre m'has aixecat els ànims quan més ho he necessitat. Adrià i Adrian, inseparables fins i tot en el nom, vau venir al laboratori carregats de riures i molts bons moments. Maria, la incorporació més recent (i seguiràs sent la novata fins el proper PhD que entri al lab...), veure com cada dia somrius fa que els dies dolents es portin millor. A tots vosaltres, gràcies pels bons records que sempre tindré.

Fora del laboratori, vull agrair a tots els amics que m'he anat trobant al llarg d'aquests cinc anys. Craig and Jürgen, my solution for real problems; Ricardo, Ernest, Alex, Juan and Martí, my bastard laddies; Laura, Helenes (la Roura i la Martí), Anna, Cris, i Busra, my best lassies. We started a beautiful group when we started, and we kept our friendship until the very end. I have enjoyed every day at your side and I hold you very dear to me. May this friendship never end (please?). No m'oblido pas de vosaltres, Salva (mi maestro cervecero), Enric i Mireia, que em feu oblidar els problemes amb vicis, birra i riures. I would like to mention also some of the most recent incorporations in the IRB with whom I have enjoyed good moments: Fede, Cyan, Marta, Inés, Dafni, Miguel and Magdi. Hanging out with you have been one of the best medicines for hard times.

Don't think I have forgotten about Helga. Erik, Chico and Adrian, I already knew how awesome you were when we first met in Krákow. You have helped me escape reality, and I truly hope our friendship will be ever-lasting, no matter how far away we will be from each other.

Ens apropem al final. Toca recordar als amics de tota la vida. Aquells que sempre heu estat allà passi el que passi. Aquells amb qui puc ser jo mateix i que se que em seguireu es-

timant per qui soc. Sandra, hem sigut grans amics des de parvulari. Se que ens veiem poc, però sempre seré a prop teu tant com se que tu hi ets quan ho necessito. Kian, creo que nuestra amistad va más allá de los límites imaginables (guiño guiño). Contigo y con Astrid me siento como en mi propia casa. Finalment, al grup de joves, amb qui tant he compartit: Jus, Lluís, Marina, Tresa i Marta. Jo soc de la opinió de que es poden tenir grups de “millors amics” en tots els àmbits de les nostres vides. Vosaltres, però, sou molt més. Sou els meus germans, que vaig tenir tanta sort de poder conèixer en uns campaments quan era un marrec. Se que m’ha costat exterioritzar les frustracions del doctorat, però sempre he sabut que us tinc i sempre tindré al meu costat. Per a tots vosaltres mencionats en aquest paràgraf, podria escriure una tesi de quant us arribo a estimar.

Els amics són crucials per ser feliç a la vida. Però sóc qui soc gràcies a la família més meravellosa que un podria desitjar. Rosa i Iaia, ens vau deixar aquests darrers anys. Allà a on sigueu, espero que estigueu en pau, i us envio el més gran dels petons. Us duré sempre al meu cor. Balel, tot i que ens vas deixar quan era molt més petit, sempre t’he tingut present al meu cor i a la meva memòria. Tiets Josep Maria, Núria, Enric i Marta i els meus cosins Enric i Núria, he tingut la sort de poder viure molt a prop vostre, i he crescut al vostre voltant, i especialment amb l’Enric i la Núria, ara que ens hem mudat junts amb les nostres parelles! Us estimo amb deliri.

A les meves tietes, Piti, Pate; els meus cosins Isa, Christian, Tito, Sílvia, Vicky, Tomás; i les nostres incorporacions més recents, en Pol, la Martina i en Marc. Vosaltres sou més que les meves tietes i els meus cosins. Sou també les meves mares i els meus germans. M’heu vist créixer, m’heu vist madurar, i m’heu cuidat com si fos el vostre fill o germà. Per tot això i el que ens queda, moltes gràcies. També gràcies als meus tiets Santiago, Montse, Jordi, Oriol i Consol, i als meus cosins Marc, Eva, Irene, Uri, Rosa, Esteban, Núria, Jordi, Ariadna, Edgard i Àlex, i també als més petitons, que tot i que ens veiem menys us estimo moltíssim.

Crec que la càrrega d’un estudiant de doctorat és, per molta ajuda que puguis rebre, és solitària i feixuga. Tot i així, et vaig poder trobar a tu per poder alliberar-la una mica més cada dia. Laura, des que et vaig conèixer ara fa 3 anys i 8 mesos he compartit la meva vida amb tu, una vida meravellosa que espero que no acabi mai. M’has vist en el pitjor dels meus moment, he sigut difícil alguns dies, però sempre has aconseguit aixecar-me els ànims per seguir lluitant. Llevar-me al teu costat cada dia és motiu suficient per poder afrontar les dificultats del dia a dia. T’estimo i t’estimaré sempre. Juntament amb tu, m’agradaria agraïr també a la M. Àngels, al Xavier pare i Xavier fill, per haver-me acollit a la vostra família des del dia que ens vam conèixer i pel vostre suport constant. Si hi ha quelcom millor que tenir una parella fantàstica és que pertanyi a una família fantàstica. Moltes gràcies també a tota la família Garrell i la família Salat per fer-me sentir com un més de la família, amb menció especial a l’Avi Francesc; sempre recordaré tots els bons moments passats amb tu i amb tota la família.

Finalment, reservo l’últim paràgraf als meus pares, Jordi i Imma, i al meu germanet, Santi. Qui soc, el que tinc i el que he aconseguit ho dec tot a vosaltres. Se que l’amor que m’heu donat des que vaig néixer no me’l podrien donar cap altres pares. He tingut el millor papa, la millor mama i el millor germà que un fill podria desitjar, i m’he desviscut perquè cada dia estigueu orgullosos de tenir-me com a fill i germà. Aquesta tesi és tant meva com vostra, per tots millors anys de vida que he pogut tenir amb vosaltres, que són tots ells. Tingueu present que us he estimat, us estimo i sempre us estimaré.

ABSTRACT

Colorectal cancer (CRC) is the second-highest cause for cancer-related mortality worldwide. Patients suffering from CRC generally don't die from primary tumours but rather from metastasis, for which there are no effective therapies to date. CRC progression has been correlated with the accumulation of mutations in four key signalling pathways: Wnt, MAPK, p53 and TGF-β. However, there are no relevant driver mutations described for CRC metastasis, which is produced primarily in the liver. Instead, main features of the tumour microenvironment (TME), such as T cell infiltration and overall levels of TGF-β, have acquired a prognostic value in CRC patients and can predict metastatic potential.

Over the years, a better understanding on the TME has led to designing novel therapies for patients with overt metastatic disease. In the past decade, immunotherapies have represented a revolution in clinical oncology. Of note, antibodies targeting the PD-1/PD-L1 inhibitory pathway have yielded promising results in solid tumours such as melanoma, non-small-cell lung cancer and bladder cancer. Nevertheless, these therapies have failed for the majority of CRC patients, who have immunologically "cold" tumours devoid of cytotoxic T cells. In the first chapter of the present thesis, we have used a novel mouse model for metastatic CRC to describe that T cell exclusion in CRC is driven by TGF-β. By blocking the TGF-β pathway using Galunisertib, an inhibitor of the TGF-β receptor 1, activated T cells were able to infiltrate liver metastasis. Consequently, by combining treatment with Galunisertib and monoclonal antibodies against PD-L1, we were able to cure full-blown liver metastases by unleashing a potent T cell-mediated cytotoxic response.

Despite the results obtained in chapter 1, the specific cellular mechanisms of this TGF-β-mediated T cell exclusion needed further elucidation. In this regard, our lab has reported that TGF-β leads to the expression of a gene signature in cancer-associated fibroblasts (CAFs) that predicts relapse in patients, and that CAFs are crucial for CRC tumour survival and metastatic colonisation. Therefore, we asked whether TGF-β-activated CAFs were also responsible for T cell exclusion in liver metastases.

The work conducted to tackle this question is divided in two chapters. In chapter 2, we have focused on investigating the biology of CAFs from CRC liver metastases, resulting in the establishment of specific markers to target fibroblasts. Moreover, we have defined two different CAF subpopulations coexisting in CRC liver metastases, one of which could be directly related with T cell exclusion. In chapter 3, we have established a genetic mouse model of CRE-LoxP-mediated recombination to specifically ablate the TGF-β receptor 2 in CAFs from liver metastases. CRE expression was driven by the promoter of Transgelin, a TGF-β target gene expressed in CAFs that strongly correlates with relapse in CRC patients. Abrogation of the TGF-β pathway in CAFs did not alter T cell infiltration in metastases. Nevertheless, combination of genetic ablation of the TGF-β receptor 2 and treatment with blocking antibodies against PD-L1 led to curative responses, strongly suggesting that TGF-β-activated CAFs are crucial for mediating T cell exclusion in metastases and evading checkpoint immunotherapy.

TABLE OF CONTENTS

Acknowledgements 7

Abstract 13

Figure index 19

Glossary 23

Introduction 29
- 1. General introduction on Colorectal Cancer (CRC) 31
  - 1.1. Epidemilogy 31
  - 1.2. Progression from benign adenomas to aggressive carcinomas 31
  - 1.3. Staging and survival 33
  - 1.4. Current therapies for CRC 33
  - 1.5. Molecular classification of CRC 34
- 2. The Transforming Growth Factor-β (TGF-β) pathway in CRC 35
  - 2.1. TGF-β is a strong predictor of patient outcome in CRC 35
  - 2.2. The CRC paradox of TGF-β 36
- 3. The tumour microenvironment 38
  - 3.1. The tumour immune microenvironment (TME) 39
    - 3.1.1. Tumour-associated inflammation 39
    - 3.1.2. Adaptive immune responses 40
    - 3.1.3. Avoiding recognition from the immune system 41
    - 3.1.4. TGF-β and the tumour immune microenvironment 42
    - 3.1.5. The revolution of immunotherapies in cancer treatment 42
  - 3.2. Cancer-associated fibroblasts (CAFs) 46
    - 3.2.1. From normal fibroblasts to CAFs 46
    - 3.2.2. Markers for fibroblasts and CAFs 48
    - 3.2.3. Sources of CAFs 48
    - 3.2.4. CAFs enhance tumour progression and metastasis 49
    - 3.2.5. Immunomodulation by CAFs 50
    - 3.2.6. Subpopulations of CAFs in tumours 52
- 4. Prognostic value of the TME in CRC 53
  - 4.1. Infiltration of lymphocytes correlates with improved outcome 53
  - 4.2. CAFs express a gene signature correlated with poor prognosis 54
- 5. TGF-β on the TME of metastatic CRC: from prognosis to novel roles 54

Results 57

1. TGF-β drives immune evasion in genetically reconstituted colon metastasis 59

2. Unravelling the biology of CAFs in liver metastasis 111

    2.1. Identification of two distinct CAF subpopulations from liver CRC metastasis 113

    2.2. Comparative analysis of α^+/β^+ vs α^-/β^+ CAFs 114

    2.3. Dynamics and origin of tumour stroma during metastatic progression 118

    2.4. CAF heterogeneity in metastases generated from distinct MTOs 119

    2.5. Variation of the tumour immune landscape in tumours from different MTOs 122

3. TGF-β-activated CAFs are pivotal for the lack of responses to checkpoint immunotherapy in CRC 127

    3.1. Identifying an appropriate genetic model for inducible fibroblast-specific CRE-LoxP recombination 129

    3.2. Transgelin is a TGF-β target expressed in CAFs 130

    3.3. *Tagln-Cre*^{ERT2} marks TGF-β-activated CAFs from CRC liver metastasis 133

    3.4. Recombination efficiency is subjected to the composition of the tumour stroma 138

    3.5. Depletion of TGFBR2 by recombination leads to a decrease of the mRNA levels of *Tgfbr2* and TGF-β target genes 140

    3.6. TGFBR2-deficient CAFs may not thrive in the tumour stroma 141

    3.7. Liver metastasis burden does not decrease upon deletion of TGFBR2 in CAFs 144

    3.8. KO mice treated with blocking antibodies against PD-L1 have improved survival 144

    3.9. Dynamics of T cell infiltration in KO mice 146

    3.10. Acute TGFBR2 deficiency in CAFs induces T cell responses in CRC metastases 148

    3.11. Long-term recombination of *Tgfbr2* in CAFs induces a memory response 150

    3.12. Ablation of TGFBR2 in CAFs synergizes with αPD-L1 therapy and triggers an adaptive immune reaction 151

Discussion 155

1. Chapter 1: TGF-β drives immune evasion in genetically reconstituted colon cancer metastasis 157

    1.1. Mouse tumour organoids of CRC: a new tool to study the fully immunocompetent TME of metastasis 157

    1.2. TGF-β is required for T cell exclusion in metastatic initiation 158

    1.3. Synergism of checkpoint immunotherapy with TGF-β inhibition leads to strong therapeutic effects 159

2. Chapter 2: Unravelling the biology of CAFs in liver metastasis 160

    - 2.1. At least two distinct CAF subpopulations coexist within CRC liver metastasis 160
    - 2.2. CAF composition is heterogeneous between tumours with the same genetic background 161
    - 2.3. Metastases enriched with myofibroblasts are immune excluded 163
- 3. Chapter 3: TGF-β-activated CAFs are pivotal for the lack of responses to checkpoint immunotherapy in CRC 165
    - 3.1. Tagln is a specific marker for TGF-β-activated CAFs in liver metastasis 165
    - 3.2. The recombination efficiency of *Tagln*+ CAFs is tumour dependent 165
    - 3.3. Abrogation of the TGF-β pathway in CAFs results in a reduction of total CAFs in the TME 166
    - 3.4. Long-term T cell infiltration is not affected by the loss of TGF-β pathway in CAFs 167
    - 3.5. Immune checkpoint therapy synergises with TGF-β pathway inhibition in CAFs to produce curative effects 167
- 4. Final remarks and future directions 169

Conclusions 171

Methodologies 177

References 191

FIGURE INDEX

Figure 1. Representation of the canonical and serrated polyp models for CRC initiation and progression. 32

Figure 2. AJCC stages for CRC patients. 34

Figure 3. The four consensus molecular subtypes for CRC. 35

Figure 4. TGF-β is a strong predictor of patient outcome. 36

Figure 5. The canonical TGF-β signalling pathway. 37

Figure 6. Stromal activation by TGF-β in advanced CRC. 37

Figure 7. The tumour microenvironment. 38

Figure 8. Inclusion of four new hallmarks of cancer to the six pre-existing hallmarks. 39

Figure 9. The cancer-immunity cycle. 41

Figure 10. The immunosuppressive roles of TGF-β on the adaptive immune system. 43

Figure 11. Current therapies and immunotherapies integrated into the cancer-immunity cycle. 44

Figure 12. A. The PD-1/PD-L1 inhibitory pathway. 45

Figure 13. Activation of quiescent fibroblasts into normal activated fibroblasts associated with wound healing or CAFs. 47

Figure 14. Different tumour types recruit different types and proportions of stromal cells. 51

Figure 15. Main cytokines expressed by CAFs with immunossupressive effects in tumours 52

Figure 16. Hypothesis of CAF subpopulations in the TME. 53

Figure 17. Fibroblast markers in healthy liver. 114

Figure 18. Fibroblast markers in CRC liver metastasis. 115

Figure 19. Characterization of fibroblast populations present in liver metastasis. 116

Figure 20. Gene expression analysis of LMCs and CAFs. 117

Figure 21. KI67 expression in CAF subpopulations. 118

Figure 22. CAFs in liver metastasis are not originated from bone marrow-derived progenitors. 119

Figure 23. Dynamic evolution of the stroma in liver metastases. 120

Figure 24. Metastases from different MTOs orchestrate distinct stromal compositions. 121

Figure 25. T cell infiltration decrease over metastatic growth. 122

Figure 26. Abundance of myofibroblasts is negatively correlated to T cell infiltration. 123

Figure 27. Distinct tumour immune microenvironment orchestrated by metastases from different MTOs. 124

Figure 28. A. Analysis of T cell localization in metastases from different MTOs. 125

Figure 29. Analysis of CRE-mediated recombination in CAFs. 130

Figure 30. TAGLN expression in CAFs predicts poor prognosis in CRC patients. 132

Figure 31. Tagln is enriched in CAFs from CRC liver metastasis in mice. 133

Figure 32. TAGLN expression in CAFs decreases upon TGF-β inhibition. 134

Figure 33. Analysis of CRE-mediated recombination in CRC liver metastases from Tagln-CreERT2 mice. 135

Figure 34. Recombination in Tagln-CreERT2 mice occurs in CAFs from liver metastases. 136

Figure 35. Both α+/β+ and α-/β+ CAFs express Tagln. 137

Figure 36. GFP+ cells express classical markers for fibroblasts. 137

Figure 37. Tagln is expressed differently in metastases from different MTOs. 138

Figure 38. Recombination efficiency in CAFs from liver metastasis depends on the MTO of origin. 139

Figure 39. Gene expression analysis of CAFs with recombined Tgfbr2. 140

Figure 40. Total number of CAFs is reduced upon TGF-β inhibition. 141

Figure 41. KO mice show a reduced number of GFP+ CAFs compared to WT mice. 142

Figure 42. Overall TAGLN expression is decreased upon genetic recombination of Tgfbr2 in CAFs. 143

Figure 43. Metastatic burden is not decreased upon deletion of TGFBR2 in CAFs. 144

Figure 44. Combination of checkpoint immunotherapy and TGFBR2 deletion in CAFs cures metastasis. 145

Figure 45. KO mice treated with checkpoint immunotherapy have extended survival. 147

Figure 46. KO mice bearing MTO140-derived metastasis have reduced burden upon treatment with checkpoint immunotherapy. 147

Figure 47. T cell infiltration is not altered upon TGFBR2 deletion in CAFs. 148

Figure 48. Acute treatment triggers T cell responses in liver metastases. 149

Figure 49. Metastases from KO mice show increased memory T cells and B cells. 150

Figure 50. Combination of TGFBR2 deletion with checkpoint immunotherapy produces synergistic effects. 151

Figure 51. Hypothetical model of CAF subpopulations in CRC liver metastasis. 164

Figure 52. Hypothetical model of the immune-derived effects of TGFBR2 ablation in CAFs. 168

Table 1. Top 40 upregulated genes expressed in FAP+ CAFs from patient CRC samples. 131

Table 2. Primers used for mice genotyping. 180

Table 3. Antibodies used for cytometry. 181

Table 4. Antibodies and specific conditions for IHC. 183

Table 5. Taqman probes used for gene expression analysis. 185

Table 6. Databases used for transcriptomic analyses in CRC human patients. 186

GLOSSARY

5-FU	5-Fluoroacil
APC (Immunology)	Antigen Presenting Cell
APC (Wnt pathway)	Adenomatous Polyposis Coli
APCmin	Adenomatous Polyposis Coli, multiple intestinal neoplasia
BCR	B Cell Receptor
CAF	Cancer-Associated Fibroblast
CALD1	Caldesmon 1
CAR T	Chimeric Antigen Receptor T cell
CD(xx)	Cluster of Differentiation (XX)
CIMP	CpG Island Methylator Phenotype
CIN	Chromosome INstability
CMS	Consensus Molecular Subtype
COL	Collagen
CRC	Colorectal Cancer
Cre^{ERT2}	Cre recombinase coupled to Estrogen RecepTor
CTL	Cytotoxic T Lymphocyte
CTLA-4	Cytotoxic T-Lymphocyte Associated protein 4
CTNNB1	CaTeNiN Beta-1
DAB	3’-DiAminoBenzidine
DC	Dendritic Cell
DDR2	Discoidin Domain Receptor tyrosine kinase 2
DLK1	Delta LiKe 1 homolog
DNA	DeoxyriboNucleic Acid
ECM	ExtraCellular Matrix
EGF	Epidermal Growth Factor
EGFR	Epidermal Growth Factor Receptor
EMT	Epithelial-to-Mesenchymal Transition

EndMT	Endothelial-to-Mesenchymal Transition
EOMES	Eomesodermin
EPCAM	EPithelial Cell Adhesion Molecule
FACS	Fluorescence-Activated Cell Sorting
FAP (Colorectal cancer)	Familial Adenomatous Polyposis
FAP (Fibroblasts)	Fibroblast Activation Protein
FDA	Food and Drug Agency
FOLFIRI	Folinic acid (Leucovorin, FOL)+Fluoroacil (F)+Irinotecan (IRI)
FOLFOX	Folinic acid (Leucovorin, FOL)+Fluoroacil (F)+Oxaliplatin (OX)
FOXP3	FOrkhead boX P3
FSP1	Fibroblast Specific Protein 1
GFAP	Glial Fibrillary Acidic Protein
GFP	Green Fluorescent Protein
GLI1	GLI family zinc finger 1
GZMB	Granyme B
HGF	Hepatocyte Growth Factor
HNPCC	Hereditary Non-Polyposis Colorectal Cancer
HNSCC	Head and Neck Squamous Cell Carcinoma
HSCs	Hepatic Stellate Cells
IF	ImmunoFluorescence
IFNγ	Interferon gamma
IGFBP7	Insuline-like Growth Factor Binding Protein 7
IgG_2	ImmunoGlobulin G 2
IHC	ImmunoHistoChemistry
IL-(xx)	Interleukin XX
IRG1	ImmunoResponsive Gene 1
ISL1	ISL LIM homeobox 1
KI	Knock-In
KO	Knock-Out
LMCs	Liver Mesenchymal Cells
LoxP	Locus of X-over P1
MAPK	Mitogen-Activated Protein Kinase

MDSC	Myeloid-Derived Suppressor Gene
MEK	Mitogen-Activated Protein Kinase Kinase
MHC	Major Histocompatibility Complex
MLH1	MutL Homolog 1
MMP	Matrix MetaloProtease
mRNA	Messenger RiboNucleic Acid
MSC	Mesenchymal Stem Cell
MSH	MutS Homolog
MSI	MicroSatellite Instability
MSS	MicroSatellite Stability
mT/mG	membrane-bound TOMATO / membrane-bound GFP
MTOs	Mouse Tumour Organoids
NG2	Neural/Glial antigen 2
NK	Natural Killer cells
NSCLC	Non-Small-Cell Lung Carcinoma
PD-1	Programmed Death receptor 1
PDAC	Pancreatic Ductal AdenoCarcinoma
PDGF	Platelet-Derived Growth Factor
PDGFR	Platelet-Derived Growth Factor Receptor
PD-L1/2	Programmed Death-Ligand 1/2
PFs	Portal Fibroblasts
Pi3K	PhosphoInositide 3-Kinase
PMS2	PMS1 homolog 2
poli-A	Poli-adenylated tail
qRT-PCR	quantitative Reverse Transcriptase Polymerase Chain Reaction
RCC	Renal Cell Carcinoma
ROI	Region Of Interest
SEA1	Surface Exclusion protein 1
SEM	Standard Error of the Mean
TAGLN	Transgelin
TAM	Tamoxifen
TBET	T-box transcription factor TBX21

TC	Tumour Centre
TCR	T Cell Receptor
TGF-β	Transforming Growth Factor Beta
TGFBR	Transforming Growth Factor Beta Receptor
Th	T helper cell
TIL	Tumour-Infiltrating Lymphocyte
TLS	Tertiary Lymphoid Structure
TME	Tumour MicroEnvironment
TN	Triple Negative
TNM	Tumour, Node and Metastasis staging
TP	Tumour Periphery
TP:TC	Ratio Tumour Periphery vs Tumour Centre
Treg	Regulatory T cell
VEGF	Vascular Endothelial Growth Factor
VEH	Vehicle
Wnt	Wingless-type MMTV integration site family
WT	Wild-type
WT1	Wilms Tumour protein 1
α-/β+ CAFs	PDGFRα- PDGFRβ+ αSMA+ CAF subpopulation
α+/β+ CAFs	PDGFRα+ PDGFRβ+ αSMA- CAF subpopulation
αSMA	Alpha Smooth Muscle Actin

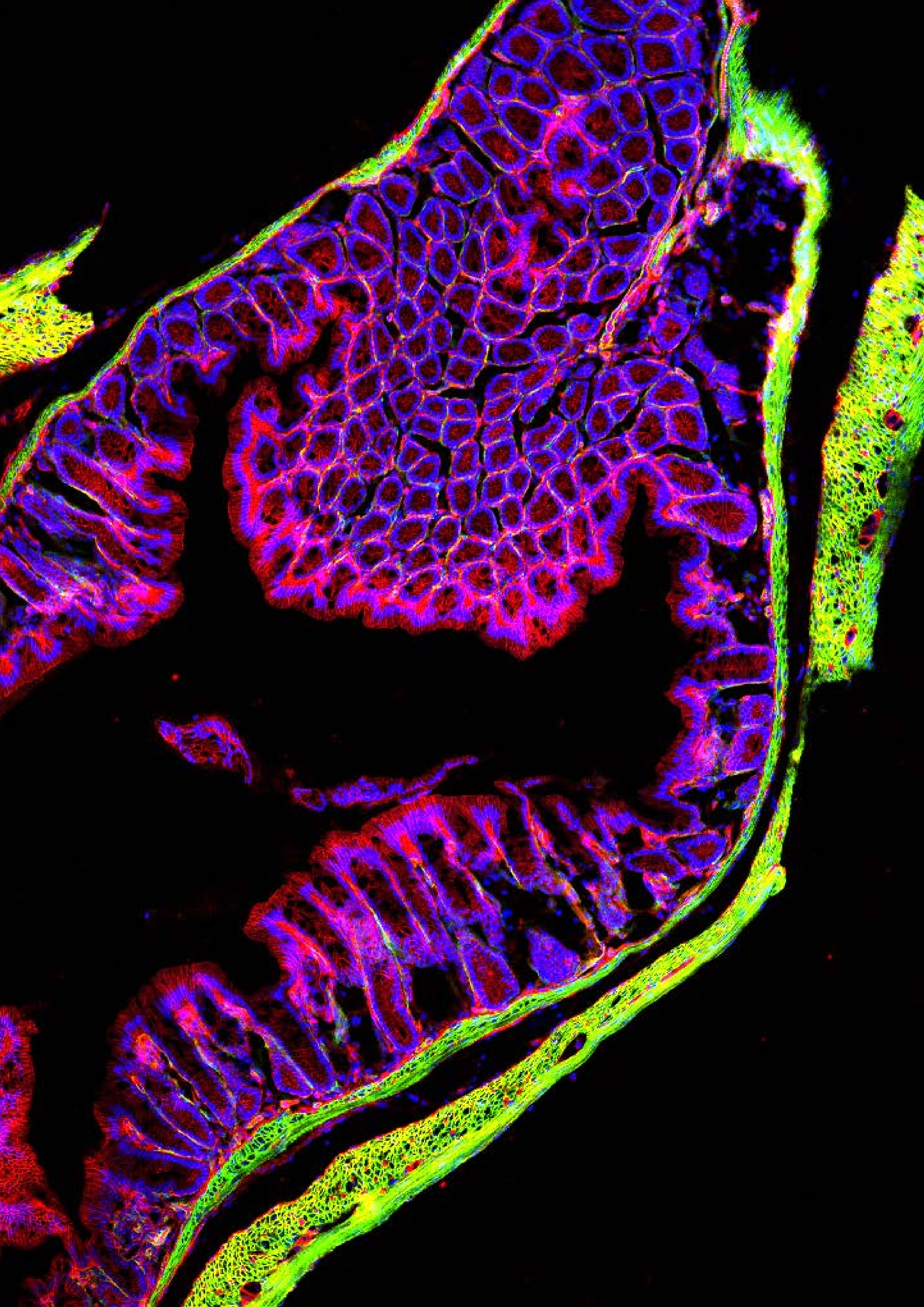

INTRODUCTION

“The good thing about science is that it’s true whether or not you believe in it”

- Neil deGrasse Tyson

1. General introduction on Colorectal Cancer (CRC)

1.1. Epidemiology

Death rates from communicable diseases have declined thanks to recent medical advances and access to an improved health care. As a result, worldwide life expectancy has increased. However, cancer-related mortality has increased by 40% over the past 40 years and it is expected to escalate further (**Bray et al., 2018**). In particular, colorectal cancer (CRC) has become the third-most prevalent type of cancer. This fact can be attributed to an increasingly ageing society and to harmful lifestyle habits such as smoking, reduced physical activity and increased dietary intake. CRC is the most diagnosed type of cancer within the Spanish society and the second-highest cause for cancer-related mortality worldwide (**Bray et al., 2018; Sociedad Española de Oncología Médica, 2019**). Age is the highest risk factor, as 90% of diagnosed CRC occur after 50 years of age (**Asociación Española Contra el Cáncer, 2018**).

CRC is originated by both genetic and environmental factors. Around a 15% of CRC patients are affected by a hereditary component (**Kuipers et al., 2015**). One of the better-understood hereditary syndromes is familial adenomatous polyposis (FAP), characterized by the appearance of a large number of polyps in the colon that could eventually lead to CRC formation. This syndrome is caused by inactivating mutations in the Adenomatous Polyposis Coli (*APC*) gene, which negatively regulates the WNT canonical pathway by binding β-catenin (**Galiatsatos and Foulkes, 2006; Lynch and de la Chapelle, 2003; Segditsas and Tomlinson, 2006**). FAP patients inherit one mutated APC copy. Therefore, the appearance of polyps is a result of inactivation of the remaining allele in the intestinal epithelium. Another major hereditary CRC subtype is Lynch syndrome, also called hereditary non-polyposis colorectal cancer (HNPCC), which accounts for 5-10% of total CRC patients. This syndrome is caused by germline mutations in DNA mismatch-repair genes, including *MLH1*, *MSH2*, *MSH6*, *PMS2* or *EPCAM* (**Fearon, 2011; Lynch et al., 2009**).

Nonetheless, about 75% of CRCs are sporadic, suggesting that environment may play the strongest role in CRC incidence. The risk of acquiring sporadic CRC is increased, however, by the presence of an affected family relative (**Kuipers et al., 2015**). Up to 80% of sporadic CRCs present *APC* mutations, characterized by chromosomal instability (CIN, or microsatellite stable [MSS]), while about 10-15% contain defects of the mismatch repair machinery, which lead to a microsatellite instability (MSI) phenotype (**Fearon, 2011; Kuipers et al., 2015; Nojadeh et al., 2018**).

1.2. Progression from benign adenomas to distant metastasis

The processes governing the formation of adenomas from normal colonic cells and their transition to adenocarcinomas have been extensively studied. As a result, two discrete models of sequential CRC progression have been proposed, which are summarized in **Figure 1** (**Kuipers et al., 2015**). The canonical model involves the formation of tubular adenomatous polyps that progress into adenocarcinomas (**Kuipers et al., 2015**). Meanwhile, between 5-10% of CRC cases originate from a subset of polyps called sessile serrated polyps (**Murcia et al., 2016**)

In 1990, Bert Vogelstein and Eric Fearon proposed for the first time a multi-stage model for CRC progression (**Fearon and Vogelstein, 1990**). This model has been extensively updated and a handful of key mutations have been correlated with every CRC stage. The starting event in more than 80% of CRC patients consists in the acquisition of inactivating mutations in *APC*, which lead to polyp formation (**Fearon, 2011; Fearon and Vogelstein, 1990**). Formation of advanced adenomas involves activating mutations of oncogenes affecting the MAPK signalling pathway. In the canonical model, these generally include point mutations in *KRAS* or amplification of the upstream Epidermal Growth Factor (EGF) receptors (**Fearon, 2011; TCGA, 2012**). On the other hand, point mutations in *BRAF* are associated with the progression of serrated polyps (**Fearon, 2011; Kuipers et al., 2015**). Further facilitating tumour progression are inactivating mutations in tumour suppressor genes included in the Transforming Growth Factor-β (TGF-β) pathway, which typically occur in *SMAD4*, and less frequently in *SMAD2/3* and *TGF-β* receptors (**Fearon, 2011; TCGA, 2012**). Another frequently occurring alteration is the inactivation of cell cycle regulator *p53* (**Fearon, 2011; TCGA, 2012**). The accumulation of these key mutations leads to full-blown colon carcinomas, which can take up to 10 to 15 years to develop (**Figure 1**).

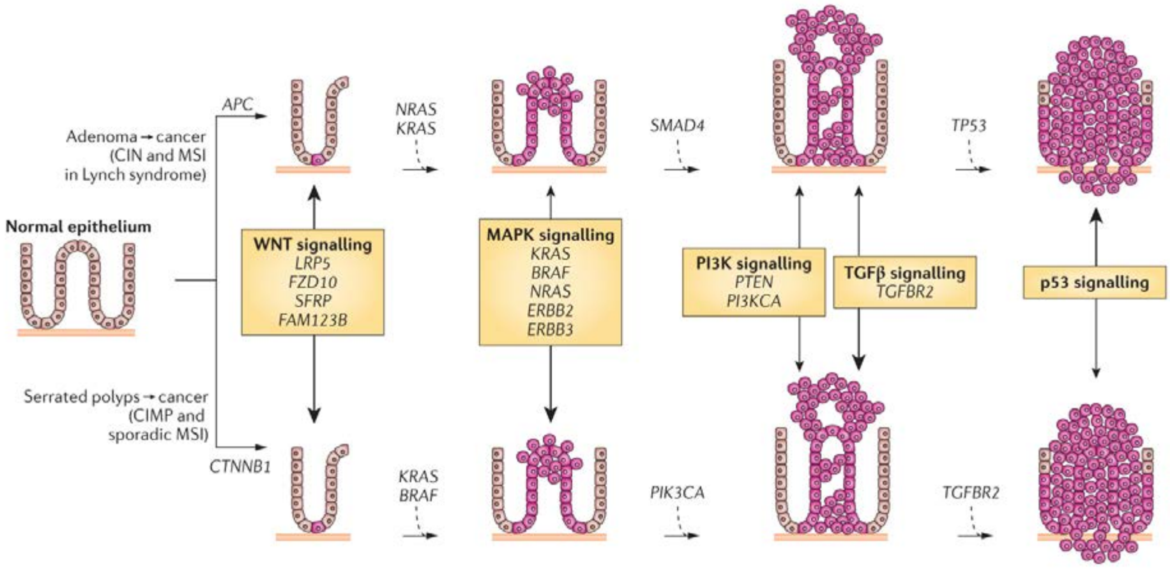
APC
Adenoma → cancer
(CIN and MSI
in Lynch syndrome)
Normal epithelium
Serrated polyps → cancer
(CIMP and
sporadic MSI)
CTNNB1
NRAS
KRAS
KRAS
BRAF
SMAD4
PIK3CA
TP53
TGFBR2
WNT signalling
LRP5
FZD10
SFRP
FAM123B
MAPK signalling
KRAS
BRAF
NRAS
ERBB2
ERBB3
PI3K signalling
PTEN
PI3KCA
TGFβ signalling
TGFBR2
p53 signalling

Figure 1. Representation of the canonical and serrated polyp models for CRC initiation and progression. The classical progression in the canonical model (upper) includes mutations in the WNT pathway (*APC*), the MAPK pathway (*NRAS*, *KRAS*), the TGF-β pathway (*SMAD4*, *TGFBR2*) and *TP53*. On the other hand, events leading to the formation of serrated polyps (lower) include the CpG island methylator phenotype (CIMP) and mutations in catenin-β1 (*CTNNB1*), followed by mutations in *BRAF* and in PI3K signalling. Both progression models share mutations included in the yellow boxes. Figure extracted from **Kuipers et al., 2015**.

During the last decade, several studies support the hypothesis of cancer stem cells that originate and fuel tumours (reviewed in **Ayob and Ramasamy, 2018**). CRC cancer stem cells express a gene program that overlaps to some extent to that of normal *LGR5*+ intestinal stem cells (**Barker et al., 2007; Dalerba et al., 2007; O'Brien et al., 2007; Ricci-Vitiani et al., 2007**). Because of their proliferative capabilities, cancer stem cells are likely to generate distant metastasis. Evidence shows that self-renewing, stem-like tumour cells are able to generate metastasis compared to differentiated-like, non-proliferating cells (**Dieter et al., 2011; Merlos-Suárez et al., 2011**).

Metastatic dissemination is an inefficient process that requires the trafficking of tumour cells through the circulation, colonization, and resuming tumour growth into distant organs. In CRC, tumour cells enter the portal circulation and rapidly colonize the liver, the primary metastatic site in CRC patients. Less frequently, CRC can also metastasize to the lungs, which require that tumour cells reach the general circulation to infiltrate the lungs (reviewed in **Tauriello et al., 2017**). In contrast to the mechanisms described for progression from adenomas to carcinomas, the processes governing metastatic dissemination from aggressive carcinomas remain poorly understood.

1.3. Staging and survival

CRC is most often classified using the Tumour, Node and Metastasis staging (TNM) established by the American Joint Committee on Cancer (AJCC), which is based in the following three parameters (**AJCC, 2009; Weiser, 2018**), assessed by histopathology:

- T: tumours are classified according to size and invasiveness. The lowest category (Tis) includes carcinomas *in situ* which have not invaded subjacent layers. Further categories define tumours that invade the submucosa (T1), the muscularis propria (T2), pericolorectal tissues (T3), and the peritoneum and/or other structures (T4).
- N: measures tumour cell spread into regional lymph nodes. N1 CRCs contain metastasis in 1-3 regional lymph nodes. N2 is assigned when 4 or more lymph node metastases have been detected.
- M: informs whether tumours have generated distant metastasis to one (M1a) or more (M1b) organs, or whether the distant peritoneal surface is involved (M1c).

According to AJCC guidelines, once TNM parameters have been determined, CRC patients are grouped into four different stages (**AJCC, 2009; Weiser, 2018; American Cancer Society; National Cancer Registration and Analysis Service**, **Figure 2**):

1) Stage 0: localized and non-invasive carcinomas *in situ*.
2) Stage I (T1-2, N0, M0): localized tumours that invade the lamina propria and muscularis mucosa. 5-year survival rate is above 90% and only localized resection surgery is required.
3) Stage II (T3-4, N0, M0): comprises tumours that spread out of the muscle layer of the colon wall without signs for lymph node metastasis. Stage II CRC patients have a 60-80% survival.
4) Stage III (T1-4, N1-2, M0): tumours become more invasive and may have invaded nearby tissues. Also, metastasis may be present in nearby lymph nodes. Adjuvant chemotherapy is required after surgery. Survival rates are 25-60%.
5) Stage IV (T1-4, N1-2, M1): tumour cells have spread to distant organs. Liver, lungs and peritoneum are primary sites for CRC tumour cells spreading and metastasis formation. Despite recent therapeutic improvements, patients with metastatic CRC have a survival rate below 8% and to date there is no effective treatment (**Yaffee et al., 2015; Yu and Cheung, 2018**).

1.4. Current therapies for CRC

For CRC, the main therapeutic strategy is removal of primary tumour with surgery, sometimes accompanied by preoperative chemotherapy or radiotherapy, the latter mainly for rectal cancer (**Aklilu and Eng, 2011; De Rosa et al., 2015**) This strategy is highly effective for tumours diagnosed at stage I (**Figure 2**). However, tumours at stage II and stage III require a combination of surgery with adjuvant therapy to reduce recurrence (**Figure 2**). Although there is no fully accepted postoperative therapy for CRC, current chemotherapeutic strategies include targeting highly proliferative tumour cells with drugs like 5-Fluoroacil (5-FU), Oxaliplatin or Irinotecan. Usually, a cocktail of cytotoxic drugs is administrated (i.e FOLFIRI [5-FU + Leucovorin + Irinotecan], FOLFOX [5-FU + Leucovorin + Oxaliplatin]) (**Aklilu and Eng, 2011**).

Simultaneously, alterations in CRC can be used as biomarkers to stratify patients into specialized therapy cohorts (**Van Schaeybroeck et al., 2011**). One example is using blocking antibodies against EGFR (Cetuximab or Panitumumab) in CRCs without mutations in *BRAF*, *KRAS* and *NRAS* (**Kuipers et al., 2015; Van Schaeybroeck et al., 2011**). Other examples are the specific inhibition of BRAF (Vemurafenib) for patients presenting serrated

AJCC	Stage I	Stage II	Stage III	Stage IV
CRC representation	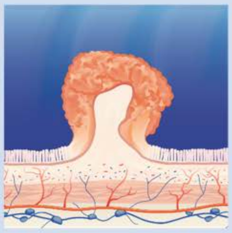	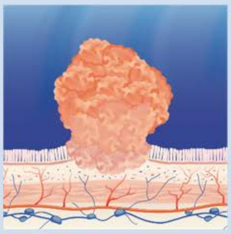	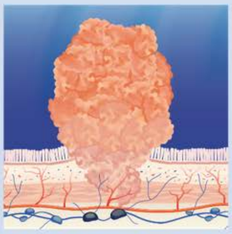	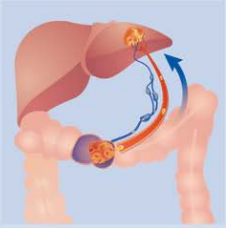
5-year survival rate	90 %	70 %	56 %	<15 %
Relapse	5 %	10 – 15 %	40 %	N/A
Standard treatment	Surgery of primary tumour	Surgery of primary tumour + chemotherapy (optional)	Surgery of primary tumour + chemotherapy	Surgery of primary tumour and metastasis + chemotherapy

Figure 2. AJCC stages for CRC patients. For each stage, the 5-year survival rate, the probability of relapse from the primary tumour and the main therapeutic strategies are represented. Relapse from primary tumour does not apply for stage IV CRC.

adenomas with mutations in this kinase (**Ursem et al., 2018**) and the inhibition of angiogenesis with anti-VEGF such as Bevacizumab (**Van Schaeybroeck et al., 2011**).

About 50% of CRC patients will develop distant metastasis, and approximately 20% of them already present synchronous liver metastasis, which are detected before or at the same time the primary tumour is diagnosed (**Verhoef et al., 2011**). Overall survival for patients with metastatic disease has improved to a median of 30 months (**Kuipers et al., 2015**). However, current therapies not only produce severe secondary effects, but also tumours develop resistances that make these strategies ineffective in the long term (**Van Der Jeught et al., 2018**). Current therapeutic strategies for metastatic CRC follow a sequence of at least two lines of treatment. When resectable metastases are restricted to the liver, surgical removal in combination with chemotherapy and/or blocking antibodies during the first line of treatment is the main treatment option and ensures up to 65% of improved survival rate (**Figure 2**). For patients with synchronous unresectable metastasis, resection of the primary tumour can be considered prior to treatment (**Modest et al., 2019; Verhoef et al., 2011**). The second line of treatment consists in combinations of fluoroacil, oxaliplatin and irinotecan with anti-EGFR and VEGF antibodies, which depend on the decision taken for the first line of treatment. A third line of treatment can be considered, but response rates are substantially reduced (**Modest et al., 2019**).

1.5. Molecular classification of CRC

Although recurrent driver mutations have been identified, non-hypermutated CRCs are highly heterogeneous (**Fearon, 2011; TCGA, 2012**). This poses a challenge in establishing a molecular classification for colorectal tumours with clinical prognostic relevance. Several independent studies have tried to classify CRC according to gene expression profiling (**Marisa et al., 2013; Sadanandam et al., 2013; De Sousa E Melo et al., 2013**). However, the similarities found were not very consistent across the different suggested classification systems.

Efforts to reconcile these classifications (**Sadanandam et al., 2014**), integrating genomic data from several sources including mutation, copy number, methylation, microRNA and proteomics, led to four robust Consensus Molecular Subtypes (CMS) (**Guinney et al., 2015**, **Figure 3**). MSI hypermutated tumours fall into the CMS1 category, which has the best survival rates in the clinic, but worsen after tumour relapse. Non-hypermutated tumours are classified across the three remaining CMS: CMS2 represents the canonical category enriched in tumours with high epithelial differentiation and upregulation of WNT and MYC targets. CMS3 encompasses tumours enriched in *KRAS* mutations, which leads to enriched metabolic epithelial signatures. Finally, CMS4 is characterized by tumours with increased stromal signatures and TGF-β signalling. Patients with tumours classified as CMS4 have worse overall survival compared to the other three groups (**Guinney et al., 2015**).

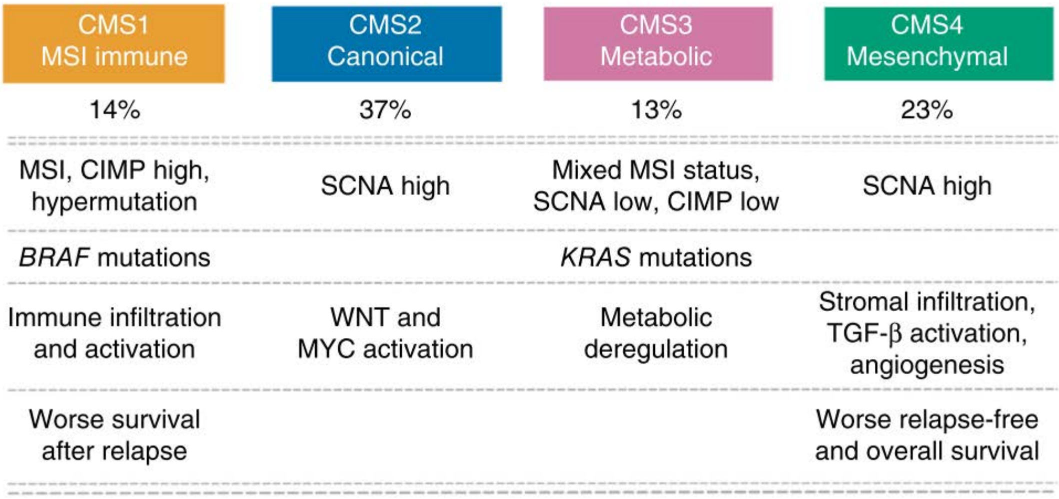

CMS1 MSI immune	CMS2 Canonical	CMS3 Metabolic	CMS4 Mesenchymal
14%	37%	13%	23%
MSI, CIMP high, hypermutation	SCNA high	Mixed MSI status, SCNA low, CIMP low	SCNA high
BRAF mutations		*KRAS* mutations	
Immune infiltration and activation	WNT and MYC activation	Metabolic deregulation	Stromal infiltration, TGF-β activation, angiogenesis
Worse survival after relapse			Worse relapse-free and overall survival

Figure 3. The four consensus molecular subtypes for CRC. Percentages represent the proportion of analysed tumours included in each category. SCNA = somatic copy number alterations. MSI = Microsatellite Instability. CIMP = CpG island methylator phenotype. Figure extracted from **Guinney et al., 2015**.

2. The Transforming Growth Factor-β (TGF-β) pathway in CRC

2.1. TGF-β is a strong predictor of patient outcome in CRC

Understanding CRC heterogeneity could help treatment decision making in the clinical setting. The CMS classification offers strong molecular similarities in tumours within a same category (**Guinney et al., 2015**). However, its use as decision criterion for patient treatment still remains questionable. It should be noted that while 30-40% of CRC patients present relapse and overt metastatic disease, only 8% of tumours at stage IV were included into this analysis, leaving this population underrepresented in this classification (**Fontana et al., 2019**). Furthermore, while some mutations are enriched in certain groups -i.e. *BRAF* in CMS1 and *KRAS* in CMS3-, CMS2 and CMS4 still contain an additional level of biological variability affecting responses to chemotherapy. Indeed, both CMS2 and CM4 can be subclassified into additional categories that are also predictive for poor outcome, which implies that the CMS classification lacks prognostic strength (**Fontana et al., 2019**).

Whereas there are a number of prognostic biomarkers used for stage II and stage III patients -i.e MSI tumours, *BRAF* and *EGFR* mutations-, the ability to predict relapse outcome and metastatic dissemination remains elusive. In an attempt to solve this issue, analysis of serum from CRC patients revealed that high levels of TGF-β1 were associated with poor outcome (**Tsushima et al., 2001**). Later, an extensive analysis of a CRC metacohort led by Alexandre Calon and Elisa Espinet in our laboratory demonstrated that stage II to IV tumours expressed higher levels of TGF-β compared to those from stage I. Moreover, they showed that the levels of TGF-β were a robust predictor of relapse in patients with stage II and stage III CRC, where patients with tumours expressing elevated levels of TGF-β had poor outcome while patients with low levels remained relapse-free in an interval of 10 years (**Calon et al., 2012**, **Figure 4**).

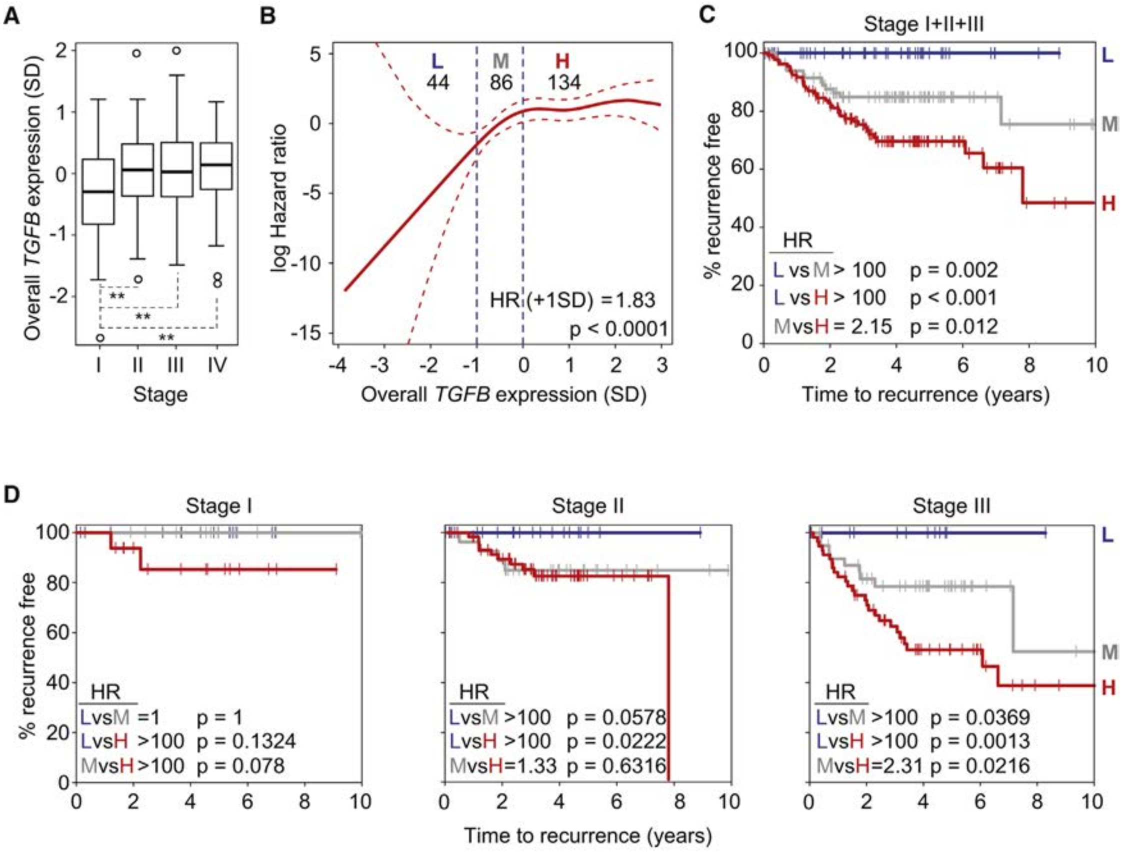

Figure 4. TGF-β is a strong predictor of patient outcome. A. Detected TGF-β expression in patients from all four AJCC CRC stages. **B.** Smooth function correlating relative expression of TGF-β with risk of recurrence. For each standard deviation of TGF-β expression, the Hazard Ratio (HR) increases by 1.83. **C.** Kaplan-Meier plots showing recurrence of CRC after therapy over time in stages I, II and III combined (**C**) and individually (**D**). Low, Medium and High groups are defined as in **B**. Figure extracted from **Calon et al., 2012**.

2.2. The CRC paradox of TGF-β

TGF-β canonical signalling pathway starts upon binding of activated TGF-β ligands (TGF-β1, β2 and β3) to TGF-β Receptor 2 (TGFBR2). TGFBR2 then heterodimerizes with TGF-β Receptor 1 (TGFBR1), whose cytoplasmic domain becomes phosphorylated by TGFBR2. As a result, SMAD2 and SMAD3 proteins become phosphorylated and form a heterotrimeric complex with SMAD4. This protein complex translocates into the nucleus, where SMAD4 binds target regions of the DNA and allows the expression of multiple target genes (**Padua and Massagué, 2009**, **Figure 5**).

TGF-β exerts numerous functions that depend on the cellular context. In epithelial cells, TGF-β induces a gene-expression program that promotes cytostasis and cell differentiation, which makes it a potent tumour suppressor (**Massagué, 2012**). Therefore, loss of TGF-β sensitivity is often required for tumour cells in order to proliferate. Indeed, *TGFBR2* and *SMAD4* are frequently mutated in CRC tumours (**Fearon, 2011; TCGA, 2012**). Interestingly, CRC tumours with mutated TGF-β pathway in an APC mutant background raise their overall

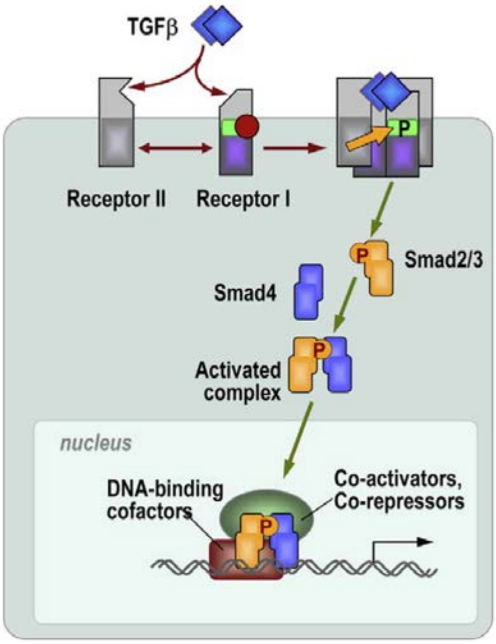

Figure 5. The canonical TGF-β signalling pathway. Upon binding TGF-β ligands, TGFBR2 dimerizes and phosphorylates TGFBR1. Signal is transduced by phosphorylating SMAD2/3, which form a protein complex with SMAD4. This complex then translocates into the nucleous and allows expression of multiple target genes together with other co-factors. Figure extracted from **Massagué and Gomis, 2006**.

TGF-β1 expression levels (**Muñoz et al., 2006**).

A duality exists by which TGF-β both inhibits tumorigenesis and promotes malignancy and relapse once tumours are established. Paradoxically, tumour epithelial cells with a truncated TGF-β pathway cannot respond to secreted TGF-β. Hence, the importance of TGF-β expression in advanced cancers lies in how it affects components of the tumour microenvironment (TME). Indeed, immunohistochemistry (IHC) stainings for phosphorylated SMAD3 (p-SMAD3) in CRC tumours show a stronger signal in the TME compared to tumour epithelial cells (**Calon et al., 2012**, **Figure 6**).

In contraposition to the notion of tumour cells as main drivers of malignancy, this phenomenon highlights how tumour progression may be a result of a complex interaction between tumour cells and a reactive TME. In CRC, as will be discussed further below, TGF-β helps create a microenvironment that promotes tumour growth and survival. Consequently, this fact opens a new frontier for novel tumour therapies that prioritize targeting cells in the TME over the proliferating tumour cells, which could also avoid possible drug resistances as the TME is genetically more stable compared to tumour epithelial cells (**Tauriello and Batlle, 2016**).

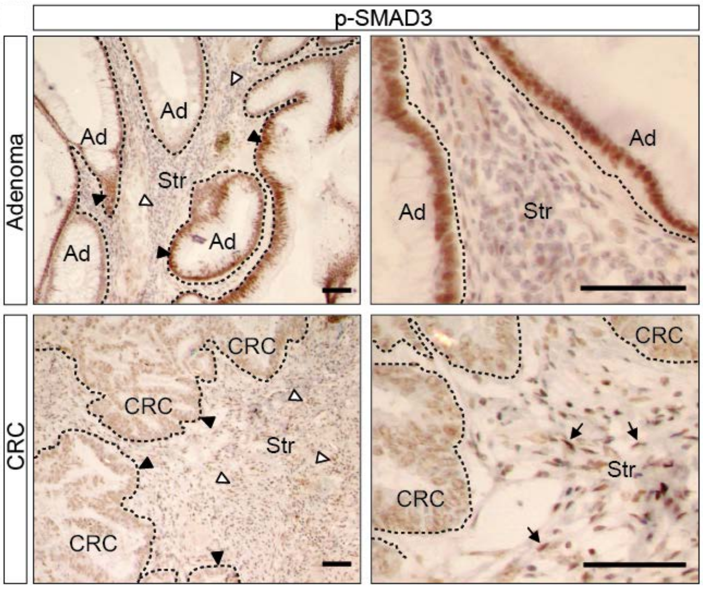

Figure 6. Stromal activation by TGF-β in advanced CRC. Immunohistochemistry stainings of p-SMAD3 in adenomas (Ad) and carcinomas (CRC). Adenomas show stronger expression of p-SMAD3 in epithelial cells, while in CRC signal is found exclusively in the tumour stroma (Str). Black arrowheads = epithelial cells. White arrowheads = stromal cells. Black arrows = stromal cells with positive staining for p-SMAD3. Figure extracted from **Calon et al., 2012**.

3. The tumour microenvironment (TME)

The concept of an existing TME in tumours is not novel, as at the end of the 19th century Stephen Paget proposed the "seed and soil" hypothesis that explains how tumour cells (the "seed") would need and take advantage from favourable non-tumoral cells located in select tissue (the "soil") for metastatic growth (reviewed in **Langley and Fidler, 2011**). However, the TME gained importance during the past two decades in contraposition of the simplistic point of view where tumours were considered as a mass of highly proliferative, mutated cells. Indicating the emerging appreciation for the TME, Douglas Hanahan and Robert Weinberg included parameters of the TME as hallmarks of cancer in their updated review (**Hanahan and Weinberg, 2011; Hanahan et al., 2000** **Figure 7**).

The TME is composed of cells surrounding and infiltrated into tumours, and includes any secreted factors, elements and physical characteristics such as pH and stiffness that compose the extracellular matrix (ECM). Cells of the TME establish complex and tight relationships with cancer epithelial cells and cancer stem cells, which typically results in a protective environment for malignant growth. The main cellular subsets found in the TME are endothelial cells, immune cells and cancer-associated fibroblasts (CAFs) (**Hanahan and Weinberg, 2011**, **Figure 7**). Within the scope of this work, we will focus specifically on immune cells and CAFs.

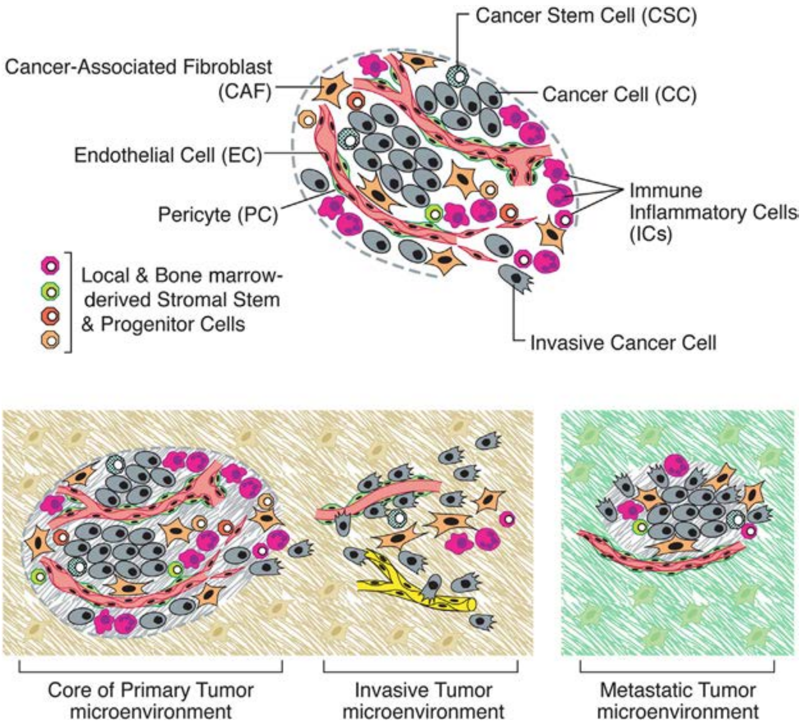
Cancer Stem Cell (CSC)
Cancer-Associated Fibroblast (CAF)
Cancer Cell (CC)
Endothelial Cell (EC)
Immune Inflammatory Cells (ICs)
Pericyte (PC)
Local & Bone marrow-derived Stromal Stem & Progenitor Cells
Invasive Cancer Cell
Core of Primary Tumor microenvironment
Invasive Tumor microenvironment
Metastatic Tumor microenvironment

Figure 7. The tumour microenvironment. Cancer cells and Cancer stem cells are embedded into an environment of non-tumoral cells that support their growth, invasion and metastasis to distant organs. Cells of the tumour microenvironment include immune cells, endothelial cells, pericytes and cancer-associated fibroblasts. Figure extracted from **Hanahan and Weinberg, 2011**.

3.1. The tumour immune microenvironment

3.1.1. Tumour-associated inflammation

Tumours are nowadays considered as entities that establish complex interactions with the immune system. The TME of most, if not all, tumours includes a wide range of inflammatory cytokines and cells. Among other features, the redefinition of the hallmarks of cancer in 2011 included cancer-related inflammation and avoiding destruction by the immune system (**Hanahan and Weinberg, 2011** **Figure 8**). These two hallmarks reflect the existence of both anti- and pro-tumoral immune responses. These opposite effects are not surprising, however, when tumours are compared to a wound: for any wound-healing process, the damaged tissue releases cytokines that recruit inflammatory cells which will destroy any foreign pathogen that has infiltrated the tissue. Once the pathogens are cleared, a second inflammatory phase will allow proliferation of neighbouring cells and extracellular matrix deposition in order to fully repair the damaged tissue (**Shaw and Martin, 2009**). As "wounds that do not heal", tumours take advantage of a chronic regenerative inflammation to support their growth (**Dvorak, 1986**). For instance, in pancreatic ductal adenocarcinoma (PDAC) tumour-associated macrophages support metastatic tumour growth by activating surrounding myofibroblasts (**Nielsen et al., 2016**).

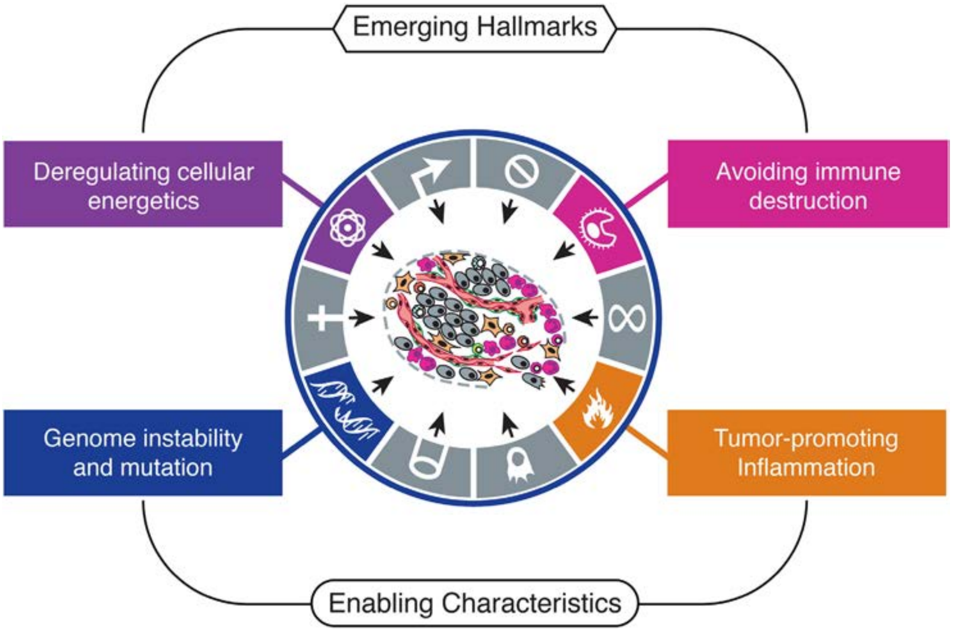
Emerging Hallmarks
Deregulating cellular energetics
Avoiding immune destruction
Genome instability and mutation
Tumor-promoting Inflammation
Enabling Characteristics

Figure 8. Inclusion of four new hallmarks of cancer to the six pre-existing hallmarks. Two of the new hallmarks describe tumour-immune interactions: tumour-promoting inflammation and avoiding immune destruction. Figure extracted from **Hanahan and Weinberg, 2011**.

Tumours recruit a variety of inflammatory cells through two different pathways: an "extrinsic" and an "intrinsic" pathway (**Mantovani et al., 2008**). The extrinsic pathway is driven by previous chronic inflammatory diseases that predispose to cancer. The first connection between immunity and tumorigenesis was established in the 19th century, with the observations that tumours often arise from chronic inflammation sites (Reviewed in **Balkwill and Mantovani, 2001**). A very good example is found in patients suffering from inflammatory bowel disease, which predisposes to development of CRC (**Jess et al., 2012**). Alternatively, the intrinsic pathway is driven by acquired mutations in tumour cells that can lead to secretion of cytokines and chemokines, which coordinate autocrine and paracrine interactions between inflammatory cells and tumour cells. These interactions in turn result in increased migration, angiogenesis and metastasis (**Anderson et al., 2017; Erreni et al., 2011; Mantovani et al., 2008**). For instance, in a model for breast cancer metastasis, upregulation of HER2 in cancer cells activates NF-κB, which in turn activates production of CCL2. Subsequently, the secretion of CCL2 attracts macrophages that promote metastatic dissemination (**Linde et al., 2018**).

However, several other studies correlate the presence of immune infiltrates with a better outcome in patients (**Barnes and Amir, 2017; Carstens et al., 2017; Galon et al., 2006**). Despite the pro-tumoral effects of inflammation, these studies imply that the immune system in the TME can execute anti-tumour effects.

3.1.2. Adaptive immune responses

Adaptive immunity is directed to an effective eradication of pathogens in a host. Pathogens contain foreign antigens that are processed by infected cells and are typically "shown" to cells of the immune system by loading them into proteins belonging to the major histocompatibility complex (MHC), which are generally divided into MHC class I (MHC-I) and class II (MHC-II). MCH-II is mainly expressed by professional antigen-presenting cells (APCs) such as dendritic cells (DCs) and macrophages, which uptake and process antigens released by destroyed pathogens and infected cells. Antigen presentation by MHC-II proteins consequently triggers the activation, trafficking and expansion of T cells to eliminate the aggression. On the other hand, MHC-I is expressed in all cell types but erythrocytes, and mediate destruction of infected cells by cytotoxic T cells (CTLs) and alternatively by natural-killer (NK) cells when the levels of MHC-I are decreased. For an effective T cell response, T cells do not only first need to encounter a foreign antigen coupled to MHC receptors, which will bind the T cell receptors (TCR) expressed on the surface of T cells (step 6, **Figure 9**), but also they require positive co-stimulation through the interaction between CD28 expressed on T cells and CD80 (B7.1) and/or CD86 (B7.2) from APCs (**Sharpe and Pauken, 2018**). Another subset of lymphocytes are B cells, which act also as APC and produce antibodies upon recognition of an antigen through their B cell receptor (BCR). Secretion of antibodies by B cells further exacerbates immune responses.

Due to the high mutational burden of many tumours, tumour cells express neoantigens that differ from those expressed by normal cells, which are recognized by the host's immune system as foreign. Therefore, tumours are under constant vigilance by immune cells and are destroyed in a process called "immune surveillance" (**Swann and Smyth, 2007**). In 2013, Daniel Chen and Ira Mellman described the steps of anti-cancer immune responses in the "Cancer-Immunity Cycle" (**Chen and Mellman, 2013**, **Figure 9**). In this cycle, neoantigens generated due to mutations or aberrant expression patterns are processed by professional APCs. Through presentation of neoantigens and the expression of activating receptors and cytokines, APCs trigger an anti-tumour T cell-mediated response. Consequently, the destroyed cancer cells release more neoantigens that further foster adaptive responses (**Chen and Mellman, 2013**).

The cancer-immunity cycle describes how adaptive immunity should typically react to any cancer, and it includes the activation of CD4+ helper 1 T cells (Th1 cells) and CD8+ cytotoxic T cells (CTLs), resulting in recognition and specific destruction of cancer cells. Infiltration of CTLs in tumours is often mediated by stromal secretion of CXCL9 and CXCL10, and upon stimulation they secrete IL-2, interferon gamma (IFNγ), Granzyme B (GZMB), and Perforin (**Chen and Mellman, 2013; Nowacki et al., 2007**). IL-2 induces activation and proliferation of T cells in a paracrine and autocrine manner (**Chen and Mellman, 2013**), whereas IFNγ induces activation of macrophages and expression of MHC-II (**Gieseck et al., 2018**). Secreted GZMB is internalized by malignant cells and, aided by Perforin, induces their de-

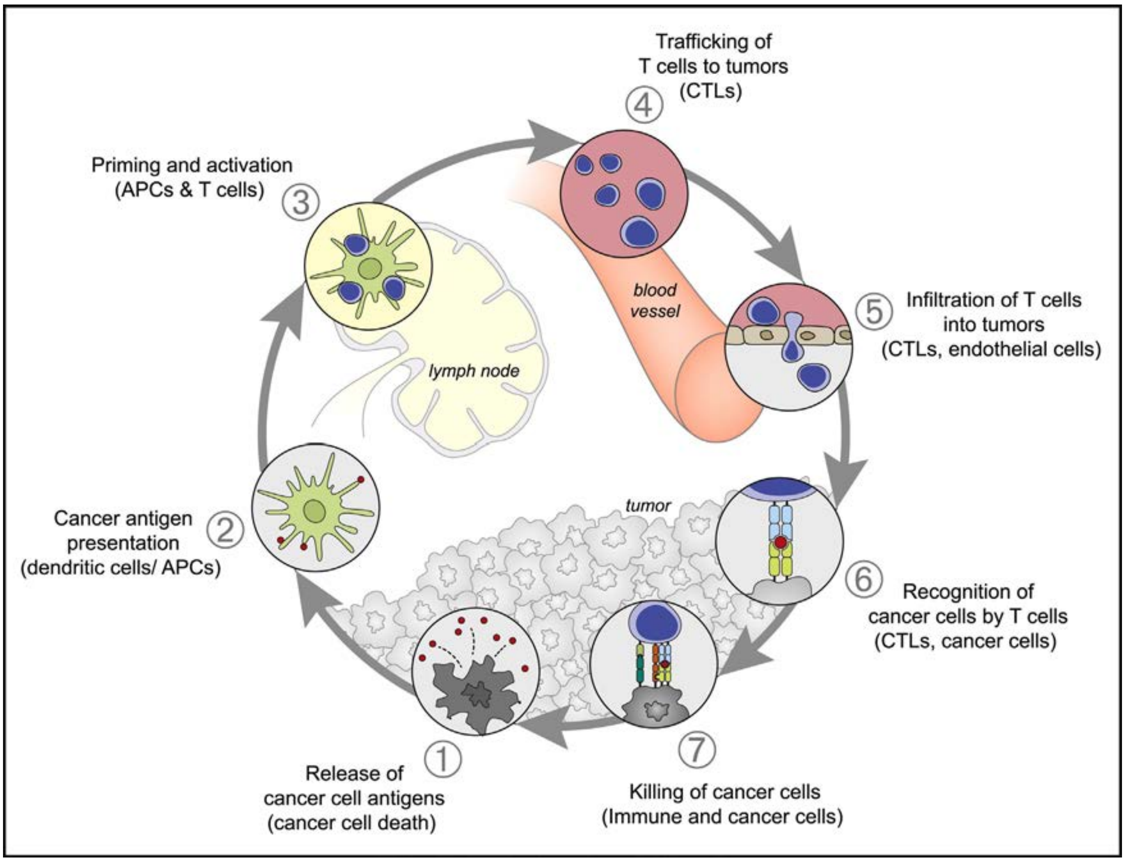
Trafficking of
T cells to tumors
(CTLs)
4
Priming and activation
(APCs & T cells)
3
blood
vessel
5
Infiltration of T cells
into tumors
(CTLs, endothelial cells)
lymph node
tumor
Cancer antigen
presentation
(dendritic cells/ APCs)
2
6
Recognition of
cancer cells by T cells
(CTLs, cancer cells)
1
Release of
cancer cell antigens
(cancer cell death)
7
Killing of cancer cells
(Immune and cancer cells)

Figure 9. The cancer-immunity cycle. Seven steps are described by Chen and Mellman, starting with the release (1) and processing of tumour antigens (neoantigens) by APCs (2). Primed APCs traffic to lymph nodes and activate T cells (3), which then travel (4) and infiltrate tumours (5). Upon recognition neoantigens loaded in the MHC complex (6), T cells mediate specific killing of cancer cells (7). After death, tumour cells release neoantigens (1) which further foster immunologic responses by restarting the cycle. Figure extracted from **Chen and Mellman, 2013**.

struction (**Waterhouse et al., 2004**). Several reports have demonstrated that deficiencies in CTLs and Th1 cells promote tumour growth, and their presence is widely accepted as a favourable prognostic marker (**Barnes and Amir, 2017**). Moreover, in some cancers T cells and B cells have been found creating lymphoid-like agglomerations called as “tertiary lymphoid structures” (TLS). These TLS are mostly found within the invasive margin and have also been associated mostly with good prognosis (**Hiraoka et al., 2016; Pagès et al., 2010; Salmon et al., 2019**).

The immunological events described in the cancer-immunity cycle belong to type 1 immune responses, which are directed against a particular pathogen or, in this case, tumour cells. On the other hand, type 2 immunity is dedicated to arrest inflammation and foster tissue repair. These responses are commonly mediated by secretion of IL-4, IL-5, IL-9 and IL-13, which activate CD4+ T cells into a helper 2 phenotype (Th2 cells) (**Gieseck et al., 2018**). In addition, tumours secrete CCL22 that recruits CD4+ FOXP3+ regulatory T cells (Tregs), which in turn also repress CTL activity (**Gajewski et al., 2013**).

3.1.3. Avoiding recognition from the immune system

For a tumour to be successful it must overcome the immunologic selective pressure. Tumours possess several mechanisms by which they can break the cancer-immunity cycle (**Figure 9**). The first example could be selection of tumour cells that avoid eradication by the immune system, a process that is called "immunoediting" (**Dunn et al., 2004, 2006; O'Donnell et al., 2019**). Consequently, immunoedited tumour clones will sustain tumour growth. In this line, some tumours have a rather low mutational burden and do not produce as many neoantigens, resulting in the generation of "immunologically cold" tumours that are poorly recognized by immune cytotoxic cells (**Bonaventura et al., 2019; Spranger, 2016**).

A second mechanism is the ability of these tumours to "mask" these neoantigens by blocking their presentation at the plasma membrane (**Bonaventura et al., 2019**). Loss of MHC-I expression by tumour cells is one recurrent strategy to avoid T cell recognition (**Bonaventura et al., 2019**). In addition, a recent study elegantly demonstrated how the immune system is blind to slow-proliferating stem cells in homeostatic tissues which express low levels of MHC-I proteins (**Agudo et al., 2018**). Although it still remains speculative, the same mechanism could exist for slow-proliferating cancer stem cells, which would become resistant to immune surveillance (**Malladi et al., 2016**).

Finally, tumour cells can express a range of inhibitory cytokines and receptors that inhibit proliferation and activation of NK cells and CTLs. Several cytokines in the TME promote recruitment or polarization of anti-inflammatory macrophages and myeloid-derived suppressor cells (MDSCs). These cells can suppress Th1 immune responses directly or through the recruitment of Treg cells (**Veglia et al., 2018**). Infiltration of Treg cells suppress CTL activity through secretion of IL-10 and TGF-β and is often associated with poor outcome in patients (**Gajewski et al., 2013; Galdiero et al., 2013; Mantovani et al., 2008; Tu et al., 2016**). On the other hand, binding of receptors such as CTLA-4/PD-L1 or NKG2A expressed in tumours by T cells and NK cells respectively suppress immune cytotoxic responses (**Spranger, 2016**). As will be discussed below, this phenomenon is currently being exploited in the clinic by blocking these inhibitory pathways in an attempt to reactivate an anti-tumoral effect of the immune system.

3.1.4. TGF-β and the tumour immune microenvironment

The TGF-β superfamily comprises the most important anti-inflammatory cytokines, including activins, BMPs and TGF-β itself. (**Chen and Ten Dijke, 2016**). TGF-β in particular has pleiotropic effects on multiple components of the immune system, exerting strong immunosuppressive effects and thereby affecting several, if not all, steps of the cancer-immunity cycle.

Secreted TGF-β in the tumour microenvironment recruits macrophages and neutrophils and induces their differentiation into the immunosuppressive M2 phenotype and MDSCs respectively. In turn, they become sources of TGF-β in the immune microenvironment. Importantly, TGF-β can inhibit antigen presentation by DCs through repression of MHC-II expression. DCs are also reprogrammed to secrete TGF-β which will further dampen anti-tumour responses (reviewed in **Batlle and Massagué, 2019**).

TGF-β can directly suppress the cytotoxic effect of CTLs and NK cells by repressing expression of IFNγ and GZMB. Furthermore, TGF-β impacts on Th1 responses by inhibiting TBET expression and inducing FOXP3, which consequently shifts the balance of CD4+ T cells into the Treg phenotype. In addition, TGF-β downregulates the expression of eomesodermin (EOMES), which in turn represses the transcriptional program related to the effector cytotoxic phenotype of CTLs (reviewed in **Batlle and Massagué, 2019**, **Figure 10**).

3.1.5. The revolution of immunotherapies in cancer treatment

The first reports of an anti-cancer immune activity were from 1908, when William Coley observed that cancer patients suffering from mild colds and fevers showed improved responses to cancer treatment (reviewed in **Mccarthy, 2006**). This relationship suggested for

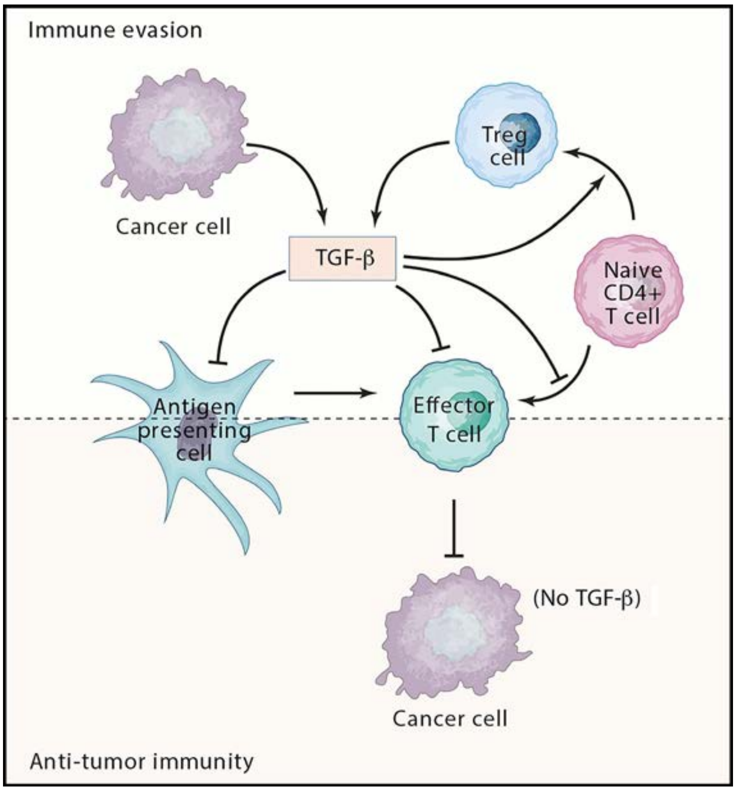

Figure 10. The immunosuppressive roles of TGF-β on the adaptive immune system. TGF-β blocks antigen presentation by APCs, effector T cell activity and differentiation of CD4+ into the Th1 phenotype. Instead, it induces differentiation of CD4+ T cells into Treg cells. Overall, these responses lead into a suppressed tumour immune microenvironment that supports tumour growth. Figure extracted from **Batlle and Massagué, 2019**.

the first time that an immune response could target tumours in patients. Further research on the immune system has led to major advances in immunotherapy. The term "immunotherapy" includes any treatment aimed to stimulate the immune system to achieve anti-tumour responses and, in a way, re-establish the integrity of the cancer-immunity cycle (**Figure 11**).

Two promising immunotherapies being developed are cancer vaccines and T cells with engineered chimeric antigen receptors (CAR T cells), which aim to foster presentation (**Figure 11**, step 2) and recognition (**Figure 11**, step 6) of tumour neoantigens, respectively (**Chen and Mellman, 2013**). Cancer vaccines introduce antigenic peptides or nucleic acids combined with adjuvants into the host (**Palucka and Banchereau, 2013**), while CAR T cells are generated *ex vivo* by first isolating circulating T cells from patients and inducing expression of recombinant T cell receptors through genetic engineering, after which they are reintroduced into the host (**Kalos and June, 2013**). Although these therapies promise encouraging results, the majority of antigens from tumour cells are also expressed by cells in the healthy tissue. T cells are tolerant to these antigens and will consequently show poor binding affinity to the pertinent MHC-antigen complex. Therefore, discovering tumour-specific antigens that produce strong and targeted immune responses remains challenging.

When an inflammatory process is resolved, T cells cease to respond upon reception of inhibitory stimuli by binding to "immune checkpoint" receptors, which compete with T cell activation triggered by CD28 binding to CD80/86 (**Ribas, 2015; Sharpe and Pauken, 2018**). The Nobel Prize of Medicine awardees James P. Allison and Tasuku Honjo were the first scientists who described how two of such inhibitory receptors, CTLA-4 and PD-1 respectively, inhibit T cell responses in mouse tumour models (**Freeman et al., 2000; Hodi et al., 2003; Iwai et al., 2005; Leach et al., 1996**). The breakthrough of this discovery, however, was that tumours can express immune checkpoint ligands as alternative mechanisms for immune evasion. Therefore, when tumour bearing mice were treated with blocking monoclonal antibodies against CTLA-4 or PD-1, anti-tumour immune responses were then re-established (**Freeman et al., 2000; Hodi et al., 2003; Iwai et al., 2005; Leach et al., 1996**).

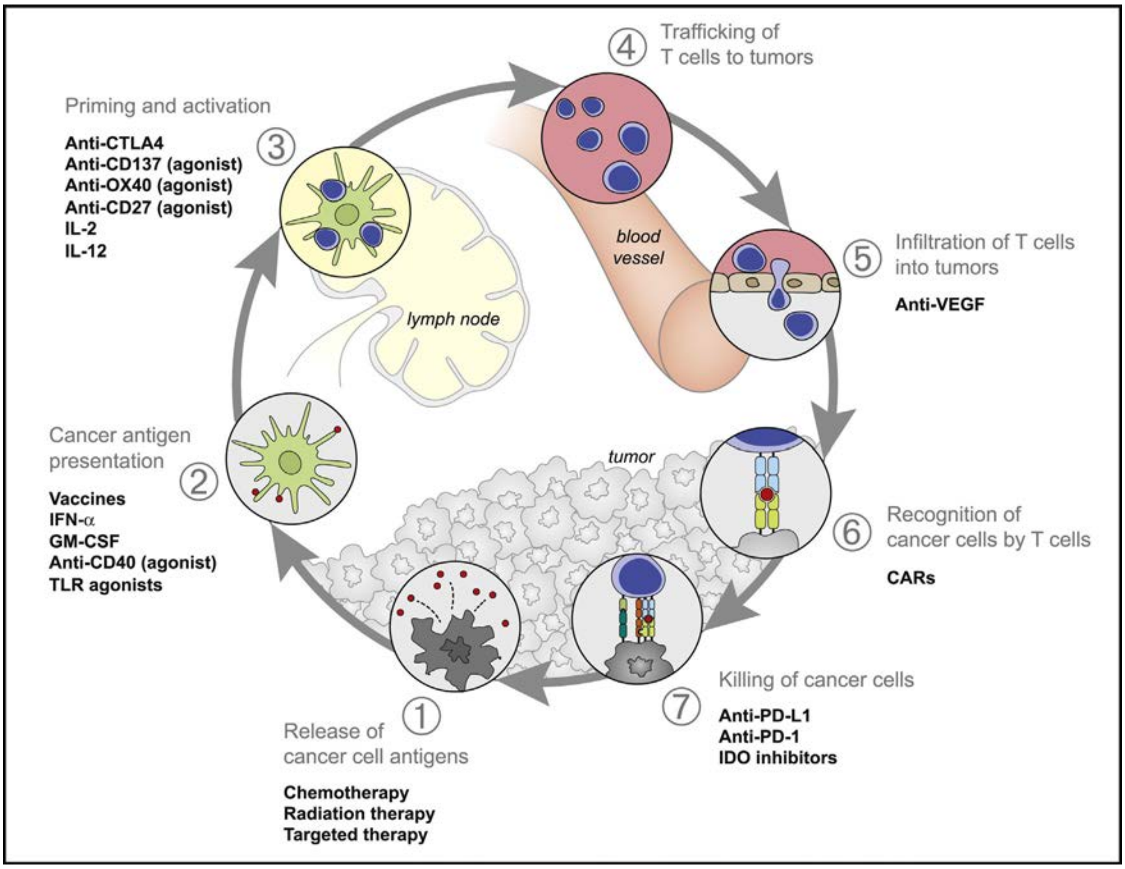
Trafficking of
T cells to tumors
④
Priming and activation
③
Anti-CTLA4
Anti-CD137 (agonist)
Anti-OX40 (agonist)
Anti-CD27 (agonist)
IL-2
IL-12
blood vessel
Infiltration of T cells into tumors
⑤
Anti-VEGF
lymph node
Cancer antigen presentation
②
Vaccines
IFN-α
GM-CSF
Anti-CD40 (agonist)
TLR agonists
tumor
Recognition of cancer cells by T cells
⑥
CARs
Killing of cancer cells
⑦
Anti-PD-L1
Anti-PD-1
IDO inhibitors
Release of cancer cell antigens
①
Chemotherapy
Radiation therapy
Targeted therapy

Figure 11. Current therapies and immunotherapies integrated into the cancer-immunity cycle. Therapeutic strategies are classified according to the step of the cancer-immunity cycle (**Figure 9**) they reinforce. Therapies including chemotherapy, radiation and targeted therapies inflict direct damage to tumour cells and foster antigen release (1). Several therapeutic strategies are directed towards increased antigen presentation and T cell priming (2 and 3), such as cancer vaccines, treatment with inflammatory cytokines (i.e. IL-2, IL-12, IFN-α) and agonists for co-stimulatory receptors (i.e. CD27, CD137). Treatment with Bevacizumab is directed to T cell extravasation from circulation (5). Engineered CAR T cells foster recognition of tumour specific antigens (6). Finally, blocking of checkpoint inhibitors such as PD-1/PD-L1 and CTLA-4 induce T cell activation and trigger cancer cell killing (3 and 7). Figure extracted from **Chen and Mellman, 2013**.

These immune checkpoint receptors counteract the activation stimuli by direct competition of CTLA-4 with CD28 to bind CD80/86 or through engagement with PD-L1/2 (**Sharpe and Pauken, 2018**). It has been shown that mice lacking of CTLA-4 and PD-1 develop autoimmune diseases, highlighting the importance of these receptors in controlling T cell responses (**Nishimura et al., 2001; Tivol et al., 1995**). In particular, PD-1/PD-L1 signalling is a relatively well-understood mechanism of T cell checkpoint inhibition. PD-1 is expressed mainly on the surface of T cells, B cells and NK cells (**Sharpe and Pauken, 2018**, **Figure 12A**). Upon activation, T cells upregulate expression of PD-1 and is sustained until the antigen is cleared, after which PD-1 expression decreases. In the event of cancer, where antigens are persistently expressed, T cells become exhausted and PD-1 expression remains high (**Sharpe and Pauken, 2018**, **Figure 12B**), although PD-1 expression *per se* does not define T cell exhaustion (**Sharpe and Pauken, 2018; Wherry, 2011**). PD-L1 can be expressed on the surface of a plethora of cells including lymphoid cells, myeloid cells such as macrophages, mesenchymal cells and even tumour epithelial cells (**Bai et al., 2017; Sharpe and Pauken, 2018**, **Figure 12A**). Induced by cytokines and interferons, IFN-γ is one of the most potent drivers of PD-L1 expression (**Garcia-Diaz et al., 2017; Katlinski et al., 2017; Ribas et al., 2017**). Therefore, its expression can be a consequence of a high secretion of

IFN-γ due to an enhanced cytotoxic activity. PD-1 can also bind PD-L2, whose expression is less abundant compared to PD-L1 (Rozali et al., 2012; Sharpe and Pauken, 2018, **Figure 12A**). The mechanisms underlying PD-1/PD-L2 signalling are poorly understood. However, recent reports point that expression of PD-L2 in the tumour stroma is crucial to dampen tumour-specific T cell responses (Lakins et al., 2018).

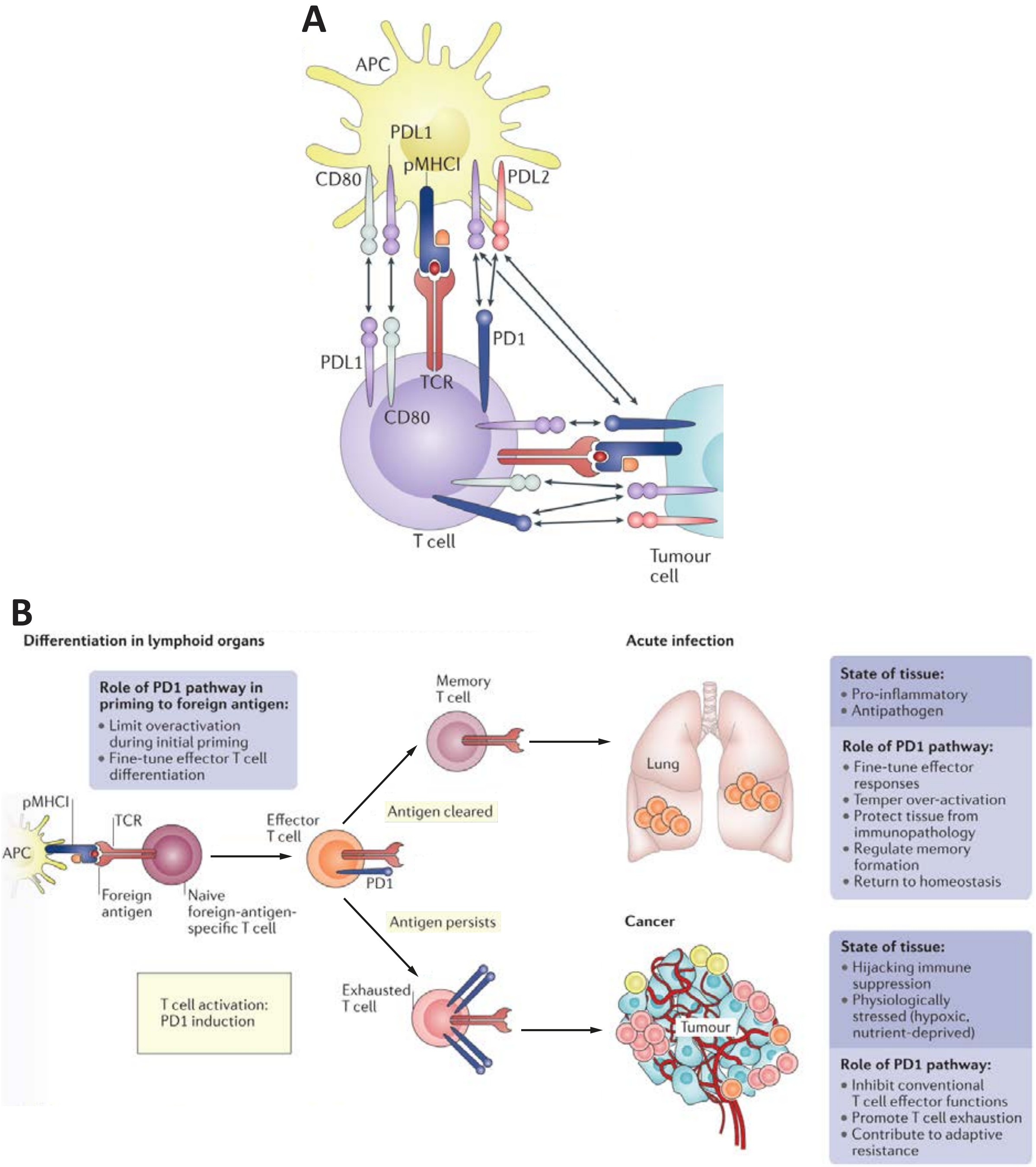
A
APC
PDL1
pMHCI
CD80
PDL2
PD1
PDL1
TCR
CD80
T cell
Tumour cell
B
Differentiation in lymphoid organs
Role of PD1 pathway in priming to foreign antigen:
• Limit overactivation during initial priming
• Fine-tune effector T cell differentiation
pMHCI
TCR
APC
Foreign antigen
Naive foreign-antigen-specific T cell
Effector T cell
PD1
T cell activation: PD1 induction
Memory T cell
Antigen cleared
Antigen persists
Exhausted T cell
Acute infection
Lung
Cancer
Tumour
State of tissue:
• Pro-inflammatory
• Antipathogen
Role of PD1 pathway:
• Fine-tune effector responses
• Temper over-activation
• Protect tissue from immunopathology
• Regulate memory formation
• Return to homeostasis
State of tissue:
• Hijacking immune suppression
• Physiologically stressed (hypoxic, nutrient-deprived)
Role of PD1 pathway:
• Inhibit conventional T cell effector functions
• Promote T cell exhaustion
• Contribute to adaptive resistance

Figure 12. A. The PD-1/PD-L1 inhibitory pathway. Summary of the PD-1/PD-L1 mechanism between T cells and APC and tumour cells. For effective inactivation of T cell responses, PD-1 from primed T cells can bind PD-L1 and PD-L2 expressed by tumour cells and the TME. PD-1 binding of PD-L1 competes with CD80, which disrupts T cell inactivation. **B.** T cell activation induces PD1 expression to limit overactivation upon antigen recognition. Once the antigen is cleared, PD1 expression is decreased and T cells become memory T cells, and tissue returns to homeostasis. Otherwise, if antigen persists, PD1 expression is sustained and T cells become exhausted, therefore promoting tumour resistance to adaptive responses. Figure adapted from Sharpe and Pauken, 2018.

Ever since the immune checkpoint mechanism was described, many therapies have been approved by the Food and Drug Agency (FDA) or are currently being tested in clinical trials. Some of the most relevant blocking antibodies used in the clinic are Ipilimumab (anti-CTLA-4), Nivolumab, Pembrolizumab (anti-PD-1), Durvalumab and Avelumab (anti-PD-L1) (**Drake et al., 2014**). In addition, alternative inhibitory receptors affecting NK cell activity have been explored and are being tested in clinical trials (Monalizumab, anti-NK2GA) (**André et al., 2018**).

The responses associated with immune checkpoint inhibition therapy are specific against tumour antigens and are T cell dependent, as they can be ablated upon depletion either of CD4+ T cells or CTLs or by neutralizing IFN-γ (**Gubin et al., 2014**). Upon treatment with anti-CTLA-4 or anti-PD-1 antibodies, there is an expansion of both memory- and effector-like CD8+ TILs specific for tumour antigens, which increase secretion of GZMB (**Kurtulus et al., 2019**). Moreover, anti-NKG2A antibodies can foster both NK and T cells anti-tumour responses. In a model of head-and-neck squamous cell carcinoma (HNSCC), combination of anti-NKG2A antibodies with cancer vaccines shows delayed relapses (**André et al., 2018; van Montfoort et al., 2018**).

Immunotherapies have offered promising results in cancers such as melanoma, non-small-cell lung cancer (NSCLC) and renal cell carcinoma (RCC) (**Drake et al., 2014**). These cancers are immunologically "hot" tumours that are frequently infiltrated by CTLs (**Drake et al., 2014; Galon and Bruni, 2019**). Cancer vaccines have produced beneficial clinical effects in melanoma and RCC, and clinical trials have offered high response rates and overall survival for these three cancers, especially in patients treated with Nivolumab (**Drake et al., 2014**). However, other cancers, such as CRC, are largely refractory to immunotherapies. Clinical trials on CRC have yielded responses in less than 5% of patients, most of which have MSI CRCs (**Le et al., 2015**). Due to the high mutational burden, MSI tumours are enriched in T cells and express high levels of immune checkpoint receptors. Therefore, MSI state is a good biomarker for successful immunotherapies (**Le et al., 2015; Llosa et al., 2015**). On the other hand, patients with MSS CRC typically have immunologically "cold" tumours with low densities of TILs, making immunotherapies more challenging (**Galon and Bruni, 2019; Jacobs et al., 2015; Le et al., 2015**).

3.2. Cancer-associated fibroblasts (CAFs)

3.2.1. From normal fibroblasts to CAFs

While CAFs are one of the most abundant components in the tumour stroma, it was not until the past decade that we started to understand their intricate biology. Once thought as a uniform population, the development of next-generation sequencing techniques, including RNA-sequencing from single cells, has deepened our knowledge on the biological and functional heterogeneity of CAFs in tumours. It is nowadays accepted that CAFs play a crucial role in promoting tumour aggressiveness and metastatic dissemination.

Virchow and later Duvall initially described fibroblasts through microscopy techniques as spindle-shaped cells resembling fibres that produce collagen (reviewed in **Kalluri, 2016**). In his review on the biology of CAFs published in 2016, Raghu Kalluri redefined the concept of fibroblast as a quiescent cell "with the potential to be activated by appropriate stimuli to become a mesenchymal stem cell (MSC)", and which reside in the interstitial tissue (**Kalluri, 2016**). This new definition poses two implications: 1) the homeostatic state of a fibroblast is that of a quiescent, non-proliferative cell with reduced metabolic activity, and 2) almost all described properties of fibroblasts are actually associated with an active state.

Active fibroblasts were first characterized in wound-healing experiments as cells with increased intracellular expression of α-smooth muscle actin (αSMA), which gave them the term of "myofibroblasts" (**Kalluri and Zeisberg, 2006; Shaw and Martin, 2009**). Although αSMA expression has always been considered as a marker for active fibroblasts in fibrotic processes and in cancer, a large number of studies have proposed several other markers associated with an active state, such as Vimentin, Fibroblast Specific Protein 1 (FSP1), and Fibroblast Activation Protein (FAP) (**Kalluri, 2016**, **Figure 13**).

In the presence of any insult, fibroblasts are activated and proliferate in response to cytokines and growth factors. Of note, platelet-derived growth factors (PDGF) and TGF-β are the main mediators of fibroblast proliferation, and TGF-β is strongly associated with fibroblast activation (**Kalluri and Zeisberg, 2006**). Activated fibroblasts express a secretory program that includes immunologic cytokines, components of the ECM such as Collagen I (COL1), COL3, COL4, COL5, Laminins and Fibronectin, and matrix metalloproteases (MMPs). This results in profound ECM remodelling, which favours epithelial cell proliferation and migration, together with recruitment of inflammatory cells to repair the damaged tissue. Once the aggression is resolved, the inactive phenotype is retrieved either by direct reversion of active fibroblasts or through apoptosis (**Kalluri, 2016**, **Figure 13**).

However, a situation of chronic fibrosis is produced during tumorigenesis. As "wounds that do not heal", fibroblasts enter into a permanently activated state, thus becoming CAFs (**Dvorak, 1986; Kalluri, 2016**). CAFs proliferate at a higher rate compared to fibroblasts from healthy tissues and lead to desmoplasia due to excessive deposition of ECM proteins (**Kalluri, 2016**). Evidence suggests that activation of CAFs could be an irreversible process governed by epigenetic changes (**Bechtel et al., 2010; Hu et al., 2005; Mrazek et al., 2014**, **Figure 13**).

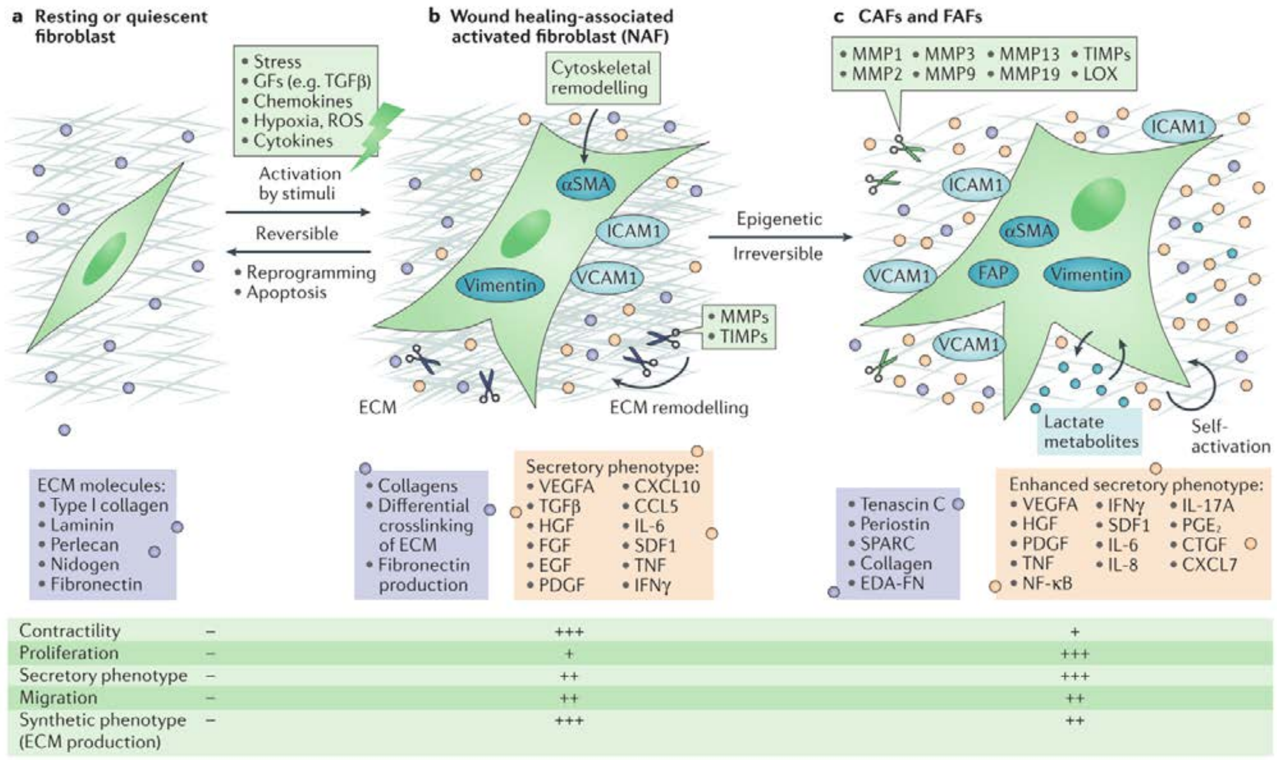
a Resting or quiescent fibroblast
b Wound healing-associated activated fibroblast (NAF)
c CAFs and FAFs
• Stress
• GFs (e.g. TGFβ)
• Chemokines
• Hypoxia, ROS
• Cytokines
Activation by stimuli
Reversible
• Reprogramming
• Apoptosis
Cytoskeletal remodelling
αSMA
ICAM1
VCAM1
Vimentin
• MMPs
• TIMPs
ECM
ECM remodelling
Epigenetic
Irreversible
• MMP1 • MMP3 • MMP13 • TIMPs
• MMP2 • MMP9 • MMP19 • LOX
ICAM1
ICAM1
αSMA
VCAM1
FAP
Vimentin
VCAM1
Lactate metabolites
Self-activation
ECM molecules:
• Type I collagen
• Laminin
• Perlecan
• Nidogen
• Fibronectin
• Collagens
• Differential crosslinking of ECM
• Fibronectin production
Secretory phenotype:
• VEGFA • CXCL10
• TGFβ • CCL5
• HGF • IL-6
• FGF • SDF1
• EGF • TNF
• PDGF • IFNγ
• Tenascin C
• Periostin
• SPARC
• Collagen
• EDA-FN
Enhanced secretory phenotype:
• VEGFA • IFNγ • IL-17A
• HGF • SDF1 • PGE₂
• PDGF • IL-6 • CTGF
• TNF • IL-8 • CXCL7
• NF-κB
Contractility – +++ +
Proliferation – + +++
Secretory phenotype – ++ +++
Migration – ++ ++
Synthetic phenotype (ECM production) – +++ ++

Figure 13. Activation of quiescent fibroblasts into normal activated fibroblasts associated with wound healing or CAFs. Purple boxes indicate secreted ECM proteins. Yellow boxes indicate cytokines secreted after fibroblast activation. Scissors include MMPs and other matrix-degrading proteins. Figure extracted from **Kalluri, 2016**.

3.2.2. Markers for fibroblasts and CAFs

One of the multiple definitions for fibroblasts has been “non-vascular, non-epithelial and non-inflammatory cells of the connective tissue” (**Kalluri and Zeisberg, 2006**). This definition highlights what could possibly be the predominant problem in fibroblast research, which is that there is no specific (pan)marker for this mesenchymal population; instead, it relies on the exclusion of endothelial, epithelial and immune cells, which each have a specific lineage marker.

To date, the common embryonic origin of all adult fibroblasts remains obscure. In fact, fibroblasts differentiate from distinct progenitors depending on the tissue they reside, resulting in different gene expression programs and proteins expressed in the surface. Lung fibroblasts, for instance, share a common *TBX4ENH+* progenitor, which derives from *GLI1+ WNT2+ ISL1+* progenitors in the developing heart (**Barron et al., 2016**). Skin fibroblasts have been reported to originate from a common progenitor expressing PDGF Receptor alpha (PDGFRα), *DLK1* and *IRIG1* (**Driskell and Watt, 2015**). Fibroblasts found in the intestinal lamina propria are thought to differentiate from *WT1+* serosal mesothelial cells, while liver mesenchymal cells are known to originate from CD34+ cells (**Chen et al., 2014b; Friedman, 2008; Powell et al., 2011**).

Differentiation from these distinctive progenitors results in the generation of mesenchymal populations whose gene expression program differs not only between distinct fibroblasts within the same tissue, but also from fibroblasts located in distant organs. A study in 2002 compared the genome-wide expression profiles of 50 fibroblast lines isolated from 16 different locations, and reported that the magnitude of difference in their gene expression programs is comparable to those found in different leukocyte populations (**Chang et al., 2002**). Following the examples above, whereas almost all mesenchymal cells in the liver, lungs and skin express PDGFRα, several subpopulations can be detected depending on expression of NG2 and PDGFRβ in lungs, *GFAP* in liver and a broad combination of markers such as CD26, *DlLK1* and *SCA1* in the skin (**Barron et al., 2016; Driskell and Watt, 2015; Friedman, 2008**). In the intestinal lamina propria, the majority of resident fibroblasts express αSMA except for a basal subpopulation that express PDGFRα instead (**Kurahashi et al., 2013; Powell et al., 2011**).

In addition to lineage heterogeneity, activated fibroblasts found in fibrotic diseases and tumours also express a wide range of markers. Some of the most common markers used to isolate fibroblasts are PDGFRα, PDGFRβ, αSMA, FAP, NG2, FSP1, DDR2, CD34, CD90, Vimentin and Desmin (**Kalluri, 2016**). However, most of these markers are not entirely specific for fibroblasts. CD34 can be found in hematopoietic and vascular tissue, and CD90 is also a general marker for stem cells. Although FAP and FSP1 have been broadly used to detect activated CAFs, they are also expressed in immune populations (**Kalluri, 2016**). Therefore, one should use these markers with caution and scrutinize their use to avoid false-positive signals.

3.2.3. Sources of CAFs

Despite recent advances in fibroblast biology, the sources for CAFs still remain partially unknown. Given the broad heterogeneity of tumour types, one could argue that there is no unique or common source of fibroblasts in cancer. Instead, several origins have been postulated to contribute to the recruitment of CAFs in the TME (**Kalluri, 2016; Xouri and Christian, 2010**).

Although CAFs acquire higher proliferative capabilities compared to normal fibroblasts, their division rate is rather low when compared to tumour cells and other cells in the TME, which opposes the idea of a mesenchymal origin of CAFs. In this direction, many studies have proposed that, in response to TGF-β, epithelial cells may attain fibroblastic features through epithelial-to-mesenchymal transition (EMT). During EMT, epithelial cells lose cell-to-cell junctions and experience cytoskeletal reorganization resulting in a fibroblast-like phenotype with increased migratory capabilities (**Alkasalias et al., 2018; Calon et al., 2014; Kalluri, 2016**). Cells that undergo EMT could possibly produce a fraction of the total CAF population. However, as TGF-β is the main mediator of EMT (**Xu et al., 2009**), it cannot explain CAF origin for tumours with epithelial cells that are insensitive to TGF-β signalling, such as many CRCs. In a similar way, endothelial cells can also undergo endothelial-to-mesenchymal transition (EndMT) in response to TGF-β as a possible source of CAFs (**Alkasalias et al., 2018; Kalluri, 2016**).

Other studies have suggested that fibrocytes contribute to the CAF population. Fibrocytes are circulating, myeloid-derived CD45+ cells originated in the bone marrow, which also acquire fibroblastic features such as COL1 production (**Abe et al., 2001; Phillips et al., 2004; Saijo et al., 2018; Zhu et al., 2016**). However, their low numbers in circulation (less than 0.5% of total CD45+ cells, reviewed in **Alkasalias et al., 2018**) makes them unlikely to produce the majority of CAFs in tumours.

Despite the multiple proposed origins of CAFs, several studies conclude that fibroblasts in tumours are derived from local sessile mesenchymal precursors. Lineage tracing experiments using a dual reporter for *COL1* and αSMA show that precursors from a donor's bone marrow are not able to generate CAFs in colon adenomas generated in an APC^{min} genetic mouse model (**Arina et al., 2016**). This concept is particularly interesting in the liver, the primary site for CRC metastasis, where almost 10% of total cells are mesenchymal precursors (**Friedman, 2008; Wells, 2014**). Indeed, in models of liver fibrosis, fate-mapping experiments point to a mesenchymal origin, especially to hepatic stellate cells, which reside in close contact with the sinusoidal endothelial cells of the liver (**Iwaisako et al., 2014; Liu et al., 2015; Mederacke et al., 2013; Sekiya et al., 2016**).

The multiple origins of CAFs in a particular tumour can be context-dependent and can be a result of multiple sources. This fact can be a cause for the heterogeneity of fibroblasts in tumours, which will be further discussed below.

3.2.4. CAFs enhance tumour progression and metastasis

A key feature of CAFs is that they promote tumour progression. Co-injection of active CAFs with tumour cells in mice leads to increased tumour burden. Moreover, a similar effect can be achieved when tumour cells are stimulated with CAF conditioned media, and the introduction of CAFs can rescue tumour growth in a model where *FSP1* is knocked out (reviewed in **Kalluri, 2016** and **Kalluri and Zeisberg, 2006**).

Upon activation, CAFs display migratory capabilities and enhance secretion of cytokines and growth factors, which create a supportive niche that favours tumour growth, invasiveness and, ultimately, metastatic colonization. Several mechanisms of direct tumour growth stimulation by CAF-secreted growth factors have been reported. A first example is CXCL12, which can both directly promote tumour growth through CXCR4 signalling, and induce angiogenesis (**Orimo et al., 2005**). It has also been shown that TGFBR2-deficient FSP1+ CAFs foster tumour progression through increased secretion of Hepatocyte Growth Factor (HGF) (**Bhowmick et al., 2004; Cheng et al., 2008**). In a model of CRC, Interleukin 11 (IL-11) secreted by CAFs enhanced survival of tumour cells in a context of metastatic colonization (**Calon et al., 2012**). On the other hand, it has been shown that tumour cells located near CAFs retain stem cell properties, which could be explained by increased WNT signalling induced by CAFs (**Saijo et al., 2018; Vermeulen et al., 2010**).

CAF-secreted factors can also foster migratory capabilities of tumour cells and metastatic spreading, especially by producing MMPs that remodel the ECM and by inducing angiogenesis through secretion of CXCL12 and VEGFA (**Cirri and Chiarugi, 2012; Kalluri, 2016**). Some studies point to the possibility of collective migration of cancer cells and CAFs, which could be responsible for tumour cell invasiveness and circulation through the bloodstream (**Gonzalez-Zubeldia et al., 2015; Labernadie et al., 2017**). For efficient metastatic colonization, some reports suggest the generation of a pre-metastatic niche that could be explained by secretion of MMPs, cytokines and growth factors by CAFs into the bloodstream either directly or through circulating exosomes (**Cirri and Chiarugi, 2012; Kalluri, 2016; Mannavola et al., 2019; Wortzel et al., 2019**).

The enormous implication of CAFs in tumour progression renders them as possible targets of cancer treatment. CAFs mediate angiogenesis through secretion of VEGFA, which can be targeted with Bevacizumab (**Kalluri, 2016**). In fibrotic diseases, Pirfenidone was proposed to efficiently target multiple signalling pathways in activated fibroblasts, and may be able to inhibit CAFs and cancer-related fibrosis as well (**Hisatomi et al., 2012; Kozono et al., 2013; Lopez-de la Mora et al., 2015; Takai et al., 2016**).

Conversely, it has been shown that fibroblasts can have tumour-suppressive roles as well: the loss of resident fibroblasts in homeostatic tissues increases susceptibility for cancer (**Franco et al., 2011**). Furthermore, depletion of myofibroblasts in a model of PDAC promoted tumour progression and reduced survival (**Özdemir et al., 2014**). Although these effects may be context-dependent, this calls for caution when using CAF-targeting therapies.

3.2.5. Immunomodulation by CAFs

The presence of TILs in tumours is generally associated with a treatment response to immunotherapy (**Uryvaev et al., 2018**). However, some tumours that have a high mutational burden and an increased number of infiltrating lymphocytes may not respond to current immunotherapies. This can be explained by intrinsic tumour properties conferred by the TME. In particular, the heterogeneity of CAFs can have an impact on the recruitment and activation of distinct immune cell types during tumorigenesis (**Salmon et al., 2019**, **Figure 14**). For a single patient, stromal composition can also vary from primary tumours to metastasis (**Jiménez-Sánchez et al., 2017**), also explained by a tissue-dependent factor discussed in **3.2.2** and **3.2.3**.

The desmoplastic reaction, which results from the deposition of proteins such as Collagens by CAFs, produces profound changes in the architecture of the ECM. This results in the creation of dense areas with packed matrix fibres, which in consequence pose a physical barrier to the entrance of T cells (**Salmon et al., 2012**, **Figure 14**). Indeed, gene signatures associated with expression of ECM-related genes are correlated with poor prognosis in patients (**Chakravarthy et al., 2018**).

Furthermore, the abundance of cytokines and chemokines secreted by CAFs has direct impacts on T cell trafficking and regulation. Chemokines such as CCL2, CCL2, CCL4 and CCL5 recruit myeloid cells into the tumours which foster tumour progression (**Turley et al., 2015**, **Figure 15**). Other reports have shown that CAF-secreted CXCL14, CXCL16 and IL-33 recruit macrophages, which in turn contribute to tumour aggressiveness and metastasis (**Allaoui et al., 2016; Vianello et al., 2006; Yang et al., 2016**). Importantly, CAFs have a direct influence on macrophage polarity: by secreting cytokines such as IL-4, IL-6, IL-10 and TGF-β, CAFs induce macrophage differentiation into the immunosuppressive phenotype M2 (**Kalluri, 2016; Turley et al., 2015**).

Although CAFs can recruit T cells by secretion of CXCL9 and CXCL10, secreted CXCL12 is associated with T cell “chemorepulsion” via signalling through CXCR4 expressed on the

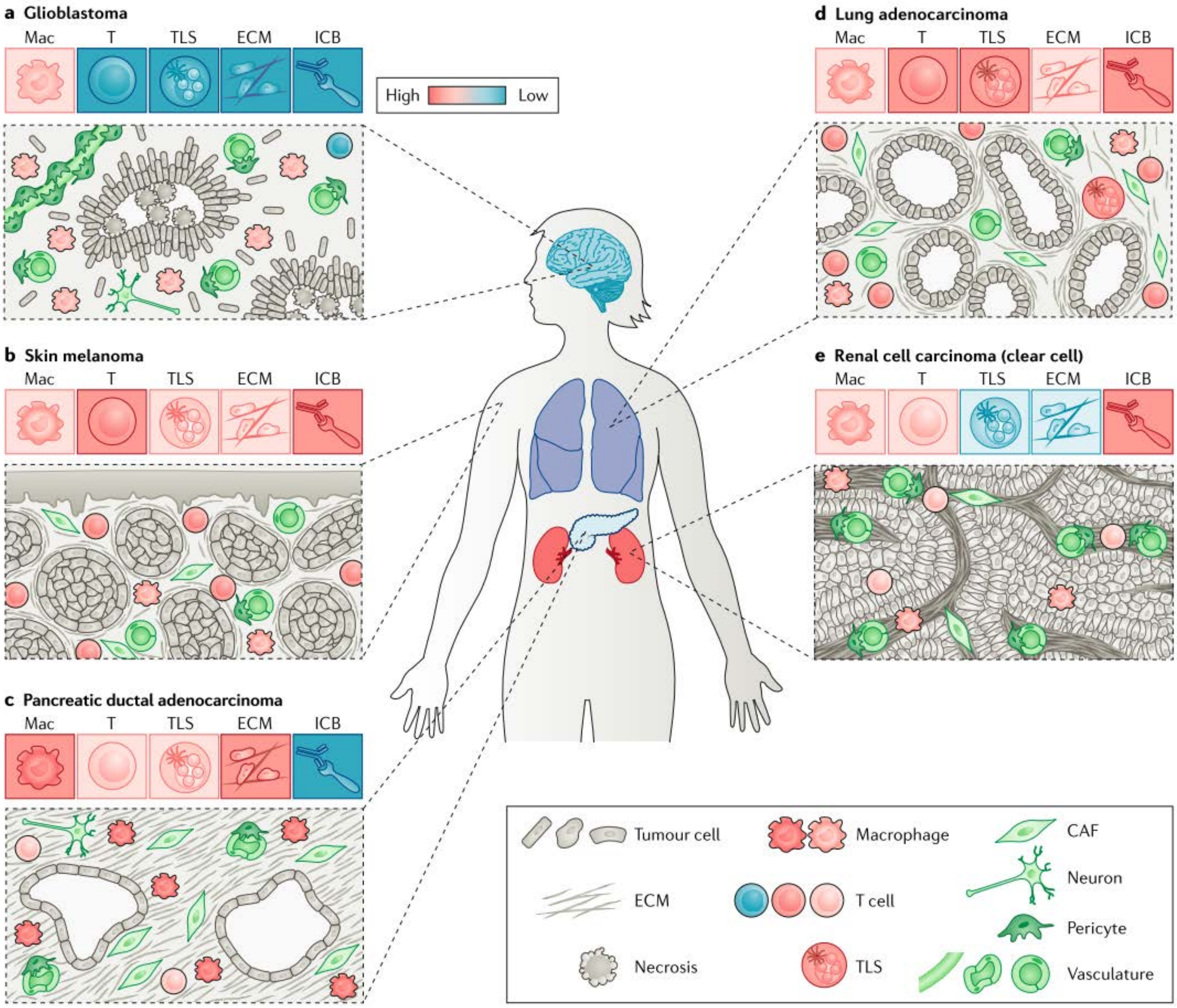
a Glioblastoma
Mac
T
TLS
ECM
ICB
High
Low
d Lung adenocarcinoma
b Skin melanoma
e Renal cell carcinoma (clear cell)
c Pancreatic ductal adenocarcinoma
Tumour cell
Macrophage
CAF
Neuron
ECM
T cell
Pericyte
Necrosis
TLS
Vasculature

Figure 14. Different tumour types recruit different types and proportions of stromal cells. Distinct stromal cells will generate a TME with different architectures. The type of stromal cells and the desmoplastic reaction generated determine the effectiveness of immune checkpoint blockade (ICB) therapies. High (red) and low (blue) presence and ICB efficacy is indicated. Figure extracted from **Salmon et al., 2019**.

surface of lymphocytes (**Joyce and Fearon, 2015; Kalluri, 2016; Turley et al., 2015; Vianello et al., 2006**, **Figure 15**). Furthermore, CAFs recruit MDSCs, B cells and Tregs, which can further inhibit Th1 responses in tumours (**Joyce and Fearon, 2015; Turley et al., 2015**), and can also impair proliferation and viability of intratumoral T cells (**Joyce and Fearon, 2015**).

Interestingly, a study in 2018 showed that CAFs can present tumour antigens loaded in the MHC-I complex, together with expression of the inhibitory checkpoint receptor PD-L2, resulting in a direct inactivation of antigen-specific CTLs. In this same study, researchers detected increased PD-L2 expression in patients with lung, colon, pancreatic and breast cancer (**Lakins et al., 2018**). Remarkably, a more recent report has provided evidence that CAFs can also present antigens loaded in MHC-II molecules, which represents a breakthrough into our current knowledge of professional APCs. These antigen-presenting CAFs lack the stimulatory receptors that canonical APCs express, which could add to the mechanism of suppression of antigen-specific T cell responses (**Elyada et al., 2019**).

Opposed to the immunosuppressive effect of CAFs, it has been reported that genetic ablation of αSMA+ CAFs in PDAC increases tumour burden by allowing infiltration of Treg cells into the tumours (**Özdemir et al., 2014**), which suggests that the immunosuppressive role of CAFs could be context-dependent.

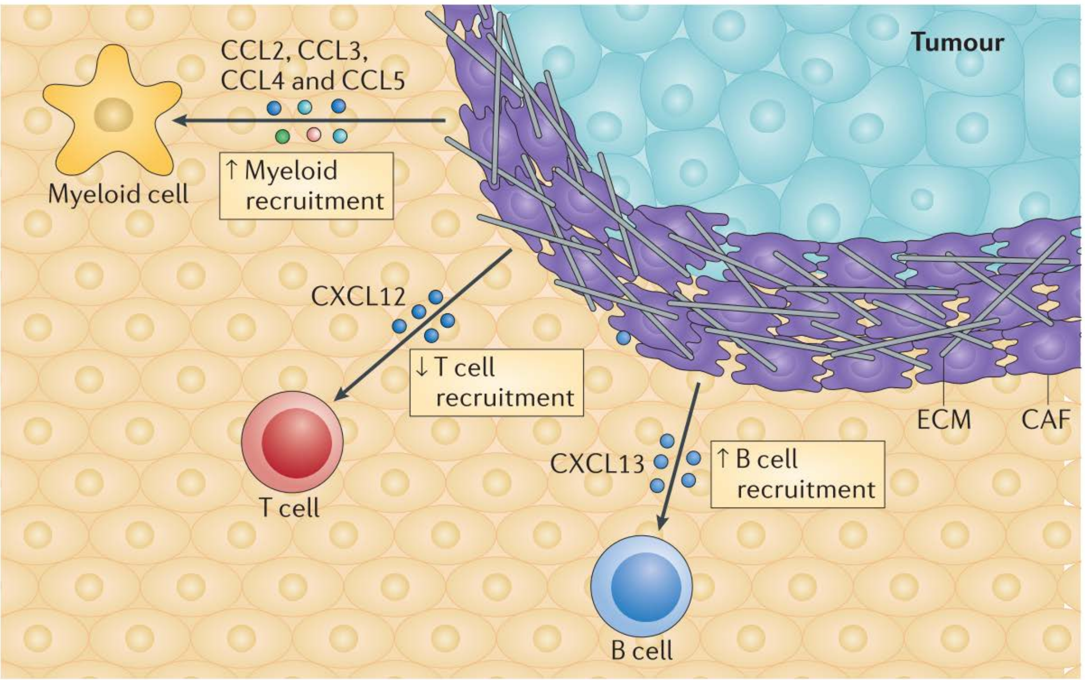

Figure 15. Main cytokines expressed by CAFs with immunossupressive effects in tumours. CAFs can avoid T cell infiltration by secreting CXCL12, and contribute to tumour progression by recruiting myeloid cells and B cells by secreting CCL2, CCL3, CCL4, CCL5 and CXCL13. Figure extracted from **Turley et al., 2015**.

3.2.6. Subpopulations of CAFs in tumours

Until recently, the majority of studies focusing on CAFs were based on the assumption that a single marker could be used to target a homogeneous stromal population. However, the multiplicity of mesenchymal embryonic progenitors and sources for activated fibroblasts in the tumour makes that assumption fairly unlikely. Instead, it has become more evident that several subpopulations coexist within a tumour and that this would be tissue-dependent, which could alter the TME composition of metastatic growth compared to the tumour of origin. In this line, an initial simple approach conducted by Hikaru Sugimoto and colleagues detected that, despite the prevalence of FSP1 expression in mouse models of both breast and pancreatic cancer, several markers associated with activated fibroblasts defined both overlapping and mutually exclusive patterns, thus identifying a heterogeneous composition of CAF subpopulations (**Sugimoto et al., 2006**). This study marked the start of support for a new hypothesis, comparable to that of T cell differentiation or macrophage polarization: it proposes that CAFs have several differentiation states with different, and possibly opposing, roles in tumour progression (**Kalluri, 2016; Öhlund et al., 2014**, **Figure 16**).

Despite the broad genetic divergence of CAFs from different tumours discussed earlier, this new hypothesis of different CAF states suggests the possible existence of functionally similar categories of activated fibroblasts. One might also speculate that these categories are plastic and CAFs might be reverted into different states upon specific stimuli. More research into this field might give birth to novel strategies to target crucial subpopulations of

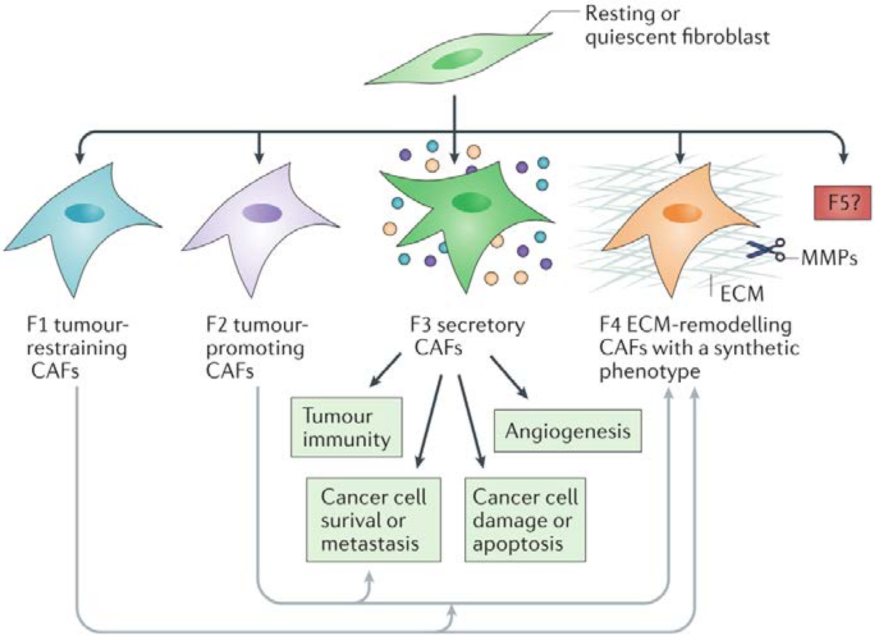
Resting or quiescent fibroblast
F5?
MMPs
ECM
F1 tumour-restraining CAFs
F2 tumour-promoting CAFs
F3 secretory CAFs
F4 ECM-remodelling CAFs with a synthetic phenotype
Tumour immunity
Angiogenesis
Cancer cell surival or metastasis
Cancer cell damage or apoptosis

Figure 16. Hypothesis of CAF subpopulations in the TME. Model proposed by Raghu Kalluri of functionally different fibroblast phenotypes, represented as F states. States could be plastic depending on appropriate stimuli. This model also proposes the existence of a particular phenotype (F3) with crucial roles in metastasis and immune suppression. Figure adapted from **Kalluri, 2016**.

CAFs as new therapeutic approaches, as well as defining consensus populations of CAFs with phenotypic similarities (**Kalluri, 2016**, **Figure 16**).

4. Prognostic value of the TME in CRC

4.1. Infiltration of lymphocytes correlates with improved outcome

It is now clear that tumour progression is not only governed by intrinsic genetic changes, but also by the composition of the TME, especially by CAFs and immune infiltrates. The TME composition is highly dynamic and evolves through tumour progression. This effect dictates the nature of immunologic responses not only within different areas of a same tumour, but may also affect distant metastases. In the end, an immunosuppressive environment fosters tumour growth and metastatic dissemination. This observation is supported by several studies showing that increased immunologic cytotoxic responses are associated with good outcome in patients.

The group of Jérôme Galon has made major contributions in determining immune-related prognosis in patients from CRC. Tumours in patients can be classified according to the type and density of T cells in the tumour centre and invasive margins by creating a parameter titled as “Immunoscore” (**Galon and Bruni, 2019; Galon et al., 2006**). Their investigations show that an increased T cell infiltration in both the tumour centre and tumour margins or in other words, high Immunoscore, is correlated with improved overall survival and decreased relapse. On a special note, CTL responses identified by the presence of CD8+ T cells and expression of factors such GZMB, Perforin, Granulysin and TBET strongly correlated with good outcome (**Camus et al., 2009; Galon et al., 2006; Pagès et al., 2005**). As mentioned earlier, MSI CRCs have better prognosis due to increased infiltration of CTLs, probably as a consequence of the high immunogenicity generated by their high mutational load (**Jacobs et al., 2015; Le et al., 2015; Llosa et al., 2015**). Furthermore, an independent study has shown a positive correlation between PD-L1 expression and good prognosis. In this study, authors found that tumours with high expression of PD-L1 were surprisingly infiltrated with CD8+ T cells, which could predict response to immunotherapy (**Droeser et al., 2013**). However, there appears to be no association between the presence of FOXP3+ Treg cells and prognosis in CRC (**Pagès et al., 2010**).

Classification of infiltrates in CRC patients could be a valuable tool to predict responses to current therapies. Moreover, understanding the mechanisms of immune evasion in non-responders might also lead to new combinatorial strategies with immunotherapies.

4.2. CAFs express a gene signature correlated with poor prognosis

One of the main issues with current CRC molecular classifications, including the newest CMS subtypes discussed previously, is that they are based on data from bulk tumours, which are not segregated according to cell types (**Fessler and Medema, 2016**).

As a matter of fact, in previous classifications to the CMS, two independent studies showed that most genes associated with poor prognosis were expressed by FAP+ CAFs rather than by tumour epithelial cells (**Calon et al., 2015; Isella et al., 2015**). Moreover, most of them were TGF-β targets, which correlates well with the observed decreased survival rates in patients with tumours bearing high levels of TGF-β, where it creates a reactive stroma (**Calon et al., 2012, 2015**). In line with this observation, elevated protein and mRNA expression of some of these target genes such as *FAP*, *CALD1* and *IGFBP7* correlated with worse outcome in CRC patients (**Calon et al., 2015**).

The TGF-β response signature expressed by CAFs could be compared with genes expressed in the 5 categories defined by Sadanandam and colleagues, where the Stem-like category showed the worst prognosis in patients (**Sadanandam et al., 2013**). This analysis showed that the gene signature defining the stem-like category was mostly enriched in CAFs. Moreover, the remaining categories with better prognosis could be further segregated depending on the expression levels of this CAF signature, resulting on a new category of "high CAF cluster expression" that showed increased relapse (**Calon et al., 2015**). Supporting the predictive strength of CAFs, a similar result was found in an independent study on PDAC (**Moffitt et al., 2015**).

Therefore, TGF-β expression levels and CAF phenotypes hold a stronger prognostic strength for patient survival than most features of tumour epithelial cells. One of the conclusions extracted from the studies led by Calon and Isella is that the epithelial gene signatures alone are not sufficiently informative for molecular classification of CRC tumours, and that further evaluation of stromal signatures could substantially benefit the molecular classification of CRC (**Calon et al., 2015; Fessler and Medema, 2016; Guinney et al., 2015; Isella et al., 2015**). Thus, whereas CMS4 tumours are clearly characterized by an increased stromal signature, it should be considered that other CMS could be subclassified into further categories depending on the CAF gene signatures that correlate to poor prognosis.

5. TGF-β on the TME of metastatic CRC: from prognosis to novel roles

As discussed above, TGF-β is the main activator of CAFs in tumours. Moreover, it can induce EMT and EndMT as sources of CAFs. Interestingly, CAFs become the main source of TGF-β in the tumour microenvironment, where it exerts immunosuppressive and pro-angiogenic roles (Reviewed in **Calon et al., 2014**).

The importance of TGF-β and CAFs in CRC progression and metastasis goes beyond the mere predictive potential. The work conducted in the group of Eduard Batlle has revealed that TGF-β is crucial for metastatic colonization and initiation. When mice were treated with Galunisertib, a TGFBR1 inhibitor currently in clinical trials, tumour cells failed to generate liver metastasis. Supporting this observation, mice transplanted with tumour cells overexpressing TGF-β had reduced survival. A similar effect could be achieved when tumour cells were coinjected with fibroblasts pre-treated with TGF-β, and further evidence showed that TGF-β-activated CAFs secreted IL-11, which promoted tumour cell survival (**Calon et al., 2012, 2015**). Of note, these studies were performed transplanting patient-derived cell lines into immunocompromised mice.

Therefore, the problem remains in dissecting the specific roles of high levels of TGF-β in an immunocompetent TME. The discussed evidence procures hints of a correlation between TGF-β expression and immune-excluded tumours. However, these observations remain correlative, and the mechanisms of TGF-β-driven immune exclusion of CRC are still poorly understood. As potent modulators of the tumour immune microenvironment, it is of special relevance to understand if and how CAFs in CRC impact on the infiltration of immune cells in response to TGF-β activation. In the era of immunotherapies, discovering these mechanisms in the context of liver metastasis could pave the way for novel stroma-targeted therapies that could be pivotal for patients with metastatic CRC.

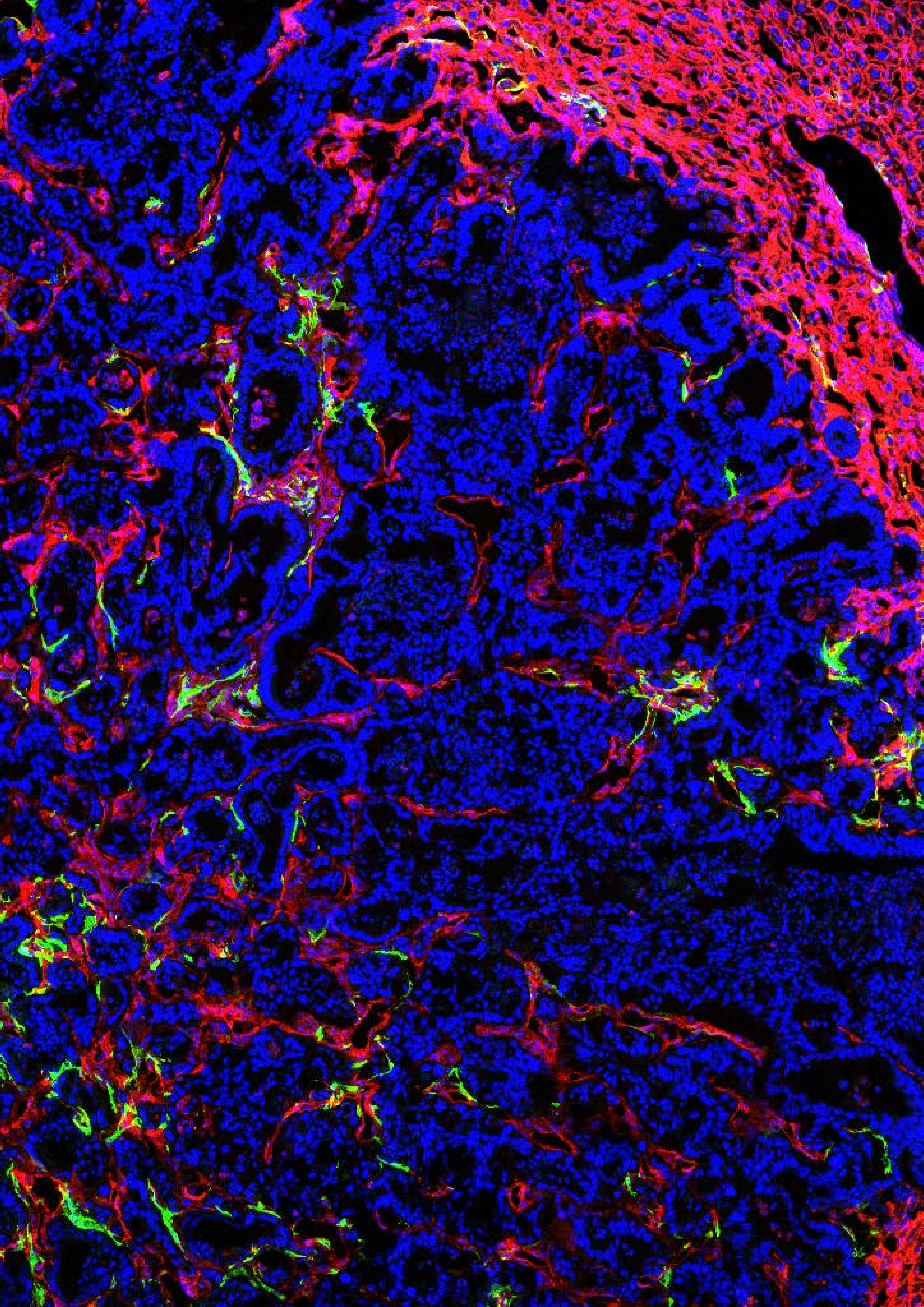

RESULTS

“Don’t let anyone rob you of your imagination, your creativity, our your curiosity. It’s your place in the world.”

- Mae Jemison

Chapter 1

TGF-β drives immune evasion in genetically reconstituted colon cancer metastasis

Summary

Patients suffering from CRC generally don't die from the primary tumour but rather succumb to metastasis, which occur primarily in the liver. Most patients generate immunologically cold, microsatellite-stable tumours, which are refractory to current checkpoint immunotherapies. Using a novel mouse model for metastatic CRC, we discovered that TGF-β promotes metastatic progression by contributing to the tumour immune exclusion. When the TGF-β pathway was inhibited using Galunisertib, a TGF-BR1 small molecule inhibitor, tumours became highly infiltrated with activated T cells. Combinational therapy of Galunisertib with monoclonal antibodies against PD-L1 produced a synergistic effect on T cells that resulted into strong curative responses in mice with overt metastatic disease. Our results suggest a novel therapeutic approach for patients with microsatellite-stable CRC metastasis.

Objectives

- Analysis of the dynamics of T cell exclusion in CRC liver metastasis.

- Investigation of the effects of TGF-β inhibition in the TME of CRC metastasis using pharmacological inhibition with Galunisertib and ubiquitous genetic ablation of the TGFBR2.

- Analysis of the immune phenotype on established CRC liver metastasis upon treatment with Galunisertib and in combination with checkpoint immunotherapy.

Publication

Tauriello, D.V.F., Palomo-Ponce, S., Stork, D., Berenguer-Llergo, A., Badia-Ramentol, J., Iglesias, M., Sevillano, M., Ibiza, S., Cañellas, A., Hernando-Momblona, X., et al. (2018). TGFβ drives immune evasion in genetically reconstituted colon cancer metastasis. Nature 554, 538–543.

LETTER

doi:10.1038/nature25492

TGFβ drives immune evasion in genetically reconstituted colon cancer metastasis

Daniele V. F. Tauriello[1,2], Sergio Palomo-Ponce[1,2], Diana Stork[1], Antonio Berenguer-Llergo[1], Jordi Badia-Ramentol[1], Mar Iglesias[2,3,4,5], Marta Sevillano[1,2], Sales Ibiza[1], Adrià Cañellas[1], Xavier Hernando-Momblona[1,2], Daniel Byrom[1], Joan A. Matarin[1], Alexandre Calon[1]†, Elisa I. Rivas[1]†, Angel R. Nebreda[1,6], Antoni Riera[1,7], Camille Stephan-Otto Attolini[1] & Eduard Batlle[1,2,6]

Most patients with colorectal cancer die as a result of the disease spreading to other organs. However, no prevalent mutations have been associated with metastatic colorectal cancers[1,2]. Instead, particular features of the tumour microenvironment, such as lack of T-cell infiltration[3], low type 1 T-helper cell ($\mathrm{T_H}1$) activity and reduced immune cytotoxicity[2] or increased TGFβ levels[4] predict adverse outcomes in patients with colorectal cancer. Here we analyse the interplay between genetic alterations and the tumour microenvironment by crossing mice bearing conditional alleles of four main colorectal cancer mutations in intestinal stem cells. Quadruple-mutant mice developed metastatic intestinal tumours that display key hallmarks of human microsatellite-stable colorectal cancers, including low mutational burden[5], T-cell exclusion[3] and TGFβ-activated stroma[4,6,7]. Inhibition of the PD-1–PD-L1 immune checkpoint provoked a limited response in this model system. By contrast, inhibition of TGFβ unleashed a potent and enduring cytotoxic T-cell response against tumour cells that prevented metastasis. In mice with progressive liver metastatic disease, blockade of TGFβ signalling rendered tumours susceptible to anti-PD-1–PD-L1 therapy. Our data show that increased TGFβ in the tumour microenvironment represents a primary mechanism of immune evasion that promotes T-cell exclusion and blocks acquisition of the $\mathrm{T_H}1$-effector phenotype. Immunotherapies directed against TGFβ signalling may therefore have broad applications in treating patients with advanced colorectal cancer.

Progression of colorectal cancer (CRC) generally coincides with successive alterations in four signalling pathways: WNT, EGFR, p53 and TGFβ[5,8]. Mice bearing compound mutations in these four pathways were recently shown to enable the study of CRC metastasis[9–11]. We crossed mice bearing conditional alleles in homologues of four key human CRC mutations: $\mathit{Apc}^{fl/fl}$, $\mathit{Kras}^{LSL\text{-}G12D}$, $\mathit{Tgfbr2}^{fl/fl}$ and $\mathit{Trp53}^{fl/fl}$ (designated A, K, T and P, respectively)[12–15], and targeted gene recombination to intestinal stem cells (ISCs) by means of the $\mathit{Lgr5}^{eGFP\text{-}creERT2}$ driver[16], which we designated L. We generated eight mouse strains bearing combinations of these mutations (Fig. 1a). Histopathological scoring demonstrated a stepwise increase in prevalence and severity of invasive adenocarcinomas along the linear progression sequence (Fig. 1b, c and Extended Data Fig. 1c–i). Ninety per cent of LAKTP mice developed carcinomas, more than half of which breached all intestinal layers (Fig. 1c). These cancers displayed a histology similar to human tumours, with mostly medium to high degrees of differentiation and abundant desmoplastic reaction (Extended Data Fig. 1d–j). Forty per cent of LAKTP mice developed metastases in the liver or lungs, or as carcinomatosis (Fig. 1d and Extended Data Fig. 1k–n), with a median latency of 66 days. Notably, mice bearing triple-mutant genotypes (LAKT, LATP or LAKP) presented with similarly invasive cancers but not metastasis (Fig. 1c). In LAKTP mice, T cells extensively infiltrated the stroma of normal mucosa and adenomas but were largely excluded from adjacent invasive cancers (Fig. 1e and Extended Data Fig. 2a). This exclusion phenotype intensified along the CRC mutational sequence (Fig. 1e). Invasive margins of compound-mutant cancers displayed high levels of stromal TGFβ activity, as indicated by the presence of phosphorylated SMAD3 (pSMAD3) (Fig. 1f and Extended Data Fig. 2b) and expression of CALD1 and IGFBP7 (Extended Data Fig. 2c, d)—two TGFβ-induced genes expressed in cancer-associated fibroblasts (CAFs) that predict poor prognosis[4]. These genetic CRC models therefore reproduce key features of the tumour microenvironment (TME) in advanced human CRCs.

We collected fresh samples from multiple primary mouse tumours or metastases and established a mouse tumour organoid (MTO) biobank (Fig. 1g). Quadruple-mutant LAKTP MTOs expanded *in vitro* independently of factors that stimulate WNT, EGF and TGFβ pathways (Fig. 1h and Extended Data Fig. 3). When injected into the caecum wall of syngeneic C57BL/6J recipients, these MTOs engrafted with a success rate of 10 out of 32 (31%) and progressed to fully invasive T3–T4 tumours (Extended Data Fig. 4a, b). Forty per cent of engrafted MTOs produced overt liver metastatic disease. We observed prominent T-cell exclusion and increased TGFβ activity in the TME in primary tumours from orthotopically transplanted LAKTP MTOs (Extended Data Fig. 4c–f). TGFβ-activated stroma is a defining feature of poor prognosis consensus molecular subtype 4 (CMS4)[7]. Transcriptomic classification indicated that LAKTP MTOs displayed the CMS4 phenotype when transplanted in the caecum of syngeneic mice, but not when cultured *in vitro* (Fig. 1i and Extended Data Fig. 5). We obtained similar results with triple-mutant MTOs. These findings confirm that stromal gene expression is required to identify poor prognosis molecular subtypes[4,17–19] (see Supplementary Discussion).

Similar to microsatellite-stable (MSS) human CRCs[20], triple- and quadruple-mutant MTOs accumulated between 0.5 and 3.5 non-synonymous coding mutations per megabase (Extended Data Fig. 6a, b), which indicates that the genomes of these tumours evolved extensively. The most prevalent mutational signature in MTOs was signature 1, characteristic of MSS CRCs[21] (Extended Data Fig. 6c). MTOs and human MSS CRCs also displayed similar numbers of predicted high-affinity MHC-I-binding neoantigens, whereas mouse CRC cell lines CT26 and MC-38 exhibited around 40 times this number (Fig. 1j). Experimental liver colonization by MTOs caused an increased metastatic burden in the *nu/nu* background compared to wild-type C57BL/6J mice (Fig. 1k), indicating that the tumours were susceptible to T-cell-mediated adaptive immunosurveillance. Indeed,

---

[1]Institute for Research in Biomedicine (IRB Barcelona), The Barcelona Institute of Science and Technology, Baldiri i Reixac 10, 08028 Barcelona, Spain. [2]Centro de Investigación Biomédica en Red de Cáncer (CIBERONC), Barcelona, Spain. [3]Department of Pathology, Hospital del Mar, 08003 Barcelona, Spain. [4]Cancer Research Programme, Hospital del Mar Research Institute (IMIM), 08003 Barcelona, Spain. [5]Autonomous University of Barcelona (UAB), Spain. [6]ICREA, Passeig Lluís Companys 23, 08010 Barcelona, Spain. [7]Department of Organic Chemistry, University of Barcelona, Martí i Franqués 1-11, 08028 Barcelona, Spain. †Present address: Cancer Research Programme, Hospital del Mar Research Institute (IMIM), 08003 Barcelona, Spain (A.C. and E.I.R.).

© 2018 Macmillan Publishers Limited, part of Springer Nature. All rights reserved.

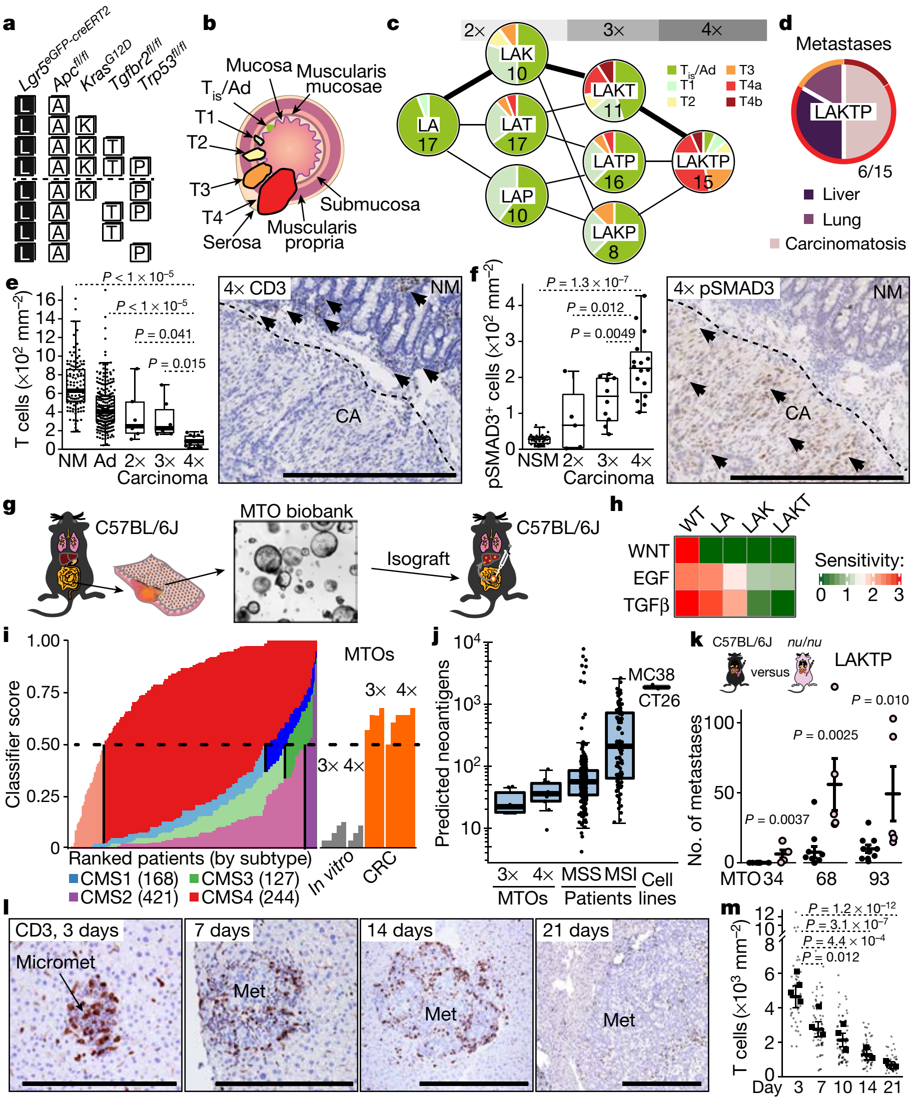

Figure 1 | Analysis of compound mutant mouse models and MTOs. **a**, Combination of alleles used to generate mouse models; dashed line distinguishes strains along the linear progression model[8] of A–K–T–P from other combinations of mutations. **b**, Classification of tumours according to the AJCC–TNM system, ranging from carcinoma *in situ* or adenoma (T_{is}/Ad) to four levels of increasingly invasive cancers (T1–T4, see Methods). **c**, Worst T-phenotype diagnosis per mouse, number of mice is indicated in the circles. The thick lines indicate the linear progression sequence. **d**, Metastasis in LAKTP mice. Outer ring, associated type of primary cancer. **e**, Box plot of T-cell density in normal mucosa (NM) and adenoma (Ad), compared to double-mutant (LAK, LAT and LAP, 2×), triple-mutant (LAKT, LAKP and LATP, 3×) and quadruple-mutant (LAKTP, 4×) cancers. $n = 119$, 242, 7, 8 and 16 regions of interest (ROIs), left to right. Right, CD3 immunohistochemistry of a LAKTP T4 carcinoma (CA), arrowheads indicate CD3$^+$ cells. Box plots have whiskers of maximum 1.5 times the interquartile range; the boxes represent first, second (median) and third quartiles. **f**, Box plot of pSMAD3$^+$ cell density in normal submucosal tissue (NSM), compared to 2×, 3× and 4× cancers, $n = 37$, 5, 10 and 16 ROIs, left to right. Right, pSMAD3 immunohistochemistry of a LAKTP T4 carcinoma, arrowheads indicate pSMAD3$^+$ cells. Two-sided Welch's *t*-test (**e**, **f**). **g**, MTO biobank and isograft technology. **h**, Mean sensitivity of MTOs to niche factors. WT, wild type. **i**, Left, cross-validation of consensus molecular subtype 4 (CMS4) classifier on human CRCs. Patients (shown as vertical bars) are ranked by subtype on the basis of classifier score. Right, classifier applied to 3× and 4× mutant MTOs *in vitro* (grey, $n = 5$ and 3, respectively) and to orthotopic isografts of those MTOs (orange, $n = 2$ and 3). **j**, Predicted MHC-I neoantigens in MTOs ($n = 6$ and 10, left and right, respectively), human CRCs ($n = 266$ and 112, left and right, respectively) and mouse CRC cell lines ($n = 2$). **k**, Liver metastasis generated by 4× MTOs in C57BL/6J or *nu/nu* mice ($n = 10$, 5, 11, 5, 10 and 5 mice, left to right; mean ± s.e.m.; two-sided Mann–Whitney *U*-test). **l**, CD3 immunohistochemistry on MTO129 liver metastases (Met) at the indicated days after intrasplenic injection. Micromet, micrometastasis. **m**, CD3$^+$ cell densities (individual metastases in grey and mean for mice in black; bars, group means ± s.e.m.); analysed with a mixed-effects linear model; $n = 4$, 3, 3, 2 and 2 mice, and $n = 39$, 58, 71, 56 and 56 tumours, left to right. Scale bars, 500 µm.

micrometastases were characterized by abundant CD3$^+$ T cells intermingled with tumour cells (Fig. 1l). Notably, T cells were progressively excluded at later time points (Fig. 1l, m).

Cell-population profiling of human or mouse CRC samples revealed that CAFs were the main contributors to TGFβ production (Extended Data Fig. 7a, b). We made use of the TGFBR1-specific inhibitor galunisertib[22] to inhibit TGFβ signalling in the TME. Treatment with galunisertib starting 11 days after transplantation of LAKTP MTOs in the caecum of syngeneic mice reduced primary tumour size, reduced the extent of carcinomatosis and blocked the appearance of liver metastases (Fig. 2a). Immunohistochemical quantification showed that galunisertib reduced the number of pSMAD3$^+$ cells (Fig. 2b) and gene expression profiling demonstrated decreased levels of TGFβ-response signatures[6] in fibroblasts (F-TBRS) and T cells (T-TBRS) (Fig. 2c).

To directly test therapeutic effects on liver metastatic disease, we inoculated LAKTP MTOs derived from either primary CRCs or liver

© 2018 Macmillan Publishers Limited, part of Springer Nature. All rights reserved.

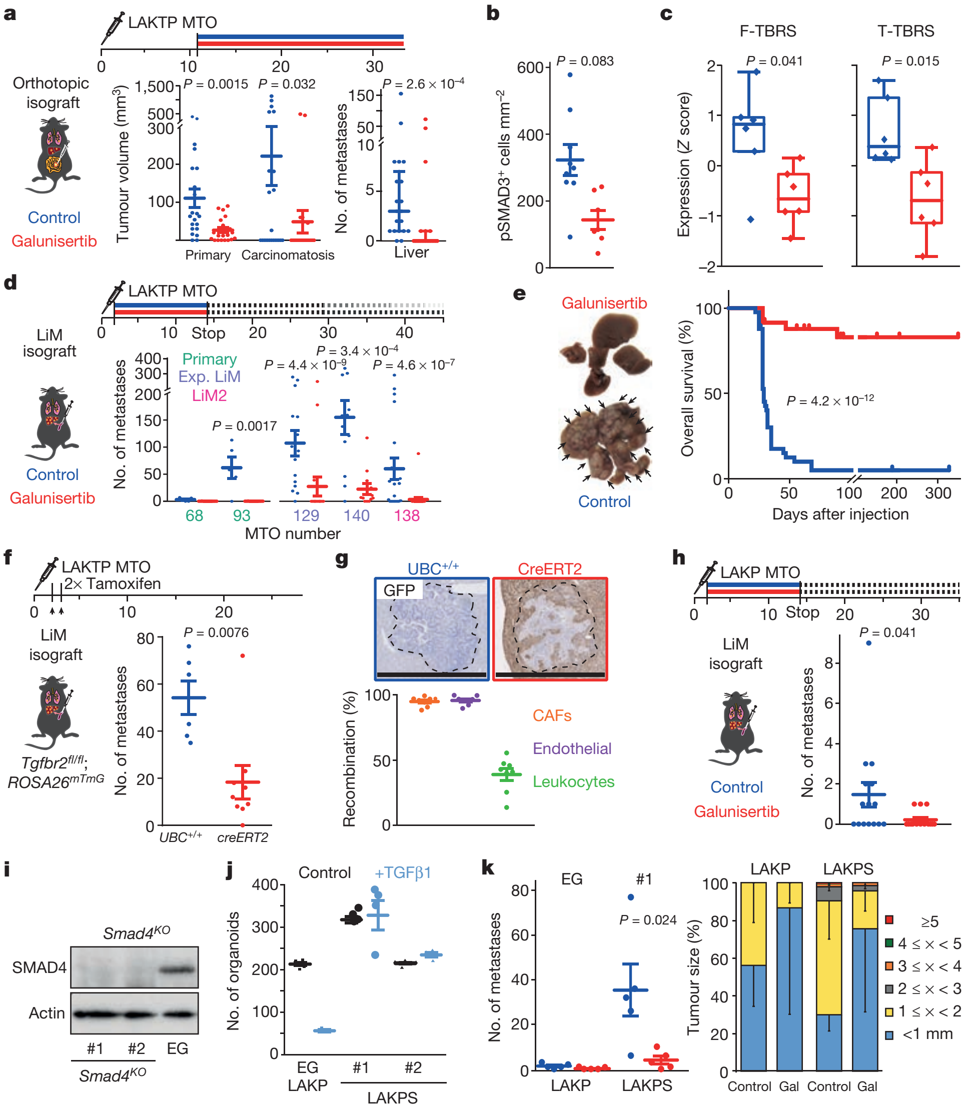

Figure 2 | Therapeutic effect of TGBβ inhibition. a, Galunisertib reduces tumour burden and metastasis in orthotopic MTO140 isografts. Middle, mean tumour volume ± s.e.m.; right, median number ± 95% confidence interval; $n = 21$ mice per condition, two-sided Mann–Whitney U test. **b**, pSMAD3$^+$ cell density (mean ± s.e.m.) in primary carcinomas ($n = 9, 7$); two-sided Student's t-test. **c**, Expression levels of TBRS in primary CRCs. Tukey box plots, $n = 6$ tumour samples, two-sided Mann–Whitney U test. **d**, Liver metastases (mean ± s.e.m.) generated by MTOs, treated with vehicle or galunisertib; $n = 5, 5, 5, 5, 15, 17, 12, 12, 20$ and 25 mice, left to right; analysed with a mixed-effects linear model. Exp. LiM, experimental liver metastasis; LiM2, second-round experimental liver metastasis. **e**, Representative livers at end point, arrows point to metastases. Kaplan–Meier survival curve of mice treated as in **d**. Control, $n = 41$ mice; galunisertib, $n = 35$ mice; Mantel–Cox test. **f**, Liver metastases (mean ± s.e.m.) in $UBC^{creERT2}$;$Tgfbr2^{fl/fl}$ mice, recombined ($n = 9$) or not ($n = 6$). **g**, Liver tumours from **f**, stained for the recombination marker GFP, representative of three experiments. Scale bars, 1 mm. The graph shows the percentage of GFP$^+$ cells (mean ± s.e.m.). **h**, Liver metastases (mean ± s.e.m.) generated by 3× LAKP MTOs. $n = 15$ and 14 mice, left and right, respectively; two-sided Mann–Whitney U test. **i**, Western blot for SMAD4 and actin of LAKP empty guide (EG)- or CRISPR-targeted (#1 and #2) $Smad4^{KO}$ organoids. **j**, LAKP or LAKPS organoids. (mean ± s.e.m., $n = 4$ technical replicates) in control medium or treated with TGFβ1. **k**, Liver metastases (mean ± s.e.m.) from LAKP (EG) and LAKPS (guide #1) MTOs. Gal, galunisertib; x, diameter. $n = 5$ mice per condition; two-sided Mann–Whitney U test. Right, tumour diameters with s.e.m., $n = 10$ mice per condition.

metastases in the portal circulation; the latter exhibited enhanced metastatic capacity (Extended Data Fig. 6e). Treatment with galunisertib markedly decreased metastatic burden for all MTOs (Fig. 2d and Extended Data Fig. 6f), effectively curing a large proportion of mice (Fig. 2e). Galunisertib blocked TGFβ signalling in the TME of metastases (Extended Data Fig. 7c–h). We also transplanted LAKTP MTOs in mice bearing floxed *Tgfbr2* alleles that express a ubiquitous CreERT2 recombinase ($UBC^{creERT2}$;$Tgfbr2^{fl/fl}$). Tamoxifen treatment induced recombination in fibroblasts, endothelial cells and leukocytes, and inhibited metastasis formation by isografted MTOs (Fig. 2f, g and Extended Data Fig. 8a). To analyse triple-mutant MTOs *in vivo*, we inoculated large numbers of cells. Four out of six tested MTOs (two LAKP and two LAKT) gave rise to metastases. However, these liver tumours remained very small (Extended Data Fig. 6g), possibly owing to niche factor dependencies[9,11,19]. Nevertheless, galunisertib treatment reduced liver metastases generated by LAKP MTOs (Fig. 2h and Extended Data Fig. 8b, c). We also introduced loss of function *Smad4* mutations (S) in LAKP MTOs using CRISPR–Cas9 technology. *In vitro*, LAKPS MTOs were resistant to the cytostatic action of TGFβ (Fig. 2i, j). *In vivo*, LAKPS formed larger numbers of liver tumours that were also larger in size than those formed by parental LAKP MTOs. Galunisertib effectively abrogated the metastatic capacity of LAKPS MTOs and, importantly,

© 2018 Macmillan Publishers Limited, part of Springer Nature. All rights reserved.

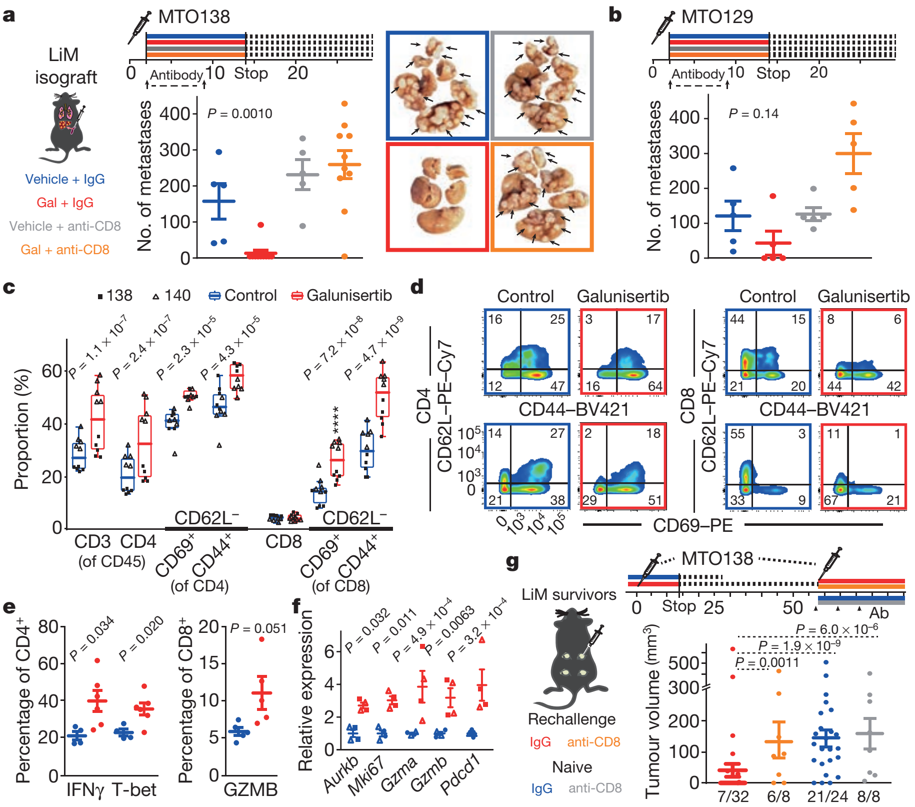

Figure 3 | TGFβ mediates immune evasion. a, **b**, Liver metastases (mean ± s.e.m.), $n = 5, 10, 5, 10$ mice, left to right (**a**), and $n = 5$ mice per condition (**b**). Two-sided Mann–Whitney *U* test. **c**–**e**, Immunophenotyping in whole livers from mice injected with MTO138 or MTO140 ($n = 5$ per condition). Tukey box plots, $n = 5$ mice per condition; analysed with a mixed-effects linear model. **d**, Flow cytometry plots from **c**, representative of two experiments. **e**, Intracellular cytokine expression (mean percentage ± s.e.m.), $n = 4, 6, 4, 6, 5$ and 5 mice, left to right; two-sided Student's *t*-tests. **f**, Relative mRNA expression (mean ± s.e.m.) on sorted CTLs from the experiment in **c**; $n = 4$ mice per condition; two-sided Student's *t*-test. **g**, Rechallenge experiment in liver metastasis survivors compared to naive hosts. Tumour volumes (mean ± s.e.m.) at end point. *x* axis, number of grown tumours/number of injections.

did not enhance growth of metastases generated by LAKP MTOs with wild-type TGFβ pathway (Fig. 2k and Extended Data Fig. 8d).

To study the kinetics of metastasis, we transduced MTOs with luciferase, which did not modify the therapeutic efficacy of galunisertib (Extended Data Fig. 8e). Bioluminescence revealed that galunisertib markedly enhanced cell killing at the onset of the exponential growth phase. However, this did not occur in *nu/nu* mice (Extended Data Fig. 8f–h). These kinetics are suggestive of an adaptive anti-tumour immune response. Indeed, the therapeutic effect of galunisertib was abolished upon depletion of CD8$^+$ cytotoxic T lymphocytes (CTLs) (Fig. 3a, b) or CD4$^+$ T-helper (T$_H$) cells (Extended Data Fig. 8i). We also transplanted MTOs in mice from the colony used to generate the original compound mutant mice. Galunisertib decreased metastatic burden in these hosts (Extended Data Fig. 8j), indicating that immunological rejection was not due to expression of exogenous antigens in MTOs such as those encoded by *eGFP* and *creERT2* transgenes.

We next assessed the status of the adaptive immune system in a transcriptomic dataset of human MSS CRC samples ($n = 981$) by measuring levels of expression signatures specific for naive or T$_H$1-activated CD4$^+$ T cells. Microsatellite-instable (MSI) CRCs displayed increased ratios of T$_H$1-to-naive T-cell genes, consistent with previous observations[23] (Extended Data Fig. 9a). In MSS CRCs, the ratio of T$_H$1 to naive cells was inversely correlated to the mean expression of *TGFB1*, *TGFB2* and *TGFB3* genes or the CAF-specific gene expression program (Extended Data Fig. 9b–f) and predicted disease relapse (Extended Data Fig. 9d, g). Therefore, abrogated T-cell differentiation, and increased TGFβ and CAF gene expression characterize a substantial subset of patients with MSS CRC and a poor prognosis.

Flow-cytometry analyses on whole livers colonized by MTOs for 7–10 days showed that there was increased recruitment of CD3$^+$ and CD4$^+$ cells after galunisertib treatment (Fig. 3c). This finding was confirmed by immunohistochemistry-based quantifications of liver sections, which also revealed an increased presence of T-bet, the master transcription factor regulating T$_H$1 cell differentiation (Extended Data Fig. 9h, i). Equivalent observations were made in treated liver metastases from parental MTOs, in experiments with orthotopic implantation, and during genetic abrogation of TGFβ signalling in the TME (Extended Data Fig. 10a–c). Importantly, both T$_H$ cells and CTLs underwent activation, indicated by the increase in CD44$^+$CD62L$^-$ and CD69$^+$CD62L$^-$ populations (Fig. 3c, d), increased levels of T-bet and IFNγ effector molecules in T$_H$ cells, and increased GZMB production and expression of proliferation genes in CTLs (Fig. 3e, f). We hypothesized that this robust immune response might immunize mice against the tumour cells. When survivors were rechallenged with the same MTO, most tumours were rejected within two weeks in the continued absence of treatment, whereas the MTOs grew efficiently in naive C57BL/6J recipients. Concurrent depletion of CD8$^+$ CTLs inhibited tumour rejection (Fig. 3g). We conclude that increased TGFβ levels in the TME limit adaptive immune responses by inhibition of the T$_H$1-effector cell phenotype.

Finally, we assessed the therapeutic action of galunisertib in mice with overt metastatic disease. Galunisertib treatment 14 days after MTO inoculation reduced metastatic burden but resulted in few complete remissions (Fig. 4a). Nevertheless, we observed increased infiltration of CD4$^+$ T cells and of T-bet$^+$ lymphocytes immediately after initiation of therapy (Extended Data Fig. 10d). Exploring resistance mechanisms to explain this mild response, we discovered that galunisertib-activated T cells exhibited marked surface expression of programmed cell-death protein 1 (PD-1) (Fig. 4b), and that metastases generated by MTOs progressively recruited stromal PD-1 ligand 1 (PD-L1)$^+$ cells—most

© 2018 Macmillan Publishers Limited, part of Springer Nature. All rights reserved.

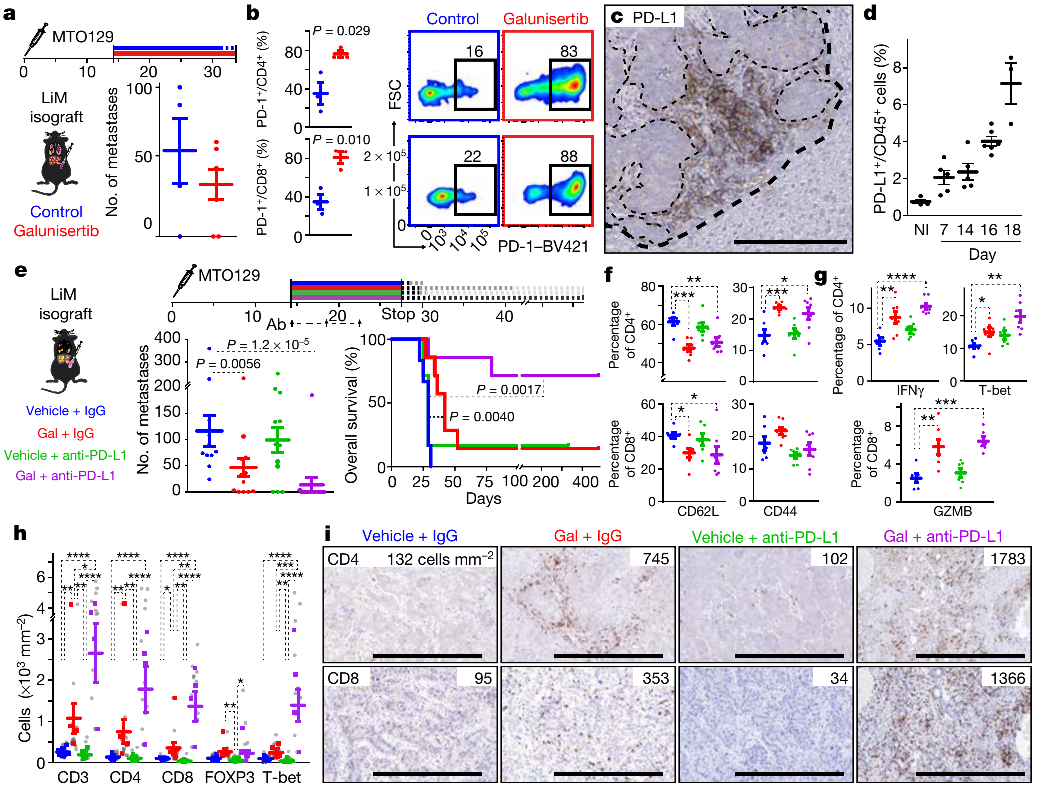

Figure 4 | Dual immunotherapy cures established metastases. **a**, Liver metastases (mean ± s.e.m.) in animals treated with galunisertib from day 14 after injection with MTO129, $n = 4$ and 6 mice, left and right, respectively. **b**, PD-1$^+$ T cells (mean ± s.e.m.) in microdissected liver metastases four days after the start of treatment (day 18), $n = 3$ per condition; two-sided Student's t-test. Right, representative density plots. **c**, PD-L1 immunohistochemistry on MTO129 liver metastases. **d**, PD-L1$^+$ leukocytes in liver metastases (mean ± s.e.m.) at indicated days after injection, or in non-injected (NI) liver, $n = 4, 5, 5, 6$ and 3, left to right. **e**, Treatment from day 14 of established liver metastases. Left, mean number of liver metastases ± s.e.m., $n = 11, 13, 12$ and 14 mice, left to right; two-sided Mann–Whitney U test; right, Kaplan–Meier survival curve; $n = 6$ (vehicle + IgG), 7 (galunisertib + IgG), 6 (vehicle + anti-PD-L1), 7 (galunisertib + anti-PD-L1), Mantel–Cox test. **f**, **g**, Surface activation markers (**f**) and intracellular markers (**g**) in mice euthanized two days after start of treatment (day 16). Mean percentage ± s.e.m., $n = 6, 7, 6, 7$ mice, left to right; two-sided Student's t-test. **h**, Cell densities quantified by immunohistochemistry from mice in **e**. Individual metastases in grey, mouse means in coloured squares; bars show group means ± s.e.m., $n = 5, 4, 4$ and 4 mice, left to right; analysed with a mixed-effects linear model. **i**, Images from the analysis in **h**; mean cell densities are indicated. Scale bars, 500 μm. $^*P < 0.05$, $^{**}P < 0.01$, $^{***}P < 0.001$, $^{****}P < 0.0001$.

prominently tumour-associated macrophages—as they expanded in size (Fig. 4c, d and Extended Data Fig. 10e, f). Treatment of mice bearing overt metastatic disease with anti-PD-L1 therapy alone had a very modest therapeutic effect (Fig. 4e). However, combined treatment with galunisertib and anti-PD-L1 antibodies induced a pronounced immune response, with increased T-bet and IFNγ levels in CD4$^+$ T$_H$ cells and increased GZMB production in CTLs, which eradicated most metastases and prolonged recurrence-free survival for over a year after cessation of treatment (Fig. 4e–g). This response was associated with a marked, synergistic increase in infiltrating lymphocytes and T-bet expression (Fig. 4h, i), indicating both a disruption of the T-cell-exclusion phenotype characteristic of progressed metastatic disease and prominent T$_H$1 immune activation.

It has been hypothesized that MSS CRCs are immunologically 'cold', that is, scarcely T-cell infiltrated and possibly non-immunogenic, and that they are therefore unlikely to benefit from immune therapies[24] (Supplementary Discussion). By contrast, our data reveal that this class of CRCs can be killed effectively by the adaptive immune system through a CTL-dependent process, which CRC cells avert by increasing TGFβ levels. Consistent with the well-established role of TGFβ signalling in suppressing differentiation and activity of T cells[25–28], we observed that a TGFβ-activated TME antagonizes the T$_H$1-effector cell phenotype. We also show that such a TME excludes T cells from tumours, a phenomenon associated with poor outcomes across cancer types[3,29,30]. Enabling immune infiltration using TGFβ inhibitors is sufficient to confer susceptibility to anti-PD-1–PD-L1 checkpoint-based therapies, a strategy that may have broad applications for treatment of cancers that grow in a TGFβ-rich environment. These results strongly suggest that inhibition of TGFβ signalling could be promising as immunotherapy for patients with MSS, stroma-rich CRCs and a poor prognosis.

Online Content Methods, along with any additional Extended Data display items and Source Data, are available in the online version of the paper; references unique to these sections appear only in the online paper.

Received 14 November 2016; accepted 2 January 2018.

Published online 14 February 2018.

1. Jones, S. *et al.* Comparative lesion sequencing provides insights into tumor evolution. *Proc. Natl Acad. Sci. USA* **105,** 4283–4288 (2008).
2. Mlecnik, B. *et al.* The tumor microenvironment and immunoscore are critical determinants of dissemination to distant metastasis. *Sci. Transl. Med.* **8,** 327ra26 (2016).
3. Galon, J. *et al.* Type, density, and location of immune cells within human colorectal tumors predict clinical outcome. *Science* **313,** 1960–1964 (2006).
4. Calon, A. *et al.* Stromal gene expression defines poor-prognosis subtypes in colorectal cancer. *Nat. Genet.* **47,** 320–329 (2015).
5. Cancer Genome Atlas Network. Comprehensive molecular characterization of human colon and rectal cancer. *Nature* **487,** 330–337 (2012).
6. Calon, A. *et al.* Dependency of colorectal cancer on a TGF-β-driven program in stromal cells for metastasis initiation. *Cancer Cell* **22,** 571–584 (2012).
7. Guinney, J. *et al.* The consensus molecular subtypes of colorectal cancer. *Nat. Med.* **21,** 1350–1356 (2015).

© 2018 Macmillan Publishers Limited, part of Springer Nature. All rights reserved.

8. Fearon, E. R. & Vogelstein, B. A genetic model for colorectal tumorigenesis. *Cell* **61,** 759–767 (1990).
9. Fumagalli, A. *et al.* Genetic dissection of colorectal cancer progression by orthotopic transplantation of engineered cancer organoids. *Proc. Natl Acad. Sci. USA* **114,** E2357–E2364 (2017).
10. O'Rourke, K. P. *et al.* Transplantation of engineered organoids enables rapid generation of metastatic mouse models of colorectal cancer. *Nat. Biotechnol.* **35,** 577–582 (2017).
11. de Sousa e Melo, F.*et al.* A distinct role for Lgr5$^+$ stem cells in primary and metastatic colon cancer. *Nature* **543,** 676–680 (2017).
12. Colnot, S. *et al.* Liver-targeted disruption of *Apc* in mice activates β-catenin signaling and leads to hepatocellular carcinomas. *Proc. Natl Acad. Sci. USA* **101,** 17216–17221 (2004).
13. Jackson, E. L. *et al.* Analysis of lung tumor initiation and progression using conditional expression of oncogenic *K-ras*. *Genes Dev.* **15,** 3243–3248 (2001).
14. Marino, S., Vooijs, M., van Der Gulden, H., Jonkers, J. & Berns, A. Induction of medulloblastomas in *p53*-null mutant mice by somatic inactivation of *Rb* in the external granular layer cells of the cerebellum. *Genes Dev.* **14,** 994–1004 (2000).
15. Levéen, P. *et al.* Induced disruption of the transforming growth factor beta type II receptor gene in mice causes a lethal inflammatory disorder that is transplantable. *Blood* **100,** 560–568 (2002).
16. Barker, N. *et al.* Identification of stem cells in small intestine and colon by marker gene *Lgr5*. *Nature* **449,** 1003–1007 (2007).
17. Isella, C. *et al.* Stromal contribution to the colorectal cancer transcriptome. *Nat. Genet.* **47,** 312–319 (2015).
18. van de Wetering, M. *et al.* Prospective derivation of a living organoid biobank of colorectal cancer patients. *Cell* **161,** 933–945 (2015).
19. Fujii, M. *et al.* A colorectal tumor organoid library demonstrates progressive loss of niche factor requirements during tumorigenesis. *Cell Stem Cell* **18,** 827–838 (2016).
20. Lawrence, M. S. *et al.* Mutational heterogeneity in cancer and the search for new cancer-associated genes. *Nature* **499,** 214–218 (2013).
21. Alexandrov, L. B. *et al.* Signatures of mutational processes in human cancer. *Nature* **500,** 415–421 (2013).
22. Rodón, J. *et al.* First-in-human dose study of the novel transforming growth factor-β receptor I kinase inhibitor LY2157299 monohydrate in patients with advanced cancer and glioma. *Clin. Cancer Res.* **21,** 553–560 (2015).
23. Llosa, N. J. *et al.* The vigorous immune microenvironment of microsatellite instable colon cancer is balanced by multiple counter-inhibitory checkpoints. *Cancer Discov.* **5,** 43–51 (2015).
24. Le, D. T. *et al.* PD-1 blockade in tumors with mismatch-repair deficiency. *N. Engl. J. Med.* **372,** 2509–2520 (2015).
25. Gorelik, L. & Flavell, R. A. Abrogation of TGFβ signaling in T cells leads to spontaneous T cell differentiation and autoimmune disease. *Immunity* **12,** 171–181 (2000).
26. Marie, J. C., Liggitt, D. & Rudensky, A. Y. Cellular mechanisms of fatal early-onset autoimmunity in mice with the T cell-specific targeting of transforming growth factor-β receptor. *Immunity* **25,** 441–454 (2006).
27. Thomas, D. A. & Massagué, J. TGF-β directly targets cytotoxic T cell functions during tumor evasion of immune surveillance. *Cancer Cell* **8,** 369–380 (2005).
28. Mehal, W. Z., Sheikh, S. Z., Gorelik, L. & Flavell, R. A. TGF-β signaling regulates CD8$^+$ T cell responses to high- and low-affinity TCR interactions. *Int. Immunol.* **17,** 531–538 (2005).
29. Chen, D. S. & Mellman, I. Elements of cancer immunity and the cancer-immune set point. *Nature* **541,** 321–330 (2017).
30. Joyce, J. A. & Fearon, D. T. T cell exclusion, immune privilege, and the tumor microenvironment. *Science* **348,** 74–80 (2015).

Supplementary Information is available in the online version of the paper.

Acknowledgements We thank E. Sancho for critical reading of this manuscript, all members of the Batlle laboratory for support and discussions, and members of the López-Bigas laboratory for help with revising the manuscript. We are grateful for the assistance of the IRB Barcelona core facilities for histopathology, functional genomics, mouse mutant and advanced digital microscopy; the flow cytometry and animal facilities of the UB/PCB; and the CRG genomic unit. D.V.F.T. held a Juan de la Cierva postdoctoral fellowship from MINECO. This work was supported by grants from the Doctor Josef Steiner Foundation, ERC advanced grant 340176, Instituto de Salud Carlos III, Olga Torres Foundation, BBVA Foundation, grant SAF-2014-53784 (MINECO) and by Fundación Botín. IRB Barcelona is the recipient of a Severo Ochoa Award of Excellence from MINECO.

Author Contributions D.V.F.T., S.P.-P., D.S. and A.Cal. performed animal husbandry and genotyping; M.S. performed immunohistochemistry; D.V.F.T. and M.I. analysed histopathology. D.V.F.T. generated MTOs, which D.V.F.T. and D.S. characterized *in vitro*; D.S. performed CRISPR experiments; C.S.-O.A. and A.B.-L. performed exome and RNA-seq analyses, other bioinformatics (CMS classifier and patient data), and statistical analyses. S.P.-P., D.V.F.T., J.B.-R., A.Cañ. and X.H.-M. performed mouse isografting; D.V.F.T., D.S. and J.B.-R. quantified immunohistochemistry. D.B., J.A.M. and A.R. synthesized galunisertib. D.V.F.T. coordinated and performed animal treatments and analysed the data. D.V.F.T., J.B.-R., S.I., E.I.R. and A.R.N. performed immunophenotyping experiments. E.B. and D.V.F.T. conceived the study, coordinated experiments and wrote the manuscript. E.B. supervised the study.

Author Information Reprints and permissions information is available at www.nature.com/reprints. The authors declare no competing financial interests. Readers are welcome to comment on the online version of the paper. Publisher's note: Springer Nature remains neutral with regard to jurisdictional claims in published maps and institutional affiliations. Correspondence and requests for materials should be addressed to E.B. (eduard.batlle@irbbarcelona.org).

Reviewer Information *Nature* thanks L. Vermeulen and the other anonymous reviewer(s) for their contribution to the peer review of this work.

© 2018 Macmillan Publishers Limited, part of Springer Nature. All rights reserved.

METHODS

Ethics and animal maintenance. All experiments with mouse models were approved by the Animal Care and Use Committee of Barcelona Science Park (CEEA-PCB) and the Catalan government. Mice were maintained in a specific-pathogen-free (SPF) facility with a 12-h light–dark cycle and given *ad libitum* access to standard diet and water. All mice were closely monitored by the authors (D.V.F.T. and S.P.-P), facility technicians (during treatments) and by an independent veterinary scientist responsible for animal welfare.

Genetically modified mice. *Lgr5-EGFP-IRES-creERT2* (B6.129P2-*Lgr5*$^{tm1(cre/ERT2)Cle}$/J; stock 008875), *LSL-K-ras*^{G12D} (B6.129S4-*Kras*^{tm4Tyj}/J; stock 008179), *p53*^{LoxP} (B6.129P2-*Trp53*^{tm1Brn}/J; stock 008462) and *Tgfbr2*^{LoxP} (B6.129-*Tgfbr2*^{tm1Karl}/J; stock 012603) mouse strains[13–16] were obtained from The Jackson Laboratory, and *Apc*^{LoxP} mice were obtained from C. Perret[12]. Mice were inbred on a C57BL/6J background and successive crosses were performed to combine alleles. In this study, we have abbreviated the alleles: L (Lgr5$^{eGFP\ creERT2}$), A (*Apc*^{LoxP}), K (*LSL-Kras*^{G12D}), T (*Tgfbr2*^{LoxP}) and P (*p53*^{LoxP}) and generated the following strains: LAK, LATK, LAPK, LATPK. For practical reasons, the strains were maintained as homozygous (*lox/lox*) when possible (A, T, P) and we used both K-heterozygous and wild-type littermates. -*UBC*^{creERT2};*Tgfbr2*$^{fl/fl}$(B6.Cg-Tg(*UBC-creERT2*)1Ejb/2J; stock 008085) and Rosa26^{mTmG} (B6.129(Cg)-Gt(ROSA)26Sortm4 (*ACTB-tdTomato-eGFP*)Luo/J; stock 007676) mice have been described previously[31,32]. The latter allele allowed us to detect recombination using the shift from tdTomato to eGFP expression.

Recombination of genetic models. To induce tumorigenesis from mutated intestinal stem cells (ISC) with preferred localization in the distal part of the intestine, adult mice (at 12–13 weeks of age) were given drinking water (*ad libitum*) containing 2.5–3% (w/v) dextran sodium sulfate (DSS) for five days, and two intraperitoneal injections of diluted (4 mg/kg) tamoxifen (Sigma; dissolved in sunflower oil with 0.5% ethanol) on days 0 and 5. Thirteen per cent of mice treated in this way died in the first two weeks, most likely owing to DSS toxicity. These mice were excluded from the analysis. Animal weight, stool type and overall appearance were scored two times per week. With increasing morbidity, mice were evaluated more frequently until the experimental end point: progressive or rapid weight loss or emaciation and poor physical appearance, characterized by anaemia, hunched posture, ungroomed appearance and lethargy. Mice were then euthanized and dissected; the wall of the peritoneum was inspected and intestines, mesentery, liver, spleen, kidneys, diaphragm and lungs were collected. After macroscopic and/or binocular analysis, tissues were washed in phosphate-buffered saline (PBS), fixed in 10% formalin solution (Sigma) overnight and embedded in paraffin. Survival statistics were analysed using GraphPad Prism software (v.7.03). Median latency of metastasis was obtained by taking the median survival time of the animals in which metastases were detected.

Although the DSS-treatment-mediated induction of inflammation is acute and subsides after 2–3 weeks, we also induced gene recombination with tamoxifen without DSS treatment. Without this acute inflammation, induction still gave rise to tumours equivalent to those described here (including invasive carcinomas). However, tumour burden tended to concentrate to the distal ileum (small intestine), leading to adenomatous carpets, causing serious complications for the mouse, including reduced life span. The benefit of DSS is that it helps to target the colon. The experiments without DSS are not included in the survival and tumour assessment of this study.

Recombination on the *UBC*^{creERT2};*Tgfbr2*$^{fl/fl}$ background was performed with two shots of 80 mg/kg tamoxifen on days two and three. One mouse was excluded from the analysis shown in Fig. 2f because it exhibited no recombination upon tamoxifen treatment.

Histology and immunohistochemistry. Standard haematoxylin and eosin and antibody staining were performed on 4-μm tissue sections using standard procedures, as described previously[4]. Antibodies against CALD1 (rabbit; Sigma HPA008066; 1:250), IGFBP7 (rabbit; Sigma HPA002196; 1:200), pSMAD2 (rabbit; Cell Signaling 3108; 1:50), CD4 (rabbit; Sino Biological 50134-R001; 1:1000), CD8 (rabbit; Biorbyt orb10325-200; 1:200), FoxP3 (rabbit; Abcam ab54501; 1:1000), T-bet (Santa Cruz sc-21003; 1:500), pSMAD3 (rabbit; Abcam ab52903; 1:500) and PD-L1 (Cell Signalling 16764988S; 1:25) were used for staining overnight at 4 °C. Antibodies against GFP (rabbit; Life Technologies A11122; 1:500) and CD3 (rabbit; DAKO IS50330; 1:30) were used for staining for 2 h at room temperature. Images of histology and immunohistochemistry were taken with a Nikon Eclipse E600 and Nikon DS-Ri1 camera or with a Hamamatsu NanoZoomer Digital Slide Scanner (20× magnification).

Histopathological quantifications. Haematoxylin- and eosin-stained sections of intestines were scored blindly for T (tumour) status by an expert pathologist (M.I.) and a second observer (D.V.F.T.) using the AJCC–TNM system: scoring for T_{is} (carcinoma *in situ*), T1 (adenocarcinoma with submucosal invasion), T2 (intramuscular invasion), T3 (transmuscular invasion; serosa intact or cannot be evaluated) or T4 (transserosal invasion; T4b when local metastasis is evident, otherwise T4a). Across all genotypes, 156 tissue samples were scored (both small intestine and large intestine: caecum, colon and rectum) from 68 mice across eight genotypes. Given the high expression of *Lgr5* in the distal ileum and caecum, these tissues were in some cases overgrown with a carpet of dysplastic tissue, making adenoma counting impossible. However, we observed no obvious correlation between the percentage of dysplastic small-intestine surface and genotype. All invasive adenocarcinomas (small and large intestine) and large intestine adenomas were counted individually, reaching a total count of 1,477 tumours.

Mouse tumour organoid generation and culture. Before tissue fixation, tumours were dissected to include potential submucosal invasion and washed in PBS. Dissected material was roughly chopped with razor blades, followed by enzymatic digestion with 200 U/ml collagenase IV in DMEM (Life Technologies) for 20 min at 37 °C. Tissue fragments were subsequently treated by mechanical disruption in DMEM with 10% FBS (Life Technologies), washed with cold PBS and filtered through 100- and 40-μm meshes. Single-cell preparations were stained with propidium iodide (PI, a membrane integrity marker) and GFP^+PI^- cells were sorted in a FACS Aria flow cytometer (BD Biosciences). Typically, around 1,000 cells were obtained and plated in a drop of cold basement-membrane extract (BME) medium (Cultrex BME Type 2, Amsbio): 40 μl in a prewarmed (37 °C) well of a standard 24-well plate (Corning). After 5 min, mouse tumour organoid culture medium (advanced DMEM/F12, supplemented with 10 mM HEPES, Glutamax, B-27 without retinoid acid (all Life Technologies), 50 ng/ml recombinant human EGF (Peprotech), 100 ng/ml recombinant human NOGGIN and 1 μM galunisertib (LY2157299, see below)) was added. NOGGIN was produced in house; expressed as a His-tagged protein in HEK293-6E cells and purified with a 5-ml nickel-affinity column and a 5-ml HisTrap HP column in an ÄKTAxpress at 4 °C. Protein fractions were pooled and desalted (HiPrep 26/10 column), and tested on mouse *Apc*-mutant adenoma organoids or on bone morphogenic protein (BMP)-sensitive patient-derived organoids, analysing *ID1* and *ID3* gene expression by quantitative PCR. In initial passages, MTO medium was supplemented with the antimicrobial reagent Normocin (InvivoGen). MTOs were cultured at 37 °C with 85–90% humidity, atmospheric O_2 and 5% CO_2.

For MTO passaging, basement-membrane extract drops were washed once with HBSS (Lonza) and treated with Trypsin-EDTA (Sigma) for 20 min at 37 °C, followed by mechanical disaggregation of organoid fragments (by pipetting) until a single-cell suspension was obtained. Trypsin was quenched with FBS, cells were washed with HBSS and replated in cold BME medium on warm plates. MTOs were frozen as trypsinized organoids (single cells or small clusters) in DMEM with 50% FBS and 10% DMSO (Sigma). Cultures were checked bimonthly for mycoplasma contamination.

CRISPR genome editing. For gene knockout, guides were designed and cloned into px330-U6-Chimeric BB-CBh-hSpCas9 (Addgene: #42230), which was modified by introducing a SV40 promoter–IRFP expression cassette downstream of hSpCas9. Guide sequences (sgRNA indicated in upper case, restriction overhang in lower case):

Smad4: #1 forward, caccgAGACAGGCATCGTTACTTGT and reverse, aaacACAAGTAACGATGCCTGTCTc; *Smad4*: #2 forward, caccgAGTTTGATGTGTCATAGACA and reverse, aaacTGTCTATGACACATCAAACTc; *mCherryLuc*: forward, caccGCGCATGAACTCCTTGATGA and reverse aaacTCATCAAGGAGTTCATGCGC.

Organoids were nucleofected using a Nucleofector 2b (Lonza) in combination with the Cell Line Nucleofector Kit V (Lonza). Organoids were trypsinized for 15 min at 37 °C to generate single cells ($1.0–1.5 \times 10^6$ cells per guide), which were resuspended in 100 μl nucleofection buffer mix containing 3 μg sgRNA and nucleofected using program A32. Subsequently, cells were plated in BME medium and cultured in full growth medium. For *Smad4* knockout mutants, three days after nucleofection, growth medium was exchanged for selection medium (+ TGFβ1). Selection of *mCherry-Luc* knockout mutants was achieved by FACS sorting of *IRFP-mCherry* double-negative cells twice.

Western blotting. Trypsinized MTO cell pellets were resuspended in lysis buffer (1 mM EDTA, 1 mM EGTA, 1% SDS) containing protease inhibitor cocktail (Sigma). Protein concentration was determined using a standard Bradford assay (BioRad) and 30 μg per sample was separated by SDS–PAGE and transferred to a PVDF membrane (Millipore). Membranes were incubated with antibodies in TBS-Tween (0.2%) containing 5% milk at room temperature for 1 h. Antibodies against SMAD4 (B-8; Santa Cruz sc7966) and actin (Abcam ab20272) were used. The secondary antibody was horseradish peroxidase (HRP)-conjugated goat anti-mouse IgG (Pierce 31430).

Immunohistochemical quantifications. Scanned CD3, CD4, CD8, FoxP3, T-bet and pSMAD3 immunohistochemistry stainings were analysed in QuPath (v.0.1.2) using the positive cell detection feature with empirical parameters. Several ROIs (tumours) were taken per section. In cases in which multiple sections per mouse or liver were considered, care was taken to avoid quantifying the same tumour

© 2018 Macmillan Publishers Limited, part of Springer Nature. All rights reserved.

ore than once. Data were processed and visualized with R and RStudio[33] (v.3.4.2 d v.1.1.383, respectively) and the ggplot2[34] package (v.2.2.1) (see Statistics and producibility).

eoantigen prediction. Single-nucleotide variants that were annotated as on-synonymous or nonsense and in-frame insertions or deletions were selected r each sample. Peptides including ten bases upstream and downstream from e alteration were extracted from the canonical protein associated with the orresponding gene and were discarded if they matched another annotated protein. uman CRC: all mutations and predicted neoantigens for human CRC samples ere downloaded from https://tcia.at/neoantigens. Samples were classified as MSS MSI according to the TCGA consortium[5].

For both mouse and human data, neoantigens were predicted using netMHCpan ftware (v.2.8). See Supplementary Methods for a detailed description.

ouse injections. For all injections, C57BL/6J (or athymic BALB/c *nu/nu*) mice ere purchased from Janvier Labs at six weeks of age and injected at seven weeks. x was matched with the origin of the tumour. Intrasplenic or portal vein injecons were used for liver colonization by the introduction of dissociated organoids ingle cells) into the portal circulation; MTOs were cultured in standard six-well lates for four days and trypsinized as described in 'Mouse tumour organoid eneration and culture'. The resulting cell suspension was filtered through 100- d 40-μm meshes (to remove clumps of cells and aggregated debris). Cells were ounted and suspended in HBSS for injection, using 2–5 × 10^5 cells in 70 μl per ouse. Intrasplenic injections were performed as previously described[4,6,35]. For ortal vein injections, a 30*G* syringe was used to inject 100 μl of cell suspension rectly into the portal vein. Mice were euthanized at 3–5 weeks, visible liver metasses were counted and data were analysed using GraphPad Prism software (v.7.03). or subcutaneous injections, MTOs were cultured in standard six-well plates for ree days and recovered with Cell Recovery Solution (BD Biosciences) for 40 min ice. Organoids were washed in HBSS and a 10% fraction was trypsinized for cell ounting (Neubauer or TC20 automated cell counter, Bio-Rad). Organoids were spended in HBSS with 30% BME, an equivalent of 1.5 × 10^5 cells was injected 2–4 locations on the flanks of each mouse. Growth was scored by palpation and olume was measured with a caliper (multiplying three orthogonal diameters and ividing by two) twice per week. In accordance with our IACUC protocol, mice ith tumours over 300 mm^3 in volume were euthanized. Intracaecum injections ere used for orthotopic isograft formation: MTOs were recovered as for subutaneous injection, and an equivalent of 5 × 10^5 cells in 11 μl was injected per ouse. Intracaecum injections were performed using a 30*G* needle under binocur guidance, adapting the protocol used in ref. 36. Mice were euthanized ten weeks ter injection and metastasis was scored macroscopically as well as histologically. lternatively, orthotopic primary tumours were generated by transplantation of 1-mm^3 piece of subcutaneously grown MTO-derived tumour (for example, for × MTO orthotopic transplantation); the piece was sutured on the tip of the ecum, which was folded over itself to mitigate carcinomatosis. Post-injection, l mice received analgesia (buprenorphine). The caliper technique was used to easure orthotopic tumour sizes after mice were killed. After measurement, pieces ere dissected from fresh tumours and lysed in TRIzol (Life Technologies). RNA as purified with the Ambion PureLink kit (Life Technologies).

ouse treatments. Galunisertib (also known as LY2157299) was synthesized in ouse and prepared as previously described[6]. Galunisertib or vehicle control was dministered by gavage in a 0.15 ml volume, twice per day, starting two days after ll injection for metastasis-initiation experiments, unless otherwise indicated reatments starting two days after injection give identical results to pre-treating vo days before injection). A 800 mg/kg dose per treatment was used for all xperiments except for the treatment of MTO138, or for the prolonged treatment f orthotopically implanted mice, in which 400 mg/kg doses were used. For *vivo* $CD8^+$ T-cell depletion, rat CD8α (YTS 169.4; BioXCell BE0117) or rat G2b (LTF-2; BioXCell BE0090) isotype-control antibodies were diluted to 1 mg/ l in PBS and 200 μl was administered per mouse by intraperitoneal injection on ays −1, 6 and 13 (unless otherwise indicated) relative to the day of MTO injection. or $CD4^-$ T_H cell depletion, rat anti-CD4α (GK1.5; BioXCell BE0003-1) or rat G2b isotype-control antibodies were used. For checkpoint immunotherapy or ual immunotherapy, we used rat PD-L1 (10F.9G2; BioXCell BE0101) or rat IgG2b TF-2; BioXCell BE0090) isotype-control antibodies.

***vivo* study design.** Experimental group sizes were practically associated to cage zes (five mice per cage) and treatment experiments were designed to have $n \geq 5$ ice per group (one or more cages). No mice were excluded from the analysis, nless explicitly indicated in the Methods. For gavage (galunisertib) treatment, as ehicle control and galunisertib are visually distinguishable, the only randomizaon we performed was the order of injecting mice: the researcher performing the jections was blinded to the treatment group. End-point criteria are equivalent to ose described in 'Recombination of genetic models'. For genetic models, litterates were used as controls and cohorts were accumulated over time for logistical reasons. Mice were excluded if no tumours were observed after a year of survival post-induction.

Statistics and reproducibility. When no statistical control for confounders was needed, numbers of metastases in each condition were compared using a two-sided Mann–Whitney *U* test with exact computation of the null hypothesis, as implemented in the wilcox_test function in the R[33] coin package[37] or in GraphPad Prism. For Fig. 2d, where data were derived from different experimental runs and/or the same treatment performed on multiple MTOs, a mixed-effect linear model was fitted in which experiment run and/or MTO were included as a random effect.

In immunohistochemical experiments and the FACS experiment shown in Fig. 3c, group mean differences were assessed using a linear model. When the data involved more than one MTO (Fig. 3c and Extended Data Figs 9h and 10a) or more than one experiment run (Extended Data Figs 9h and 10c), these variables were included in the models as covariates. When multiple observations per mouse were derived, a mixed-effects linear model was fitted that included the mouse as a random effect (Figs 1m, 4h and Extended Data Figs 9h, 10a, c, d); otherwise, a standard linear regression model (only fixed effects) was used for analysis (Extended Data Fig. 10b).

In all cases, a fourth root was used to transform the outcomes in order to fulfil the assumptions of the linear models. Immunohistochemical quantifications: besides plotting individual tumours (grey), results were represented at the mouse level (coloured or black squares or MTO-dependent symbols) and at group level using the adjusted means and standard error of the means derived by the models in their original scale, after undoing the transformation. To achieve this, standard error of the means were computed by simulation from the corresponding model[38]. Wald tests derived from the linear models were used to perform pairwise comparisons between experimental conditions. A 5% level was chosen for statistical significance. All the analyses were performed using R[33]. Mixed-effects models were fitted using the R packages lme4[39] and lmerTest[40].

For the Kaplan–Meier survival curve after galunisertib treatment (Fig. 2e), all censored mice were metastasis-free when killed. Some mice were euthanized at the end point of control mice (severe morbidity), in order to count nodules at the same time point. Metastasis-burdened mice (≥1 tumour) were scored as death events, whereas disease-free mice were censored from the plot (ticks, zeroes in Source Data).

Tukey box plots in Figs 1e, f, j, 2c 3c and Extended Data Figs 3d, 7a and 9a–c, have whiskers of maximum 1.5 times the interquartile range; the boxes represent first, second (median) and third quartiles. In Fig. 1c, *P* values for comparison of phenotype severity, defined as severe (T3 or higher) versus less severe (<T3), are 0.0002 for LAKTP versus combined 3× genotypes, and <0.0001 for LAKTP versus combined 2× genotypes and for LAKTP versus LA (Fisher's exact test). We also tested for the presence (≥T1) or absence of carcinomas and the *P* values for these comparisons are: 0.0013 for LAKTP versus 3×, 0.0005 for LAKTP versus 2×, and <0.0001 for LAKTP versus LA (Fisher's exact test). The immunohistochemistry images in Fig. 1e, f are representative of four independent experiments. In Fig. 1i, numbers of patients are indicated; MTOs *in vitro*: 3×, $n = 5$ individual MTOs; and 4×, $n = 3$; plotted values are means of biological duplicates. MTOs orthotopically transplanted: 3×, $n = 2$ individual MTOs (MTO54 and 207); 4×, $n = 3$ individual MTOs (MTO68, 93 and 140); plotted values are biological duplicates (2*n*). The experiment in Fig. 1l, m was performed once. Besides providing individual *P* values, this model was used for the overall assessment of galunisertib treatment effect: control mean (95% confidence interval), 24.0 (10.5–47.7) versus galunisertib: 0.084 (0.00–0.81); $P = 1.2 \times 10^{-12}$. Data are from ten independent experiments. In Fig. 2e, data are from seven independent experiments, using either MTO129 or MTO138. In Fig. 2h, data are from MTO54 and MTO220, combined. Figure 2i, j, using MTO220, is representative of two independent experiments. Western blot source data are shown in Supplementary Fig. 1. In Fig. 2k, right, the values are fraction of total ± s.e.m. Data are from experiment with empty guide or from guides #1, #2 LAKP and S combined, from two independent experiments. The experiment in Fig. 3a was performed with MTO138, and the experiment in Fig. 3b was performed with MTO129. In Fig. 3g, *P* values refer to the comparison between: anti-CD8 and IgG in the survivors ($P = 0.0043$); rechallenge IgG and naive IgG, and between rechallenge IgG and naive anti-CD8 ($P < 0.0001$); two-sided Mann–Whitney *U* test. Figure 4b, c are representative of two experiments. In Fig. 4d, MTO129 is injected. In Fig. 4f, *P* values are for CD4 and CD62L: 0.0002 (control versus galunisertib) and 0.0051 (control versus double); CD44: 0.0008 (control versus galunisertib) and 0.0297 (control versus double); CD8 and CD62L: 0.0159 (control versus galunisertib) and 0.0181 (control versus double). In Fig. 4g, *P* values are for CD4 and IFNγ: 0.0099 (control versus galunisertib) and <0.0001 (control versus double); T-bet: 0.0208 (control versus galunisertib) and 0.0017 (control versus double); CD8 and GZMB: 0.0054 (control versus galunisertib) and 0.0001 (control versus double). For Fig. 4h, all *P* values are listed in Source Data. The experiment in Fig. 4i was performed once.

Patient data analysis. We used five publicly available Affymetrix microarray datasets from the NCBI GEO repository, which include gene expression and

© 2018 Macmillan Publishers Limited, part of Springer Nature. All rights reserved.

clinical information from a total of 1,194 patients with CRC. In order to obtain CD4-naive and CD4$^+$ T$_H$1 profiles, we carried out a differential expression analysis on gene expression dataset GSE22886[41]. We defined the CD4 naive signature to include genes that are upregulated at least threefold in both CD4-naive versus T$_H$1 and in CD4-naive versus Th2; Benjamini–Hochberg false discovery rate[42] (FDR) $< 5\%$ in both comparisons. Similarly, the CD4-T$_H$1 signature included genes that were upregulated at least threefold compared to CD4-naive, and limma FDR $< 5\%$. Association with metastasis was evaluated using a frailty Cox proportional hazards model. Statistical significance was assessed by means of a log-likelihood ratio test, and Wald tests were used for pairwise comparisons when necessary. Association of expression intensities was evaluated as continuous variables assuming a linear relationship with the logarithm of the relative risk. Sample groups of low, medium and high expression levels were defined using the tertiles of the intensity distribution after correction for technical effects. For visualization purposes, Kaplan–Meier curves were estimated for groups of tumours showing low, medium and high gene or signature expression. Only samples from patients diagnosed in stages I, II and III were taken into consideration for these analyses. The threshold for statistical significance was set at 5%. All analyses were carried out using R[33,43]. See Supplementary Methods for a detailed description.

Classification of mouse tumours according to consensus molecular subtypes. We used the *k*-top scoring pairs (*k*-TSP) algorithm and trained the classifier for a binary outcome (CMS4 versus not-CMS4) in 960 samples. See Supplementary Methods and Extended Data Fig. 5 for a detailed description.

Data availability. MTO whole-exome sequencing and RNA sequencing analysis (RNA-seq) data have been deposited in the ENA archive with accession number PRJEB22559. Expression array data are available at GEO with accession number GSE103562. Computer code is available upon request. Source Data are available in the online version of the paper.

31. Ruzankina, Y. *et al.* Deletion of the developmentally essential gene *Atr* in adult mice leads to age-related phenotypes and stem cell loss. *Cell Stem Cell* **1,** 113–126 (2007).
32. Muzumdar, M. D., Tasic, B., Miyamichi, K., Li, L. & Luo, L. A global double-fluorescent Cre reporter mouse. *Genesis* **45,** 593–605 (2007).
33. R Core Team. *R: a Language and Environment for Statistical Computing* http://www.r-project.org (R Foundation for Statistical Computing, 2017).
34. Wickham, H. *ggplot2: Elegant Graphics for Data Analysis* (Springer, 2009).
35. Warren, R. S., Yuan, H., Matli, M. R., Gillett, N. A. & Ferrara, N. Regulation by vascular endothelial growth factor of human colon cancer tumorigenesis in a mouse model of experimental liver metastasis. *J. Clin. Invest.* **95,** 1789–1797 (1995).
36. Céspedes, M. V. *et al.* Orthotopic microinjection of human colon cancer cells in nude mice induces tumor foci in all clinically relevant metastatic sites. *Am. J. Pathol.* **170,** 1077–1085 (2007).
37. Hothorn, T., Hornik, K., Van der Wiel, M. A. & Zeileis, A. A Lego system for conditional inference. *Am. Stat.* **60,** 257–263 (2006).
38. Gelman, A. & Hill, J. Data analysis using regression and multilevel/hierarchical models. *J. Stat. Softw.* **30,** 1–5 (2009).
39. Bates, D., Maechler, M., Bolker, B. M. & Walker, S. Fitting linear mixed-effects models using lme4. *J. Stat. Softw.* **67,** 1–48 (2015).
40. Kuznetsova, A., Brockhoff, P. B. & Christensen, R. H. B. lmerTest Package: tests in linear mixed effects models *J. Stat. Softw.* **82,** 1–26 (2015).
41. Abbas, A. R. *et al.* Immune response in silico (IRIS): immune-specific genes identified from a compendium of microarray expression data. *Genes Immun.* **6,** 319–331 (2005).
42. Benjamini, Y. & Hochberg, Y. Controlling the false discovery rate: a practical and powerful approach to multiple testing. *J. R. Stat. Soc. B* **57,** 289–300(1995).
43. Gentleman, R., Carey, V., Huber, W., Irizarry, R. & Dudoit, S. (eds) *Bioinformatics and Computational Biology Solutions using R and Bioconductor.* https://doi.org/10.1007/0-387-29362-0 (Springer, 2005).

© 2018 Macmillan Publishers Limited, part of Springer Nature. All rights reserved.

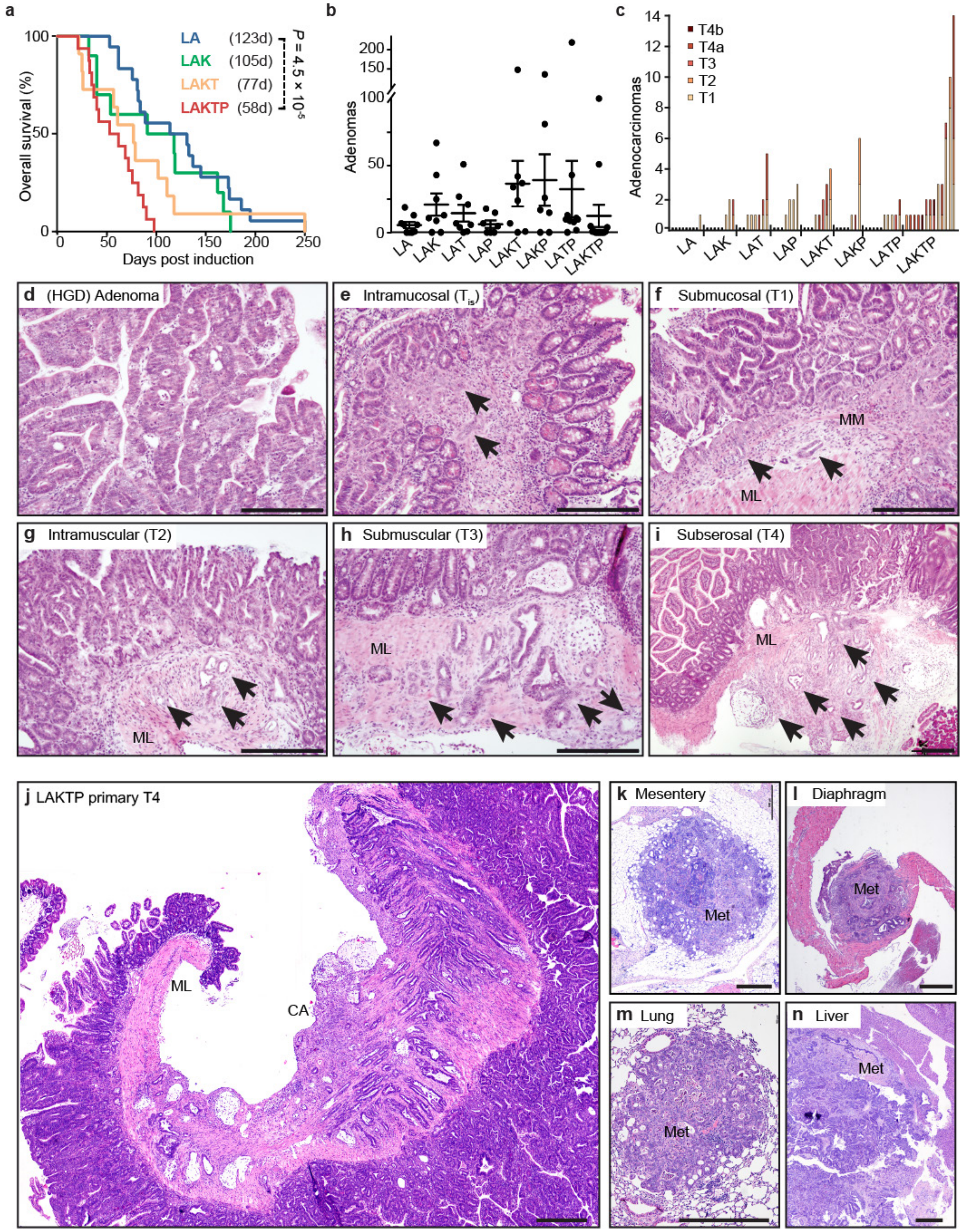
a
100
50
0
Overall survival (%)
0
50
100
150
200
250
Days post induction
LA (123d)
LAK (105d)
LAKT (77d)
LAKTP (58d)
P = 4.5 × 10-5
b
Adenomas
200
150
100
50
0
LA
LAK
LAT
LAP
LAKT
LAKP
LATP
LAKTP
c
Adenocarcinomas
14
12
10
8
6
4
2
0
T4b
T4a
T3
T2
T1
LA
LAK
LAT
LAP
LAKT
LAKP
LATP
LAKTP
d (HGD) Adenoma
e Intramucosal (Tis)
f Submucosal (T1)
MM
ML
g Intramuscular (T2)
ML
h Submuscular (T3)
ML
i Subserosal (T4)
ML
j LAKTP primary T4
ML
CA
k Mesentery
Met
l Diaphragm
Met
m Lung
Met
n Liver
Met

Extended Data Figure 1 | See next page for caption.

© 2018 Macmillan Publishers Limited, part of Springer Nature. All rights reserved.

Extended Data Figure 1 | Additional description of the genetic mouse models. a, Kaplan–Meier survival curves for LA ($n = 18$ mice), LAK ($n = 10$), LAKT ($n = 11$) and LAKTP ($n = 16$) mice, as days post-tamoxifen induction of recombination in intestinal stem cells. Median survival is indicated in parentheses; Mantel–Cox test. **b**, Number of tumours (adenomas and carcinomas) in the large intestine, by genotype. Numbers for individual mice ($n = 9$ (LA), 8 (LAK, LAT and LAKT), 7 (LAP and LAKP), 10 (LATP), and 13 (LAKTP)) are indicated, as well as mean ± s.e.m. **c**, Number and grade of adenocarcinomas per individual mouse (bars), by genotype. *P* value for pairwise comparisons of tumour number: LA versus 2×, 0.0198; LA versus 3×, 0.0337; LA versus LAKTP, 0.0001; 2× versus LAKTP, 0.0051; and 3× versus LAKTP, 0.0014; $n = 9$ mice (LA), 8 (LAK, LAT, LAKT), 7 (LAP, LAKP), 10 (LATP), 13 (LAKTP); two-sided Mann–Whitney *U* test. **d**–**i**, Example images of tumour types scored by the TNM criteria, representative of 23 independent experiments. Arrows indicate invasive cells or glands, absent in an adenoma (**d**), restricted to the mucosa in an *in situ* tumour (Tis, **e**), breaching the muscularis mucosae (MM) in a submucosal invasive tumour (T1, **f**), penetrating the muscle layer (ML) in an intramuscular invasive tumour (T2, **g**), reaching the serosa layer beyond the ML in a submuscular invasive tumour (T3, **h**), or infringing all layers including the serosa in a subserosal or T4 tumour (**i**). **j**, Representative micrograph of an haematoxylin- and eosin-stained invasive subserosal adenocarcinoma (T4) of an LAKTP mouse. Carcinoma (CA) glands are indicated, invading through the muscle layer (ML). **k**–**n**, Examples of spontaneous metastases (Met) in the mesentery, diaphragm, liver and lung of induced LAKTP mice, each image is representative of two experiments. Scale bars, 500 μm.

© 2018 Macmillan Publishers Limited, part of Springer Nature. All rights reserved.

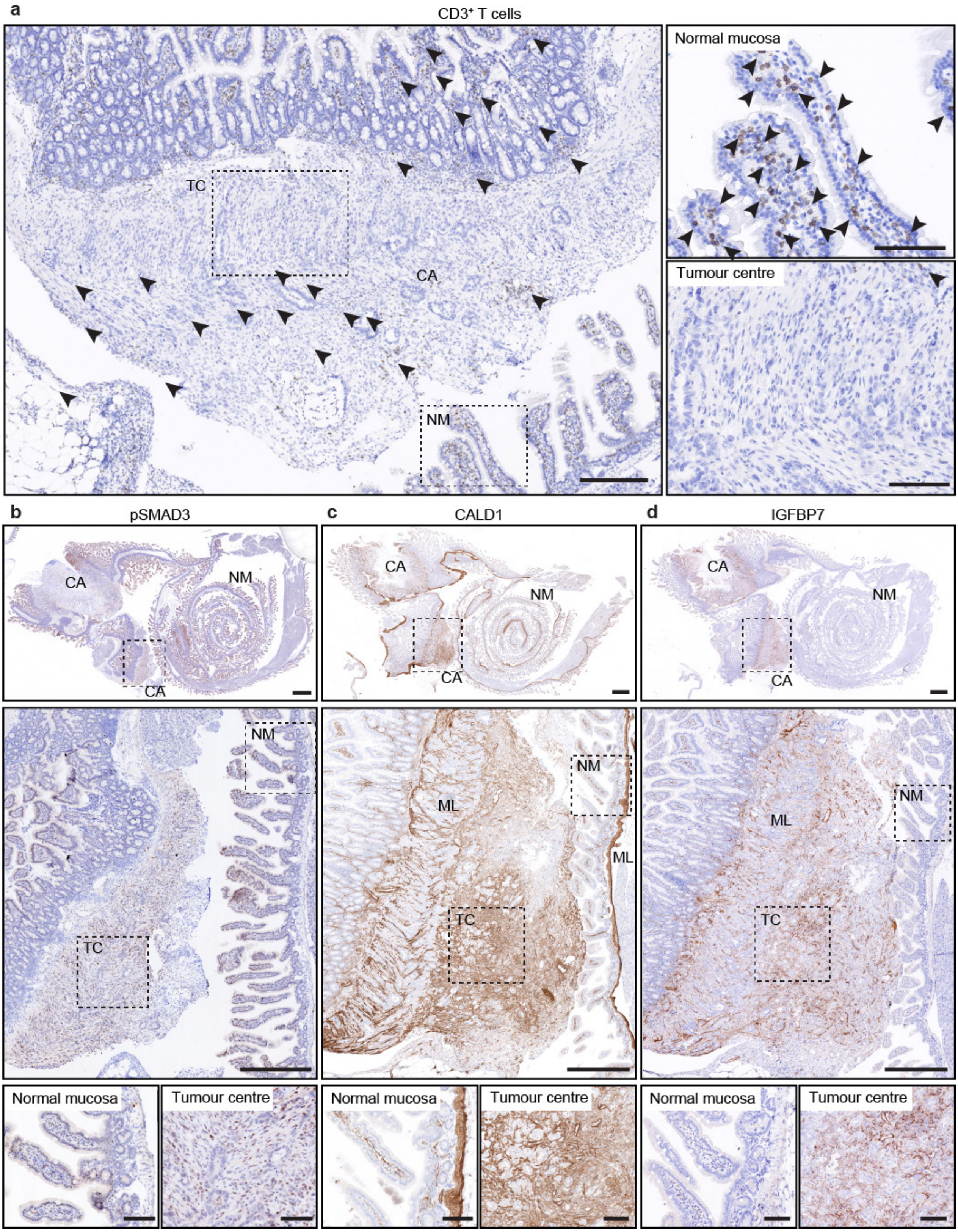
a
CD3⁺ T cells
TC
CA
NM
Normal mucosa
Tumour centre
b
pSMAD3
CA
NM
CA
NM
TC
Normal mucosa
Tumour centre
c
CALD1
CA
NM
CA
NM
ML
ML
TC
Normal mucosa
Tumour centre
d
IGFBP7
CA
NM
CA
NM
ML
TC
Normal mucosa
Tumour centre

Extended Data Figure 2 | Analysis of the TME of LAKTP adenocarcinomas in the genetic model. a, Immune infiltration in LAKTP carcinomas. Immunohistochemistry for CD3, indicating infiltrating T cells, in an intestinal adenocarcinoma of an LAKTP mouse. Insets show a magnified view of normal mucosa and tumour centre (TC). Arrowheads indicate T cells. **b–d**, Markers of TGFβ activation and poor prognosis in LAKTP carcinomas in a representative section of intestine with two aggressive invasive adenocarcinomas. **b**, Staining for pSMAD3. Note nuclear staining in stromal cells of the tumour centre. **c**, Staining for CALD1. Note that it is expressed in the muscle layer throughout the intestine, and in a subset of cells in the stroma of the normal mucosa. In the tumour centre of invasive carcinomas, the staining intensity is clearly higher, especially in fibroblast-like cells. **d**, Staining for IGFBP7, which is barely detectable in the normal mucosa. Expression is strong in the TME of the tumour centre. Images are representative of four independent experiments Scale bars, 1 mm (**b–d**, top); 500 μm (**a**, left; **b–d,** middle); 100 μm (all other panels).

© 2018 Macmillan Publishers Limited, part of Springer Nature. All rights reserved.

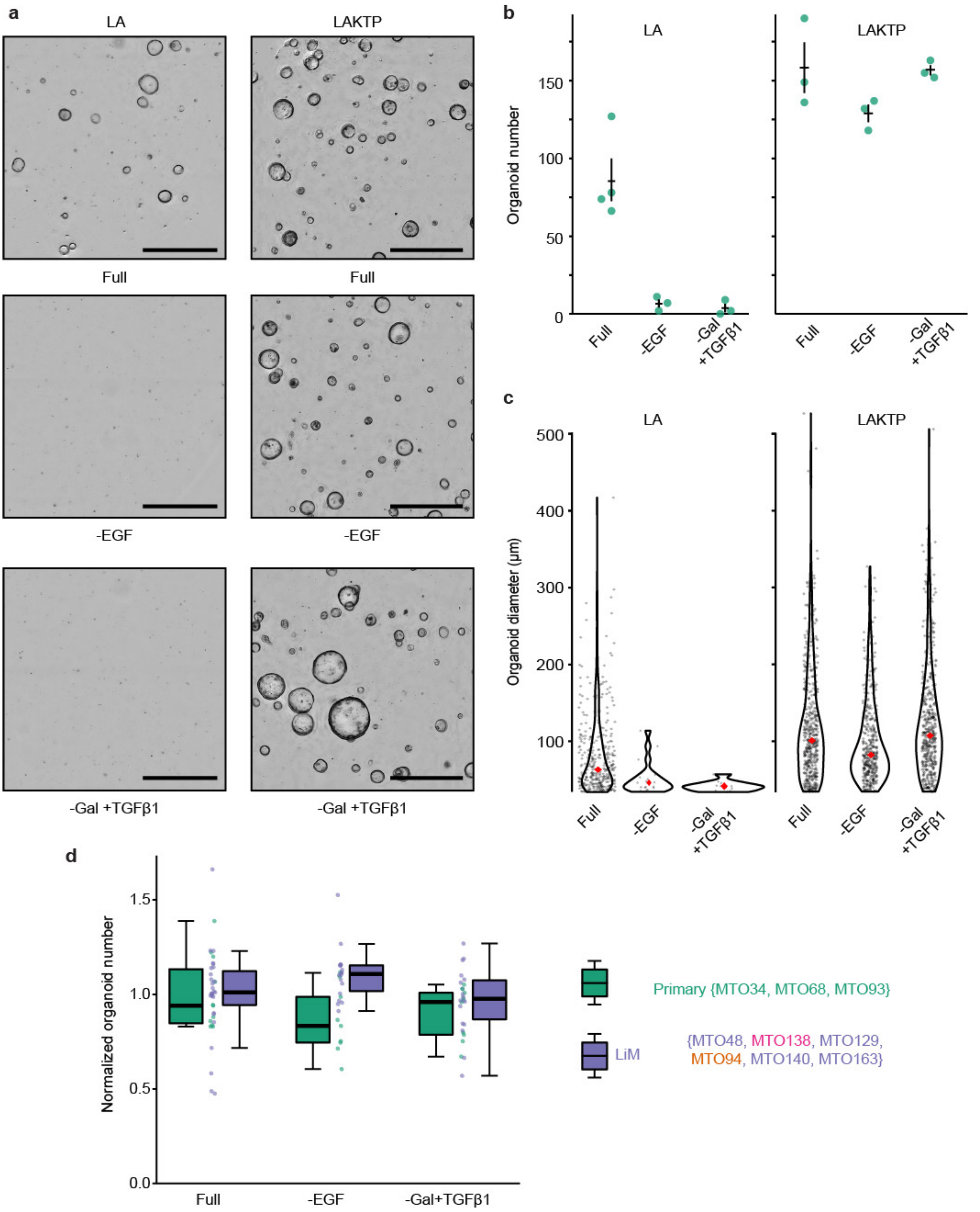

Extended Data Figure 3 | Niche factor analysis of MTOs *in vitro*. Organoid formation assay in different media with representative MTOs from LA and LAKTP mice. **a**, Images obtained by automated plate scanning, *z*-stack projection and stitching of the niche factor requirement assay. Shown are full medium, medium without EGF and medium without galunisertib (Gal) but with TGFβ1. **b**, Results from automated organoid detection for the MTOs shown in **a**, each data point shows the number of organoids in three replicate wells for representative analyses. Data are shown as mean ± s.e.m. **c**, Organoid diameter was calculated from detected pixel area. Data points are individual organoids, pooled from triplicate wells. Violin plots and medians are shown. **d**, Summary of all data obtained from different LAKTP MTOs analysed in triplicates, from both primary tumours and liver metastases. Data (individual values and Tukey box plots) are normalized to the mean of full medium. Scale bars, 1 mm.

© 2018 Macmillan Publishers Limited, part of Springer Nature. All rights reserved.

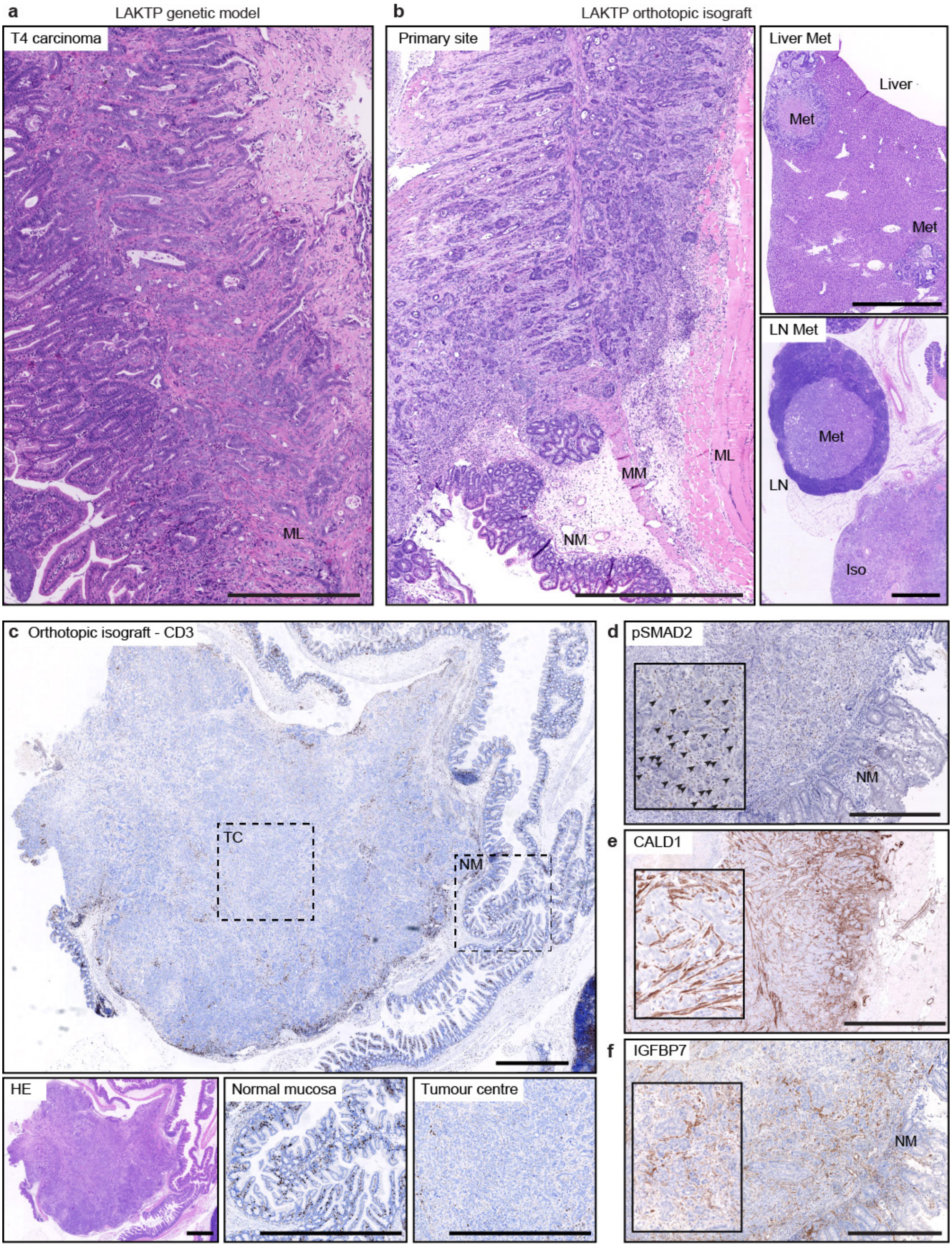
a
LAKTP genetic model
T4 carcinoma
ML
b
LAKTP orthotopic isograft
Primary site
MM
ML
NM
Liver Met
Liver
Met
Met
LN Met
Met
LN
Iso
c
Orthotopic isograft - CD3
TC
NM
HE
Normal mucosa
Tumour centre
d
pSMAD2
NM
e
CALD1
f
IGFBP7
NM

Extended Data Figure 4 | Histology and TME of primary tumours from orthotopically isografted LAKTP MTOs. a, **b**, Haematoxylin and eosin staining of a LAKTP-T4 carcinoma in the genetic model (**a**) and of a recapitulated adenocarcinoma developed from orthotopically isografted LAKTP MTO93 (**b**). Liver and lymph node (LN) metastasis observed in orthotopic isografted mouse (**b**, right panels). Iso, primary isograft. **c**–**f**, Markers of poor prognosis in isografted primary tumours. **c**, Immunohistochemistry for the T-cell marker CD3 (**c**, main panel and right, bottom right two panels) and haematoxylin and eosin stain (**c**, bottom left) of an orthotopic isograft, with typical glandular differentiation. Note that there are few infiltrating T cells in the tumour centre (**c**, bottom right), compared to the periphery and the normal mucosa (**c**, middle right). **d**–**f**, An orthotopically isografted, invasive primary tumour, stained for pSMAD2 (**d**, arrows indicate positive stromal cells), CALD1 (**e**) and IGFBP7 (**f**). Images represent three independent experiments. Scale bars, 1 mm (**c**, main and bottom left); 500 μm (all other panels).

© 2018 Macmillan Publishers Limited, part of Springer Nature. All rights reserved.

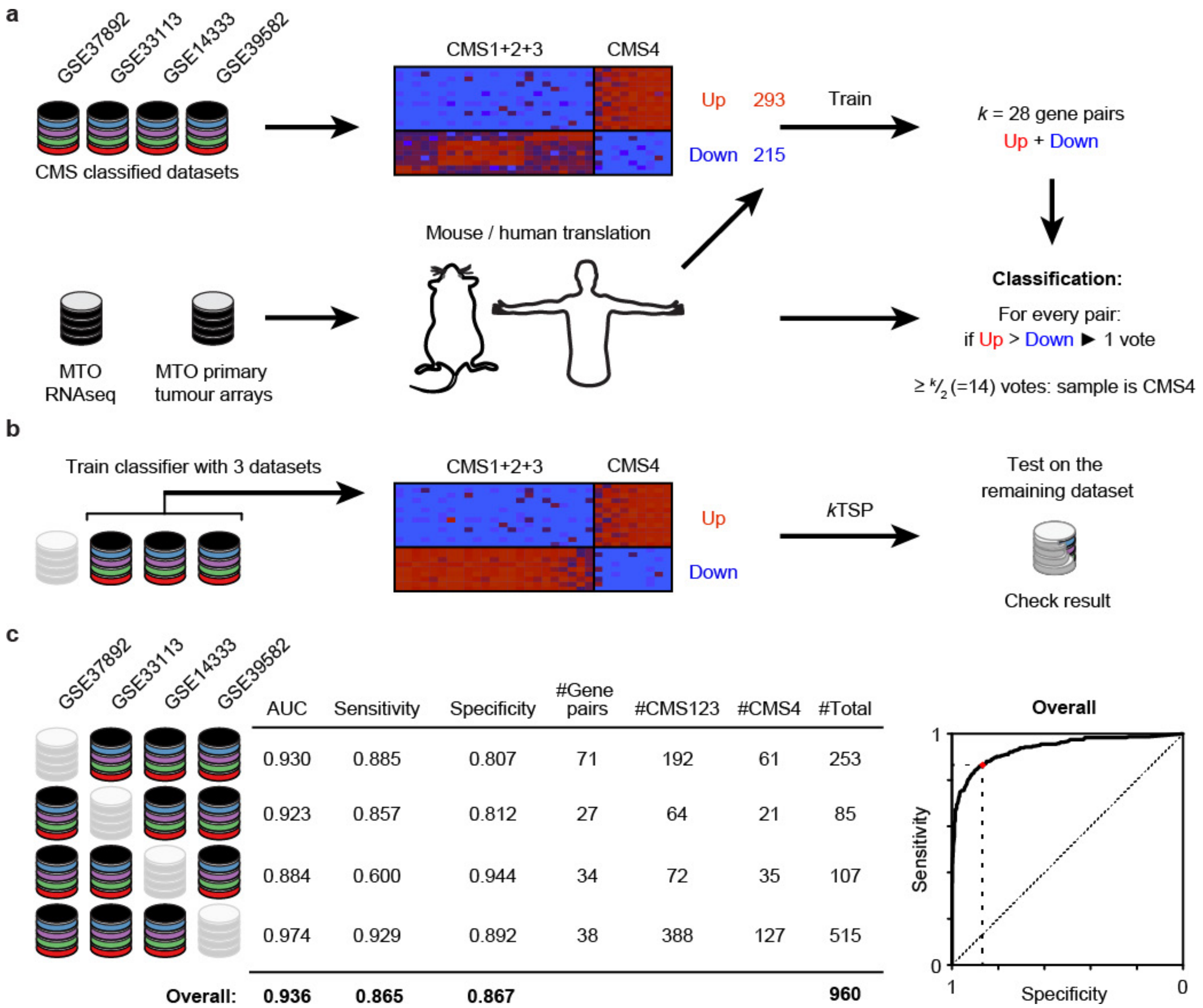
a
GSE37892
GSE33113
GSE14333
GSE39582
CMS classified datasets
CMS1+2+3
CMS4
Up 293
Down 215
Train
k = 28 gene pairs
Up + Down
Mouse / human translation
MTO RNAseq
MTO primary tumour arrays
Classification:
For every pair:
if Up > Down ▶ 1 vote
≥ k/2 (=14) votes: sample is CMS4
b
Train classifier with 3 datasets
CMS1+2+3
CMS4
Up
Down
kTSP
Test on the remaining dataset
Check result
c
GSE37892
GSE33113
GSE14333
GSE39582
Overall
Sensitivity
Specificity
1
0
1
0

AUC	Sensitivity	Specificity	#Gene pairs	#CMS123	#CMS4	#Total
0.930	0.885	0.807	71	192	61	253
0.923	0.857	0.812	27	64	21	85
0.884	0.600	0.944	34	72	35	107
0.974	0.929	0.892	38	388	127	515
Overall: 0.936	**0.865**	**0.867**				**960**

Extended Data Figure 5 | Schematic of the CSM4 classifier, using the *k*-TSP algorithm. a, A metacohort of four pooled human CRC datasets with CMS annotation is used to find upregulated and downregulated genes in the CMS4 subtype (434 with >1.5-fold change and 300 with <0.8-fold change). To ensure usability in mouse samples, candidate genes are filtered by high-confidence homology between the two species. The *k*-TSP algorithm selects from among the up- and down-regulated genes the optimal set of pairs that correctly classifies CMS4 samples. The resulting classifier is applied to mouse samples by comparing the expression of pairs of genes. For each sample, the score is increased by one unit if the expression of the 'Up' gene is greater than that of the 'Down' gene. The maximum score for CMS4 classification is 14. **b**, Cross-validation by a leave-one-out approach. To assess performance, we repeatedly trained a classifier on three out of the four human datasets and tested using the remaining dataset. **c**, Results of the leave-one-out analysis. Area under the curve (AUC) was computed after re-scaling the classifier scores to the range between zero and one. Right, receiver operating characteristic curve.

© 2018 Macmillan Publishers Limited, part of Springer Nature. All rights reserved.

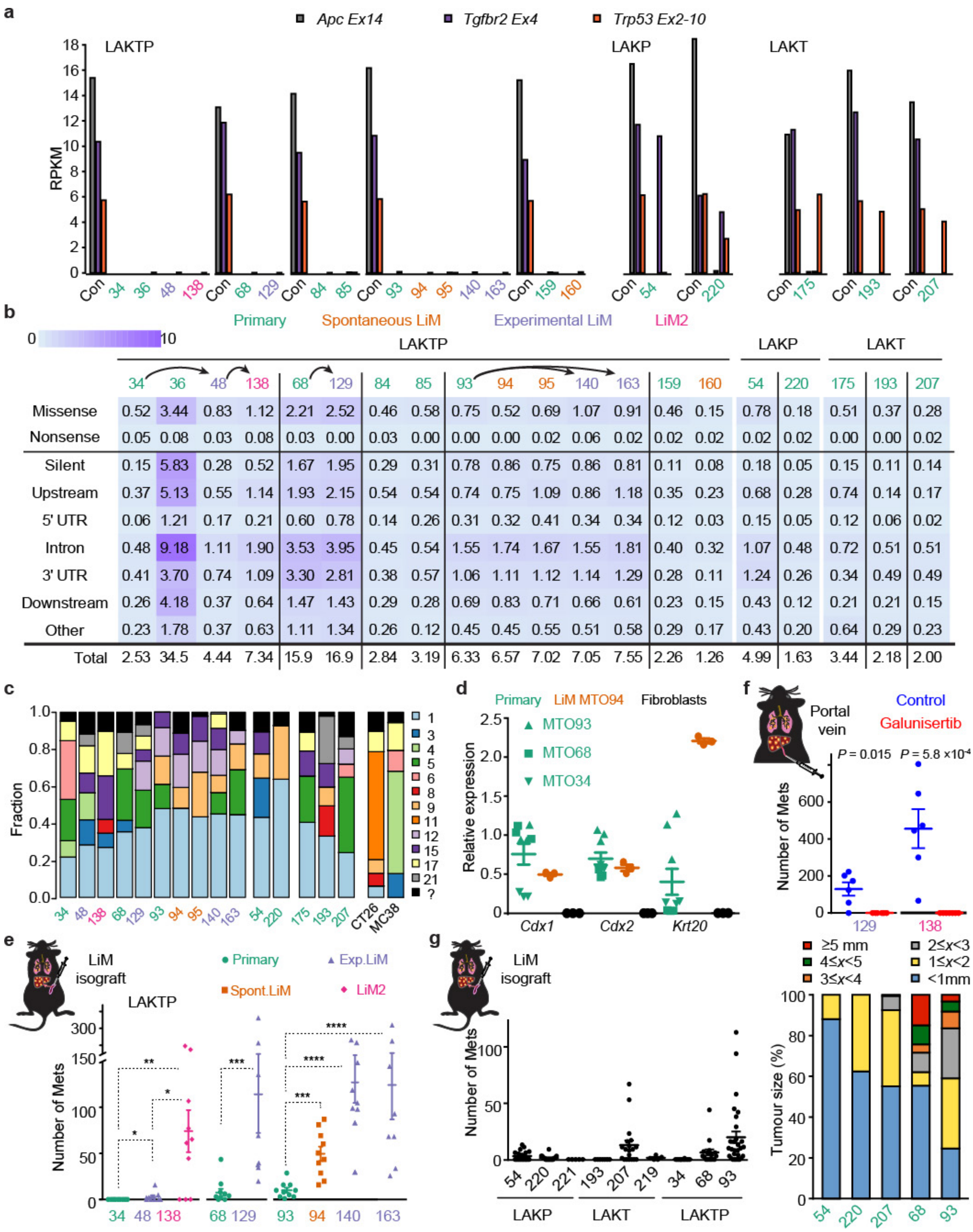

	LAKTP															LAKP		LAKT		
	34	36	48	138	68	129	84	85	93	94	95	140	163	159	160	54	220	175	193	207
Missense	0.52	3.44	0.83	1.12	2.21	2.52	0.46	0.58	0.75	0.52	0.69	1.07	0.91	0.46	0.15	0.78	0.18	0.51	0.37	0.28
Nonsense	0.05	0.08	0.03	0.08	0.03	0.00	0.03	0.00	0.00	0.00	0.02	0.06	0.02	0.02	0.02	0.02	0.02	0.00	0.00	0.02
Silent	0.15	5.83	0.28	0.52	1.67	1.95	0.29	0.31	0.78	0.86	0.75	0.86	0.81	0.11	0.08	0.18	0.05	0.15	0.11	0.14
Upstream	0.37	5.13	0.55	1.14	1.93	2.15	0.54	0.54	0.74	0.75	1.09	0.86	1.18	0.35	0.23	0.68	0.28	0.74	0.14	0.17
5' UTR	0.06	1.21	0.17	0.21	0.60	0.78	0.14	0.26	0.31	0.32	0.41	0.34	0.34	0.12	0.03	0.15	0.05	0.12	0.06	0.02
Intron	0.48	9.18	1.11	1.90	3.53	3.95	0.45	0.54	1.55	1.74	1.67	1.55	1.81	0.40	0.32	1.07	0.48	0.72	0.51	0.51
3' UTR	0.41	3.70	0.74	1.09	3.30	2.81	0.38	0.57	1.06	1.11	1.12	1.14	1.29	0.28	0.11	1.24	0.26	0.34	0.49	0.49
Downstream	0.26	4.18	0.37	0.64	1.47	1.43	0.29	0.28	0.69	0.83	0.71	0.66	0.61	0.23	0.15	0.43	0.12	0.21	0.21	0.15
Other	0.23	1.78	0.37	0.63	1.11	1.34	0.26	0.12	0.45	0.45	0.55	0.51	0.58	0.29	0.17	0.43	0.20	0.64	0.29	0.23
Total	2.53	34.5	4.44	7.34	15.9	16.9	2.84	3.19	6.33	6.57	7.02	7.05	7.55	2.26	1.26	4.99	1.63	3.44	2.18	2.00

Extended Data Figure 6 | See next page for caption.

© 2018 Macmillan Publishers Limited, part of Springer Nature. All rights reserved.

Extended Data Figure 6 | Genetic and functional analyses of MTOs. **a**, Whole-exome sequencing of MTOs. Number of reads for the recombined exons in reads per kilobase per million mapped reads (RPKM) in MTOs and their matched host tail DNA (Con). Mouse genotypes are indicated. **b**, Overview of the different LAKTP MTOs analysed, including experimental metastatic descendance (indicated by arrows), and heat map and table of the number of indicated type of somatic mutation per Mb of sequenced exome. **c**, Mutational signatures[21] in the MTOs and mouse monolayer cell lines CT26 and MC38. As in human MSS CRC, mutations in MTOs (but not in the cell lines) are predominantly of type 1. **d**, mRNA expression of intestinal epithelial genes *Cdx1*, *Cdx2* and *Krt20* in cultured MTOs derived from primary tumours MTO34, 68 and 93, and spontaneous liver metastasis MTO94, compared to mouse liver fibroblasts. Values are relative to $2^{-\Delta C_t}$ for *Ppia*, normalized to the value for MTO93; and are shown as three technical replicates with mean ± s.e.m. **e**, Number of liver nodules after intrasplenic injection of primary LAKTP tumour and spontaneous or experimental liver metastasis (LiM)-derived MTOs in syngeneic C57BL/6J mice. Data points represent individual mice; data are mean ± s.e.m. *P* values (95% confidence interval) are MTO34 ($n = 10$ mice) versus MTO48 ($n = 9$): 0.0325 (−2−0), MTO48 versus MTO138 ($n = 10$): 0.0305 (−108–0); MTO34 versus MTO138: 0.0031 (−108−0); MTO68 ($n = 11$) versus MTO129 ($n = 8$): 3.2×10^{-4} (−207 to −30); MTO93 ($n = 10$) versus MTO94 ($n = 10$): 1.1×10^{-4} (−60 to −19); MTO93 versus MTO140 ($n = 9$): 2.2×10^{-5} (−149 to −81); MTO93 versus MTO163 ($n = 8$): 9.1×10^{-5} (−220 to −31); two-sided Mann–Whitney *U* test. **f**, Number of liver nodules (mean ± s.e.m.) after inoculation of disaggregated MTO129 or MTO138 directly into the portal vein in syngeneic animals. Data are from individual mice, $n = 6$ per condition. 95% confidence interval: MTO129, (−223−0) and MTO138 (−805 to −66); two-sided Mann–Whitney *U* test. **g**, Number of liver nodules (mean ± s.e.m.) of intrasplenically injected 3× and 4× MTOs, $n = 22$ mice (MTO54), 20 (MTO220), 5 (MTO221), 7 (MTO193), 19 (MTO207), 5 (MTO219), 14 (MTO34), 16 (MTO68) and 29 (MTO93). Right, distribution of tumour diameters.

© 2018 Macmillan Publishers Limited, part of Springer Nature. All rights reserved.

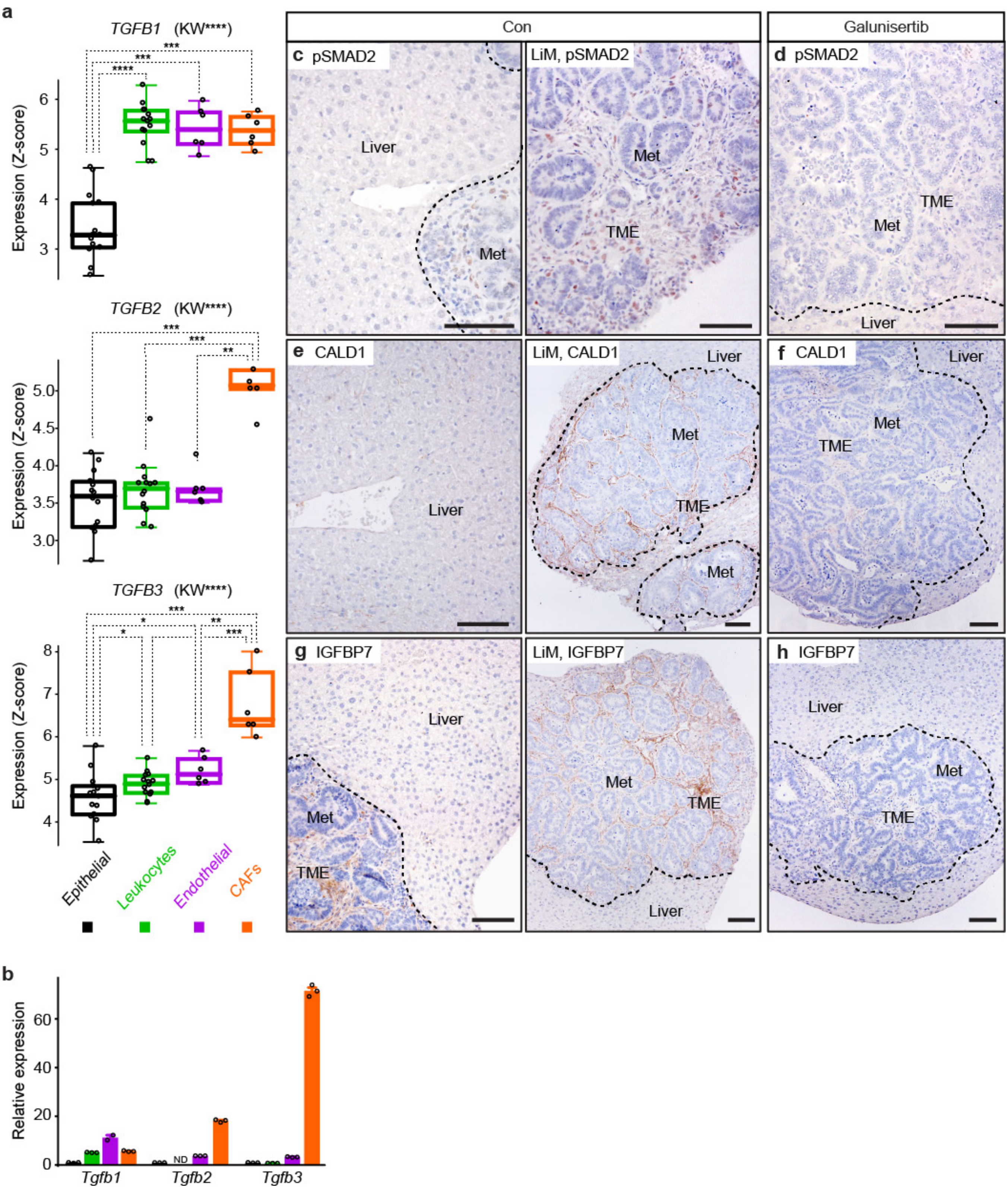

Extended Data Figure 7 | See next page for caption.

© 2018 Macmillan Publishers Limited, part of Springer Nature. All rights reserved.

Extended Data Figure 7 | Source of tumoral TGFβ and pathway blockade *in vivo*. **a**, **b**, *TGFB1*–*TGFB3* (**a**) *or Tgfb1*–*Tgfb3* (**b**) mRNA expression levels in sorted cell populations from disaggregated human CRCs (**a**) or mouse liver metastasis (**b**). First, epithelial cancer cells, immune cells, endothelial cells and CAFs were sorted with labelled antibodies against EPCAM, CD45 ($n = 14$ patients for each), CD31 and FAP ($n = 6$ for each) for human and PDGFRB for mouse. Subsequently, RNA from sorted cells was extracted and analysed by microarray (human) or reverse transcription–quantitative PCR (RT–qPCR) (mouse). **a,** Standardized expression data are shown as *z* score. Individual values and Tukey box plots; *P* values are for *TGFB1*: epithelial versus leukocytes, 7.5×10^{-6}; epithelial versus endothelial, 6.2×10^{-4}; epithelial versus CAFs, 6.2×10^{-4}; and the Kruskal–Wallis (KW) *P* value is 6.3×10^{-6}. For *TGFB2*: CAFs versus epithelial, 6.2×10^{-4}; CAFs versus leukocytes, 8.4×10^{-4}; CAFs versus endothelial, 0.0051; the Kruskal–Wallis *P* value is 0.0017. For *TGFB3*: epithelial versus CAFs, 6.2×10^{-4}; epithelial versus leukocyte, 0.0409; epithelial versus endothelial, 0.0150; leukocyte versus CAFs, 6.2×10^{-4}; endothelial versus CAFs, 0.0051; the Kruskal–Wallis *P* value is 8.5×10^{-5}. Direct comparisons using two-sided Mann–Whitney *U* test. Data are shown as mRNA expression levels normalized to epithelial cells, mean ± s.e.m. from technical triplicates; *Tgfb2* was undetectable (ND) in leukocytes. Note that in both settings, *TGFB1* is expressed by all stromal cell types, *TGFB2* and *TGFB3* are mainly expressed by CAFs. Expression in epithelial cancer cells is comparatively low. **c**–**h**, Immunohistochemistry for TGFβ target gene products in the TME of MTO138-derived liver metastases, representing two independent experiments (**c**, **e**, **g**), as well as for the inhibition of stromal TGFβ signalling by galunisertib (**d**, **f**, **h**). **c**, **d**, Micrographs of sections of liver metastases stained for pSMAD2. **e**, **f**, Staining reveals expression of the TGFβ target CALD1 exclusively in the metastatic TME. Treatment with galunisertib for three days abrogates expression of this cytoplasmic protein. **g**, **h**, Staining for the TGFβ target IGFBP7, which is exclusively expressed in the metastatic TME. Treatment with galunisertib for three days abrogates expression of this secreted protein. Scale bars, 100 μm.

© 2018 Macmillan Publishers Limited, part of Springer Nature. All rights reserved.

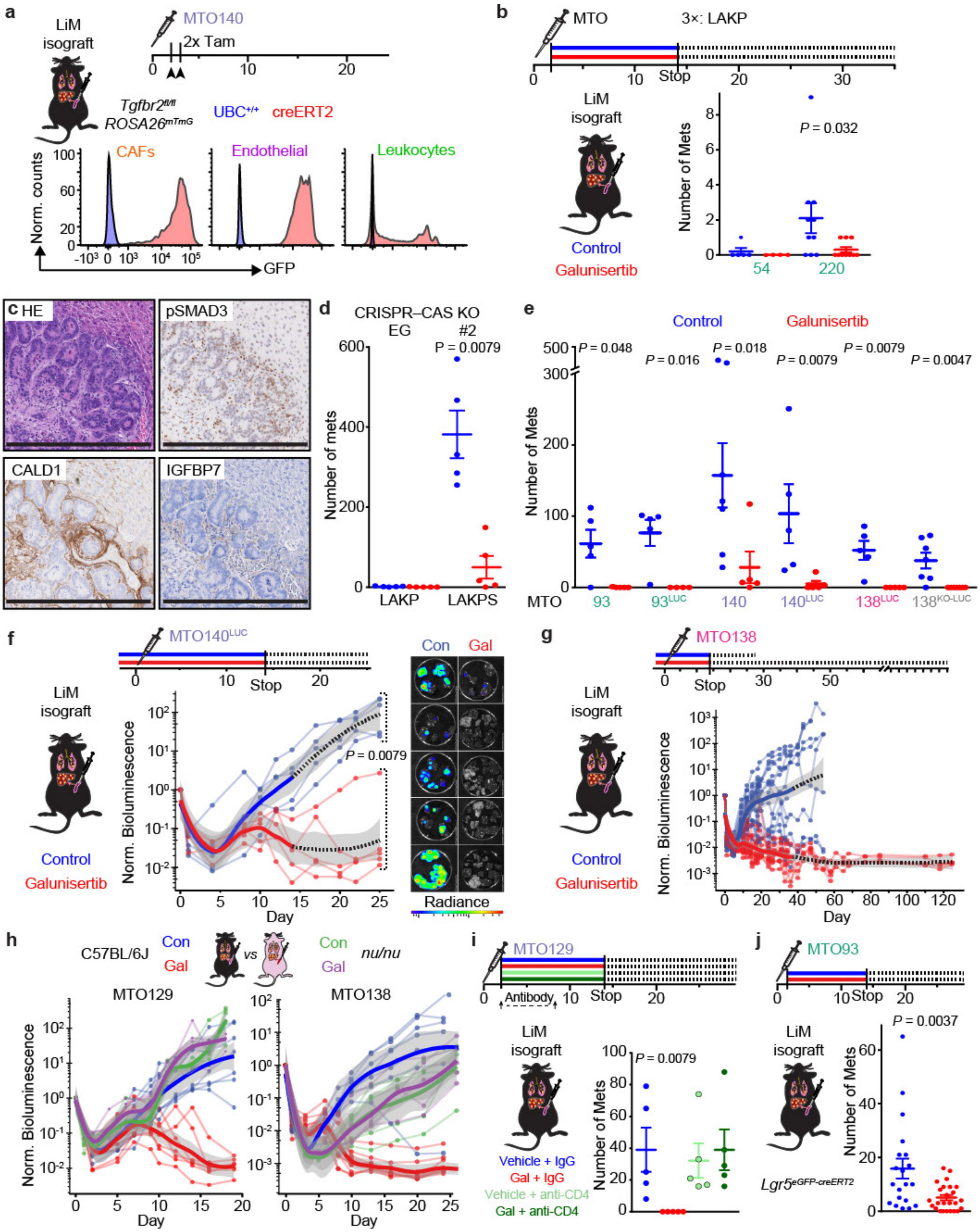

Extended Data Figure 8 | See next page for caption.

© 2018 Macmillan Publishers Limited, part of Springer Nature. All rights reserved.

Extended Data Figure 8 | Characterization of MTOs in metastatic experiments. a, Representative examples of GFP positivity measured by flow cytometry, indicating genetic recombination in the $UBC^{creERT2};Tgfbr2^{fl/fl}$ genetic model (representative of three independent experiments). **b**, Liver metastases counted five weeks after intrasplenic injection of LAKP MTO54 or MTO220 and treatment from day 2 to day 14 with galunisertib (red; $n=4$ mice for MTO54 and $n=10$ for MTO220) or control (blue; $n=5$ mice for MTO54 and $n=10$ for MTO220), mean ± s.e.m., 95% confidence interval for MTO220 is (−3–0), from a two-sided Mann–Whitney U test. **c**, Stromal TGFβ activation markers in LAKP MTO liver tumours, both supporting the classification of these tumours as CMS4 (Fig. 1i) and explaining the efficacy of galunisertib in **b**; representative of two independent experiments. **d**, Number of nodules five weeks after injection of LAKP empty guide or LAKPS (LAKP + S) MTOs and treatment with galunisertib (red) or control (blue), mean ± s.e.m., 95% confidence interval for LAKPS is (−554 to −176), $n=5$ mice per condition; two-sided Mann–Whitney U test. **e**, Number of liver nodules (mean ± s.e.m.) four weeks after intrasplenic injection of MTOs (either unlabelled or with mCherry–luciferase vector, or after CRISPR knockout of the mCherry–luciferase coding region for MTO138), after treatment. 95% confidence intervals are: for MTO93, (−113–0), $n=5$ mice per condition; MTO93-LUC: (−104 to −4), $n=5$ control and $n=4$ galunisertib; MTO140, (−297 to −21), $n=7$ control and $n=5$ galunisertib; MTO140-LUC, (−251 to −21), $n=5$ per condition; MTO138-LUC, (−86 to −8), $n=5$ per condition; MTO138-KO-LUC, (−70 to −13), $n=7$ per condition; two-sided Mann–Whitney U test. **f**, Longitudinal intravital bioluminescence imaging (BLI) quantification (photons s^{-1}, normalized to day 0) of an intrasplenic metastasis initiation experiment with MTO140 in C57BL/6J mice treated with galunisertib or control until day 14, $n=5$ mice per condition. Points and lines represent individual mice, trend lines (bold) show a LOESS model with 95% confidence interval (grey band). 95% confidence interval for the difference at day 25: (−222.7 to −23.9), two-sided Mann–Whitney U test. **g**, BLI (as in **f**) of a metastasis-initiation experiment with MTO138 in C57BL/6J mice, $n=24$ control mice, $n=15$ galunisertib. **h**, BLI (as in **f**) of galunisertib treatment in intrasplenic liver colonization assays with MTO129 or MTO138, in C57BL/6J ($n=7$ mice per condition, except for MTO138 + Gal, $n=11$) or athymic *nu/nu* mice ($n=5$ per condition). Note the complete absence of treatment effect in the mice lacking functional T cells. **i**, Number of liver nodules (mean ± s.e.m.) in mice intrasplenically injected with MTO129 and treated with galunisertib alone or with antibodies against CD4 or IgG control. 95% confidence interval for galunisertib versus control is (−79 to −8), $n=5$ mice per condition; two-sided Mann–Whitney U test. **j**, Number of liver nodules (mean ± s.e.m.) after intrasplenic injection of MTO93 in syngeneic, $Lgr5^{eGFP\text{-}creERT2}$ mice—from the colonies that gave rise to the 3× and 4× genetic models—treated with galunisertib (red) or control (blue). 95% confidence interval is (−13 to −1), $n=20$ control mice and $n=25$ for galunisertib; two-sided Mann–Whitney U test. Scale bars, 500 μm.

© 2018 Macmillan Publishers Limited, part of Springer Nature. All rights reserved.

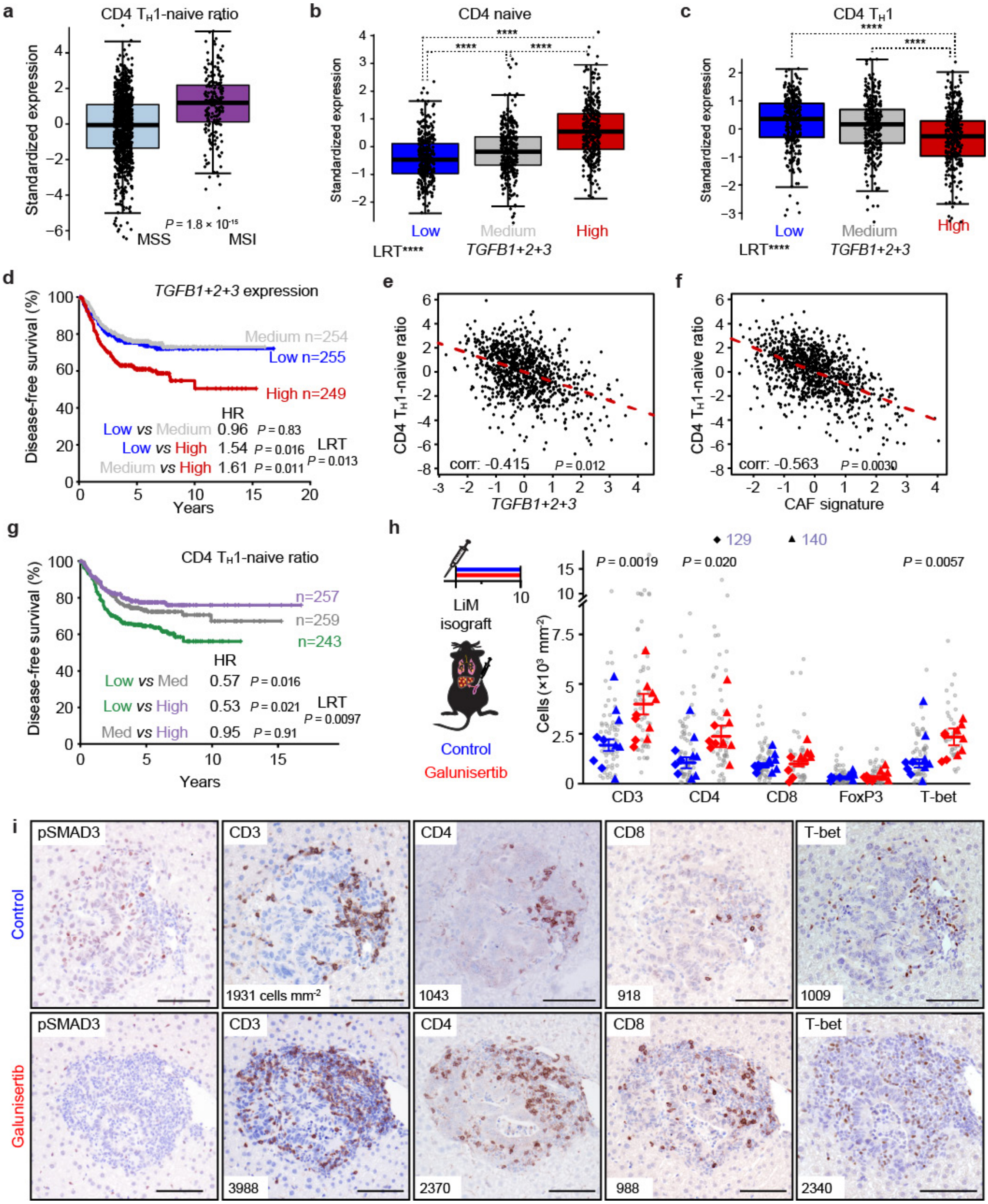

Extended Data Figure 9 | See next page for caption.

© 2018 Macmillan Publishers Limited, part of Springer Nature. All rights reserved.

Extended Data Figure 9 | Immune modulation by TGFβ in CRC. A human meta-cohort was used to analyse the interaction of TGFβ expression levels and T-cell-activation state. **a**, Expression signature ratio between active CD4 T_H1 and naive CD4 T cells differs significantly between MSS and MSI patients. Standardized expression for individual patients and Tukey box plots; MSS, $n = 981$ samples; MSI, $n = 198$; two-sided Wald test. **b**, **c**, Expression signature for naive CD4 T cells (**b**) and T_H1-differentiated CD4 T cells (**c**) in patients with low, medium and high expression of *TGFB1*–*TGFB3*. Standardized expression for individual patients and Tukey box plots. *P* values (**b**): low versus medium ($n = 327$), 1.7×10^{-4}; low versus high, 2.2×10^{-16}; medium versus high, 2.2×10^{-16}. *P* values (**c**): low versus medium, 0.0503; low versus high, 6.8×10^{-14}; medium versus high, 8.1×10^{-8}; $n = 327$ patient samples per group; two-sided Wald test. The log-likelihood ratio test *P* value is 2.2×10^{-16} for **b** and 2.3×10^{-14} for **c**. **d**, *TGFB1–3* mRNA expression levels predict poor prognosis. Hazard risk (HR) 95% confidence intervals are: low versus medium, (0.65–1.42); low versus high, (1.08–2.20); medium versus high, (1.12–2.32); $n = 255$ patient samples (low), $n = 254$ (medium) and $n = 249$ (high); two-sided Wald test. **e**, **f**, Correlation between ratio of CD4 T_H1 versus naive CD4 signatures and *TGFB1–3* mRNA expression levels (**e**) or expression of a FAP^+ CAF signature (**f**) in $n = 981$ MSS patient samples. Pearson correlation coefficients are indicated; two-sided Wald test. **g**, Kaplan–Meier curves for relapse-free survival for patients according CD4 T_H1-naive signatures ratio. Hazard risk 95% confidence intervals are: low versus medium (0.40–0.81), low versus high (0.37–0.78), medium versus high (0.64–1.41); $n = 243$ (low), $n = 259$ (medium) and $n = 257$ (high); two-sided Wald test. **h**, Cell densities in micrometastases 10 days after injection, treated with vehicle (control, blue) or galunisertib (red); shown are individual MTO129 and MTO140 tumour values and mouse means (diamonds and triangles, respectively), together with group mean ± s.e.m. derived from a mixed-effects linear model; $n = 4$ mice per condition (MTO129) and $n = 6$ for MTO140. **i**, Representative images of immunohistochemistry of the MTO140 micrometastases quantified in **h**. Mean cell densities (cells mm^{-2}) are indicated. Images represent two independent experiments. Scale bars, 100 μm.

© 2018 Macmillan Publishers Limited, part of Springer Nature. All rights reserved.

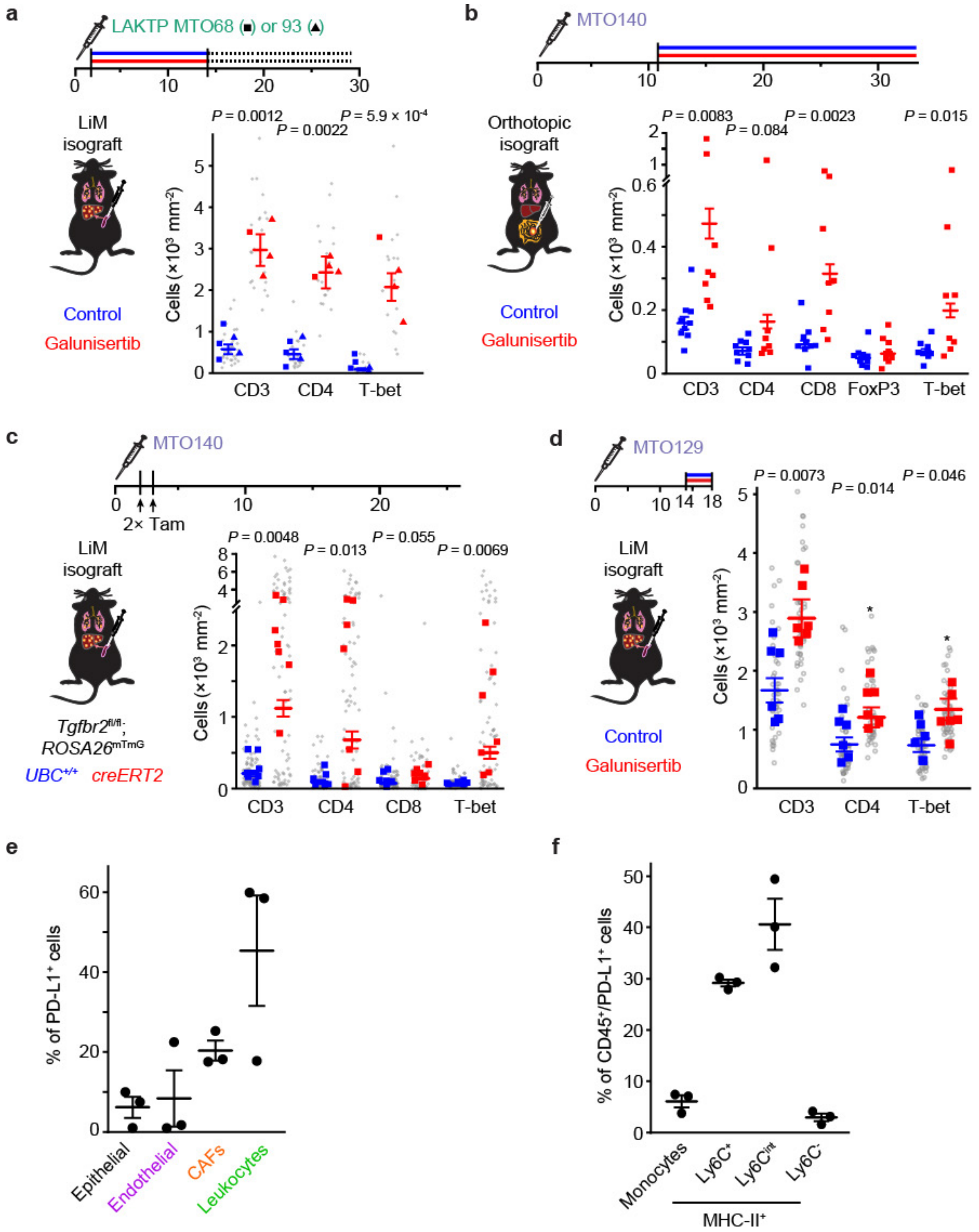

Extended Data Figure 10 | TGFβ inhibition and the tumour immune microenvironment. a–d, Densities of tumour-infiltrating lymphocytes in galunisertib (Gal, red) or control (blue) treated liver metastases derived from primary LAKTP MTOs (**a**), in treated orthotopically injected MTO-derived primary cancers (**b**), in liver metastases in the $UBC^{creERT2}$;$Tgfbr2^{fl/fl}$ background compared to $UBC^{+/+}$;$Tgfbr2^{fl/fl}$ control (**c**), or two days after start of treatment in established liver metastases (**d**; treatment started on day 14). Shown are individual tumours (grey circles, **a**, **c**, **d**), mouse means (squares, or triangles for MTO93, **a**), and group means ± s.e.m. Data are analysed with a mixed-effects linear model; in (**a**) $n = 5$ (control) or $n = 4$ (galunisertib) mice per condition; in (**b**), $n = 9$ (control) or $n = 8$ (galunisertib) mice per condition; in (**c**), $n = 5$ ($UBC^{+/+}$) or $n = 7$ ($UBC^{creERT2}$;$Tgfbr2^{fl/fl}$) mice per condition; and in (**d**), $n = 6$ mice per condition. **e**, Distribution of cell types within the PD-L1^{+} population (mean ± s.e.m.) in microdissected tumours (euthanized at day 18, four days after treatment start); $n = 3$ mice. **f**, Myeloid cell types (gated for CD45/(CD11b and/or CD11c)) within the CD45^{+} PD-L1^{+} population. Mean ± s.e.m. percentage of $n = 3$ mice.

© 2018 Macmillan Publishers Limited, part of Springer Nature. All rights reserved.

nature research

Corresponding author(s): Eduard Batlle

☐ Initial submission ☐ Revised version ☒ Final submission

Life Sciences Reporting Summary

Nature Research wishes to improve the reproducibility of the work that we publish. This form is intended for publication with all accepted life science papers and provides structure for consistency and transparency in reporting. Every life science submission will use this form; some list items might not apply to an individual manuscript, but all fields must be completed for clarity.

For further information on the points included in this form, see Reporting Life Sciences Research. For further information on Nature Research policies, including our data availability policy, see Authors & Referees and the Editorial Policy Checklist.

▸ Experimental design

1. Sample size	
Describe how sample size was determined.	Experimental group sizes were practically associated to cage sizes (5 mice/cage) and treatment experiments were designed to have n >= 5 per group (1 or more cages) .
2. Data exclusions	
Describe any data exclusions.	In the DSS/tam induction of the genetic model, 13% of mice died in the first 2 weeks from DSS treatment and were excluded from analysis. One mouse was excluded from the Fig. 2f because it showed no recombination upon tamoxifen treatment. In the KM survival curve in Fig 2e, some cohorts of mice (Con and Gal) were sacrificed at endpoint of Con (metastasis-associated severe morbidity) for tumour nodule count. Fully cured Gal mice that were culled this way were censored from the survival plot (ticks).
3. Replication	
Describe whether the experimental findings were reliably reproduced.	All experiments were reproducible.
4. Randomization	
Describe how samples/organisms/participants were allocated into experimental groups.	Because daily drug treatments were given as one type per cage (to avoid confusion and errors), we found the best way to randomize was to inject mice with tumour organoids in semi-random order: balanced among the predetermined treatment arms so as to not have any difference in cell viability but otherwise unpredictable to the person doing the injection.
5. Blinding	
Describe whether the investigators were blinded to group allocation during data collection and/or analysis.	T (tumour) status scoring from H&E stained sections was performed by two blinded observers. As stated above, the investigator doing the injection was blinded to treatment arm. In addition, the technicians doing the daily drug administrations were blinded to the experiment design including groups. Data collection and analysis was not blinded.

Note: all studies involving animals and/or human research participants must disclose whether blinding and randomization were used.

6. Statistical parameters

For all figures and tables that use statistical methods, confirm that the following items are present in relevant figure legends (or in the Methods section if additional space is needed).

n/a	Confirmed	
☐	☒	The exact sample size (*n*) for each experimental group/condition, given as a discrete number and unit of measurement (animals, litters, cultures, etc.)
☐	☒	A description of how samples were collected, noting whether measurements were taken from distinct samples or whether the same sample was measured repeatedly
☐	☒	A statement indicating how many times each experiment was replicated
☐	☒	The statistical test(s) used and whether they are one- or two-sided (note: only common tests should be described solely by name; more complex techniques should be described in the Methods section)
☐	☒	A description of any assumptions or corrections, such as an adjustment for multiple comparisons
☐	☒	The test results (e.g. *P* values) given as exact values whenever possible and with confidence intervals noted
☐	☒	A clear description of statistics including central tendency (e.g. median, mean) and variation (e.g. standard deviation, interquartile range)
☐	☒	Clearly defined error bars

See the web collection on statistics for biologists for further resources and guidance.

▸ Software

Policy information about availability of computer code

7. Software

Describe the software used to analyze the data in this study.	We used R (v3.4.2), RStudio (v1.1.383) and FIJI/ImageJ (v1.51d), and have custom codes that are available upon request. In addition, we used QuPath (v0.1.2), GraphPad Prism (v7.03), netWHCpan (v2.8), bwa (v bwa-0.7.4), Sambamba (v0.5.9), Picard (v1.128), GATK (v3.5), snpEff (v4.1), deconstructSigs (c1.8.0), Star (v2.3.0e), GeneAtlas, FlowJo (v10.4),

For manuscripts utilizing custom algorithms or software that are central to the paper but not yet described in the published literature, software must be made available to editors and reviewers upon request. We strongly encourage code deposition in a community repository (e.g. GitHub). *Nature Methods* guidance for providing algorithms and software for publication provides further information on this topic.

▸ Materials and reagents

Policy information about availability of materials

8. Materials availability

Indicate whether there are restrictions on availability of unique materials or if these materials are only available for distribution by a for-profit company.	The MTO biobank established in this paper is available to the community upon request, subject to restrictions imposed by the original mouse strain MTAs. All other materials are readily available from indicated standard commercial sources.

9. Antibodies

Describe the antibodies used and how they were validated for use in the system under study (i.e. assay and species).	Only commercial antibodies have been used: Rat αCD8α (YTS 169.4; BioXCell BE0117) or Rat αCD4α (GK1.5; BioXCell BE0003-1) or Rat IgG2b (LTF-2, BioXCell BE0090) isotype control antibodies were used for in vivo T cell depletion. All routinely validated and confirmed by flow cytometry analysis on peripheral blood (by us). Rat αPD-L1 (10F.9G2; BioXCell BE0101) or Rat IgG2b (LTF-2, BioXCell BE0090) isotype control antibodies were used for PD-1/PD-L1 therapy. Validation reported on supplier's website. For IHC, we used: Antibodies against CALD1 (Rabbit, Sigma, ref HPA008066; 1:250), IGFBP7 (Rabbit, Sigma, HPA002196; 1:200), phopsho-SMAD2 (rabbit, Cell Signaling, ref 3108; 1:50), CD4 (Rabbit, Sino Biological, ref 50134-R001; 1:1000), CD8 (Rabbit, Biorbyt, ref orb10325-200; 1:200), FoxP3 (Rabbit, Abcam, ref ab54501, 1:1000), T-bet (Santa Cruz, ref sc-21003; 1:500), phospho-SMAD3 (Rabbit, Abcam, ref ab52903; 1:500) and PD-L1 (Cell Signalling, ref 16764988S; 1:25); staining o/n at 4ºC. We used anti-GFP (Rabbit, Life Technologies, ref A11122; 1:500), anti-CD3 (Rabbit, DAKO, ref. IS50330; 1:30), staining for 2h at room temperature. Antibodies were validated extensively by the provider (including westernblot analysis) and confirmed by the authors for specific localization and--in case of TGF-beta targets--on modulation upon pathway inhibition in vivo. The following (routinely used and community-validated) antibodies were used for flow cytometry staining: anti-CD45 (clone 30-F11), anti-CD4 (clone GK1.5), anti-aCD8 (clone 53-6.7), anti-CD69 (clone H1.2F3), anti-CD104b (PDGFRb, clone APB5), and anti-MHCII (clone M5/114.15.2) were obtained from eBioscience; Epcam (clone EBA-1), anti-CD3e (clone 145-2C11), anti-CD44 (clone G44-26), CD62L (clone MEL-14), anti-IFNγ (clone XMG1.2), anti-CD274 (PD-L1, clone MIH-5), and anti-Ly6C (clone AL-32) were obtained from BD Pharmingen; anti-CD31 (clone 390) was obtained from Abcam; and anti-CD11b (clone M1/70), anti-CD11c (clone H418), anti-GZMB (GB11), anti-CD279 (PD-1, clone 29F.1A12), anti-CD8a (clone 53-6.7), anti-T-bet (clone 4B10), anti-Ly6G (clone 1A8) were obtained from BioLegend. Extra validation was performed by comparing expression in internal controls (known negative populations). For Westernblot, we used antibodies against SMAD4 (B-8, Santa Cruz, ref: sc7966) and actin (Abcam, ref: ab20272), validated on protein size and by knockout (SMAD4).

10. Eukaryotic cell lines

a. State the source of each eukaryotic cell line used.	Mouse tumour organoids were derived from genetic models in our lab. MC38 and CT26 murine cell lines as well as L cells producing Wnt3a (L-Wnt3a) were obtained from the ATCC.
b. Describe the method of cell line authentication used.	Cancer cell lines used were exome sequenced. Wnt3a production was tested in a cellular reporter assay, sensitive to Wnt ligands.
c. Report whether the cell lines were tested for mycoplasma contamination.	Mycoplasma contamination was tested for (bi-monthly) and always negative.
d. If any of the cell lines used are listed in the database of commonly misidentified cell lines maintained by ICLAC, provide a scientific rationale for their use.	None were used

Animals and human research participants

Policy information about studies involving animals; when reporting animal research, follow the ARRIVE guidelines

11. Description of research animals

Provide details on animals and/or animal-derived materials used in the study.	Genetic models: We used inbred (backcrossed) C57BL/6J mice in which we induced recombination at age 12-15 weeks, observing up to 1 year after induction or sacrificing upon severe morbidity. From tumours/polyps in this model we derived tumour organoids (MTOs) to study metastasis vastly more efficiently than otherwise possible with purely genetic (spontaneous) mouse models. Injection and transplantation of these MTOs was performed again in C57BL/6J hosts or in BALB/c Nude mice, aged 7-8 weeks. (This age limit was made more flexible (7-10 weeks) when injecting in cohorts of genetic mice such as the UBC-creERT2;Tgfbr2-fl/fl or Lgr5-creERT2 hosts, to reduce total numbers of litters necessary.) Experimental mice were typically observed for 3-5 weeks, but treatment survivors are being kept for over 1 year after injection. All mice were closely monitored by authors, facility technicians (during treatments) and by an external veterinary scientist responsible for animal welfare.

Policy information about studies involving human research participants

12. Description of human research participants

Describe the covariate-relevant population characteristics of the human research participants.	No human research subjects.

nature research

Corresponding author(s): Eduard Batlle

☐ Initial submission ☐ Revised version ☒ Final submission

Flow Cytometry Reporting Summary

Form fields will expand as needed. Please do not leave fields blank.

Data presentation

For all flow cytometry data, confirm that:

☒ 1. The axis labels state the marker and fluorochrome used (e.g. CD4-FITC).

☒ 2. The axis scales are clearly visible. Include numbers along axes only for bottom left plot of group (a 'group' is an analysis of identical markers).

☒ 3. All plots are contour plots with outliers or pseudocolor plots.

☒ 4. A numerical value for number of cells or percentage (with statistics) is provided.

Methodological details

5. Describe the sample preparation.	Livers with tumours were removed, lobules (and in case of micro-dissection: individual liver metastases) were carefully dissected and finely minced with scalpels. The tissue was enzymatically digested in 10 ml of DMEM supplemented with 10% FBS, 1% HEPES, sodium pyruvate, glutamine, streptomycin and penicillin and 0.1% β -mercaptoethanol (Gibco) and containing 1 mg/ml Collagenase A (Roche), 0.2 mg/ml Dispase II (Sigma) and 0.2 mg/ml DNAse I (Roche), during 25 min at 37ºC with rotation. The enzymatic reaction was quenched by the addition of 30 ml of ice-cold DMEM (10% FBS, supplement). Cell suspension was filtered through a 70 µm cell strainer (BD). The filter was washed with 10 ml of ice-cold 10% FBS DMEM and the cells were pelleted at 280 g for 5 min at 4ºC. Lysis of erythrocytes was performed in Red Cell Lysis Buffer (RCLB, 155 mM NH4Cl, 12 mM NaHCO3, 0.1 mM EDTA) during 4 min at room temperature and immediately washed with ice-cold 10% FBS DMEM, followed by filtration through a 70 µm cell strainer and centrifugation. Sequentially, cells were purified by centrifugation 30 min at 2,400 rpm in 40/80 Percoll (Sigma) gradient. Cells were resuspended in DMEM (10% FBS, supplement; FACS buffer).
6. Identify the instrument used for data collection.	Flow cytometry analysis and cell separation were performed in a FACSAriaFusion flow cytometer (Beckton Dickinson).
7. Describe the software used to collect and analyze the flow cytometry data.	Data were analyzed using FlowJo software v10.4.
8. Describe the abundance of the relevant cell populations within post-sort fractions.	Purity was not assessed
9. Describe the gating strategy used.	Figure 1g (MTO biobank generation): To sort Lgr5-GFP+ tumour cells, we gated: Cells/Single cells/Living cells/GFP+. Figures 2g, ED Figs 7b and 8a: To assess genetic recombination in the UbC-CreERT2; Tgfbr2fl/fl; R26mTmG model, or to sort tumour cell populations, we gated: Living cells/Cells/ Single cells/PDGFRb+ (CAFs). From the negative population, we followed: Endothelial cells CD31+/CD45- and Leukocytes CD31-/CD45+, further refined to small size and good viability. Figure 3c-d: T-cell activation markers were assessed inside: Living cells/Cells/Single cells, than CD45+/ CD3+, then CD4+/CD8- or CD4-/CD8+. Figure 3e and 4g: T-cell cytokine levels were assessed inside: Living cells/Cells/Single cells/CD45+/CD3+/

nature research | flow cytometry reporting summary

June 2017

NK1.1-, then CD4+/CD8- or CD8+/CD4-. Figure 3f: CD8+ T cells were sorted using gates: Living cells/Cells/Single cells/CD45+/CD19-/MHCII-/CD3+/CD4-/CD8+. Figure 4b: PD-1 expression was assessed inside: Living cells/Cells/Single cells/CD45+/CD3+, then CD4+/CD8- or CD8+/CD4-. Figure 4d and ED Fig 10e: PD-L1 populations were determined using: Living cells/Cells/Single cells/PD-L1+. Within these we measured for CAFs (PDGFRb+/Epcam-) or Epithelial cells (PDGFRb-/Epcam+). From the double-negative population, we followed: Endothelial cells (CD31+/CD45-) and Leukocytes (CD45+/CD31-). Fig. 4d: PD-L1 was measured inside Living cells/Cells/Single cells/CD45+. Figure 4f: For T-cell activation markers we gated: Living cells/Cells/Single cells/CD45+/CD3+/NK1.1-, then CD4+/CD8- or CD8+/CD4-. ED Fig. 10f: Myeloid populations were assessed inside: Living cells/Cells/Single cells/CD45+/PD-L1+/Ly6G-/Ly6C+/CD11b+.

Tick this box to confirm that a figure exemplifying the gating strategy is provided in the Supplementary Information. ☐

SUPPLEMENTARY INFORMATION

doi:10.1038/nature25492

Tauriello et al.

TGF-beta drives immune evasion in genetically reconstituted colon cancer metastasis

Supplementary Information

Contents

Source data westernblots

Supplementary Discussion

Supplementary Discussion References

Supplementary Acknowledgements

Supplementary Methods

Supplementary Methods References

Supplementary Fig. 1 - Source data westernblots

Fig. 2i raw images

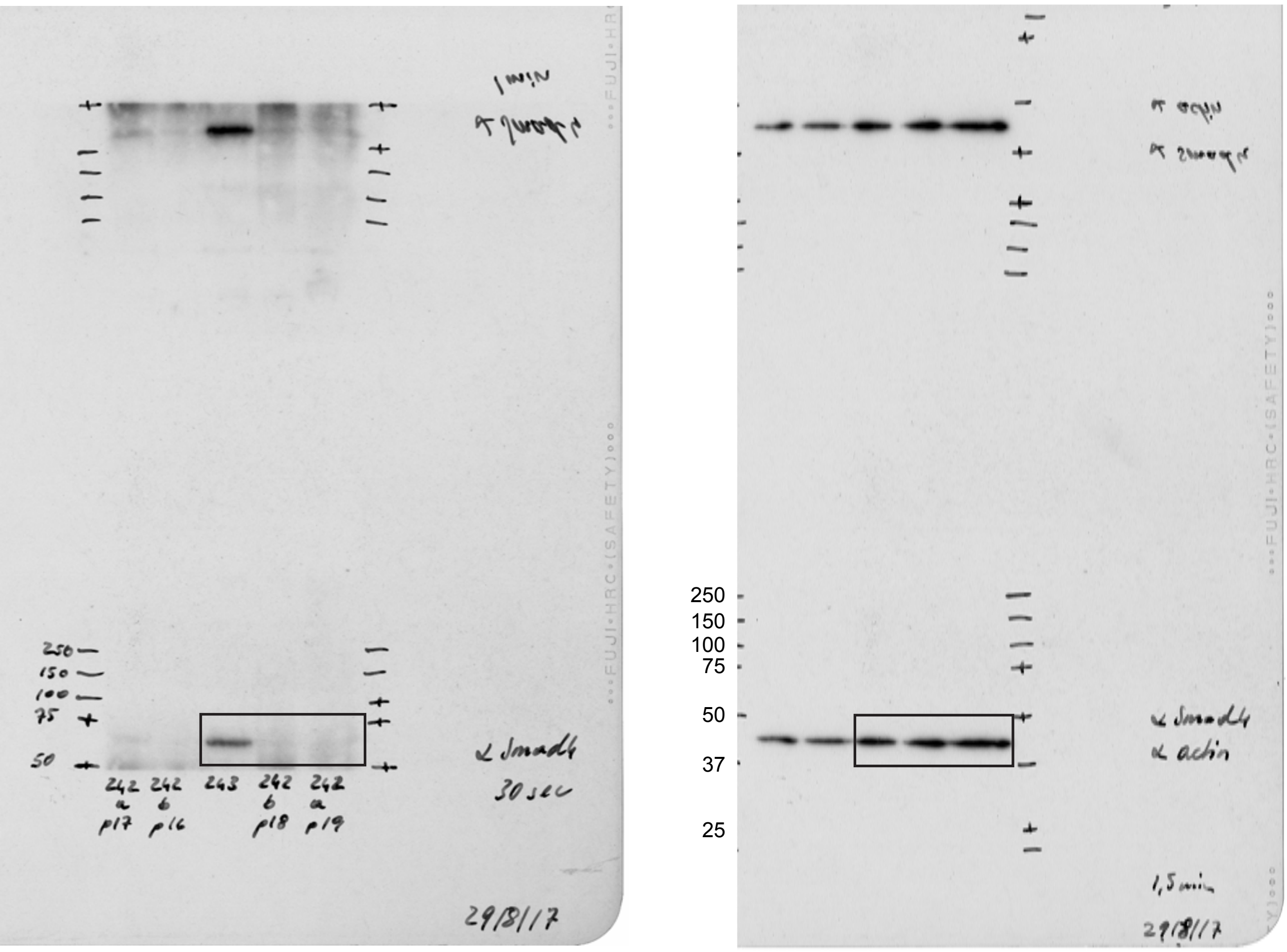
250
150
100
75
50
242 a p17
242 b p16
243
242 b p18
242 a p19
α Smad4
30 sec
29/8/17
250
150
100
75
50
37
25
α Smad4
α actin
1,5 min
29/8/17

Supplementary Discussion

The mutant mice and MTOs described herein are models to study poor prognosis human MSS CRC. Mutations in the four driver pathways render tumour cells independent of ISC niche factors, a feature that enables autonomous growth in unfavourable environments such those encountered by disseminated tumour cells in foreign organs as previously observed[1–4]. We found that malignancy co-evolves with changes in the TME reminiscent of those associated to poor prognosis CRCs such as T cell exclusion[5,6] and prominent recruitment of TGF-beta activated CAFs[7,89]. The finding that the penetrance of metastasis is ultimately modulated by the TME supports previous studies indicating that features of the immune system and the tumour stroma can help prognosticate the evolution of the disease in patients[5,7,9,10]. Recent consensus molecular classifications of CRC revealed the existence of a poor prognosis patient subset - CMS4 - characterized by prominent desmoplastic reaction, high TGF-beta levels and expression of signatures that indicate immunosuppression[8,11]. We show triple and quadruple mutant MTOs, when grown orthotopically, can be classified as CMS4 CRCs. It is, however, important to consider that frequency of genetic alterations in the main driver genes does not substantially differ between CMS2, CMS3 and CMS4 subtypes (the three subtypes that encompass most of the MSS patients)[8], implying that genotype – or at least mutations in the key oncogenes and tumor suppressor that modulate CRC progression - does not completely define molecular subtypes. It remains vital to characterize which other features and processes drive the acquisition of a TGF-beta activated TME.

It has been proposed that MSS CRCs are immunologically cold due to low mutational burden and therefore that they are unlikely to benefit from immune therapies[12]. In contrast, we found that metastatic cells from this class of CRCs can be effectively killed by the adaptive immune system through a CTL-dependent process, which CRC cells avert by raising TGF-beta levels. This finding provides a rationale for the overarching association between TGF-beta-driven gene programmes in the TME and poor prognosis in CRC[5,7,8,10,13]. We described two TGF-beta-driven mechanisms that cooperatively dampen immune responses. First, TGF-beta impacts directly on the capacity of T cells to mount a robust adaptive anti-tumor response. We observed a tight association between lack of T cell differentiation towards a Th1 effector phenotype and TGF-beta levels in CRCs. In line with this finding, mice deficient for *Tgfbr2* in T cells develop an early onset autoimmune syndrome characterized by premature differentiation of naïve CD4$^+$ T helper cell to a Th1 phenotype[14,15]. Mice that express a dominant negative *Tgfbr2* in T cells showed improved T-cell responses against melanoma and thymoma cell lines[16]. The expression of T-bet, the master transcription factor to drive the Th1 effector phenotype, is directly repressed by TGF-beta signalling[17]. TGF-beta signalling also inhibits CD8$^+$ T responses to T cell receptor stimuli[18–20]. In addition, the immunosuppressive TME imposed by TGF-beta is likely the result of a coordinated effect on multiple immune and non-immune cell types[10].

Second, our data also reveal that a TGF-beta-activated TME excludes T cells from tumours, a phenomenon that characterizes MSS CRCs as well as many other cancer types[5,21,22]. The mechanisms of immune exclusion remains poorly understood but it may occur through direct action of TGF-beta on T cells or/and indirectly through regulation of certain cytokines and extracellular matrix proteins by TME components such as CAFs and endothelial cells[23,24]. Nevertheless, facilitating T cell infiltration through TGF-beta inhibition appears a pre-requisite for enabling anti-tumour responses by the adaptive immune system. In the particular case of CRC, blockade of immune exclusion by Galunisertib is sufficient to confer susceptibility to PD1/PDL1 checkpoint-based therapies, a strategy that may have broad application for treatment of multiple cancer types that thrive in a TGF-beta rich environment. Our findings can also be interpreted such that TGF-beta-mediated immune evasion operates hierarchically upstream of the PD1/PD-L1 inhibitory checkpoint.

Whereas future studies should be aimed at dissecting the relevance of each of these responses for CRC immune evasion, our results immediately suggest the use of TGF-beta signalling inhibitors as immunotherapy (possibly in combination with other imunnotherapies[25]) for patients with metastastatic CRC and in particular with poor prognosis CMS4 tumours. The tumour suppressor role of TGF-beta in epithelial cancer cells has warned against the use of TGF-beta inhibitors for cancer therapy[10]. Yet, we show that mice bearing metastases with an intact TGF-beta pathway are eradicated by TGF-beta inhibition implying that benefits of unleashing the immune system prevails in this setting and that TGF-beta based-immunotherapies may be safe in a broad range of CRC patients. Finally, although our experiments demonstrate a dependency on a TGF-beta-activated TME during metastasis formation, it remains to be proven that these results truly reflect therapeutic potential to eliminate residual CRC cells present in AJCC Stage II and Stage III CRC patients after surgical removal of the primary tumour. At present there is lack of CRC models that faithfully reproduce disease relapse after therapy.

Supplementary Discussion References

1. Fujii, M. *et al.* A Colorectal Tumor Organoid Library Demonstrates Progressive Loss of Niche Factor Requirements during Tumorigenesis. *Cell Stem Cell* **18,** 827–838 (2016).

2. Matano, M. *et al.* Modeling colorectal cancer using CRISPR-Cas9–mediated engineering of human intestinal organoids. *Nat. Med.* **21,** 256–62 (2015).

3. Drost, J. *et al.* Sequential cancer mutations in cultured human intestinal stem cells. *Nature* **521,** 43–47 (2015).

4. Fumagalli, A. *et al.* Genetic dissection of colorectal cancer progression by orthotopic transplantation of engineered cancer organoids. *Proc. Natl. Acad. Sci.* **114,** E2357–E2364 (2017).

5. Galon, J. *et al.* Type, density, and location of immune cells within human colorectal tumors predict clinical outcome. *Science* **313,** 1960–4 (2006).

6. Mlecnik, B. *et al.* The tumor microenvironment and Immunoscore are critical determinants of dissemination to distant metastasis. *Sci. Transl. Med.* **8,** 327ra26 (2016).

7. Calon, A. *et al.* Stromal gene expression defines poor-prognosis subtypes in colorectal cancer. *Nat. Genet.* **47,** 320–329 (2015).

8. Guinney, J. *et al.* The consensus molecular subtypes of colorectal cancer. *Nat. Med.* **21,** 1350–1356 (2015).

9. Isella, C. *et al.* Stromal contribution to the colorectal cancer transcriptome. *Nat. Genet.* **47,** 312–9 (2015).

10. Tauriello, D. V. F. & Batlle, E. Targeting the Microenvironment in Advanced Colorectal Cancer. *Trends in Cancer* **2,** 495–504 (2016).

11. Becht, E. *et al.* Immune and Stromal Classification of Colorectal Cancer Is Associated with Molecular Subtypes and Relevant for Precision Immunotherapy. *Clin. Cancer Res.* **22,** 4057–4066 (2016).

12. Le, D. T. *et al.* PD-1 Blockade in Tumors with Mismatch-Repair Deficiency. *N. Engl. J. Med.* **372,** 2509–2520 (2015).

13. Calon, A. *et al.* Dependency of Colorectal Cancer on a TGF-β-Driven Program in Stromal Cells for Metastasis Initiation. *Cancer Cell* **22,** 571–584 (2012).

14. Gorelik, L. & Flavell, R. A. Abrogation of TGFbeta signaling in T cells leads to spontaneous T cell differentiation and autoimmune disease. *Immunity* **12,** 171–81 (2000).

15. Marie, J. C., Liggitt, D. & Rudensky, A. Y. Cellular Mechanisms of Fatal Early-Onset Autoimmunity in Mice with the T Cell-Specific Targeting of Transforming Growth Factor-beta Receptor. *Immunity* **25,** 441–454 (2006).

16. Gorelik, L. & Flavell, R. A. Immune-mediated eradication of tumors through the blockade of transforming growth factor-beta signaling in T cells. *Nat. Med.* **7,** 1118–1122 (2001).

17. Gorelik, L., Constant, S. & Flavell, R. A. Mechanism of transforming growth factor beta-induced inhibition of T helper type 1 differentiation. *J. Exp. Med.* **195,** 1499–505 (2002).

18. Thomas, D. A. & Massague, J. TGF-beta directly targets cytotoxic T cell functions during tumor evasion of immune surveillance. *Cancer Cell* **8,** 369–380 (2005).

19. Mehal, W. Z., Sheikh, S. Z., Gorelik, L. & Flavell, R. A. TGF-beta signaling regulates CD8+ T cell responses to high- and low-affinity TCR interactions. *Int. Immunol.* **17,** 531–538 (2005).

20. Zhang, N. & Bevan, M. J. TGF-beta signaling to T cells inhibits autoimmunity during

lymphopenia-driven proliferation. *Nat Immunol* **13,** 667–673 (2012).

21. Chen, D. S. & Mellman, I. Elements of cancer immunity and the cancer–immune set point. *Nature* **541,** 321–330 (2017).

22. Joyce, J. A. & Fearon, D. T. T cell exclusion, immune privilege, and the tumor microenvironment. *Science (80-.).* **348,** 74–80 (2015).

23. Kraman, M. *et al.* Suppression of antitumor immunity by stromal cells expressing fibroblast activation protein-alpha. *Science (80-.).* **330,** 827–830 (2010).

24. Feig, C. *et al.* Targeting CXCL12 from FAP-expressing carcinoma-associated fibroblasts synergizes with anti-PD-L1 immunotherapy in pancreatic cancer. *Proc. Natl. Acad. Sci. U. S. A.* **110,** 20212–7 (2013).

25. Tauriello, D. V. F., Calon, A., Lonardo, E. & Batlle, E. Determinants of metastatic competency in colorectal cancer. *Molecular Oncology* **11,** 97–119 (2017).

Supplementary Acknowledgements

We thank Natalia Plana, Carolina Sanchez and Edgar Cristóbal Lecina for technical assistance, Francisco Barriga for materials, Raquel Batlle, Gonzalo Fernández Miranda and Raúl Méndez for mouse strains, Elena Sancho for help with the manuscript and important support, and Cristina Mendez for logistic support. From our outstanding facilities, we wish to thank from histopathology: Neus, Mònica, Begoña, Alicia, Anaïs and Antonia; from functional genomics: Nacho and David; from advanced digital microscopy: Sébastien and Anna; from flow cytometry: Jaume, Sonia, Chary and Ricardo; from the animal facilities: Steve, Barbara, Ferran, Conchi, Jesús, Rosa, Javi, Julia, Jordi, Vanessa and Fernando; and from the CRG genomic unit: Jochen, Anna and Maria.

Supplementary Methods

Cell lines

Murine cell lines MC38, CT26 and L-Wnt3a were obtained from ATCC and cultured in DMEM with 10% FBS. For MC38 and CT26, gDNA and mRNA was harvested from trypsinized, cultured cells and exome/RNA sequenced with the same protocols as for MTOs. Cell lines were regularly tested for mycoplasma contamination.

In vitro crypt niche factor dependency assays

Starting with full MTO-medium (above), we used combinations leaving out components, or adding 5 ng/ml recombinant human TGF-β1 (Peprotech) while removing galunisertib (+TGFB1). Wildtype normal intestinal organoids were obtained from a naïve C57BL/6J mouse, using the crypt shaking method[5], and cultured in MTO-medium supplemented with 1 μg/ml RSPO-1 and 50% v/v Wnt3a-CM. MTOs were never cultured with either supplement and WT organoids did not survive in MTO-medium without them. RSPO-1 was produced in-house[6] and Wnt3a-CM (from L-Wnt3a cells) was produced and tested according to previously described methods[7].

For Fig. 1h: MTOs were seeded in standard 48^{well} plates in triplicate as single cells and growth/death was manually scored at day 2, 4 and 6. Pictures were taken on day 5. Sensitivity was defined as difference in growth/survival compared to the control. This was assessed both manually, where 3 was the maximum level (0 *vs* +++), or using automated imaging (Olympus CellR/ScanR multiwell plate scanner; individual wells were scanned in a 5x4x8 (x-y-z) matrix) followed by ImageJ[8] analysis (Raw images were projected, stitched and analysed for automated organoid counting by ImageJ macros written by Anna LLado and Sébastien Tosi (IRB Barcelona ADM core facility); the result is shown in Extended Data Fig. 3a). Although the analyses were in high concordance, the heatmap is composed of data from the former. For each genotype, between 3 and 7 MTOs were analysed, p-values were calculated using the 0-3 sensitivity scores: for the LA-LAKTP EGF comparison $p=0.0001$, for the LA-LAKTP TGFB1 comparison: $p<0.0001$, and for the LAK-LAKTP TGFB1 comparison: $p=0.0010$ (two-sided MWW tests). Data were analysed and represented using R (v 3.4.2)[9], RStudio (v 1.1.383) and the *ggplot2* package (v 2.2.1)[10]. For diameter calculations, organoid sphericality was assumed.

Whole exome sequencing

Genomic DNA was harvested from cultured MTOs (median passage 5), as well as from mouse tail fragments, and purified using the GenElute kit (Sigma). Library prep was done using NebNext Ultra and the exome selection was done using SeqCapEZ developer (4 reaction, 110624_MM9_exome_ L2R_D02_EZ_Hx1; Cat. No. 06740278001, NimbleGen-Roche). Exome enrichment reaction was done in pools of 5 or 6 libraries. Sequencing was done HiSeq2500, Paired End, 125nts (2x125, v4); one lane per pool.

Reads preprocessing: Paired end reads were aligned to the mm10 version of the mouse genome using the mem algorithm implemented in the bwa software[11] (bwa-0.7.4) with default parameters. SAM files were sorted and indexed using Sambamba (v0.5.9; http://lomereiter.github.io/sambamba/) and duplicated reads removed with the Picard software (v1.128; https://github.com/broadinstitute/picard). Read qualities were recalibrated using the Genome Analysis Tool Kit (GATK, v3.5)[12].

Somatic SNP and INDEL calling: For each control-sample pair processed BAMs were compared using MuTect2 from GATK with default parameters. No extra filtering was applied other than the PASS/REJECT call from the Mutect2 algorithm. We decided to include mutations marked as “clustered_events” since some positive controls (e.g. Kras (G12V) mutation in CT26) were otherwise excluded. Resulting VCF files were annotated with *snpEff* (v4.1)[13]. Somatic mutation load was computed with respect to the total length of the non-overlaping regions captured in the exome capture kit.

We constructed mutational signatures using the somatic mutations found in each of our samples. We normalized by the overall trinucleotide frequency in the mouse exome and compared against the human mutational signatures[14] using the algorithm implemented in the deconstructSigs software (v1.8.0)[15]. We removed signature "1B" from the initial set since it has been reported to be a linear combination of signatures 1 and 5[16].

RNA sequencing

mRNA was harvested from cultured MTOs and purified using the Ambion PureLink RNA mini kit (Life Technologies). Library prep was done using the Illumina kit Truseq Stranded mRNA Sample Prep kit. Sequencing was done on the HiSeq 2500, Paired End, 50nts (2x50, v4) with pools of 8-10 samples (one pool per lane). Paired end reads were aligned to the mm10 version of the mouse genome using the Star software (v2.3.0e)[17]. Expression was estimated using the R package *casper*[18]. The full expression matrix was normalized by quantiles.

Neoantigen prediction

Affinity prediction in mouse samples: SNVs annotated as non-synonymous or nonsense and inframe insertions or deletions were selected for each sample. Protein sequences were downloaded from Biomart using the *biomaRt* package[19] and the "mmusculus_gene_ensembl" dataset available on July 2017. A peptide including 10 bases up and downstream from the alteration was extracted from the canonical protein associated with the corresponding gene. Resulting peptides matching any other annotated protein were discarded from the dataset. MHC haplotypes for the C57BL (haplotype b) and BalbC (haplotype d) mouse strains were obtained from the Affymetrix eBioscience mouse haplotype table [http://tools.thermofisher.com/content/sfs/brochures/Mouse_Haplotype_Table.pdf]. All samples in the mouse cohort belong to the C57BL/6J strain except for the CT26 cell line, which has been reported as BalbC[20]. Peptides and the corresponding haplotypes for each sample were submitted to the netMHCpan affinity prediction software (v2.8)[21].

Human colorectal cancer mutations and neoantigens database: Total number of mutations and predicted neoantigens for human colorectal cancer (CRC) samples were downloaded from [https://tcia.at/neoantigens]. Samples were classified as MSS or MSI according to the TCGA consortium[22]. As well as for mouse, neoantigens in the CRC database were predicted using the netMHCpan software.

Affinity thresholds in mouse and human predictions: In order to find comparable thresholds between human and mouse affinity values, we generated 600,000 predictions from 12 human haplotypes and random peptides. We found good equivalence between a cutoff of 500nM and a 2% rank threshold, which has been used to filter the mouse dataset.

Neoantigen filtering: The CRC predicted neoantigens were filtered by a maximum affinity of 500nM and minimum expression of 0 (log2) RPKM[23]. Neoantigens in mouse samples were filtered with the following criteria: 2% Rank affinity as reported by netMHCpan and 0 RPKM of the mean expression of all available replicates for the corresponding gene.

Lentiviral infection of MTOs

For bioluminescent tracking, MTOs were infected with a lentivirus encoding an mCherry-firefly luciferase fusion reporter construct, followed by an IRES-Zeocin or IRES-Puro resistance cassette[3], cloned under control of the Ubiquitin promotor in a FUW vector[24]. Virus was produced using packaging constructs in HEK293T cells in DMEM 10% FBS medium, and filtered. Trypsinized organoids (single cells) were suspended in ultra-low attachment plates (Corning) in MTO-medium and treated with successive rounds of infection (adding virus-containing medium 50% v/v) in the presence of 8 µg/ml polybrene. After a week, MTOs were put back in BME drops and selected with 50 µg/ml zeocin or 0.5-1 µg/ml puromycin (InvivoGen). After 2-3 weeks, selected cells were sorted for mCherry expression.

Tumour dynamics with Bioluminescence imaging

Growth kinetics of luciferase-expressing MTOs were tracked with in vivo bioluminescence, using an IVIS-Spectrum (Perkin Elmer) imager. Animals were anesthetized with 2.5% isofluorane and received a retro orbital injection with 50 ul D-luciferin at 15 mg/ml (Resem BV). Mice were shaved before every measurement using electrical trimmers. For quantification, two or more images per mouse (typically in the 0.5-60s exposure range, bin 4-16) were averaged, quantifying the total flux (photons s^{-1}) of a ROI spanning the abdomen (IC) or lower thorax and upper abdomen (IS). Values were normalized per mouse on the value on day 0, measured 5 min after injection. Data were processed and visualized with R/RStudio[9] and ggplot2[10]. Depicted are longitudinal curves, connecting measurements of individual mice, and the group smooth (*LOESS*, span = 0.5) with 95% confidence interval. LOESS stands for locally weighted regression and is a non-parametric regression method analogous to a moving average in time[25].

Patient data analysis: Transcriptomic datasets

In this study, we used five Affymetrix microarray datasets publicly available in the NCBI GEO repository, which include gene expression and clinical information from a total of 1.194 CRC patients: briefly, GSE14333[26] contains a pool of 290 patients with CRC treated at 2 different hospitals: the Peter MacCallum Cancer Centre (Australia) and the H. Lee Moffitt Cancer Center (United States); the GSE33113[27] data set includes 90 patients with AJCC stage II disease collected at the Academic Medical Center in Amsterdam (the Netherlands); GSE39582[28] includes expression and clinical data for 566 patients with CRC collected for the Cartes d'Identité des Tumeurs (CIT) program, from the French Ligue Nationale Contre le Cancer; GSE3782 (https://www.ncbi.nlm.nih.gov/geo/query/ acc.cgi?acc=GSE37892, accessed 20/10/2016) is a series of stage II and III CRC patients collected at five different hospitals from France (Marseille La Timone, Nice Lacassagne, Marseille Institut Paoli-Calmettes, Paris Lariboisiare, Nancy Brabois and Paris Saint-Antoine); and GSE38832[29] contains transcriptomic and clinical information from 127 patients treated at the H. Lee Moffitt Cancer Center (United States). In order to facilitate the integration of the datasets, samples from centres contributing with less than 10 samples (GSE37892: Marseille La Timone and Nancy Brabois; GSE38832: Nashville Veterans Affaires Medical Center) were excluded, leaving a total of 1.179 samples for downstream analyses.

Patient data analysis: Microarray processing

Processing of microarray samples was carried out separately for tumour samples of each dataset using packages *affy*[30] and *affyPLM*[31] from Bioconductor[32]. Raw CEL files were normalized using RMA background correction and summarization[33]. Standard quality controls were performed in order to identify abnormal samples[34] regarding: a) spatial artefacts in the hybridization process (scan images and pseudo-images from probe level models); b) intensity dependences of differences between chips (MvA plots); c) RNA quality (RNA digest plot); d) global intensity levels (boxplot of perfect match log-intensity distributions before and after normalization and RLE plots); e) anomalous intensity profile compared to the rest of samples (NUSE plots, Principal Component Analyses). Technical information concerning samples processing and hybridization was retrieved from the original CEL files: date of scanning were collected in order to define scan batches in each dataset separately; technical metrics described by Eklund AC and Szallasi Z[35] were computed and recorded as additional features for each sample. Probeset annotation was performed using the information available in Affymetrix web page (Affymetrix Analysis Center. Netaffx. https://www.affymetrix.com/analysis/ index.affx, accessed 07/27/2016). Each dataset was a-priori corrected by potential sources of bias due to technical variability. For doing so, a linear model was fitted to each gene and dataset separately including centre, three Eklunds' metrics (PM IQR, RMA IQR and RNA DEG), scanning day and the interaction between centre and Eklunds' metrics. This correction was carried out using a mixed-effect model in which gender, age at diagnosis, tumour location and microsatellite instability (MSI) status were also included as covariates, when available. Scanning day was modelled as a random effect in these models. The five transcriptomic datasets were then merged in a unique expression matrix after applying quantile normalization[36]. Finally, expression data from each dataset was standardized at probeset level using GSE39582 as a reference; for each dataset and probeset, we selected randomly a subset of samples from GSE39582 matching the same clinical characteristics regarding gender, age, tumour location and MSI, and then centred and scaled the dataset according to these parameters.

Patient data analysis: MSI imputation

MSI status was imputed in each dataset separately, based on the expression of genes included in a published transcriptomic signature[37]. For doing so, clustering analysis was performed on this signature via non-parametric density estimation[38,39]. Accuracy of this imputation was evaluated in dataset GSE39582, which included annotation of microsatellite-stable (MSS) and -instable (MSI) samples in their clinical information (97% and 80% accuracy for MSS and MSI samples, respectively).

Patient data analysis: Signatures summarization

To summarize the signatures analysed in this work, Z-scores were computed for each gene and each sample in the unique corrected expression matrix, which were then averaged across all genes included in the profile. The resulting score was centred and scaled across samples.

Patient data analysis: CD4 Th1 and Naive signatures

In order to obtain CD4 naive and CD4 th1 profiles, we carried out a differential expression analysis on gene expression dataset GSE22886[40]. Analyses were performed separately for HG-133A and HG-133B platforms using a linear model with empirical shrinkage[41] as implemented in *limma* R package[31]. We defined the CD4 naive signature to include genes that are at least 3 fold upregulated both in CD4 naive vs. Th1 and in CD4 naive vs. Th2, and Benejamini and Hochbergs' False Discovery Rate (FDR)[42] < 5% in both comparisons. Similarly, the CD4 Th1 signature included genes that were at least 3 fold upregulated compared to CD4 naive, and limma FDR < 5%. These signatures were summarized as scores as described in the previous sections. Relative expression of Th1 and Naive cells were then measured by means of the difference of these scores, which corresponds to a log-ratio in the original scale of the microarray intensities.

Patient data analysis: Association analyses

To test the association between expression profiles, a mixed-effect model was fitted to each gene/signature independently in which scan day was included as a random effect, and centre, Eklunds' metrics and the interaction between both were introduced as covariates. Association was assessed using the corresponding Wald and Likelihood Ratio Test (LRT) provided by the linear model. As measure of association and for continuous variables, we computed the Pearson's Correlation Coefficient after correction by technical effects using the mixed-effect model described in the previous section; for categorical variables, adjusted group means and corresponding intervals at 95% confidence were calculated. Association with Cancer Associated Fibroblasts (CAFs) was assessed using a FAP signature derived from human CRC sorted cells (see section *Gene expression in tumour cell populations*). To assess association with overall TGFB levels, a signature was created using microarray probesets *203085_s_at*, *220406_at* and *209747_at*, respectively, as these probesets correlated better with measurements of *TGB1*, *TGFB2* and *TGFB3* obtained by qRT-PCR data[3]. When assessing correlation between TGF-beta and any signature, probesets mapping to *TGFB1*, *TGFB2* or *TGFB3* were previously excluded from the later. For visualization purposes, scatter plots and boxplots were yielded using the technical adjusted values for expression intensities.

The estimates of the association between Th1 and Naive cells ratios and the *TGF-beta* and the FAP signatures were compared with the overall trend observed in the whole genome. For doing so, we generated a null distribution for the correlation coefficients between *TGF-beta* and the scores derived for random signatures. We randomly selected the same number of genes as those corresponding to the original naïve and Th1 signatures and computed the score's ratio. *TGF-beta* probes were excluded for the *TGF-beta* correlation analysis. Bilateral p-values were computed from 10,000 repetitions. The threshold for statistical significance was set at 5%. All these analyses were carried out using the R[9,31] packages *lme4*[43] and *lmerTest*[44].

Patient data analysis: Survival analyses

Association with metastasis was evaluated using a frailty Cox proportional hazards model as previously described[45] and implemented[46]. Statistical significance was assessed by means of a Log-likelihood Ratio Test (LRT), while Wald tests were used for pairwise comparisons when necessary. Association of expression intensities was evaluated as continuous variables assuming a linear relationship with the logarithm of the relative risk. Sample groups of low, medium and high expression levels were defined using the tertiles of the intensity distribution after correction by technical effects, as described in the previous section. When evaluating expression intensities, technical effects were included in the models as covariates. In an analogous way to the correlation analyses, scan batch was included as a random effect in the frailty Cox models. Hazard Rations (HR) and their corresponding 95% confidence intervals were computed as a measure of association. For visualization purposes, Kaplan-Meier curves were estimated for groups of tumours showing low, medium and high gene or signature expression. Only samples from patients diagnosed in stages I, II and III were taken into consideration for these analyses. The threshold for statistical significance was set at 5%. All analyses were carried out using R[9,31].

To compare the risk estimations with the general trend observed in the dataset, we generated a null distribution in the same way described in the previous section. As with the original signature, a Cox model was used to compute the statistic of the three pairwise comparisons for random scores and a bilateral p-value was computed from 10,000 repetitions.

MTO-derived whole tumour expression data

cDNA Library preparation and amplification were performed with the WTA2 kit (Sigma-Aldrich) from 25 ng of starting material. The cDNA was amplified for 17 cycles and purified using PureLink Quick PCR Purification Kit (Invitrogen). Quantification of amplified cDNA was done on a Nanodrop ND-1000 spectrophotometer (Thermo-Fisher Scientific, Waltham, MA, USA). 8.5 ug of the cDNA from each sample was fragmented and labelled with the GeneChip Mapping 250 K Nsp assay kit (Affymetrix). Hybridization was performed using the GeneAtlas Hyb, Wash and Stain Kit for 3' IVT arrays. Samples were denatured at 96°C for 10 min prior to incubation in the Affymetrix GeneAtlas Mouse MG-430 PM Array Strip. Hybridization was performed for 16 h at 45 °C in the GeneAtlas Hybridization Oven. Washing and Stain steps after hybridization were performed in the GeneAtlas Fluidics Station, following the specific script for Mouse MG-430 PM Arrays. Arrays were scanned with GeneAtlas Scanner using default parameters, and the generation of Cel files for bioinformatics analysis was done with GeneAtlas software (all Affymetrix).

As for human transcriptomic datasets, CEL files from organoids-derived mice whole tumours were normalized with RMA[33] using the Bioconductor R packages *affy*[30] and *affyPLM*[31]. Standard quality controls (see section Patient data analysis: Microarray processing) discarded the presence of abnormal samples. For probeset annotation we used the informationa available in the Affymetrix web page (Affymetrix Analysis Center. Netaffx. https://www.affymetrix.com/analysis/index.affx, accessed 08/01/2017).

TBRS comparisons:

Previous to the summarization of TBRS signatures, the expression matrix was corrected a-priori by Eklund's metrics[35] RMA.IQR and RNA.DEG, as they were observed to be an important source of technical variability. For such correction, a linear model was used with no other variables included as covariates. Signatures scores were computed independently for samples with three or four mutations. Scores between treatment conditions were compared using a two-sided Mann-Whitney-Wilcoxon test.

Classification of mice tumours according to CMS (extended)

To assess the similarity to the poor-prognosis CMS4 phenotype[47], we first attempted to use the Single-Sample-Predictor (SSP) provided in their original work. Nevertheless, this analysis did not succeed in classifying any of the samples being tested. For this reason, we hypothesized that the differences of platform and/or species between the training (human) and test data (mice) could be harming the performance of this classifier.

As an alternative method, we used *k*-Top Scoring Pairs (*k*TSP)[48] as implemented in the switchBox R package[49]. *k*TSP is a ranked-based method that relies in the ordering in small number of features within each sample and, thus, is very suitable in multi-platforms settings in comparison with other top-performer methods[50]. This *k*TSP classifier was trained for a binary outcome (CMS4 vs not-CMS4) in 960 samples with CMS annotation provided by the original work (168 CMS1, 421 CMS2, 127 CMS3 and 244 CMS4)[47]. The concordance between the SSP and *k*TSP methods was assessed in two human datasets that did not participate in the definition of the CMS classification: GSE38832 and GSE44076[51]; phi coefficients were 0.83 and 0.80 for these series, respectively:

GSE38832		*k*TSP	
		CMS1/2/3	CMS4
SSP	CMS1/2/3	67	7
	CMS4	0	23
	Not classified	16	9

GSE44076		*k*TSP	
		CMS1/2/3	CMS4
SSP	CMS1/2/3	61	4
	CMS4	0	8
	Not classified	13	12

Overall, these results suggested that, as *k*TSP could be more suitable for handling platforms and species differences between training and test datasets, it still retained the good classification performance attributable to SSP.

Previous to any attempt of classification, both mice and human CRC data were summarized from probeset to gene level (Entrez). For doing so, we computed the first principal component from all probesets mapping to the each gene. This component was then centred and scaled to the weighted mean of the means and standard deviations of the probesets using the corresponding contribution to the component as weight. The sign of the component was eventually changed to be congruent to the sign of the probeset contributing the most to the component. Next, mice genes were translated to their corresponding human homologous using the Mouse Genome Informatics Database[52]. Only high confidence homologous genes according to Biomart[53,54] were kept for downstream analyses (Mouse Orthology Confidence=1 and Mouse Gene-order conservation score=100; 10.015 genes). Genes to be included in the model were pre-selected from those over-expressed (1.5 fold-change minimum difference; 293 genes) or under-expressed (1.25 fold-change minimum difference; 215 genes) in CMS4 samples compared with any other subtype in the patients transcriptomic dataset. The classifier was internally tested in the training set of human samples by cross-validation leaving one dataset out for test at each iteration. A classifier trained with all the human samples available was then applied to the mice tumours using a simple rule of majority of votes. The decision cut-off was set at the midpoint of the maximum number of votes, which corresponds to the number of gene pairs used for classification. For visualization purposes, the number of votes for each classifier (cross-validation and training) were re-scaled to a score ranging between zero and one in order to represent all the classification results at the same scale.

Gene pairs:

UP	DOWN
MSRB3	*EPT1*
FERMT2	*RMI1*
EFEMP2	*ASF1B*
SPOCK1	*STIL*
DDR2	*CCNA2*
TAGLN	*HMGB2*
CCDC80	*CDC45*
GLI3	*KIF18A*
TNS1	*UNG*
STON1	*WHSC1*
PTRF	*KIF18B*
SFRP2	*HK2*
MGP	*RBM47*
GAS1	*DONSON*
BNC2	*PLK4*

SLIT2	*CCDC134*
DPYSL3	*EIF4E*
AEBP1	*RHPN2*
PCDH7	*FAM83F*
MAP1B	*FANCD2*
CRYAB	*HOOK1*
PRRX1	*CDCA2*
FBN1	*EZH2*
MXRA8	*GMCL1*
PTGIS	*CENPA*
ZFPM2	*ORC1*
MLLT11	*SPAG5*
MYL9	*TMEM54*

In agreement with the reasoning of a single-sample classifier, SSP and *k*TSP were both applied to a version of the mice data previous to any correction by technical effects. In addition, *k*TSP was also trained before technical corrections were applied to the human transcriptomic dataset. For the concordance analyses between SSP and *k*TSP, GSE44076 cel files were downloaded from GEO and processed with RMA using packages *affy*[30] and *affyPLM*[31] from Bioconductor[32].

Flow cytometry: single cell suspension preparation

Livers with tumours were removed, lobules (and in case of micro-dissection: individual liver metastases) were carefully dissected and finely minced with scalpels. The tissue was enzymatically digested in 10 ml of DMEM supplemented with 10% FBS, 1% HEPES, sodium pyruvate, glutamine, streptomycin and penicillin and 0.1% β -mercaptoethanol (Gibco) and containing 1 mg/ml Collagenase A (Roche), 0.2 mg/ml Dispase II (Sigma) and 0.2 mg/ml DNAse I (Roche), during 25 min at 37ºC with rotation. The enzymatic reaction was quenched by the addition of 30 ml of ice-cold DMEM (10% FBS, supplement). Cell suspension was filtered through a 70 µm cell strainer (BD). The filter was washed with 10 ml of ice-cold 10% FBS DMEM and the cells were pelleted at 280 g for 5 min at 4ºC. Lysis of erythrocytes was performed in Red Cell Lysis Buffer (RCLB, 155 mM NH_4Cl, 12 mM $NaHCO_3$, 0.1 mM EDTA) during 4 min at room temperature and immediately washed with ice-cold 10% FBS DMEM. After filtration through a 70 µm cell strainer and centrifugation. Sequentially, cells were purified by centrifugation 30 min at 2,400 rpm in 40/80 Percoll (Sigma) gradient. Cells were resuspended in-DMEM (10% FBS, supplement; FACS buffer).

Flow cytometry: immunophenotyping analysis and sorting

Cells were incubated 10 min on ice in FACS buffer in the presence of anti-CD16/CD32 (clone 93, eBioscience) to block Fc receptor. Mix of conjugated antibodies was added in the presence of anti-CD16/CD32 and the cells were stained during 20 min on ice. After staining, cells were washed and labelled for cell viability with the LIVE/DEAD Fixable Cell Dead stain kit (Life Technologies) during 7 min. For cytokine analysis, cell suspensions were incubated 4 h in PMA/ionomycin (Sigma-Aldrich) and brefeldin A (eBioscience) at 37 °C. Intracellular staining was performed using IC fixation/permeabilization kit (eBioscience). Cells were stained using PBS, 1% FBS, 1% HEPES and 0.6% EDTA (Gibco).

Gating strategies: Figure 1g (MTO biobank generation): To sort Lgr5-GFP+ tumour cells, we gated: Cells/Single cells/Living cells/GFP+. Figures 2d, S9b andS11a: To assess genetic recombination in the *UbC-CreER*^{T2}*; Tgfbr2*$^{fl/fl}$*; R26*^{mTmG} model, or to sort tumour cell populations, we gated: Living cells/Cells/Single cells/PDGFRb+ (CAFs). From the negative population, we followed: Endothelial cells CD31+/CD45- and Leukocytes CD31-/CD45+, further refined to small size and good viability. Figure 3h: T cell activation markers were assessed inside: Living cells/Cells/Single cells, than CD45+/CD3+, then CD4+/CD8- or CD4-/CD8+. Figure 3i and 4j: T cell cytokine levels were assessed inside: Living cells/Cells/Single cells/CD45+/CD3+/NK1.1-, then CD4+/CD8- or CD8+/CD4-. Figure 3j: CD8+ T cells were sorted using gates: Living cells/Cells/Single cells/CD45+/CD19-/MHCII-/CD3+/CD4-/CD8+. Figure 4d: PD-L1 expression was assessed inside: Living cells/Cells/Single cells/CD45+/CD3+, then CD4+/CD8- or CD8+/CD4-. Figure 4e: PD-L1 populations were determined using: Living cells/Cells/Single cells/PD-L1+. Within these we measured for CAFs (PDGFRb+/Epcam-) or Epithelial cells (PDGFRb-/Epcam+). From the double-negative population, we followed: Endothelial cells (CD31+/CD45-) and Leukocytes (CD45+/CD31-). Figure 4g: PD-L1 was measured inside Living cells/Cells/Single cells/CD45+. Figure 4i: For T cell activation markers we gated: Living cells/Cells/Single cells/CD45+/CD3+/NK1.1-, then CD4+/CD8- or CD8+/CD4-. Figure S13d: Myeloid populations were assessed inside: Living cells/Cells/Single cells/CD45+/PD-L1+/Ly6G-/Ly6C+/CD11b+/CD11c+/-.

Flow cytometry analysis and cell separation were performed in a FACSAriaFusion flow cytometer (Beckton Dickinson). Data were analyzed using FlowJo software (v 10.4).

The following antibodies were used for the staining: anti-CD45 (clone 30-F11), anti-CD4 (clone GK1.5), anti-aCD8 (clone 53-6.7), anti-CD69 (clone H1.2F3), anti-CD104b (PDGFRb, clone APB5), and anti-MHCII (clone M5/114.15.2) were obtained from eBioscience; Epcam (clone EBA-1), anti-CD3e (clone 145-2C11), anti-CD44 (clone G44-26), CD62L (clone MEL-14), anti-IFNγ (clone XMG1.2), anti-CD274 (PD-L1, clone MIH-5), and anti-Ly6C (clone AL-32) were obtained from BD Pharmingen; anti-CD31 (clone 390) was obtained from Abcam; and anti-CD11b (clone M1/70), anti-CD11c (clone H418), anti-GZMB (GB11), anti-CD279 (PD-1, clone 29F.1A12), anti-CD8a (clone 53-6.7), anti-T-bet (clone 4B10), anti-Ly6G (clone 1A8) were obtained from BioLegend.

Gene expression in tumour cell populations

RNA from sorted cells was processed and amplified as previously described[55]. For mouse liver metastases: To assess *Tgfb1*, *-2* and *-3* mRNA levels, we performed RT-qPCR with triplicate reactions (each 5 ng of cDNA) in a StepOne instrument (Thermo Fisher) with Taqman probes (*Tgfb1* Mm01178819_m1; *Tgfb2* Mm00436955_m1; *Tgfb3* Mm00436960_m1; endogenous control *Actb* Mm00607939_s1). Other probes used are: *Aurkb* Mm_01718140_m1, *mKi67* Mm01278617_m1, *Gzma* Mm01304452_m1, *Gzmb* Mm00442837_m1, *Pdcd1* Mm01285676_m1, and *Gapdh* Mm99999915_g1.

Sorted CRC populations from human samples were described previously[1,3]. Briefly, two GEO data sets were used to characterize gene profiles according to specific gene expression in tumour cell subpopulations: GSE39395 and GSE39396[3]. In these datasets and as described previously[3], FACS was used to separate the following populations from 14 fresh CRC samples: CD45+/EpCAM−/CD31−/FAP− ,CD45−/EpCAM+/CD31−/FAP−, CD45−/EpCAM−/CD31+/FAP− and CD45−/EpCAM−/CD31−/FAP+. To homogenize these two expression matrices, dataset GSE39396 was centred and scaled pairwise to the mean and standard deviation of GSE39395. A signature of Cancer Associated Fibroblasts (CAFs) was derived from the resulting expression matrix. For doing so, we selected probesets overexpressed in the CD45−/EpCAM−/CD31−/FAP+ samples with a three minimum fold and raw p-value < 0.05 compared to any other cell population. These analyses were performed using a linear model with empirical shrinkage[41] as implemented in *limma* R package[31]. Also TGF-b levels by cell populations were assessed in this dataset using Kruskal Wallis (KW) and two-sided Mann-Whitney tests.

Supplementary Methods References

1. Calon, A. *et al.* Stromal gene expression defines poor-prognosis subtypes in colorectal cancer. *Nat. Genet.* **47,** 320–329 (2015).

2. Warren, R. S., Yuan, H., Matli, M. R., Gillett, N. A. & Ferrara, N. Regulation by vascular endothelial growth factor of human colon cancer tumorigenesis in a mouse model of experimental liver metastasis. *J. Clin. Invest.* **95,** 1789–1797 (1995).

3. Calon, A. *et al.* Dependency of colorectal cancer on a TGF-beta-driven program in stromal cells for metastasis initiation. *Cancer Cell* **22,** 571–584 (2012).

4. Céspedes, M. V. *et al.* Orthotopic microinjection of human colon cancer cells in nude mice induces tumor foci in all clinically relevant metastatic sites. *Am. J. Pathol.* **170,** 1077–85 (2007).

5. Merlos-Suárez, A. *et al.* The Intestinal Stem Cell SignatureIdentifies Colorectal Cancer Stem Cells and Predicts Disease Relapse. *Cell Stem Cell* 511–524 (2011). doi:10.1016/j.stem.2011.02.020

6. Jung, P. *et al.* Isolation and in vitro expansion of human colonic stem cells. *Nat Med* **17,** 1225–1227 (2011).

7. Tauriello, D. V. F. *et al.* Loss of the tumor suppressor CYLD enhances Wnt/beta-catenin signaling through K63-linked ubiquitination of Dvl. *Mol. Cell* **37,** 607–19 (2010).

8. Schindelin, J., Rueden, C. T., Hiner, M. C. & Eliceiri, K. W. The ImageJ ecosystem: An open platform for biomedical image analysis. *Mol. Reprod. Dev.* **82,** 518–529 (2015).

9. Team, R. C. R: A language and environment for statistical computing. *R Foundation for Statistical Computing, Vienna, Austria* (2016). at <http://www.r-project.org>

10. Wickham, H. *ggplot2: Elegant Graphics for Data Analysis.* (Springer-Verlag New York, 2009). at <http://ggplot2.org>

11. Li, H. & Durbin, R. Fast and accurate short read alignment with Burrows-Wheeler transform. *Bioinformatics* **25,** 1754–1760 (2009).

12. DePristo, M. A. *et al.* A framework for variation discovery and genotyping using next-generation DNA sequencing data. *Nat. Genet.* **43,** 491–8 (2011).

13. Cingolani, P. *et al.* A program for annotating and predicting the effects of single nucleotide polymorphisms, SnpEff: SNPs in the genome of Drosophila melanogaster strain w 1118; iso-2; iso-3. *Fly (Austin).* **6,** 80–92 (2012).

14. Alexandrov, L. B. *et al.* Signatures of mutational processes in human cancer. *Nature* **500,** 415–421 (2013).

15. Rosenthal, R., McGranahan, N., Herrero, J., Taylor, B. S. & Swanton, C. DeconstructSigs: delineating mutational processes in single tumors distinguishes DNA repair deficiencies and patterns of carcinoma evolution. *Genome Biol.* **17,** 31 (2016).

16. Alexandrov, L. B. *et al.* Clock-like mutational processes in human somatic cells. *Nat. Genet.* **47,** 1402–1407 (2015).

17. Dobin, A. *et al.* STAR: ultrafast universal RNA-seq aligner. *Bioinformatics* **29,** 15–21 (2013).

18. Rossell, D., Stephan-Otto Attolini, C., Kroiss, M. & Stöcker, A. Quantifying alternative splicing from paired-end RNA-seq data. *Ann. Appl. Stat.* **8,** 309 (2014).

19. Durinck, S., Spellman, P. T., Birney, E. & Huber, W. Mapping identifiers for the integration of genomic datasets with the R/Bioconductor package biomaRt. *Nat. Protoc.* **4,** 1184–91 (2009).

20. Castle, J. C. *et al.* Immunomic, genomic and transcriptomic characterization of CT26 colorectal carcinoma. *BMC Genomics* **15,** 190 (2014).

21. Andreatta, M. & Nielsen, M. Gapped sequence alignment using artificial neural networks: application to the MHC class I system. *Bioinformatics* **32,** 511–517 (2016).

22. Cancer Genome Atlas Network, T. Comprehensive molecular characterization of human colon and rectal cancer. *Nature* **487,** 330–7 (2012).

23. Charoentong, P. *et al.* Pan-cancer Immunogenomic Analyses Reveal Genotype-Immunophenotype Relationships and Predictors of Response to Checkpoint Blockade. *Cell Rep.* **18,** 248–262 (2017).

24. Lois, C., Hong, E. J., Pease, S., Brown, E. J. & Baltimore, D. Germline transmission and tissue-specific expression of transgenes delivered by lentiviral vectors. *Science* **295,** 868–72 (2002).

25. Cleveland, W. S. & Devlin, S. J. Locally Weighted Regression: An Approach to Regression Analysis by Local Fitting. *J. Am. Stat. Assoc.* (2012).

26. Jorissen, R. N. *et al.* Metastasis-associated gene expression changes predict poor outcomes in patients with Dukes stage B and C colorectal cancer. *Clin. Cancer Res.* **15,** 7642–7651 (2009).

27. De Sousa E Melo, F. *et al.* Methylation of cancer-stem-cell-associated wnt target genes predicts poor prognosis in colorectal cancer patients. *Cell Stem Cell* **9,** 476–485 (2011).

28. Marisa, L. *et al.* Gene Expression Classification of Colon Cancer into Molecular Subtypes: Characterization, Validation, and Prognostic Value. *PLoS Med.* **10,** e1001453 (2013).

29. Tripathi, M. K. *et al.* Nuclear factor of activated T-cell activity is associated with metastatic capacity in colon cancer. *Cancer Res.* **74,** 6947–6957 (2014).

30. Gautier, L., Cope, L., Bolstad, B. M. & Irizarry, R. A. Affy - Analysis of Affymetrix GeneChip data at the probe level. *Bioinformatics* **20,** 307–315 (2004).

31. Gentleman, R. *Bioinformatics and Computational Biology Solutions Using R and Bioconductor. Journal of the American Statistical Association* **102,** (Springer New York, 2005).

32. Gentleman, R. *et al.* Bioconductor: open software development for computational biology and bioinformatics. *Genome Biol.* **5,** R80 (2004).

33. Irizarry, R. A. *et al.* Exploration, normalization, and summaries of high density oligonucleotide array probe level data. *Biostatistics* **4,** 249–264 (2003).

34. Gentleman, R., Huber, W., Carey, V., Irizarry, R. & Dudoit, S. *Bioinformatics and Computational Biology Solutions Using R and Bioconductor*. *Book* (Springer Science+Business Media, 2005).

35. Eklund, A. C. & Szallasi, Z. Correction of technical bias in clinical microarray data improves concordance with known biological information. *Genome Biol.* **9,** R26 (2008).

36. Bolstad, B. M., Irizarry, R. A., Åstrand, M. & Speed, T. P. A comparison of normalization methods for high density oligonucleotide array data based on variance and bias. *Bioinformatics* **19,** 185–193 (2003).

37. Jorissen, R. N. *et al.* DNA copy-number alterations underlie gene expression differences between microsatellite stable and unstable colorectal cancers. *Clin. Cancer Res.* **14,** 8061–8069 (2008).

38. Azzalini, A. & Torelli, N. Clustering via nonparametric density estimation. *Stat. Comput.* **17,** 71–80 (2007).

39. Azzalini, A. & Menardi, G. Clustering via Nonparametric Density Estimation: The *R* Package pdfCluster. *J. Stat. Softw.* **57,** 1–26 (2014).

40. Abbas, A. R. *et al.* Immune response in silico (IRIS): immune-specific genes identified from a compendium of microarray expression data. *Genes Immun.* **6,** 319–331 (2005).

41. Smyth, G. K. Linear Models and Empirical Bayes Methods for Assessing Differential Expression in Microarray Experiments Linear Models and Empirical Bayes Methods for Assessing Differential Expression in Microarray Experiments. *Stat. Appl. Genet. Mol. Biol.* **3,** 1–26 (2004).

42. Benjamini, Y. & Hochberg, Y. Controlling the False Discovery Rate: A Practical and Powerful Approach to Multiple Testing. *J. R. Stat. Soc. Ser. B* **57,** (1995).

43. Bates, D., Maechler, M., Bolker, B. M. & Walker, S. lme4: Linear mixed-effects models using Eigen and S4. (2015). at <http://arxiv.org/abs/1406.5823>

44. Kuznetsova, A., Bruun Brockhoff, P. & Christensen, Haubo Bojesen, R. lmerTest: Tests in Linear Mixed Effects Models. R package version 2.0-32. (2016). at <https://cran.r-project.org/package=lmerTest>

45. Therneau, T. M., Grambsch, P. M. & Pankratz, V. S. Penalized Survival Models and Frailty. *J. Comput. Graph. Stat.* **12,** 156–175 (2003).

46. Therneau, T. M. coxme: Mixed Effects Cox Models. R package version 2.2-5. (2015). at <https://cran.r-project.org/package=coxme>

47. Guinney, J. *et al.* The consensus molecular subtypes of colorectal cancer. *Nat. Med.* **21,** 1350–1356 (2015).

48. Tan, A. C., Naiman, D. Q., Xu, L., Winslow, R. L. & Geman, D. Simple decision rules for classifying human cancers from gene expression profiles. *Bioinformatics* **21,** 3896–3904 (2005).

49. Afsari, B., Fertig, E. J., Geman, D. & Marchionni, L. switchBox: an R package for k–Top Scoring Pairs classifier development. *Bioinformatics* **31,** 273–274 (2015).

50. Marchionni, L., Afsari, B., Geman, D. & Leek, J. T. A simple and reproducible breast cancer prognostic test. *BMC Genomics* **14,** 336 (2013).

51. Sanz-Pamplona, R. *et al.* Aberrant gene expression in mucosa adjacent to tumor reveals a molecular crosstalk in colon cancer. *Mol. Cancer* **13,** 46 (2014).

52. Blake, J. A. *et al.* Mouse Genome Database (MGD)-2017: community knowledge resource for the laboratory mouse. *Nucleic Acids Res.* **45,** D723–D729 (2017).

53. Durinck, S. *et al.* BioMart and Bioconductor: a powerful link between biological databases and microarray data analysis. *Bioinformatics* **21,** 3439–3440 (2005).

54. Smedley, D. *et al.* The BioMart community portal: an innovative alternative to large, centralized data repositories. *Nucleic Acids Res.* **43,** W589-98 (2015).

55. Gonzalez-Roca, E. *et al.* Accurate Expression Profiling of Very Small Cell Populations. *PLoS One* **5,** e14418 (2010).

Chapter 2

Unravelling the biology of CAFs in liver metastasis

Summary

CAFs play important roles in CRC liver metastasis. Previous data published by our lab has proved that TGF-β triggers a gene expression program in CAFs that defines poor prognosis in patients and promotes tumour growth and survival. However, the contribution of CAFs to the TGF-β-mediated immune excluded phenotype remains opaque. We have investigated the biology of CAFs from CRC liver metastasis. Our results have shown the existence of at least two different subpopulations of CAFs, whose composition varies depending on the MTO used for metastasis generation. The abundance of myofibroblasts, one of the two discovered subpopulations, could acquire immunosuppressive roles, as it correlated with the immune exclusion in metastases. The understanding of CAF subtypes will help dissect the mechanisms of immune evasion, and may contribute to the development of novel, more specific therapies against metastatic disease. Moreover, we aim to explore the CAF-immune system relationship taking advantage of both the novel models for advanced CRC developed in the laboratory and genetic tools that enable the specific ablation of the TGFBR2 in CAFs. The results obtained under this chapter helped us to assign fibroblast-specific markers to genetically target the TGF-β pathway in CAFs in chapter 3.

Objectives

- Comphrehension of the biology and find specific markers for CAFs in CRC liver metastasis using the MTO model

- Establishment of a pipeline for CAF isolation and analysis.

- Analysis of the relationship between CAFs and tumour immunity in CRC liver metastasis.

2.1 Identification of two distinct CAF subpopulations from liver CRC metastasis

In **chapter 1**, we reported that TGF-β has a crucial role in mediating resistance to the adaptive immune system in CRC (**Tauriello et al., 2018**). Tauriello and colleagues generated a genetic mouse model that recapitulates the biology of advanced colorectal tumours, including metastasis. Tumours arising in this model were isolated and kept *in vitro* as Mouse Tumour Organoids (MTOs). These 3D-cultured primary cells could be successfully transplanted into syngeneic, immunocompetent C57BL/6J mice to recapitulate metastatic disease. When the TGF-β pathway was blocked by either Galunisertib administration or ubiquitous genetic ablation of the TGFBR2, T lymphocytes were able to infiltrate CRC liver metastases. This effect synergized with monoclonal antibodies against PD-L1, resulting in strong therapeutic effects on mice with overt metastatic disease, completely eradicating cancers in the majority of cases (**Tauriello et al., 2018**). However a precise understanding of the cellular processes leading to TGF-β-mediated immune rejection remains to be elucidated.

As mentioned in the introduction, our lab showed that TGF-β induces a gene signature that predicts clinical outcome (**Calon et al., 2012**). The majority of the TGF-β target genes that predict poor prognosis are expressed by the tumour stroma, especially by CAFs (**Calon et al., 2015**). This suggests a potential role for these cells in TGF-β-mediated immune evasion. Using the MTO platform to generate CRC liver metastasis (**Tauriello et al., 2018**), we aimed to explore the role of TGF-β-activated CAFs in mediating immune evasion. Our strategy was based on specifically deleting the TGFBR2 in CAFs during the growth and progression of murine CRC liver metastasis, using established and precise *in vivo* recombination tools. However, as discussed in the introduction, one of the main problems in fibroblast biology is their heterogeneity and the lack of a well-established surface pan-marker (**Kalluri, 2016**). This poses a major challenge to select a suitable marker to identify and genetically target CAFs. We thus decided to first explore the biology of normal liver-resident fibroblasts as well as of fibroblasts found in MTO-derived liver metastases (CAFs).

Hepatic stellate cells (HSCs) and portal fibroblasts (PFs) in the liver, which will be collectively referred as liver mesenchymal cells (LMCs), have been previously characterized (**Friedman, 2008; Wells, 2014**). Consequently, we used antibodies against the two isoforms of the receptor for Platelet-Derived Growth Factor (PDGFRα and PDGFRβ) to label these LMCs. We also used alpha Smooth Muscle Actin (αSMA), the classical marker for myofibroblasts. As expected, LMCs expressed both PDGFRα and PDGFRβ, but not αSMA. The latter was found expressed only in perivascular cells surrounding central veins, portal veins and portal arteries. These cell types were also expressing PDGFRβ but no PDGFRα (**Figure 17A**).

Mice transplanted by intrasplenic injection with MTOs generate full-blown liver CRC metastasis in 3-4 weeks (**Figure 19A**). For these experiments, we used MTO129, a mouse CRC organoid model that carry the four main driver mutations (*Apc*, *Kras*^{G12D}, *p53* and *Tgfbr2*; see **Tauriello et al., 2018** for details). Previous experiments showed that MTO129 exhibit the best therapeutic responses to TGFBR1 inhibitory therapy (see **Chapter 1, Tauriello et al., 2018**). Using the same three markers, we determined that all stained CAFs expressed PDGFRβ, whereas staining for PDGFRα and αSMA was mutually exclusive (**Figure 17B-C**). The exclusion pattern between PDGFRα and αSMA was confirmed in metastases generated by of additional quadruple mutant MTOs (data not shown). Thus, we concluded that two CAF subpopulations coexist in liver metastasis: 1) PDGFRα^{+}/PDGFRβ^{+}/αSMA^{-} CAFs (α^{+}/β^{+}) that may be similar to LMCs and 2) αSMA+ myofibroblasts that do not express PDGFRα (PDGFRα^{-}/PDGFRβ^{+}/αSMA^{+} CAFs, α^{-}/β^{+}). In advanced metastasis, α^{+}/β^{+} CAFs appeared as a minor subpopulation, mostly in the tumour margins and were especially detectable in portal areas, whereas the centre of the tumour was enriched in α^{-}/β^{+} CAFs (**Figure 18**).

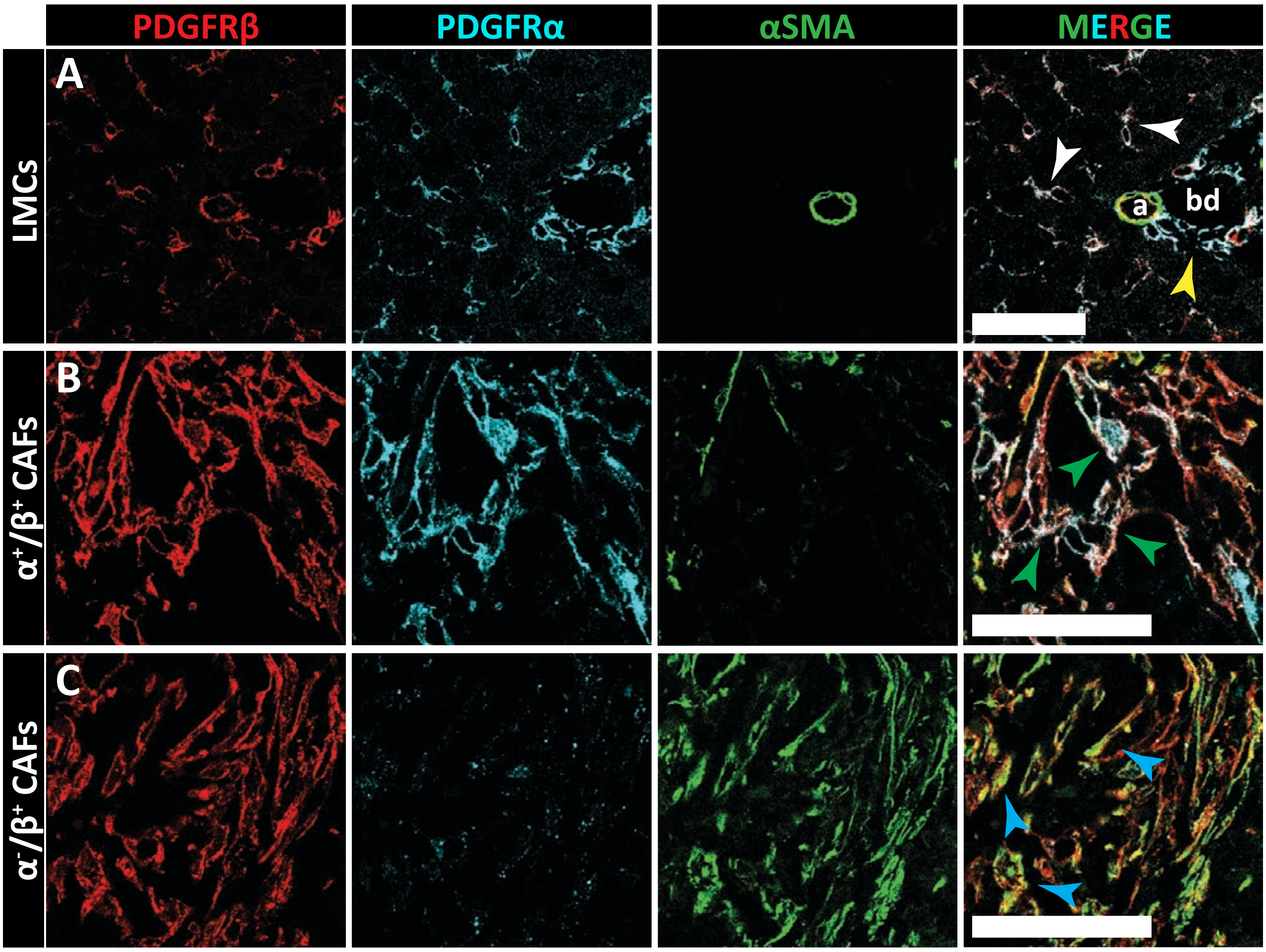

Figure 17. Fibroblast markers in healthy liver. A. Detailed view of a portal area from a healthy liver in homeostasis stained for PDGFRα, PDGFRβ and αSMA. Yellow arrowhead: portal fibroblasts. White arrowhead: hepatic stellate cells. a: artery, bd: bile duct. **B, C.** Sections from a MTO-derived liver metastasis showing α^+/β^+ CAFs (**B**, PDGFRα+, PDGFRβ+, αSMA-, green arrowheads) and α^-/β^+ CAFs (**C**, PDGFRα-, PDGFRβ+, αSMA+, blue arrowheads).

2.2 Comparative analysis of α^+/β^+ vs α^-/β^+ CAFs

Based on the above data, we leveraged the expression of PDGFRα and PDGFRβ to distinguish fibroblasts subpopulation present in liver metastasis. In particular, we compared α^+/β^+ CAFs from α^-/β^+ CAFs (**Figure 19A-B**). To analyse these two subpopulations, we sacrificed mice after 3 weeks of MTO inoculation. Macroscopic metastatic nodules were resected *ex vivo*. The remaining liver tissue was processed separately (**Figure 19A**). From dissected metastatic nodules, we identified the total CAF fraction using fluorescence-activated cell sorting (FACS) by selecting EPCAM-/CD31-/CD45-/PDGFRβ+ cells, and then we sorted α^+/β^+ and α^-/β^+ CAFs by further selecting PDGFRα+ and PDGFRα- cells respectively (**Figure 19B**). LMCs were sorted by selecting PDGFRβ+, PDGFRα+ cells from normal liver tissue (**Figure 19A**). We validated the fibroblastic nature of LMCs and both CAF subpopulations compared to EPCAM+ tumour cells, CD31+ endothelial cells and CD45+ leukocytes using qRT-PCR. Both mesenchymal populations were enriched in *Pdgfr*β and were negative for *Epcam*, *Cd31* and *Cd45* (**Figure 19C**).

Having established a pipeline for PDGFRβ+ fibroblast isolation in both naïve livers (LMCs) and metastases (CAFs), we compared the expression of TGF-β targets in the two populations. As expected, most TGF-β targets were upregulated in CAFs compared to LMCs except for *Cald1* and *Igfbp7*, two bonafide TGF-β which showed equal expression between

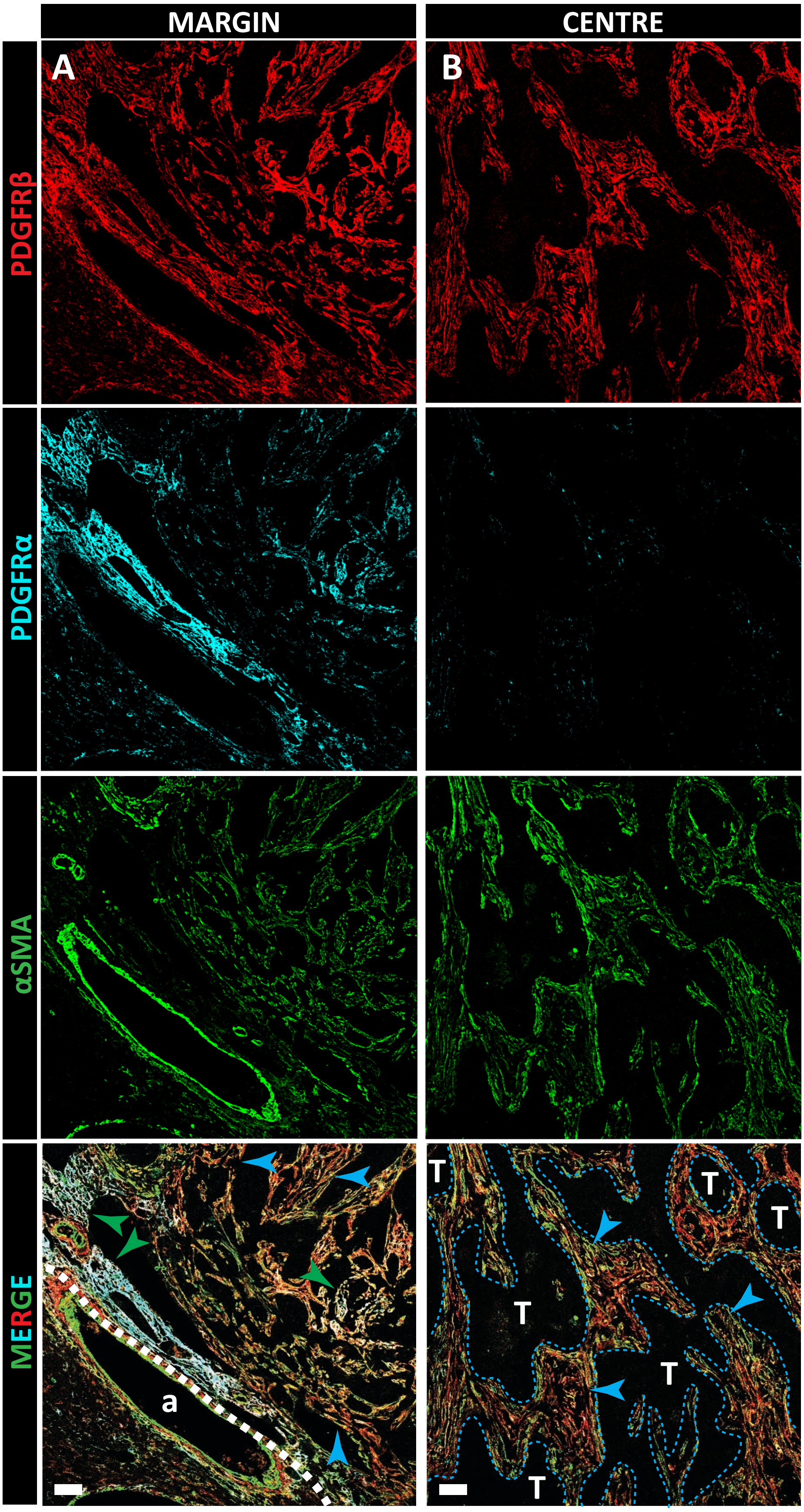

Figure 18. Fibroblast markers in CRC liver metastasis. Overview from a liver metastasis 3 weeks after MTO129 inoculation. α^+/β^+ CAFs were found mainly in the tumour margins (**A**) while α^-/β^+ CAFs exclusively composed stroma in the tumour centre (**B**). White dashed line delineates tumour margin. Blue dashed lines delineate tumour glands (T) from tumour stroma. Scale bars = 50 μm. Green arrowheads: α^+/β^+ CAFs. Blue arrowheads: α^-/β^+ CAFs.

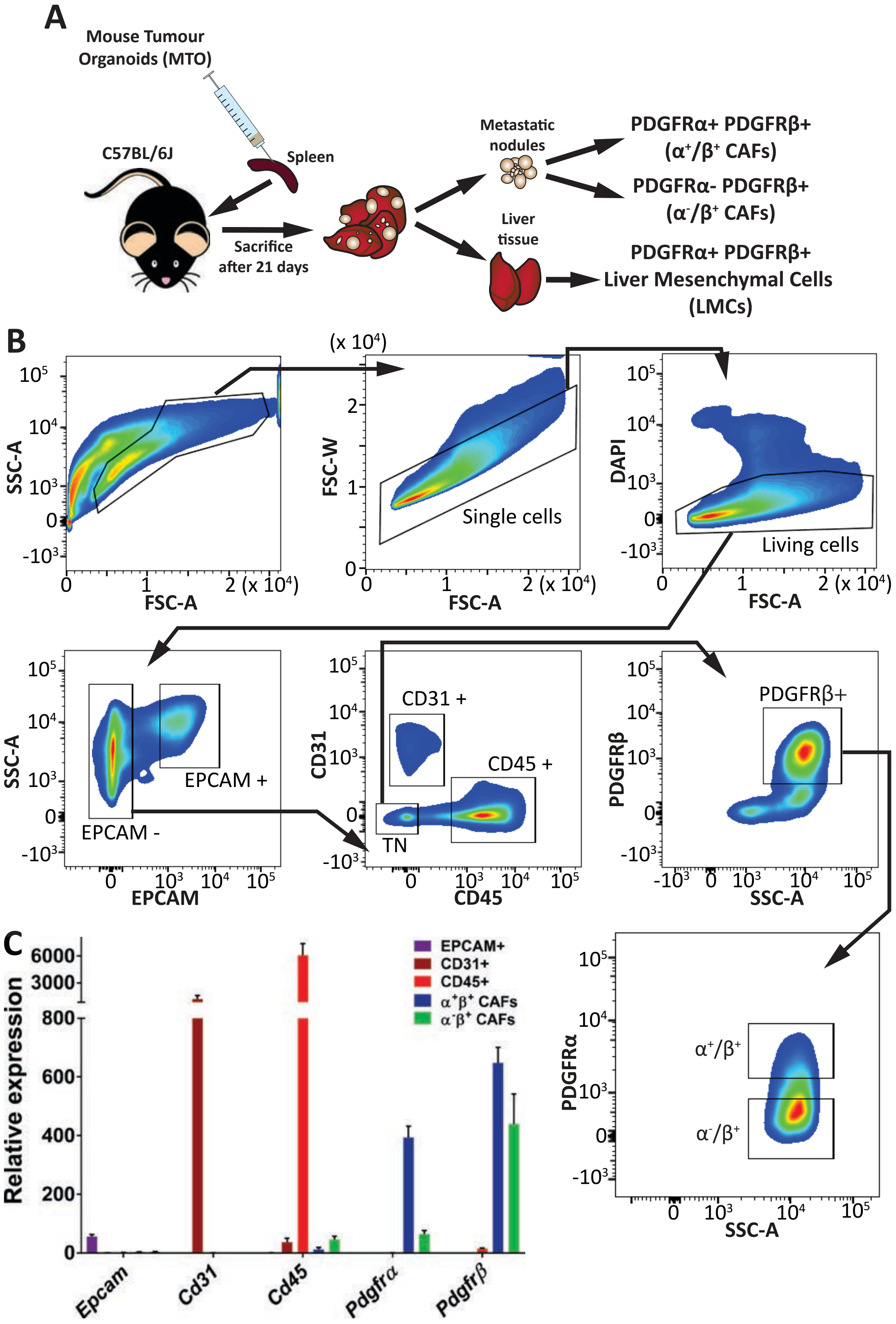

Figure 19. Characterization of fibroblast populations present in liver metastasis. A. Schematic representation for the analysis of CAF subpopulations from murine CRC liver metastasis as well as homeostatic livers. MTOs are injected into the spleen of syngeneic C57BL/6J mice, which allows direct liver colonization of tumour cells. After 3 weeks of tumour growth, metastatic nodules can be visually detected and separated from unaffected liver tissue. CAFs were sorted from resected tumours, whereas LMCs were sorted from the remaining liver fragments. **B.** Representative gating strategy for fibroblast isolation by FACS. From viable, single cells, epithelial cells, endothelial cells and leucocytes are excluded by subsequent negative selection of Epcam, CD31 and CD45, respectively. Triple negative (TN) cells were then gated for PDGFRβ for CAF/LMC selection. CAF subpopulations are discriminated according to PDGFRα expression. **C.** Purity control of sorted populations from the tumour microenvironment. Bars represent upper detection limits.

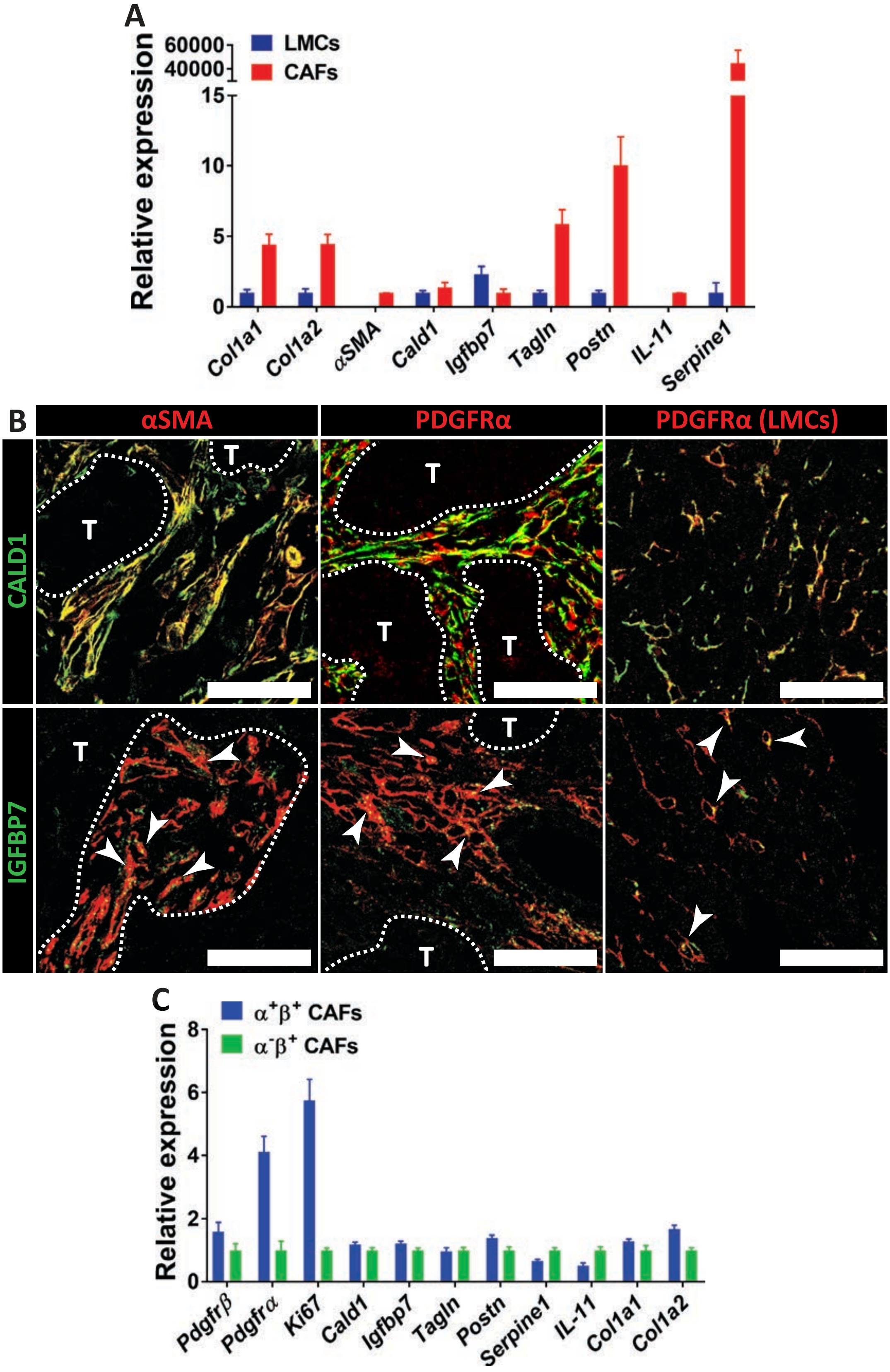

Figure 20. Gene expression analysis of LMCs and CAFs. A. Gene expression comparison between CAFs and LMCs. Expression of αSMA and *IL-11* was not detected in LMCs. Detected Ct of αSMA and *IL-11* in CAFs were 26.61 and 30.47 respectively. **B.** Immunofluorescence stainings of CALD1 and IGFBP7 in α^+/β^+ CAFs (PDGFRα+) and α^-/β^+ CAFs (αSMA+) in tumours and liver parenchyma (PDGFRα+ LMCs). Dashed lines limit tumour glands (T) with the stromal compartment. White arrowheads: mesenchymal cells expressing IGFBP7. Scale bars = 50 µm. **C.** Gene expression comparison between α^+/β^+ and α^-/β^+ CAFs. Bars represent upper detection limits in **A** and **C**.

the two populations (**Figure 20A-B**). Subsequently, we compared the expression of TGF-β targets between α$^+$/β$^+$ and α$^-$/β$^+$ CAFs. We did not observe major differences in the expression of TGF-β targets between both CAF subpopulations (**Figure 20C**). However, we found *Ki67* expression upregulated in α$^+$/β$^+$ CAFs, which may suggest that α$^+$/β$^+$ CAFs have a higher proliferative potential than α$^-$/β$^+$ CAFs (**Figure 20C, Figure 21**). From these preliminary analysis we concluded that both α$^+$/β$^+$ and α$^-$/β$^+$ CAFs show a similar level of activation by TGF-β. It is also tempting to speculate that α$^+$/β$^+$ CAFs might be the precursors of α$^-$/β$^+$ myofibroblasts.

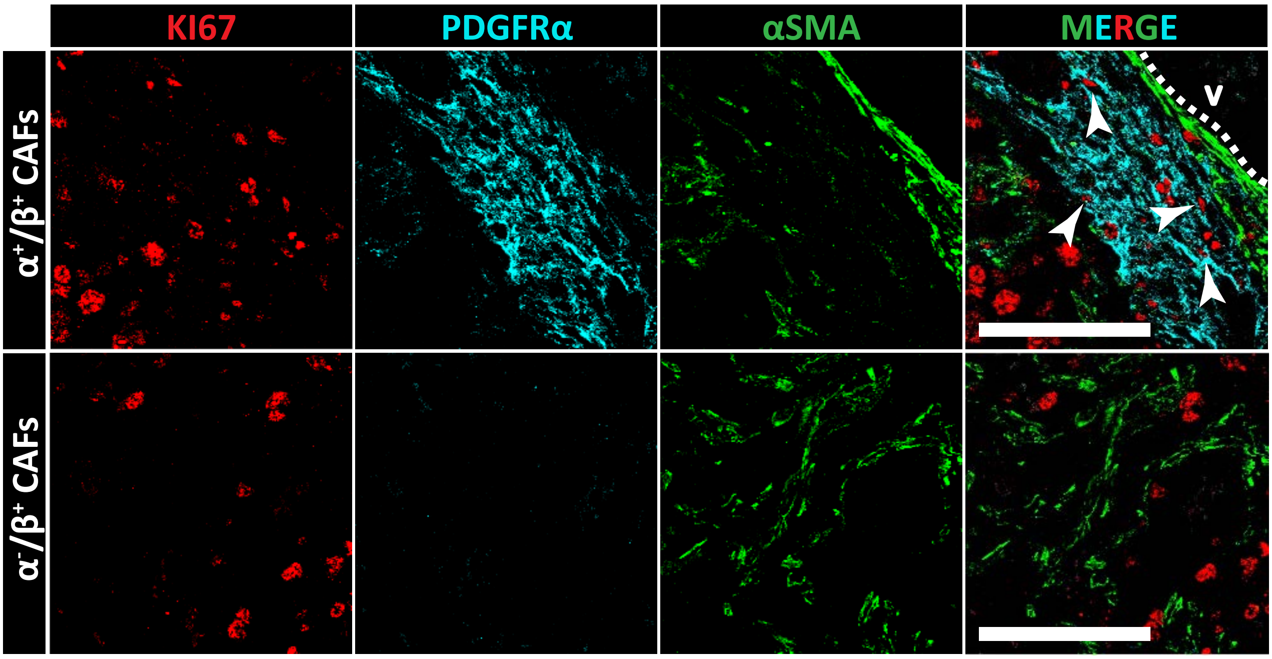

Figure 21. KI67 expression in CAF subpopulations. Sections from MTO-derived liver metastases showing stainings of KI67, PDGFRα and αSMA**.** Sections are taken from one same tumour, focusing on regions enriched in α$^+$/β$^+$ CAFs (upper row) or α$^-$/β$^+$ CAFs (lower row). White arrowheads show α$^+$/β$^+$ CAFs positive for KI67 expression. Dashed line delineates the tumour margin. Scale bars = 50 µm. V = vein.

2.3 Dynamics and origin of tumor stroma during metastatic progression

We next investigated the potential origin of CAFs in liver metastasis. According to previous studies on liver fibrosis and HCC, LMCs are the main source for active myofibroblasts (**Iwaisako et al., 2014; Kramann et al., 2014; Liu et al., 2015; Mederacke et al., 2013; Sekiya et al., 2016**). Nevertheless, we wanted to verify if bone marrow-derived progenitors (fibrocytes) also contributed to the generation of CAFs in our model. To this end, we generated bone marrow chimeric mice by transplanting bone marrow from a GFP mouse donor into irradiated C57BL/6J mice. GFP labels bone marrow derived cells that localized in the stroma of metastases, possibly giving rise to most cells of myeloid and lymphoid origin. Yet, neither of both CAF subpopulations in tumours showed any GFP expression, strongly suggesting that CAFs in CRC liver metastasis derive from local LMCs (**Figure 22**).

As α$^+$/β$^+$ CAFs showed increased expression of Ki67, we speculated that the generation of α$^-$/β$^+$ myofibroblasts was a consequence of post-proliferative differentiation of α$^+$/β$^+$ CAFs. The results in section **2.2** (**Figure 20, Figure 21**, **Pages 115-116**) describe the stromal content of advanced metastatic disease at 21 days post inoculation of MTOs. Given the association of αSMA expression to myofibroblast differentiation, we evaluated the presence of αSMA+, α$^-$/β$^+$ CAFs in histological sections from mice bearing MTO129-derived metatasis at two and three weeks after MTO inoculation (**Figure 23**). We observed that indeed the stromal area positive for αSMA increased over time (**Figure 23**).

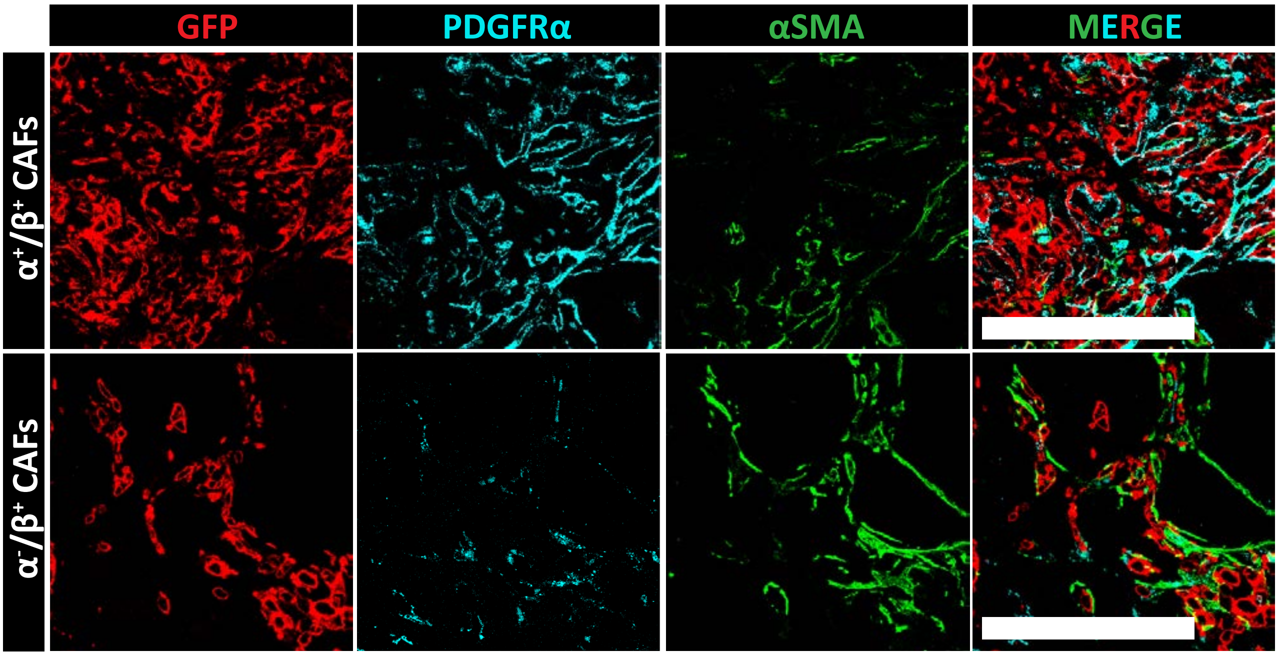

Figure 22. CAFs in liver metastasis are not originated from bone marrow-derived progenitors. Sections from MTO-derived metastasis showing stainings of GFP, PDGFRα and αSMA, from a chimeric C57BL/6J mouse with a GFP bone marrow. Sections are taken from one same tumour, focusing on α$^+$/β$^+$ CAFs (upper row) or α$^-$/β$^+$ CAFs (lower row). Scale bars = 100 μm.

Overall, these data suggest that the evolution of liver metastasis stroma is a dynamic process, with a progressive recruitment and activation of myofibroblasts. A plausible model is that activated LMCs give rise to α$^+$/β$^+$ CAFs, which subsequently proliferate and generate α$^-$/β$^+$ myofibroblasts in the tumour stroma. Testing this hypothesis would require lineage-tracing experiments.

2.4 CAF heterogeneity in metastases generated from distinct MTOs

The biobank of MTOs developed in the Batlle lab contained tumour cells extracted from different mice, which are grouped according to the number and type of engineered genetic alterations that they carry (**Tauriello et al., 2018**). We compared the stroma from metastases generated from three different quadruple mutant MTOs: MTO129, MTO138 and MTO140, all of which share an elevated metastatic potential when implanted in syngeneic animals (**Chapter 1**). MTO129 and MTO140 were isolated from male mice, whereas MTO138 was isolated from a female mouse. Despite the three MTO carry the same CRC driver mutations, RNAseq data from these MTOs grown *in vitro* showed different expression values for *Tgf-β* and *Pdgf*, two main growth factors for CAFs (**Kalluri and Zeisberg, 2006**). All three MTOs expressed similar levels of *Tgf-β1*. However, *Tgf-β2* and *-β3* were upregulated in MTO129. Moreover, MTO129 exhibited increased levels of *Pdgf*, especially *Pdgf-A* and *-C*, compared to MTO138 and MTO140. (**Figure 24A**).

We suspected that these differences in *Tgf-β* and *Pdgf* expression could have a direct effect on CAF's behaviour or heterogeneity. To explore this possibility, we transplanted MTO129, MTO138 and MTO140 into syngeneic C57BL/6J mice and allowed them to generate liver metastases for 3 weeks as in **Figure 19A** (**Page 114**). Metastatic nodules were analysed by flow cytometry as described in **Figure 19B** (**Page 114**). Despite all three tumours had a similar number of total CAFs (**Figure 24B**), differences in the proportions of CAF subpopulations were observed between metastases: MTO129 tumours showed a higher content of α$^+$/β$^+$ CAFs, whereas most CAFs from MTO138 and MTO140 tumours were α$^-$/β$^+$ CAFs (**Figure 24C**). Given that PDGFRα and αSMA are mutually exclusive in CAFs from liver metastasis

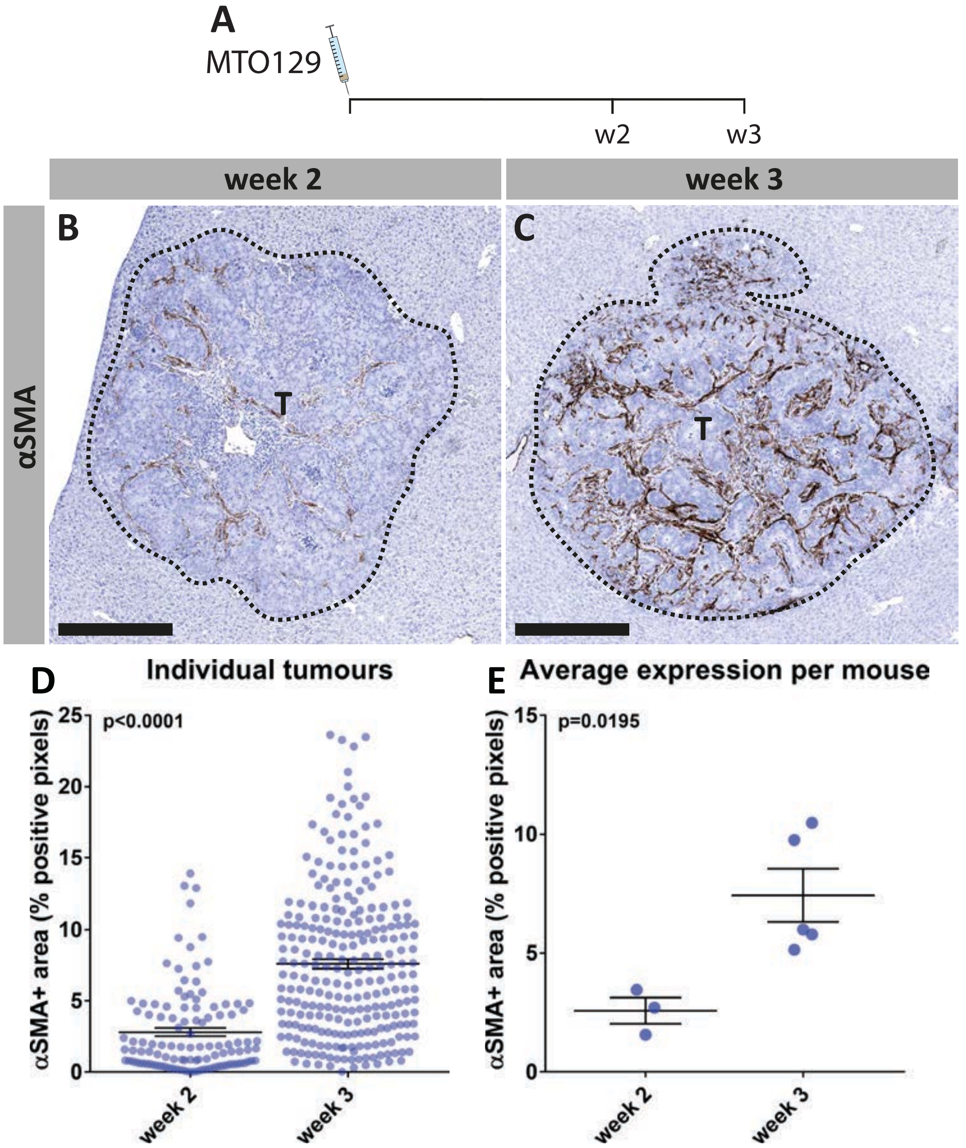
A
MTO129
w2
w3
week 2
week 3
B
C
αSMA
T
T
D
Individual tumours
p<0.0001
αSMA+ area (% positive pixels)
0
5
10
15
20
25
week 2
week 3
E
Average expression per mouse
p=0.0195
αSMA+ area (% positive pixels)
0
5
10
15
week 2
week 3

Figure 23. Dynamic evolution of the stroma in liver metastases. A. Schematic representation of the experimental design. **B-C.** Representative IHC images showing DAB staining of αSMA+ myofibroblasts at 2 weeks (**B**) and 3 weeks (**C**) after MTO129 transplantation. T = tumour. Scalebars = 500 µm. **D.** Quantification of the percentage of αSMA+ area represented as % of positive pixels detected within a metastatic nodule. Each plotted dot represents a single nodule. 42 nodules on average were quantified for 3 (week 2, left) and 5 mice (week 3, right). **E.** Average αSMA+ expression per mouse relative to **D**. Averages and SEM are represented in **D** and **E**. Unpaired test was performed in **D** and **E**.

(**Figure 17, Figure 18, pages 112-113**), we can assume that α^{-}/β^{+} CAFs detected by flow cytometry are indeed αSMA+ CAFs, and therefore that MTO138 and MTO140 tumours are enriched in myofibroblasts.

In parallel, metastatic nodules were isolated for RNA extraction and analysis. We compared expression levels of the three *TGF-β* isoforms in bulk RNA. In contrast to the results obtained by RNAseq from *in vitro* cultured MTO cells, *Tgf-β1* mRNA expression within an intact tumour environment was significantly higher in tumours generated from MTO140, followed by MTO138-derived metastases. Likewise, *Tgf-β3* expression was also increased in both MTO140- and MTO138-derived metastases, with minimal differences. *Tgf-β2* expres-

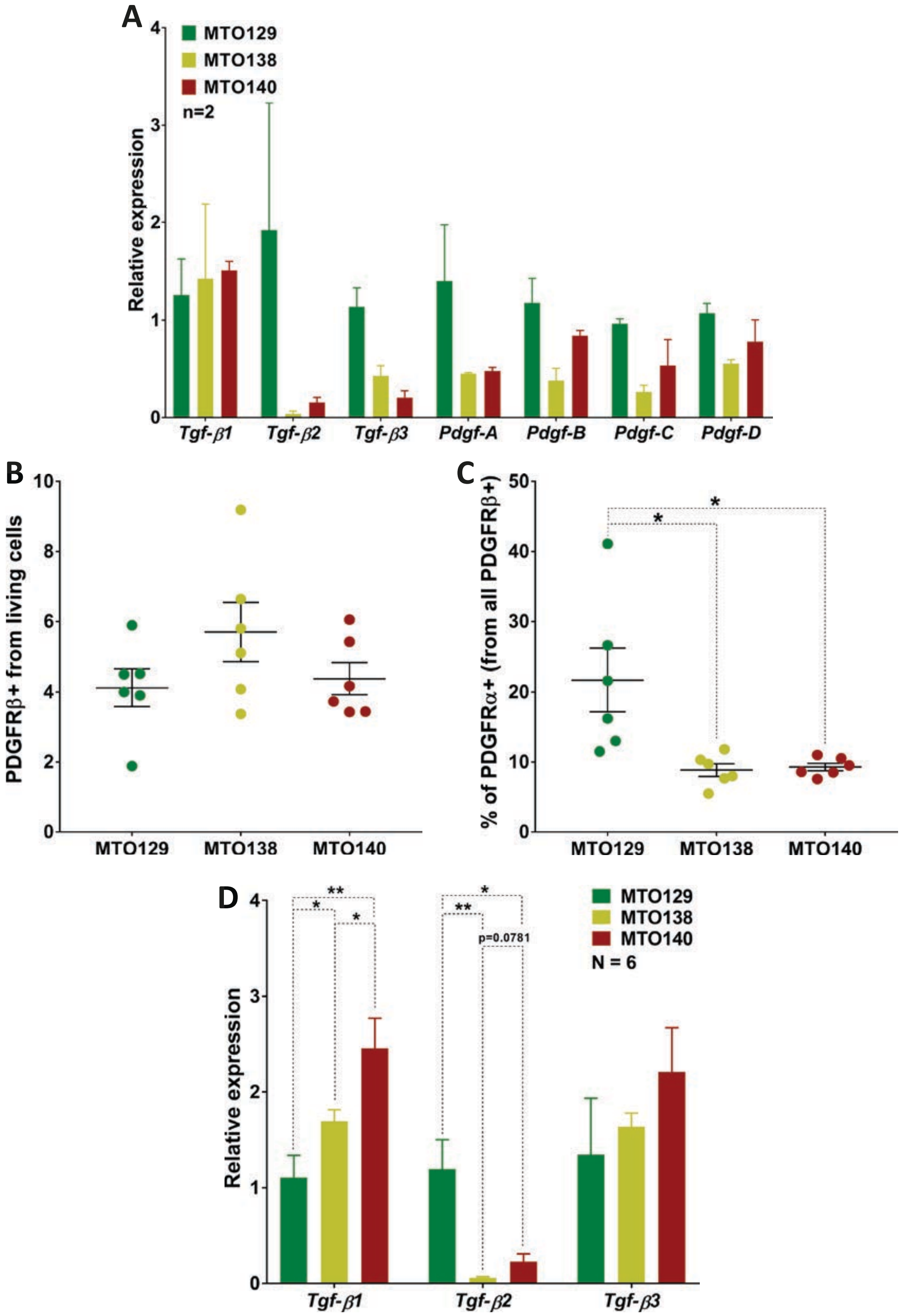

Figure 24. Metastases from different MTOs orchestrate distinct stromal compositions. A. Relative expression of *Tgf-β* and *Pdgf* isoforms by RNAseq analysis of the indicated MTOs grown *in vitro*. Two replicates were used for each MTO. Bars in represent standard deviation. **B.** Percentage of total PDGFRβ+ CAFs in dissected metastasis generated by the indicated MTOs analysed by flow cytometry. **C.** Abundance of α^+/β^+ CAFs in the same metastases. Results are represented as percentage of PDGFRα expression within total PDGFRβ+ CAFs. Averages and SEM are shown. **D.** Relative expression of *Tgf-β1*, *-β2* and *-β3* from bulk tumour mRNA. 6 replicates were used for each MTO. Bars represent SEM. Unpaired t test was performed in **C** and **D**. * = p-value < 0.05, ** = p-value < 0.01.

sion differences remained unaltered (**Figure 24D**). Overall, these data suggest that CAF composition differs depending on the MTO of origin, which in turn influences the overall TGF-β environment. Specifically, this may indicate that α⁻/β⁺ CAFs, which are more abundant in MTO138- and MTO140-derived metastases, are linked to higher *Tgf-β1* and *-β3* expression.

2.5 Variation of the tumour immune landscape in tumours from different MTOs

In **chapter 1**, we already described immune exclusion occurring in tumours arising in the quadruple mutant genetic mouse models (**Figure 1L** from Tauriello et al., 2018). In particular, we report that density of tumour infiltrating CD3+ lymphocytes decreased over time, as tumours grow in size (**Figure 25, chapter 1**). As CAFs establish tight relationships with the

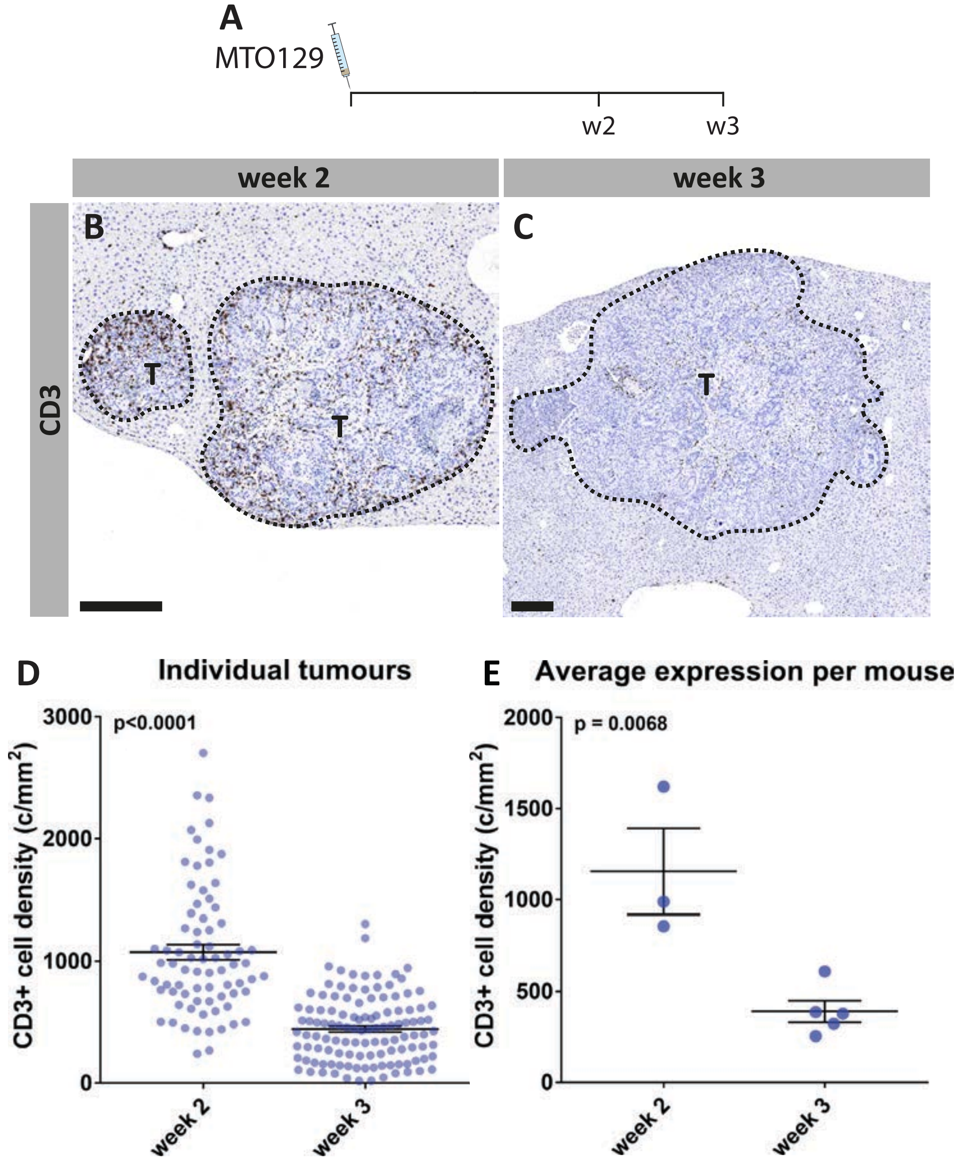
A
MTO129
w2
w3
week 2
week 3
CD3
B
C
T
T
T
D
Individual tumours
p<0.0001
CD3+ cell density (c/mm^2)
3000
2000
1000
0
week 2
week 3
E
Average expression per mouse
p = 0.0068
CD3+ cell density (c/mm^2)
2000
1500
1000
500
0
week 2
week 3

Figure 25. T cell infiltration decrease over metastatic growth. A. Experimental design. **B-C.** Representative IHC images showing DAB staining of CD3+ T cells in histological sections from liver metastasis generated 2 weeks (**B**) and 3 weeks (**C**) after MTO129 transplantation. T = tumour. Scalebars = 250 µm.**D.** Density of CD3+ cells represented as number of positive DAB detected cells per mm^2 of the region of interest (ROI) delimiting metastatic nodules. Each dot represents a single nodule. 30 nodules on average were quantified for 3 (week 2, left) and 5 mice (week 3, right). **E.** Average CD3+ density per mouse relative to **D**. Average and SEM is represented in **D** and **E**. Unpaired t test was performed in **D** and **E**.

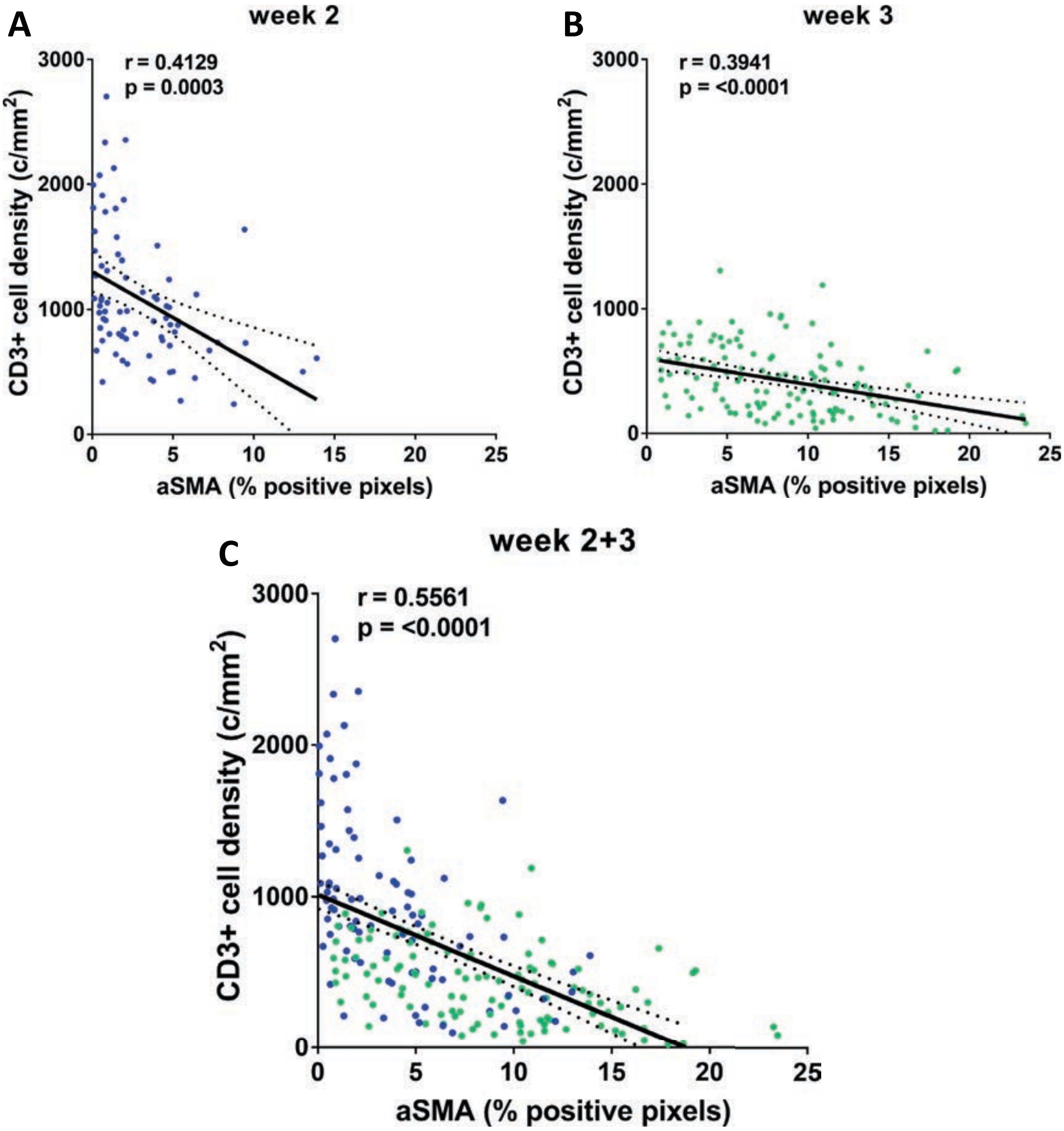

Figure 26. Abundance of myofibroblasts is negatively correlated to T cell infiltration. Correlation between αSMA+ values from **Figure 23** (**page 118**) with CD3+ density values from **Figure 25** (**page 120**). Analysis was performed for 2 weeks (**A**) and 3 weeks after tumour inoculation independently (**B**) and in combination (**C**). Regression lines are represented. Dashed lines represent 95% confidence interval. Correlation was calculated using the Pearson test in all plots.

tumour immune landscape, we next asked whether the two aforementioned CAF subpopulations in CRC liver metastasis have differential effects on anti-tumour immune responses. We counted number of T cells per area (CD3+ cell density) and assessed expression of αSMA during metastatic growth and found that the progressive decrease in T cell infiltration correlated negatively with the presence of αSMA+ CAFs (**Figure 26**) suggesting a relationship between α^-/β^+ CAF abundance and T cell exclusion.

To approach whether CAFs affected differential lymphocyte recruitment, we investigated immune mediators produced by CAFs. Analysis by qRT-PCR showed that α^+/β^+ and α^-/β^+ CAFs expressed distinct immune mediators. For instance, α^+/β^+ CAFs were relatively enriched in *IL-6*, *IL-33*, *Ccl5*, *Ccl9* and *Cxcl12* expression, whereas *Ccl12*, *Cxcl9*, *Tnf*-α and *Pd-l1* were expressed at higher levels in α^-/β^+ CAFs (**Figure 27A**). We speculated that the observed differences in cytokine production, combined with the proportions of α^+/β^+ and α^-/β^+

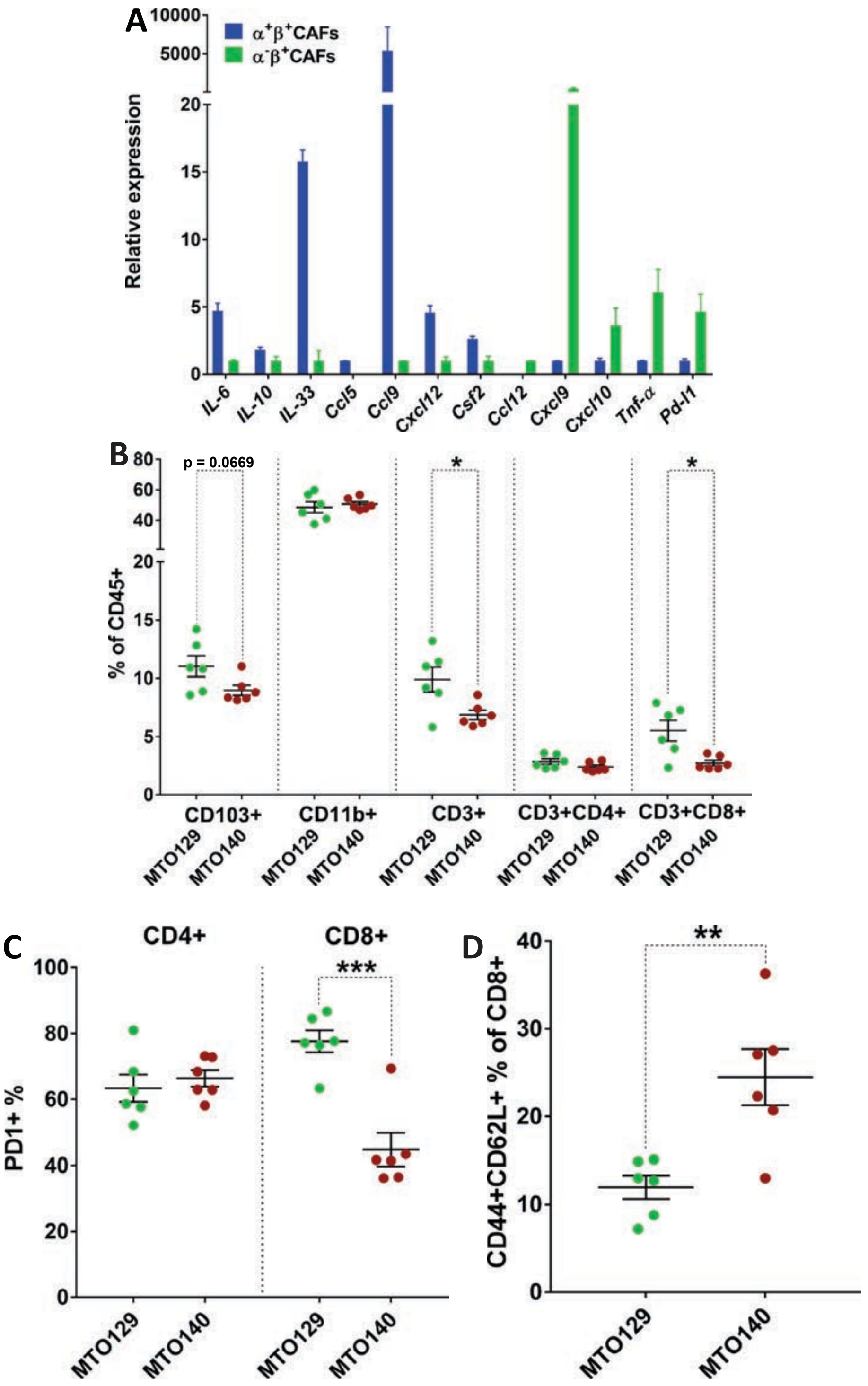

Figure 27. Distinct tumour immune microenvironment orchestrated by metastases from different MTOs. A. mRNA expression levels of the indicated cytokines in α^+/β^+ and α^-/β^+ CAFs by qRT-PCR analysis. Bars represent upper detection limits. Results are representative of 2 sample replicates. **B.** Proportion of dendritic cells (CD103+), myeloid cells (CD11b+), T cells (CD3+), helper T cells (CD4+) and cytotoxic T cells (CD8+) in metastases generated from MTO129 and MTO140 3 weeks after implantation analysed by flow cytometry. Proportions are relative to total CD45+ leukocytes. **C.** Percentage of PD-1 expressing cells within CD4+ and CD8+ T cells in same liver metastases as in (**B**). **D.** Percentage of memory CD8+ T cells (CD44+ CD62L+) in same tumours as in **B**. Averages and SEM are represented for **B-D**. Unpaired t test was performed in **B-D**. * = p-value < 0.05, ** = p-value < 0.01, *** = p-value < 0.001.

CAFs in tumours, could affect the configuration of the tumour immune landscape. Therefore, we compared metastases derived from MTO129 and MTO140, which showed the largest differences in CAF composition and overall TGF-β production (**Figure 24C-D, page 119**). A general overview showed no differences in the CD3- CD11b+ myeloid compartment, and only a slight decrease in CD3- CD103+ dendritic cells in MTO140-derived metastases compared to MTO129. The most evident differences were observed in the lymphoid compartment. MTO140-derived metastases showed a reduction in CD3+ T cells, which was associated with a decrease in CD8+ T cells (**Figure 27B**). Moreover, CD8+ cells in metastases derived from MTO140 showed lower levels of PD-1, which is expressed at the surface when T cells are activated (**Sharpe and Pauken, 2018, Figure 27C**), and a 2-fold enrichment in CD44+CD62L+ cells, which suggest a higher proportion of memory T cells (**Krishnan et al., 2007, Figure 27D**).

In parallel, we compared how T cells were located in both tumour types using IHC. To this end, we quantified CD3+ cells in the tumour margin, or in the periphery, compared to the tumour centre in histological sections. The resulting TP:TC ratio was a measure of T cell exclusion (**Figure 28A**). Lymphocytes in MTO140-derived tumours showed a strong T cell exclusion pattern (TP:TC mean ratio = 3.547), while T cells in MTO129 were randomly located in the tumour centre and tumour margin (TP:TC mean ratio = 1.423) (**Figure 28B**).

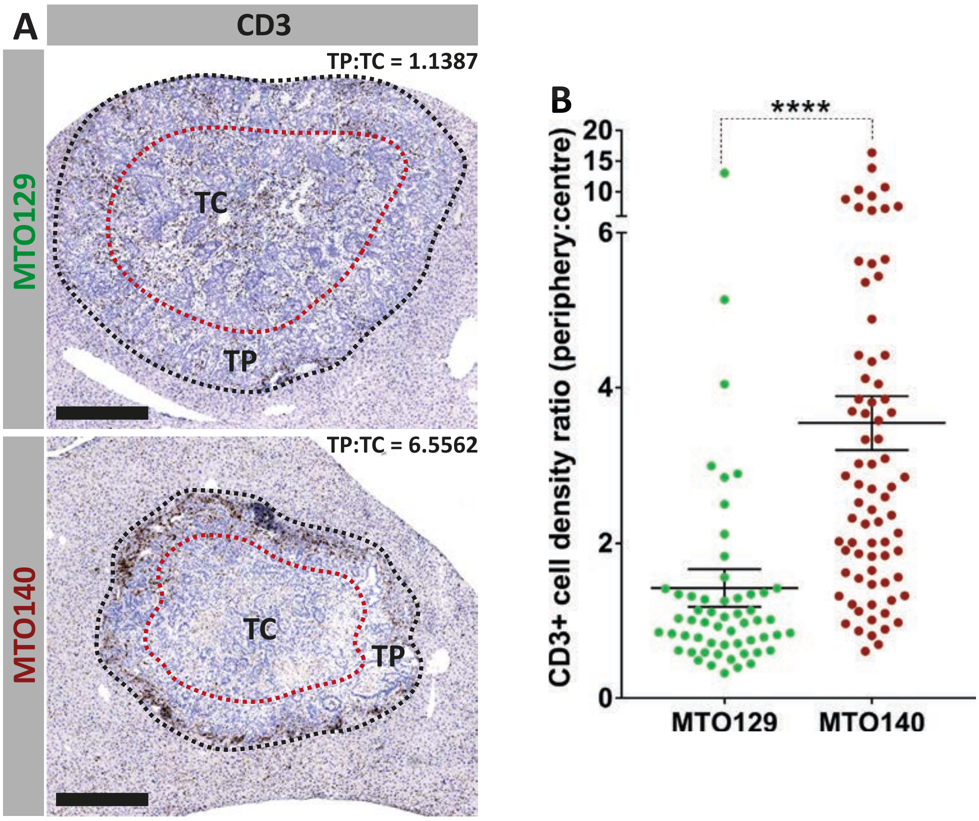

Figure 28. A. Analysis of T cell localization in metastases from different MTOs. Definition of Tumour centre (TC) and tumour periphery (TP) in representative images of liver metastases generated by MTO129 and MTO140 3 weeks after implantation. TP:TC was defined as the ratio between CD3+ densities calculated in the tumour periphery versus the tumour centre. For each representative image, the TP:TC ratio is indicated. **B.** Average T cell exclusion ratio (TP:TC) in metastases from MTO129 and MTO140. Each dot represents an individual tumour. N= 56 nodules obtained from 2 mice (MTO129, left) and 46 nodules obtained from 3 mice (MTO140, right). Averages and SEM are represented. Unpaired t test was performed. **** = p-value < 0.0001. Scalebars = 500 μm

These preliminary results indicate that tumours from different MTOs orchestrate distinct immune reactions in the TME from liver metastases and support the notion of a direct immune regulation by the CAF composition. In particular, a higher abundance of α^-/β^+ cells (i.e. in MTO140-derived metastases) correlates with increased immune repression and T lymphocyte exclusion phenotype, which apparently affects CD8+ cytotoxic T cells. These findings warrant further analysis of immune populations in distinct MTOs and functional analysis to test the role of different cytokines secreted by CAFs populations in the regulation of the immune system.

Chapter 3

TGF-β-activated CAFs are pivotal for the lack of responses to checkpoint immunotherapy in CRC

Summary

The results exposed in chapter 2 suggest a role for TGF-β-activated CAFs in shaping the tumour immune microenvironment. In this chapter, we sought genetic proof of concept by inhibiting TGF-β signalling specifically in fibroblasts. Among four different mouse CRE-deleter strains tested, we chose mice expressing the CRE enzyme regulated by the Transgelin promoter to induce specific recombination of the TGF-β receptor 2 in CAFs. We found that Tagln expression was expressed in CAFs from CRC metastasis and activated mesenchymal cells in the liver. Deletion of TGFBR2 in Tagln+ CAFs induced a non-persistent, early adaptive immune response. This immune response was enough to cure metastasic disease when genetic recombination of Tgfbr2 was combined with monoclonal antibodies against PD-L1. We conclude that TGF-β-activated CAFs are crucial for mediating tumour immune exclusion and evading checkpoint immunotherapy. Further investigations in this chapter aim to uncover the specific cellular mechanism(s) of CAF-mediated immune exclusion.

Objectives

- Establishment and optimization of a genetic mouse model for conditional recombination of the TGFBR2 in CAFs

- Analysis of the effects of TGFBR2 deletion in CAFs from CRC liver metastasis in tumour growth and CAF behaviour

- Investigation of the cellular mechanisms of TGF-β-mediated T cell exclusion upon genetic ablation of the TGFBR2 in CAFs

3.1. Identifying an appropriate genetic model for inducible fibroblast-specific Cre-loxP recombination

In CRC, TGF-β-activated CAFs are crucial mediators of tumour progression and survival (**Calon et al., 2012, 2015**). Consequently, the main challenge of this project is to dissect the role of CAFs in mediating immune responses in CRC liver metastasis due to TGF-β activation. The MTO technology developed in the Batlle Laboratory recreates the metastatic disease in syngeneic genetically modified mice. Thus, the strategy of choice was to ablate selectively the TGF-β receptor 2 in CAFs, through conditional recombination of the *Tgfbr2* floxed allele (**Levéen et al., 2002**) using the CRE-deleter system. In this system, CRE recombination enzyme is coupled to a modified Estrogen Receptor biding domain (ERT) (**Feil et al., 1996**). Upon reception of tamoxifen, a selective estrogen receptor modulator, the CRE enzyme is translocated into the nucleus and mediates specific recombination of engineered DNA regions with flanking LoxP sequences.

Fibroblasts represent a major source of extracellular matrix proteins such as Collagens. *Col1a2* encodes the production of the alpha chain 2 of type 1 Collagen, which is the most abundant Collagen form found in the extracellular matrix (**Kalluri, 2016**). On the other hand, *Pdgfrα* is defined as one of the main mesenchymal markers of fibroblasts in several homeostatic tissues (**Hayes et al., 2014**), including the liver. In **chapter 2**, we verified that all LMCs expressed *Pdgfrα*, as well as demonstrated the existence of a subpopulation of PDGFRα+ CAFs in liver metastasis (α^+/β^+). As mentioned, these might retain a proliferative potential and perhaps represent a CAF progenitor population. Hepatic Stellate Cells (HSCs) comprise the main LMC population residing in the liver parenchyma, and we and others have hypothesised that LMCs are the source of CAFs (**Iwaisako et al., 2014; Liu et al., 2015; Mederacke et al., 2013; Sekiya et al., 2016**). *Gfap* is a marker for HSCs, and *Gfap-GFP* KI mice show nuclear GFP expression in all HSCs in the liver (**Scholten et al., 2010**). Based on these findings, we chose genetically modified mouse models whose *Cre*^{ERT2} expression was controlled by the fibroblast-specific promoters for *Col1a2*, *Pdgfrα* and *Gfap* (**Ganat et al., 2006; Rivers et al., 2008; Zheng et al., 2002**).

Prior to investigating the effects of the TGFBR2 deletion in CAFs, we tested the efficiency of the selected *Cre*^{ERT} driver lines in targeting the CAFs in liver metastases. *Pdgfrα-Cre*^{ERT2} mice were crossed with mice bearing a STOP-tdTomato conditional reporter inserted in the *Rosa26* locus. Mice expressing *Col1a2-Cre*^{ERT} and *Gfap-Cre*^{ERT2} were crossed with mice expressing the dual fluorescent mTomato/mGFP reporter (*mT/mG*) from the *Rosa26 locus*. *mTmG* mice express constitutive TdTomato in their cellular membranes. Upon activation of the CRE enzyme, the TdTomato cassette is eliminated via recombination and membrane-bound GFP becomes expressed (**Muzumdar et al., 2007**). These mice are widely used to track CRE-driven recombination *in vivo*.

MTO129 was transplanted into *Pdgfrα-Cre*^{ERT2}*; tdTomato*, *Col1a2-Cre*^{ERT}*; mT/mG*, and *Gfap-Cre*^{ERT2}*; mT/mG* mice, respectively. The background of these strains was C57BL/6J. Mice from the 3 strains were administered tamoxifen and sacrificed at 3 weeks after MTO inoculation by intrasplenic injections. Liver histological sections from *Pdgfrα-Cre*^{ERT2} mice were stained for TdTomato whereas sections from the other two mouse models were stained for GFP. After an exhaustive analysis of recombination efficiencies in all three models, we concluded that recombination of the floxed alelles was not sufficiently achieved in any of the three mouse models. *Col1a2-Cre*^{ERT} was the line showing the best recombination, yet only a minor fraction of CAFs showed GFP expression (**Figure 29A**). In marked contrast to what was reported for *Gfap-Gfp* KI mice, *Gfap-Cre*^{ERT2} mice only showed recombination in some pericytes surrounding the portal circulatory system (**Figure 29B**). No GFP staining was observed in HSCs nor in CAFs (**Figure 29B**). Remarkably, livers from *Pdgfrα-Cre*^{ERT2} mice did not show recombined cells at all (**Figure 29C**), despite recombination was effective for skin

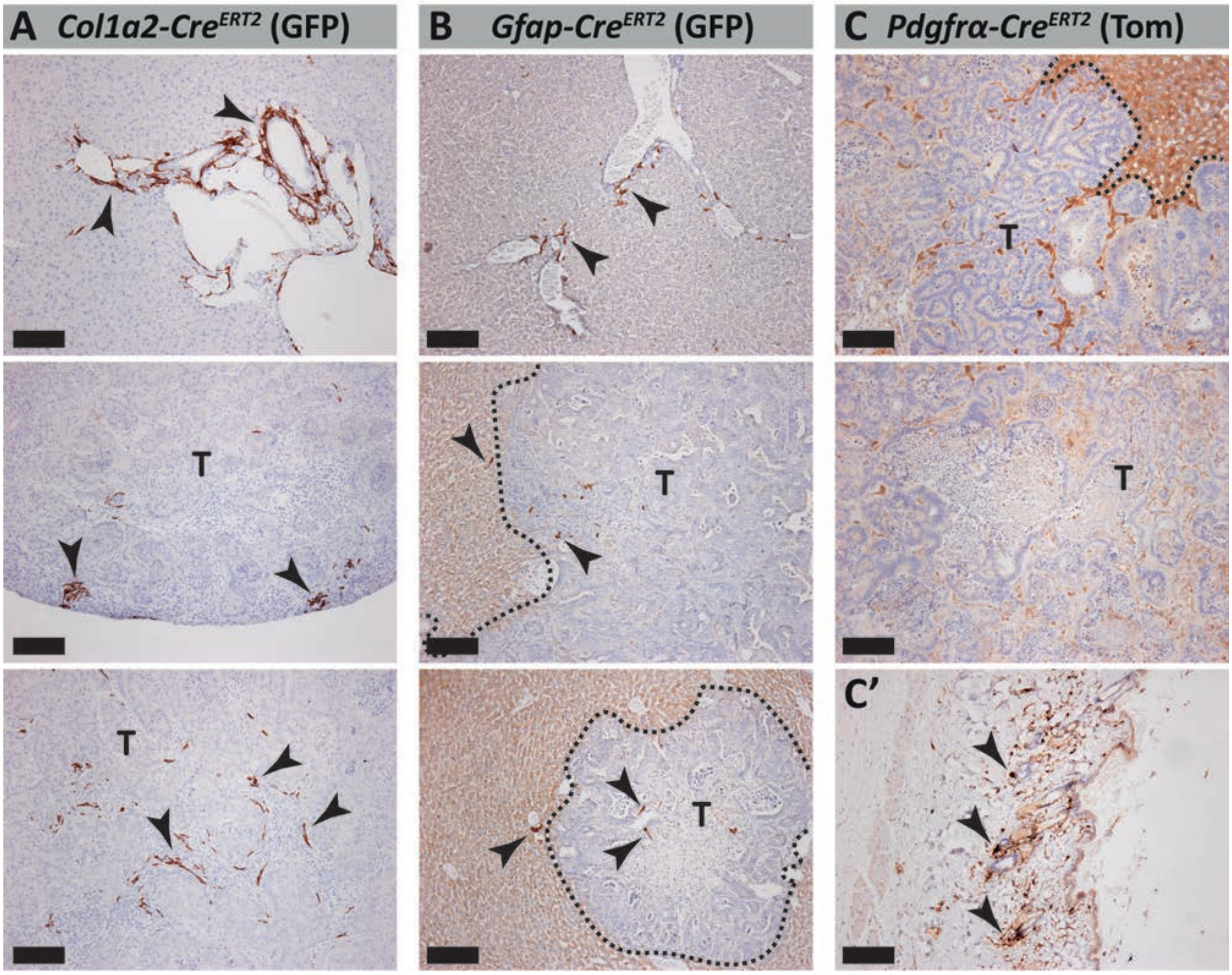

Figure 29. Analysis of CRE-mediated recombination in CAFs. A. DAB IHC staining of GFP reporter in tumours from tamoxifen-induced *Col1a2-Cre*^{ERT2} mice. **B.** DAB IHC staining of GFP reporter in liver metastases from tamoxifen induced *Gfap-Cre*^{ERT2} mice. **C.** DAB staining of Tomato reporter in tumours from tamoxifen induced *PDGFRα-Cre*^{ERT2} mice. Only background staining can be appreciated. **C'** Positive control for Tomato staining in skin sections from *PDGFRα-Cre*^{ERT2} mice. Dashed lines delineate tumour margins. Arrowheads = positive cells. T = Tumour. Scale bars = 100 µm.

fibroblasts as reported (**Driskell et al., 2013**, **Figure29C'**). Therefore, analyses of CAFs using these mouse models were discontinued.

3.2. Transgelin is a TGF-β target expressed in CAFs

The CRE-deleter mouse strains described above did not prove useful to target fibroblasts in the liver. We resorted to the human CAF expression profiles previously generated in the laboratory from CRC samples (**Calon et al., 2015**). Amongst the top genes expressed specifically in CAFs (FAP+) compared to leukocytes (CD45+), tumour cells (EPCAM+) and endothelial cells (CD31+), we identified Transgelin (*TAGLN*, **Table 1, Figure 30A**). TAGLN is an actin-associated protein with roles in smooth muscle development and is expressed in CAFs from several tumours (**Assinder et al., 2009**). TAGLN in CAFs induces Matrix Metaloprotease 2 production (MMP2), which in turn enhances tumour motility by ECM degradation (**Yu et al., 2013**).

Table 1. Top 40 upregulated genes expressed in FAP+ CAFs from patient CRC samples (Calon et al., 2015). P values and Fold-change (F-CHANGE) compare Gene expression of FAP+ cells with CD31+, CD45+ and EPCAM+ cells. *TAGLN* is highlighted in red.

SYMBOL	GENE TITLE	P-VALUE	F-CHANGE
COL3A1	Collagen, type 3, alpha 1	$3.85 \cdot 10^{-16}$	264.824
COL1A1	Collagen, type 1, alpha 1	$5.92 \cdot 10^{-18}$	242.931
COL1A2	Collagen, type 1, alpha 2	$2.96 \cdot 10^{-20}$	202.704
LUM	Lumican	$1.25 \cdot 10^{-20}$	146.325
DCN	Decorin	$2.03 \cdot 10^{-20}$	133.728
CTSK	Cathepsin K	$4.68 \cdot 10^{-19}$	90.1717
C1S	Complement component 1, s subcomponent	$8.43 \cdot 10^{-21}$	84.2331
THBS2	Thrombospondin 2	$2.42 \cdot 10^{-18}$	76.7825
COL5A1	Collagen, type 5, alpha 1	$1.86 \cdot 10^{-15}$	75.6144
COL6A3	Collagen, type 6, alpha 3	$5.85 \cdot 10^{-16}$	71.4269
ANTXR1	Anthrax toxin receptor 1	$3.67 \cdot 10^{-17}$	69.1553
CXCL14	Chemokine (C-X-C motif) ligand 14	$1.79 \cdot 10^{-17}$	65.3497
C3	Complement component 3	$2.24 \cdot 10^{-14}$	49.6829
VCAN	Versican	$4.71 \cdot 10^{-16}$	49.5741
SFRP2	Secreted frizzled-related protein 2	$1.72 \cdot 10^{-09}$	45.4074
COL6A1	Collagen, type 6, alpha 1	$2.22 \cdot 10^{-17}$	44.8130
C1R	Complement component 1, r subcomponent	$4.64 \cdot 10^{-20}$	39.1093
POSTN	Periostin, osteoblast specific factor	$5.39 \cdot 10^{-13}$	38.2549
COL5A2	Collagen, type 5, alpha 2	$1.98 \cdot 10^{-17}$	37.7361
ADAMTS2	ADAM metallopeptidase with thrombospondin type 1, motif 2	$7.92 \cdot 10^{-16}$	36.7660
IGFBP5	Insulin-like growth factor binding protein 5	$3.10 \cdot 10^{-14}$	36.3180
CRISPLD2	Cysteine-rich secretory protein LCCL domain containing 2	$1.43 \cdot 10^{-13}$	36.0931
MXRA5	Matrix-remodelling associated 5	$2.20 \cdot 10^{-13}$	35.7596
MMP3	Matrix metallopeptidase 3 (stromelysin 1, progelatinase)	$3.98 \cdot 10^{-11}$	34.0229
ISLR	Immunoglobulin superfamily containing leucine-rich repeat	$1.56 \cdot 10^{-13}$	31.9483
CCDC80	Coiled-coil domain containing 80	$6.80 \cdot 10^{-12}$	30.9467
CALD1	Caldesmon 1	$1.38 \cdot 10^{-17}$	30.1658
TIMP2	TIMP metallopeptidase inhibitor 2	$1.02 \cdot 10^{-14}$	29.9732
CDR1	Cerebellar degeneration-related protein 1	$2.01 \cdot 10^{-15}$	29.0029
TAGLN	**Transgelin**	$\mathbf{2.57 \cdot 10^{-14}}$	**28.7278**
COL12A1	Collagen, type 12, alpha 1	$3.24 \cdot 10^{-15}$	27.6265
INHBA	Inhibin, beta A	$1.21 \cdot 10^{-12}$	26.9607
ADAMDEC1	ADAM-like, decysin 1	$3.78 \cdot 10^{-11}$	26.1050
AEBP1	AE binding protein 1	$4.82 \cdot 10^{-17}$	25.1416
GREM1	Gremlin 1	$3.99 \cdot 10^{-14}$	24.8750
COL8A1	Collagen, type 8, alpha 1	$4.03 \cdot 10^{-15}$	24.8640
CHI3L1	Chitinase 3-like 1 (cartilage glycoprotein-39)	$5.35 \cdot 10^{-08}$	24.2195
MMP1	Matrix metallopeptidase 1 (interstitial collagenase)	$2.31 \cdot 10^{-09}$	23.3814
DKK3	Dickkopf 3 homolog	$2.82 \cdot 10^{-13}$	23.1309
SERPINF1	Serpin peptidase inhibitor, clade F	$7.47 \cdot 10^{-15}$	23.0962

We found *TAGLN* expression enriched in CRCs classified as CMS4 (**Figure 30B**), which comprises tumours with high levels of *TGF-β* and a prominent stromal infiltration (**Guinney et al., 2015**). Furthermore, patients with tumours classified as CMS4 have worse prognosis (**Guinney et al., 2015**). In accordance with these observations, and with previous observations from the Batlle lab (**Calon et al., 2015**), we found that stage I-III CRCs with high levels of *TAGLN* exhibit a poor clinical outcome, i.e. increase risk of relapse after therapy (**Figure 30C-D**).

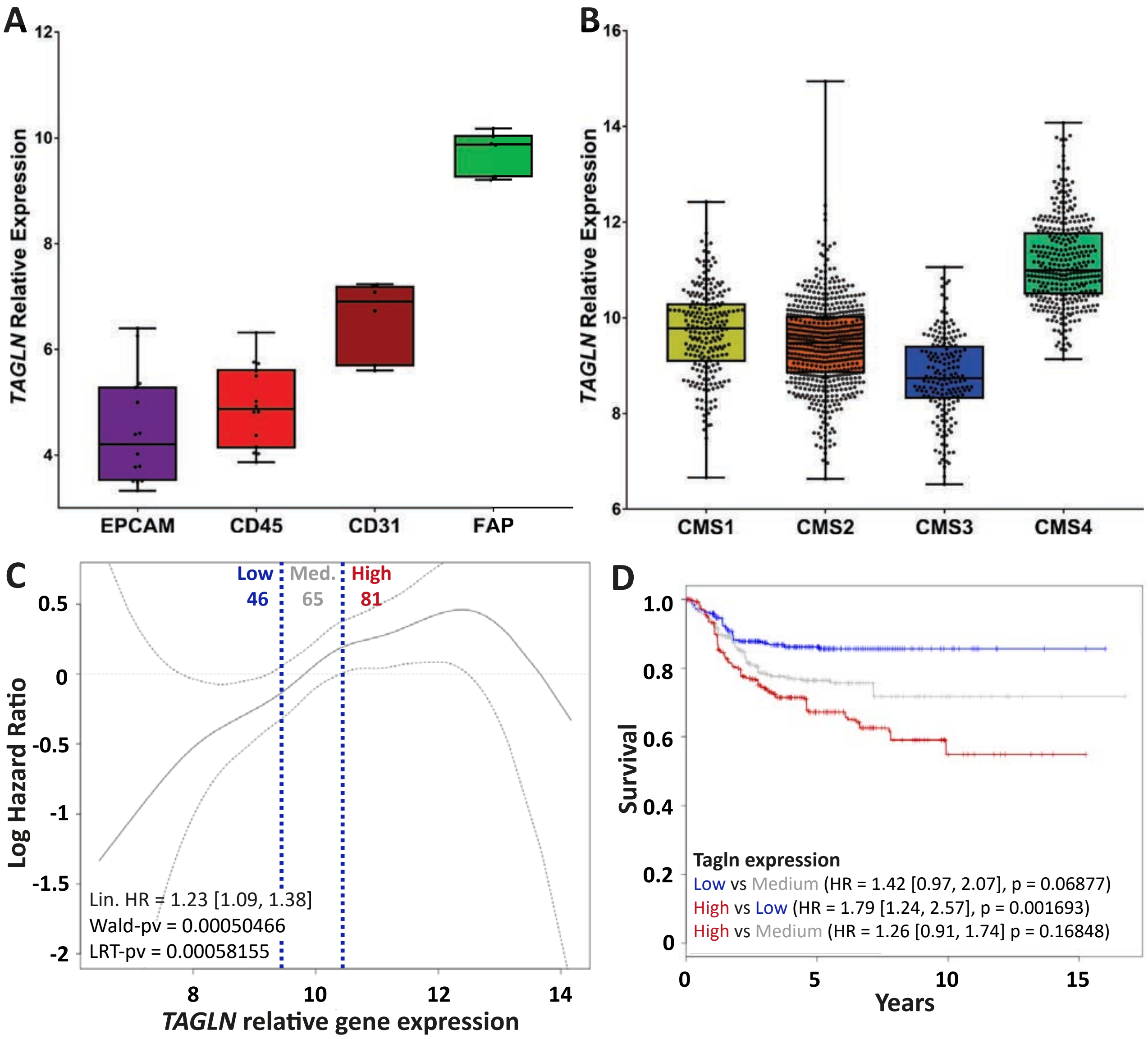

Figure 30. *TAGLN* expression in CAFs predicts poor prognosis in CRC patients. A. *TAGLN* expression in epithelial cells (EPCAM), endothelial cells (CD31), leukocytes (CD45) and CAFs (FAP) sorted from patient-derived CRC samples. Microarray Data from **Calon et al., 2015**. **B.** *TAGLN* expression accross all CMS defined by Guinney and colleagues (**Guinney et al., 2015**). **C.** Smooth function correlating *TAGLN* mRNA expression with relative risk of recurrence in MSS CRC patients. Non-primary tumours were excluded from this analysis. Black dashed lines represent 95% confidence interval. Blue dashed lines separate the threshold for patient selection. Hazard Ratio (HR) is indicated with 95% confidence interval and it represent the risk of relapse for every standard deviation in expression. **D.** Kaplan-Meier showing MSS CRC patient recurrence-free survival stratified into the three groups, which are defined in **C** by low (blue, *TAGLN* relative expression < 9.434, 46 patients), medium (grey, *TAGLN* relative expression = 9.434 – 10.453, 65 patients) and high (red, *TAGLN* relative expression > 10.453, 81 patients) *TAGLN* relative expression. HR and p values compare relapse-free survival over time according to *TAGLN* expression levels. HR are indicated with 95% confidence interval.

To validate the transcriptomic data analysed *in silico,* we examined *Tagln* expression in the MTO metastatic model. To this end, we sorted epithelilal (EPCAM+), endothelial (CD31+), immune (CD45+) and PDGFRβ+ cells from 3 liver metastases 3 weeks after injection and subsequently analysed *Tagln* expression by qRT-PCR. We observed a very large enrichment in *Tagln* expression in PDGFRβ+ CAFs compared to the other three cell populations (**Figure 31**). We also demonstrated that *Tagln* expression is upregulated in PDGFRβ+ CAFs compared to LMCs, in a similar fashion to other TGF-β target genes tested (**Figure 20A, page 115**). Moreover, both α^+/β^+ and α^-/β^+ CAF subpopulations showed similar expression levels of *Tagln* (**Figure 20C, page 115**). Altogether, these data suggest that *Tagln* could be a suitable marker to target CAFs in CRC.

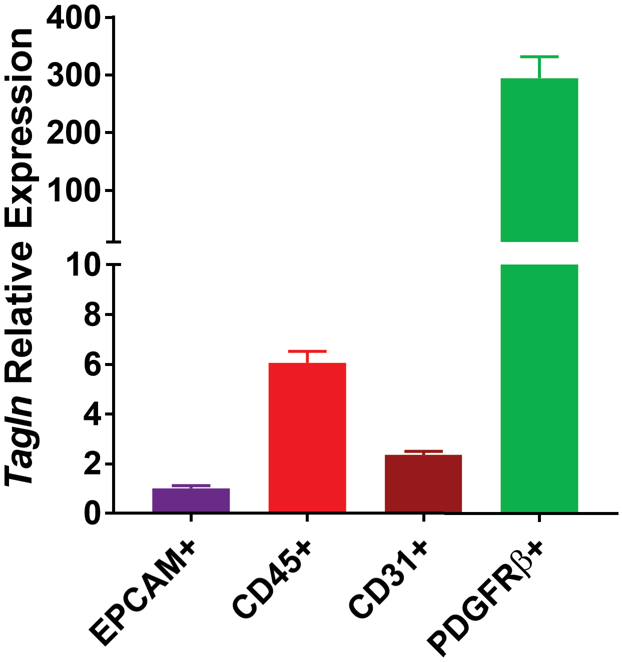

Figure 31. *Tagln* is enriched in CAFs from CRC liver metastasis in mice. *Tagln* expression in epithelial cells (EPCAM+), endothelial cells (CD31+), leukocytes (CD45+) and CAFs (PDGFRβ+) sorted from mouse liver metastasis. Bars represent upper detection limits of mRNA expression.

To confirm that *Tagln* upregulation in CAFs is mediated by TGF-β, we treated mice bearing MTO129-derived liver metastasis with the TGFBR1 inhibitor Galunisertib, by oral gavage. Treatment started at day 13 after tumour transplantation, and mice were sacrificed 3 and 8 days after treatment had started (**Figure 32A**). Histological analysis of control mice treated with vehicle showed that TAGLN expression increased over time (**Figure 32B, D-E**). However, mice treated with Galunisertib showed a significant reduction of TAGLN protein expression in CAFs, which was further downregulated after 8 days of treatment (**Figure 32C-E**).

These analyses demonstrate a very significant enrichment of *TAGLN* expression in TGF-β-activated CAFs present in patients and in the MTO metastatic model, and therefore suggest that the *Tagln* promoter could represent an attractive tool to target the TGF-β pathway in CAFs using the Cre-loxP system.

3.3. *Tagln-Cre*^{ERT2} marks TGF-β-activated CAFs from CRC liver metastasis

We obtained *Tagln-cre*^{ERT2} knocking mice from the laboratory of Robert Feil (**Kühbandner et al., 2000**) and crossed these mice with the *mT/mG* reporter strain (**Figure 33A**). Livers from naive mice treated with tamoxifen showed expression of GFP limited to pericytes surrounding the central and portal veins as well as portal arteries (**Figure 33B**). This pattern resembled that of αSMA expression in homeostasis (**Figure 17A, page 112**). We also used these mice to inoculate quadruple mutant MTOs. Treatment with tamoxifen revealed that GFP was abundantly expressed in CAFs of the tumour stroma. We also found GFP+ fibroblastic-like cells in the liver surrounding metastasis, which are likely HSCs that become TGF-β-activated in proximity to the tumour mass (**Figure 33C-D**). This finding, however, deserves further analyses.

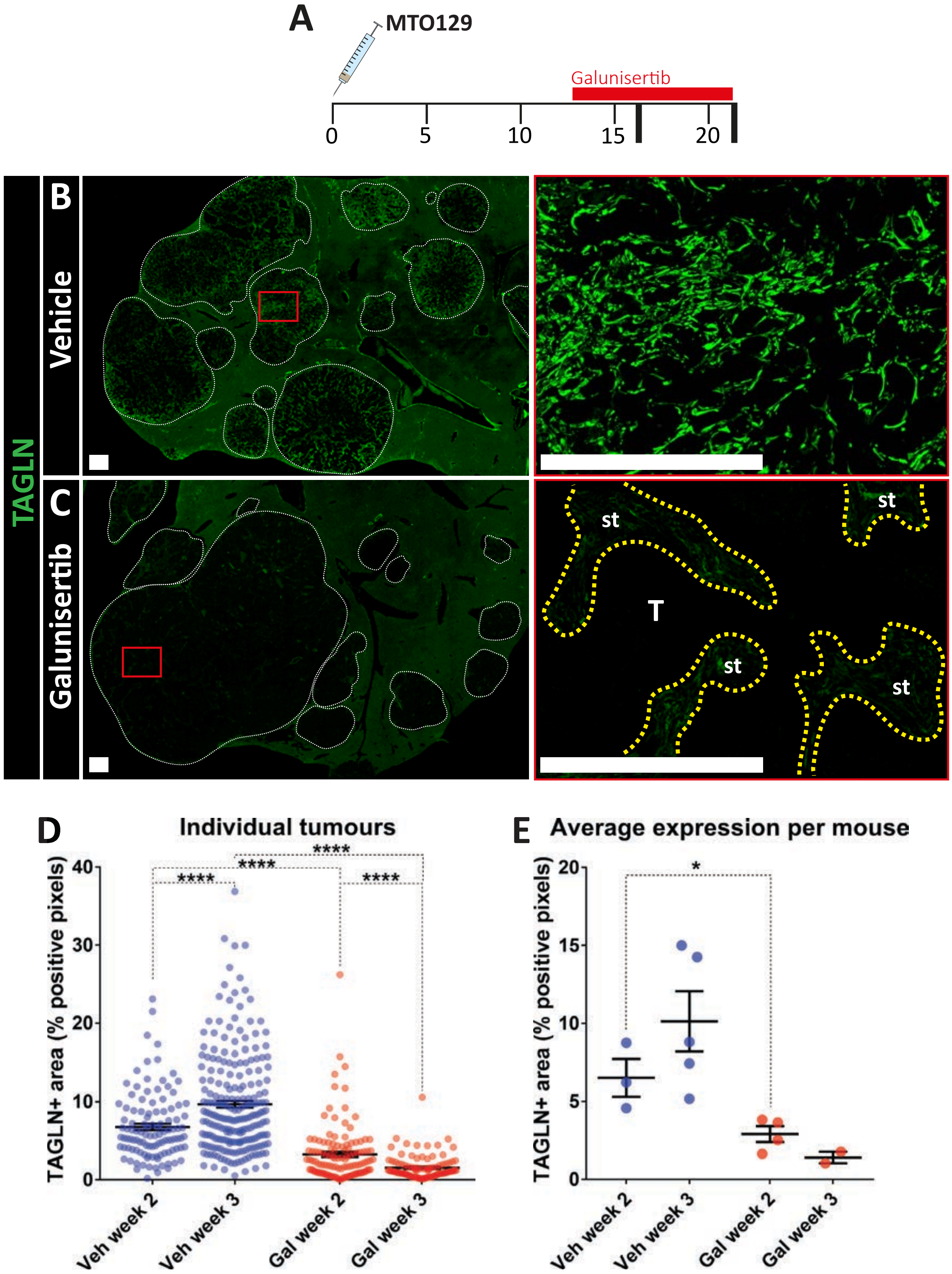
A
MTO129
Galunisertib
0
5
10
15
20
TAGLN
B
Vehicle
C
Galunisertib
st
T
st
st
st
D
Individual tumours
TAGLN+ area (% positive pixels)
0
10
20
30
40
****
****
****
****
Veh week 2
Veh week 3
Gal week 2
Gal week 3
E
Average expression per mouse
TAGLN+ area (% positive pixels)
0
5
10
15
20
*
Veh week 2
Veh week 3
Gal week 2
Gal week 3

Figure 32. TAGLN expression in CAFs decreases upon TGF-β inhibition. A. Schematic representation of experimental design. Mice were treated from day 13 after MTO inoculation with vehicle (control, Veh, blue) or Galunisertib (Gal, red) for either 3 or 8 days, and sacrificed at 16 or 21 days, respectively. **B-C.** Low (left) and high (right) magnification pictures of IF staining of TAGLN in representative liver metastases from control (**B**) and treated (**C**) mice. White dashed lines limit metastatic nodules. Yellow dashed lines separate tumour glands from the stroma. St = stroma. T= Tumour gland. **D.** Percentage of TAGLN+ area represented as % of positive pixels detected within a metastatic nodule. Each dot represents a single nodule. 40 nodules on average were counted for 3, 5, 4 and 2 mice from left to right. **E.** Average of TAGLN+ area per mouse relative to **D**. Averages and SEM are represented in **D** and **E**. Unpaired t test was performed in **D** and **E**. Scale bars = 500 µm. * = p-value < 0.05, **** = p-value < 0.0001.

To confirm that GFP was exclusively expressed in CAFs, we analysed liver metastases from mice treated with tamoxifen by flow cytometry. This analysis showed that GFP+ cells overlapped with the PDGFRβ+ population, and not with either CD31+ or CD45+ stromal populations (**Figure 34A**). This finding was confirmed by immunofluorescence (IF), where recombined GFP-expressing CAFs co-localised with PDGFRβ staining, including both α^+/β^+ and α^-/β^+ CAF subpopulations described in **chapter 2** (**Figures 34B-D, Figure 35**). Furthermore, recombined CAFs showed expression of CALD1, one of the top upregulated TGF-β target genes (**Calon et al., 2015**; **Figure 34E**). qRT-PCR analysis validated that isolated GFP+ cells were enriched in *Tagln* expression (**Figure 36A**) together with other classical fibroblast markers such as *Col1a1*, *Col1a2*, both *Pdgfr* isoforms and *αSMA*, when compared to EPCAM+, CD31+ and CD45+ populations (**Figure 36B**). Furthermore, *Cre* mRNA expres-

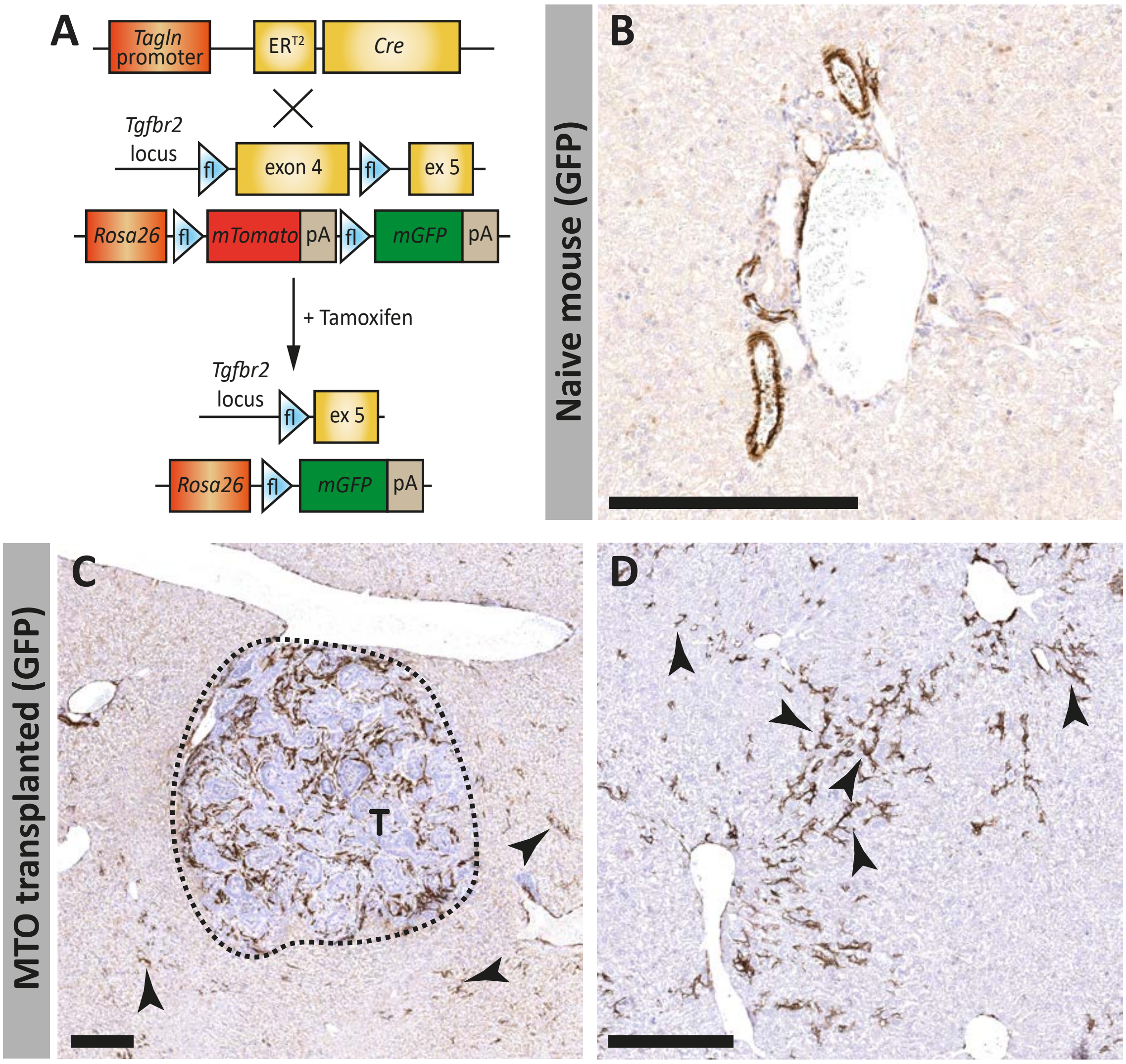

Figure 33. Analysis of CRE-mediated recombination in CRC liver metastases from *Tagln-Cre*^{ERT2} mice. A. Schematic representation of the *Tagln-Cre*^{ERT2}*; mT/mG; Tgfbr2*$^{f/f}$ mouse model. Mice were homozygous for the *mT/mG* dual fluorescence reporter, which expresses membrane-bound tdTomato (*mTomato*) constitutively. *tdTomato* is followed by a poli-A/stop region that prevents membrane-bound GFP (*mGFP*) from being expressed, until the floxed *mTomato* is excised by CRE-mediated recombination. Two loxP sites flank exon 4 of *Tgfbr2*. Upon tamoxifen-mediated recombination, the *Tgfbr2* gene in *Tagln*-expressing cells becomes truncated and GFP is expressed. **B.** IHC staining of GFP in naïve livers from *Tagln-Cre*^{ERT2}*; mT/mG; Tgfbr2*$^{+/+}$ mice. **C-D.** IHC staining of GFP in 2 different liver sections from *Tagln-Cre*^{ERT2}*; mT/mG; Tgfbr2*$^{+/+}$ mice transplanted with MTOs, focusing on a tumour area (**C**) and the liver parenchyma (**D**). Dashed line in **C** delineates the tumour margin. T = tumour. Arrowheads = recombined LMCs. Scalebars = 250 μm.

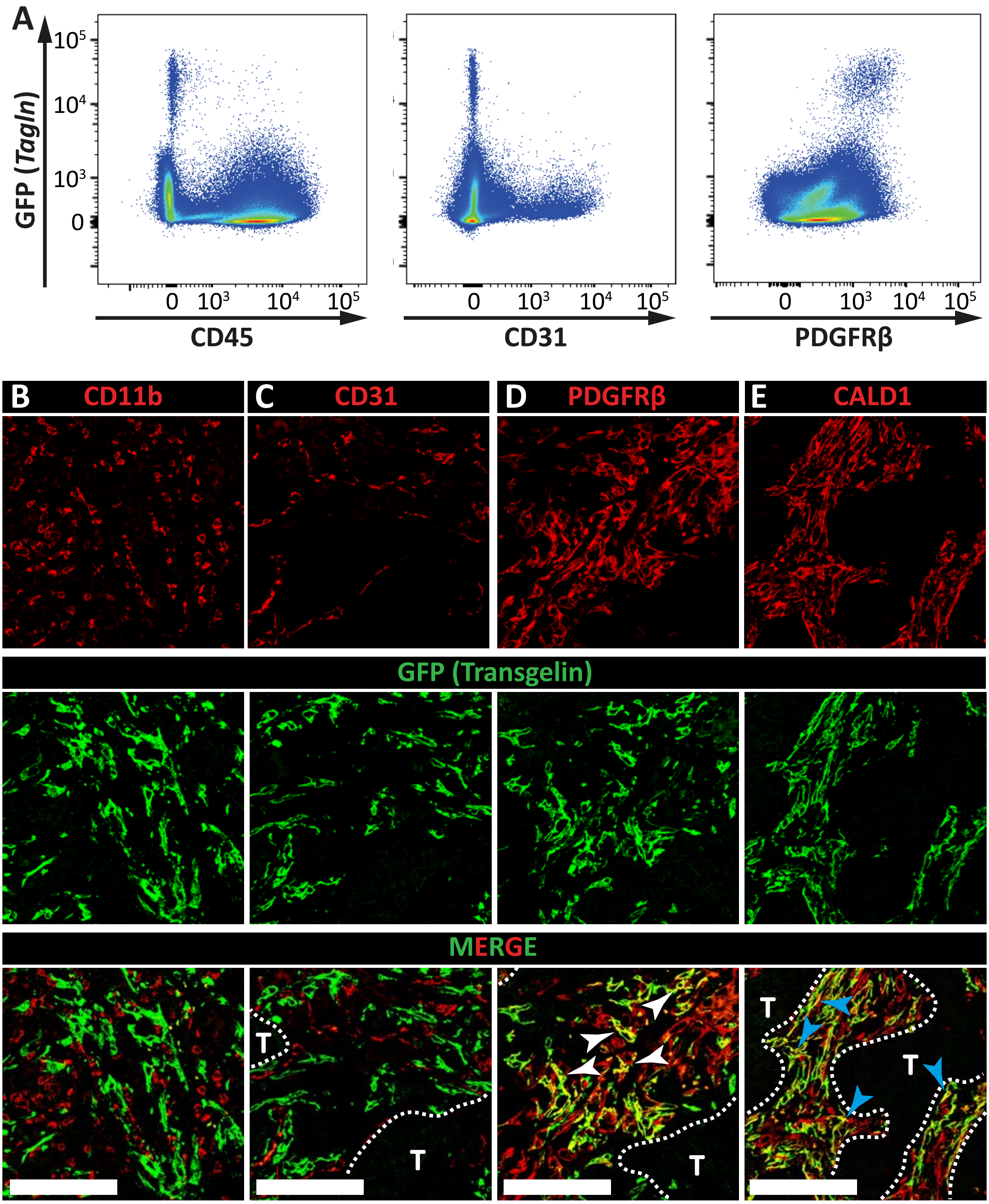
A
GFP (*Tagln*)
10^5
10^4
10^3
0
0 10^3 10^4 10^5
CD45
0 10^3 10^4 10^5
CD31
0 10^3 10^4 10^5
PDGFRβ
B CD11b
C CD31
D PDGFRβ
E CALD1
GFP (Transgelin)
MERGE
T
T
T
T
T

Figure 34. Recombination in *Tagln-Cre*^{ERT2} mice occurs in CAFs from liver metastases. A. Flow cytometry analysis of GFP fluorescence in *Tagln*-expressing cells from *Tagln-Cre*^{ERT2}; *mT/mG* mice compared to CD45, CD31 and PDGFRβ expression. **B-E.** Representative IF co-stainings of GFP from *Tagln*-expressing cells and CD11b (**B**), CD31 (**C**), PDGFRβ (**D**) and CALD1 (**E**). Dashed lines limit tumour glands (T) with the tumour stroma. White arrowheads show CAFs co-expressing GFP and PDGFRβ. Blue arrowheads show CAFs co-expressing GFP and CALD1. Scalebars = 200 μm.

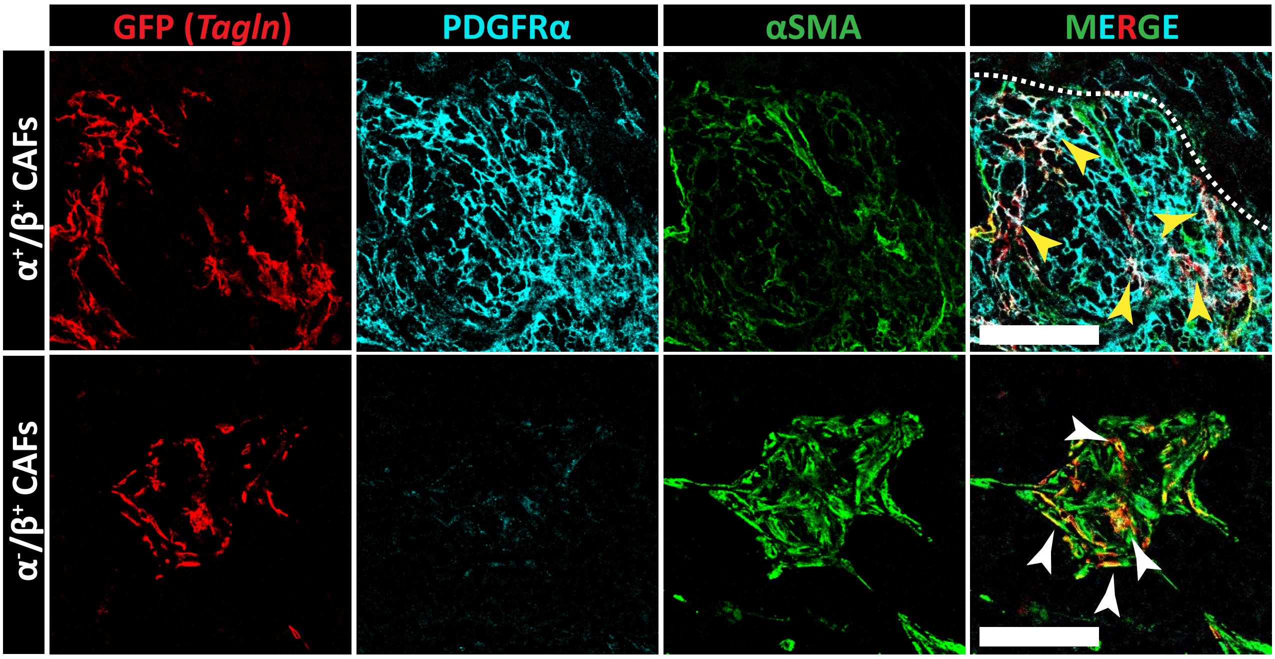

Figure 35. Both α^+/β^+ and α^-/β^+ CAFs express *Tagln*. Sections from MTO-derived liver metastasis showing IF stainings of GFP (*Tagln*), PDGFRα and αSMA. Sections are taken from one same tumour, focusing on α^+/β^+ CAFs (upper row) or α^-/β^+ CAFs (lower row). Yellow arrowheads show PDGFRα+ CAFs (α^+/β^+ CAFs) expressing GFP. White arrowheads show αSMA+ CAFs (α^-/β^+ CAFs) expressing GFP. Dashed line delineates the tumour margin. Scale bars = 100 µm.

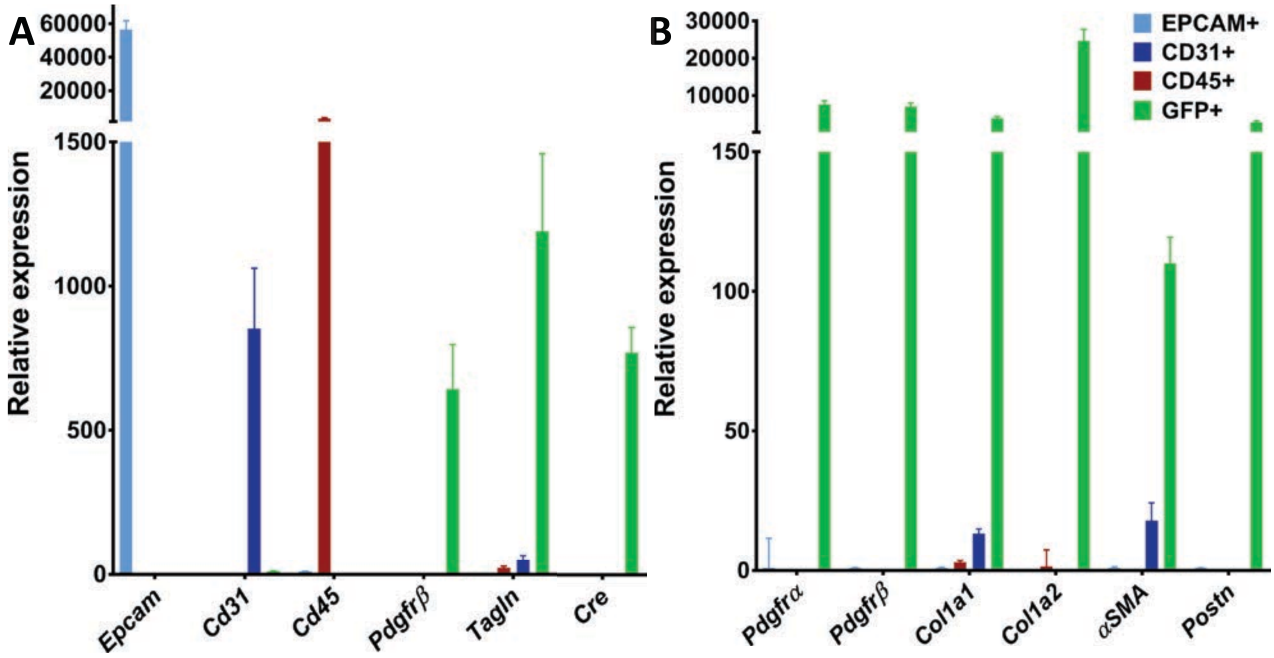

Figure 36. GFP+ cells express classical markers for fibroblasts. A. qRT-PCR analysis to control for the enrichment in mRNA expression of the indicated specific markers for each of the FACS isolated populations (GFP+ cells compared to EPCAM+, CD31+ and CD45+ cell populations). **B.** mRNA expression of fibroblast genes in GFP+ cells compared to EPCAM+, CD31+ and CD45+ cells. Bars represent upper detection limits in **A** and **B**. Plots are representative of 2 sample replicates.

sion was limited to the GFP+ population (**Figure 36A**). Therefore, we tentatively concluded that *Tagln-Cre*^{ERT2} mice represent a good genetic model to specifically target TGF-β-activated CAFs in CRC liver metastasis.

3.4. Recombination efficiency is subjected to the composition of the tumour stroma

As described in **chapter 2**, composition of CAFs in the TME differs depending on the transplanted MTO. We argued that this could influence the overall levels of TGF-β and, consequently, the expression of stromal TGF-β targets such as *Tagln*. In turn, this could affect the recombination efficacy of the *Tagln-Cre*^{ERT2} genetic mouse model.

Thus, we evaluated the mRNA expression levels of *Tagln* in tumours originated from the three MTOs used in chapter 2, namely MTO129, MTO138 and MTO140. MTO140-derived metastases expressed the highest levels of *Tagln* (**Figure 37A**). *Tagln* mRNA levels showed a positive correlation with *TGF-β1* and *TGF-β3* mRNA levels (**Figure 37B, D**), which were also higher in MTO140 metastases (please see **Figure 24D, page 119**).

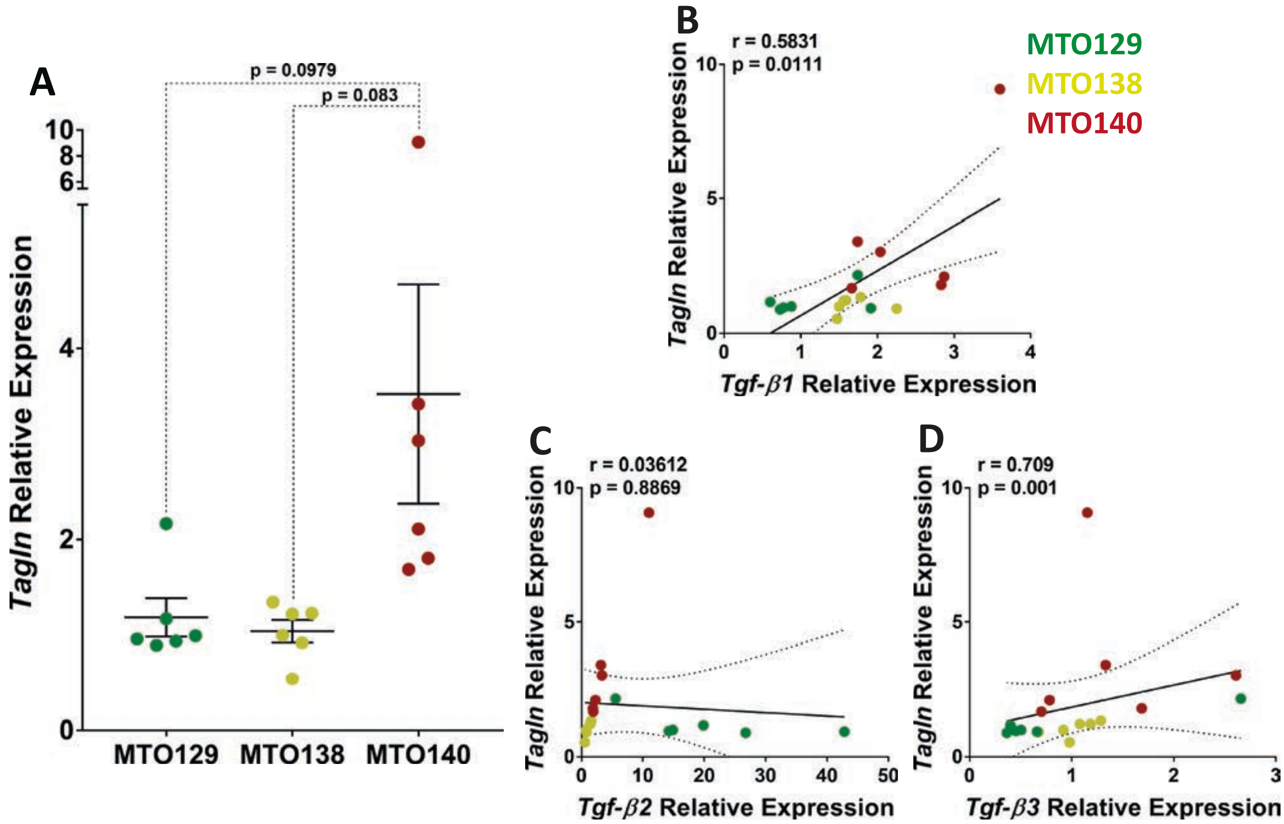

Figure 37. *Tagln* is expressed differently in metastases from different MTOs. A. *Tagln* expression in tumour bulk mRNA from MTO129 (green), MTO138 (yellow) and MTO140 (red). Average mRNA expression and SEM are represented. **B-D.** Correlation of *Tagln* expression with *Tgf-β1* (**B**), *-β2* (**C**) and *-β3* expression (**D**) reported in **Figure 24D** (**page 119**). Regression lines are represented. Dashed lines represent the 95% confidence interval. Correlation was calculated using the Spearman test.

To assess recombination efficiency, we inoculated MTO129 and MTO140 into *Tagln-Cre*^{ERT2} mice. We tested two different tamoxifen treatment regimens: 1) by administrating three doses of tamoxifen in three consecutive days, starting at day 18 after MTO inoculation (acute treatment); or 2) two doses a week starting at day 7 after MTO inoculation and until the experimental end point (long-term treatment) (**Figure 38A**). Upon sacrifice, we quantified number of GFP+ cells by flow cytometry on dissociated metastases. In both treatment options, PDGFRβ+ CAFs from MTO140-derived metastases displayed more GFP+ events compared to MTO129 (**Figure 38B-C**). Therefore, metastases generated from different MTOs will influence the recombination efficiency of our *Tagln-Cre*^{ERT2} mouse model. This effect probably depends on the overall TGF-β levels present in the TME and the differential recruitment of *Tagln*-expressing CAFs by each MTO.

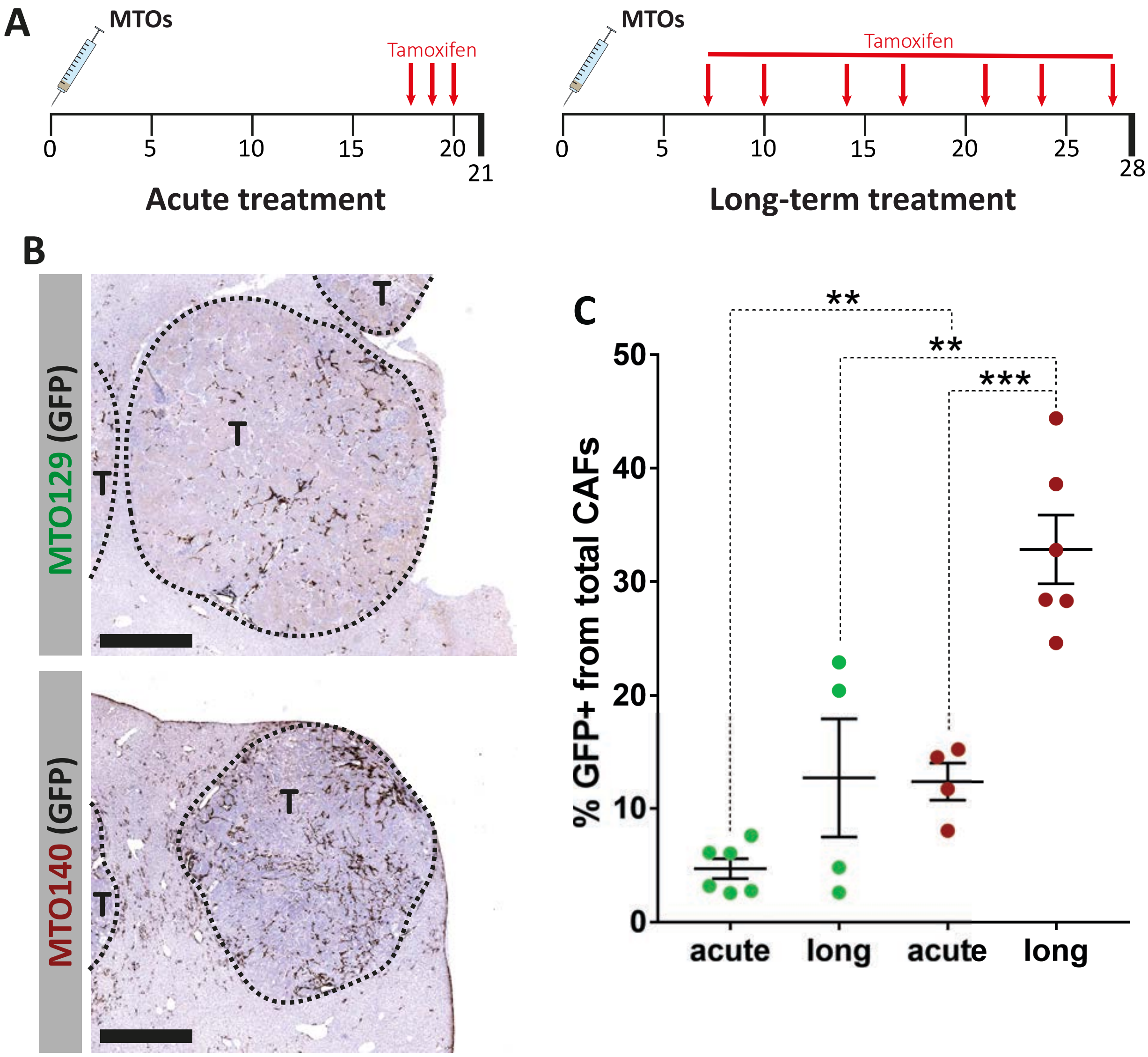

Figure 38. Recombination efficiency in CAFs from liver metastasis depends on the MTO of origin. A. Schematic representation of acute and long-term tamoxifen treatments. For acute treatment, mice were treated with tamoxifen three consecutive days, starting at day 18 after tumour transplantation, and sacrificed the day after the last administration. For long-term treatment, tamoxifen was administered twice per week, with 3-4 days of difference between each administration. **B**. Representative images of IHC staining of GFP from *Tagln*-expressing CAFs in liver metastases generated by MTO129 and MTO140. Dashed lines delineate tumour margins. T = Tumour. Scalebars = 1 mm. **C.** Proportion of GFP+ CAFs quantified by flow cytometry within total PDGFRβ+ CAFs in metastases derived from MTO129 and MTO140, using both tamoxifen treatment strategies (acute and long-term). Averages and SEM are represented. Unpaired t test was performed. ** = p-value < 0.01, *** = p-value < 0.001.

3.5. Depletion of TGFBR2 by recombination leads to a decrease of the mRNA levels of *Tgfbr2* and TGF-β target genes

To test whether the *Tagln-Cre*^{ERT2} mouse model was specifically targeting the TGFβ program functionally, we transplanted MTO129 and MTO140 into these mice and treated them with an acute tamoxifen regime as detailed in the previous section (**Figure 39A**). We then sorted un-recombined GFP- PDGFRβ+ CAFs and recombined GFP+ PDGFRβ+ CAFs, and compared them by qRT-PCR.

We compared CAFs from mice carrying at least one wild-type allele for the *Tgfbr2* (*Tagln-Cre*^{ERT2}; *Tgfbr2*$^{+/+}$ or *Tagln-Cre*^{ERT2}; *Tgfbr2*$^{+/f}$, which will be collectively termed WT or *Tgfbr2*$^{+/[+/f]}$) with mice carrying two copies of the floxed allele (*Tagln-Cre*^{ERT2}*; Tgfbr2*$^{f/f}$, termed KO). In WT mice, GFP+ PDGFRβ+ CAFs from MTO140-derived metastases reported a modest upregulation in *Tagln* mRNA levels, together with similar increases in *IL-11* and *Serpine1* (**Figure 39B**), two genes upregulated by TGF-β in CAFs (**Calon et al., 2015**, **Figure 20A, page 115**). In KO mice, however, not only *Tgfbr2* was downregulated in GFP+ CAFs, but also TGF-β target genes, including *Tagln,* exhibited decreased expression levels (**Figure 39C**).

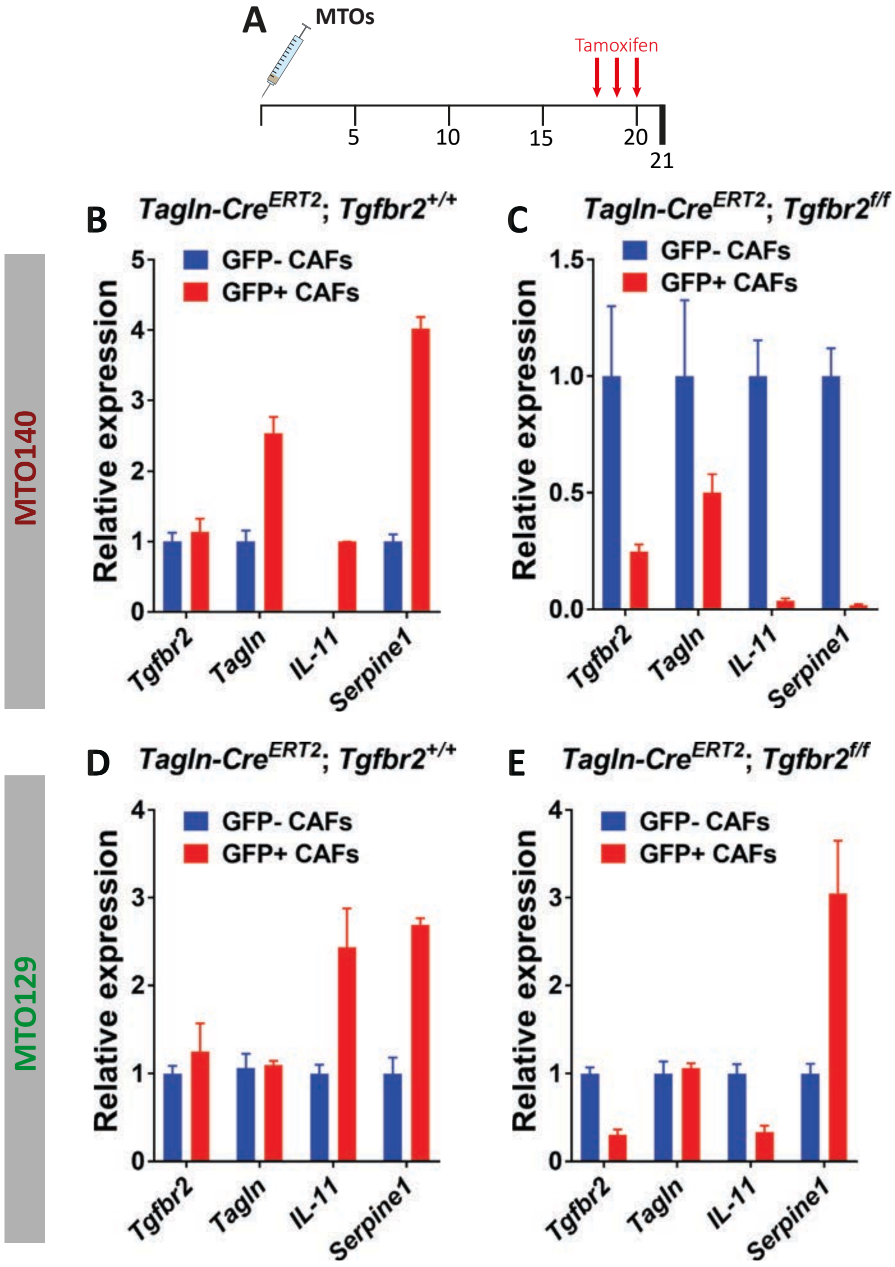

Figure 39. Gene expression analysis of CAFs with recombined *Tgfbr2*. **A.** Schematic representation of acute treatment with tamoxifen, which was applied for **B, C, D** and **E. B, B.** Comparison of *Tgfbr2* and TGF-β targets expression between GFP- PDGFRβ+ (blue) and GFP+ PDGFRβ+ (red) CAFs in WT (**B**) and KO mice (**C**) inoculated with MTO140 **D, E.** Comparison of *Tgfbr2* and TGF-β targets expression between GFP+ PDGFRβ+ and GFP- PDGFRβ+ CAFs in WT (**D**) and KO mice (**E**) inoculated with MTO129. Bars represent upper detection limits for all plots. Each plot is representative of 2 biological replicates.

On the other hand, GFP+ CAFs from MTO129-derived tumours in KO mice also displayed downregulation of *Tgfbr2* expression. However, we could not detect any obvious difference in *Tagln* expression or downregulation in TGF-β targets (**Figure 39D-E**). In conclusion, we could confirm inducible recombination of the *Tgfbr2 in CAFs* present in metastasis and shutdown of the TGF-β program, which was particularly evident in CAFs from MTO140 metastases.

3.6. TGFBR2-deficient CAFs may not thrive in the tumour stroma

In the Batlle lab, we have reported extensively that TGF-β pathway inhibition leads to downregulation of the expression of TGF-β targets expressed by CAFs in the tumour stroma (**Chapter 1, Calon et al., 2012, 2015; Tauriello et al., 2018**). However, it remains poorly characterized how does this inhibition affect CAFs functionally. We hypothesised that the apparent loss of TGF-β target gene expression may be due not only to reduced expression levels within CAFs, but could also be explained by a reduction in the number of CAFs. To address this issue, we quantified the areas stained by PDGFRβ in liver metastases in C57BL/6J mice treated with Galunisertib compared to control mice. After 3 days of Galunisertib treatment, the PDGFRβ+ stained area per metastatic nodule was significantly decreased compared to control mice (**Figure 40A-B, D**). When TAGLN expression was normalized to PDGFRβ, the differences in TAGLN expression triggered by Galunisertib treatment reported in **Figure 32E** (week 2, **page 132**) were no longer significant (**Figure 40C**), suggesting that the reduction

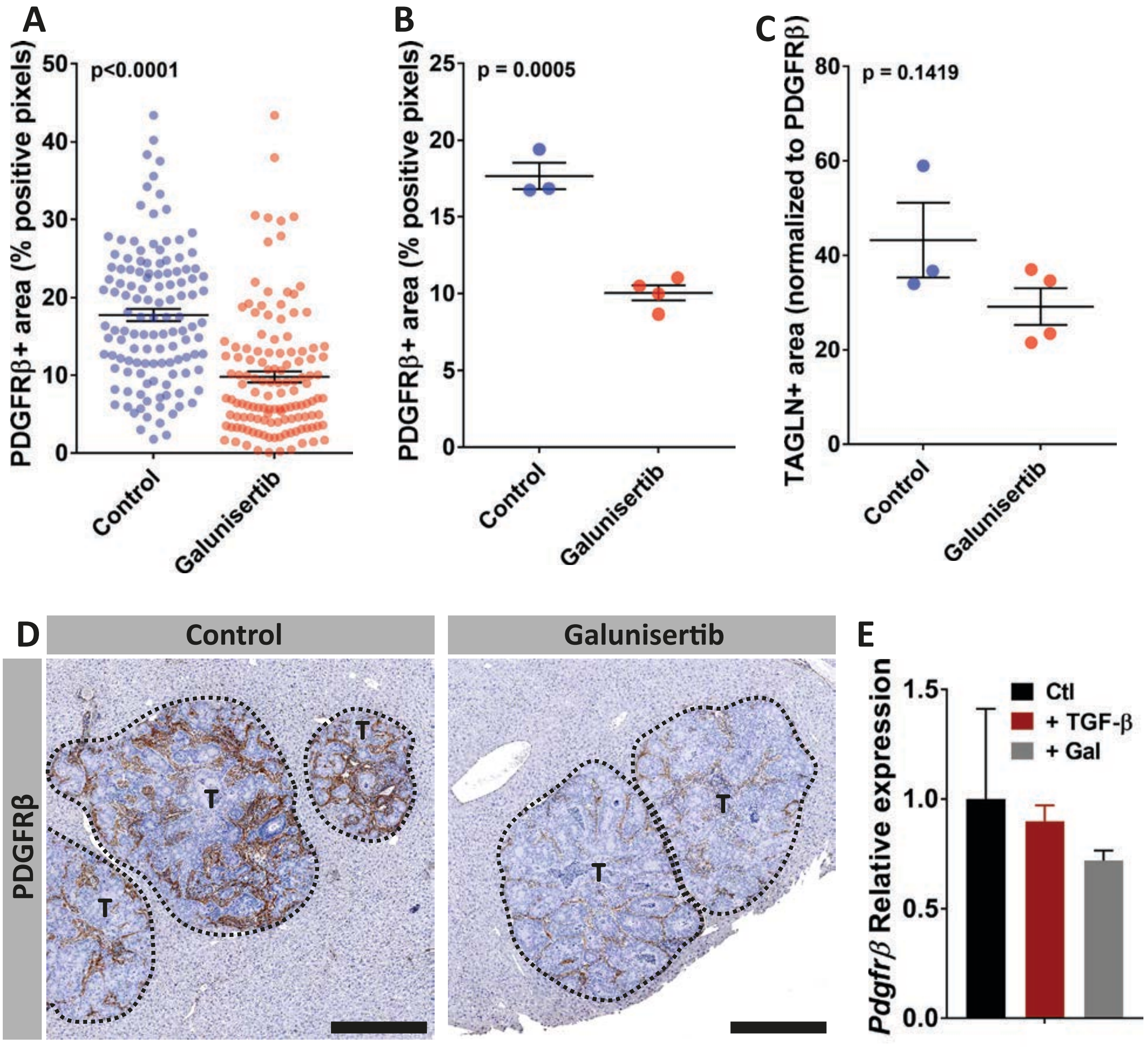

Figure 40. Total number of CAFs is reduced upon TGF-β inhibition. A. Percentage of PDGFRβ+ area represented as % of positive pixels detected within a metastatic nodule, in control mice (blue) and mice treated 3 days with Galunisertib (red). Each dot represents a single metastatic nodule. 36 nodules on average were analysed from 3 control mice and 4 mice treated with Galunisertib. **B.** Average of PDGFRβ+ area per mouse relative to **A**. **C.** Average of TAGLN+ area per mouse from **Figure 32** (**page 132**) normalized to PDGFRβ values from **A**. Unpaired t test was performed in **A-C**. **D.** Representative IHC images showing DAB staining of PDGFRβ+ CAFs at 2 weeks after MTO129 transplantation, in control mice and mice treated with Galunisertib. Dashed lines delineate tumour margins. T = tumour. Scalebars = 500 µm. **E.** mRNA expression of *Pdgfr*β in control mouse *in vitro* LMCs and treated with TGF-β or Galunisertib (Gal). Bars represent upper limits of mRNA expression. Results are representative of 2 experimental replicates.

in TAGLN expression upon inhibition treatment with Galunisertib is, at least partially, due to a reduction of total number of CAFs in the tumour stroma. Of note, PDGFRβ expression is not driven by TGF-β signalling in *in vitro* cultured fibroblast (**Figure 40E**) indicating that we can use this marker as a surrogate of CAF abundance in WT and KO mice.

We thus hypothesized that the loss of TGF-β signalling in the *Tagln-Cre*^{ERT2} genetic model may result in loss of CAFs. As described in sections **3.4** and **3.5** (**Figure 38, Figure 39, pages 137-138**), the CAF recombination strategy was most efficient in MTO140-derived metastases. Therefore, we chose this MTO to test this hypothesis. We inoculated WT and KO mice with MTO140. A group of 14 mice was treated with an acute regime of tamoxifen, whereas another group of 12 mice received long-term treatment (**Figure 41**). In both treatment conditions, the number of GFP+ from total PDGFRβ+ CAFs was reduced in KO mice compared to WT mice (**Figure 41**). Histological analysis of TAGLN expression in mice treated with long-term regime showed that KO mice expressed lower levels of TAGLN in the tumour stroma (**Figure 42**). These data point to the possibility that *Tgfbr2 KO* CAFs cannot thrive in metastases. This effect may translate into an overall downregulation of the CAF TGF-β gene program in liver metastases.

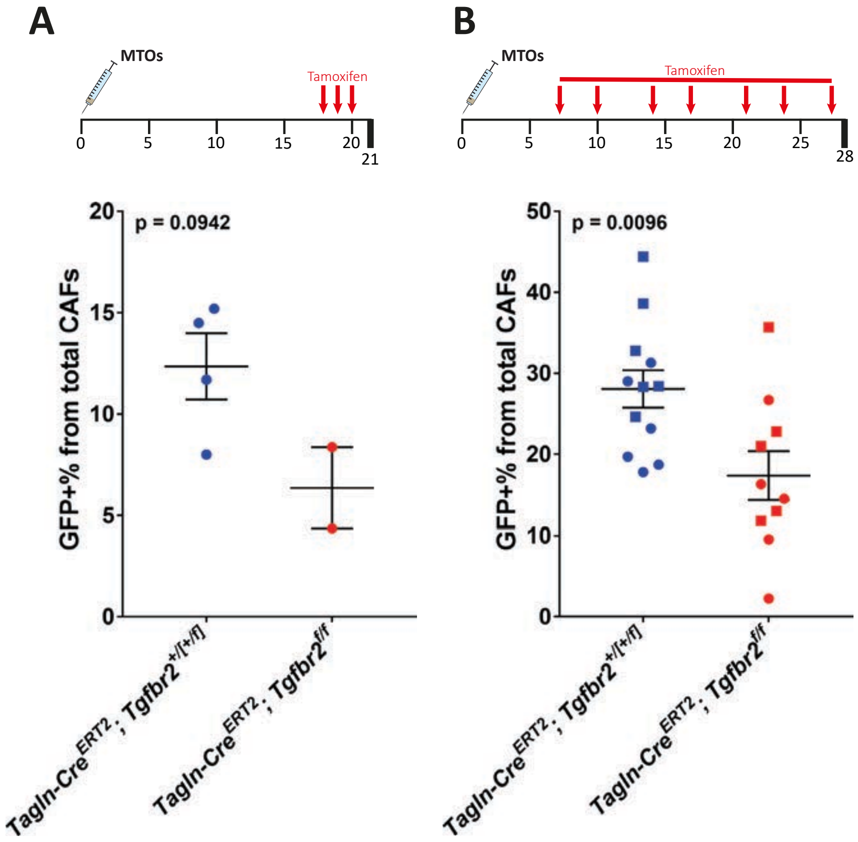

Figure 41. KO mice show a reduced number of GFP+ CAFs compared to WT mice. Percentage of GFP+ cells analysed by flow cytometry from total PDGFRβ+ CAFs in WT (blue) and KO (red) mice treated with either acute (**A**) or long-term tamoxifen regime (**B**). Two independent experiments were performed with the same conditions for long-term treatment (**B**, circles and squares). Group averages and SEM are represented. Unpaired t test was performed in all plots.

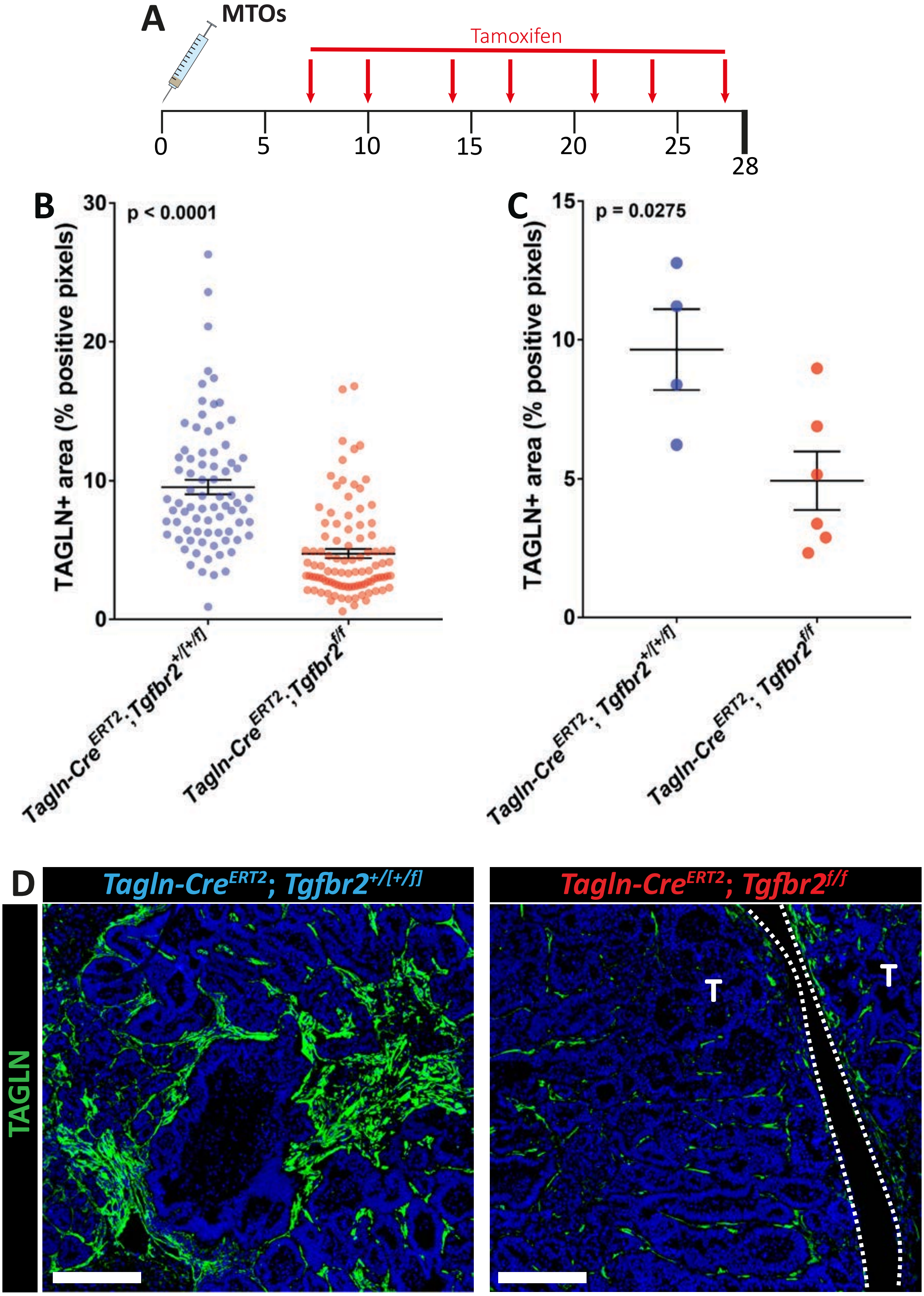

Figure 42. Overall TAGLN expression is decreased upon genetic recombination of *Tgfbr2* in CAFs. A. Schematic representation of long-term tamoxifen treatment. **B.** Percentage of TAGLN+ area represented as % of positive pixels detected within a metastatic nodule, in WT (blue) and KO mice (red) after a long-term tamoxifen treatment. 12 nodules on average were analysed from 4 WT mice and 6 KO mice (from left to right, respectively). **C.** Average of TAGLN area per mouse relative to **B**. Averages and SEM are represented in **B** and **C**. Unpaired t test was performed in **B**-**C**. **D**. Representative IF images of TAGLN expression in WT (left) and KO mice (right). Dashed lines delineate tumour margins. T = tumour. Scale bars = 250 µm

3.7. Liver metastasis burden does not decrease upon deletion of TGFBR2 in CAFs

Having defined that the *Tagln-Cre*^{ERT2} mouse model targets specifically TGF-β-activated CAFs, we next assessed the effect of TGF-β pathway ablation in CAFs on metastatic growth. We inoculated MTO129, MTO138 and MTO140 into WT and KO mice and treated them with a long-term regime of tamoxifen. MTO129 and MTO138 were previously transfected with a luciferin construct, which allows monitoring the kinetics of tumour growth *in vivo* (**Tauriello et al., 2018**). For both tumour types, there was no obvious variation in tumour burden upon tamoxifen-driven CAF recombination, except for MTO138, where KO mice showed increased tumour burden (**Figure 43**). Therefore, inhibition of the TGF-β pathway in CAFs alone does not offer a curative response by itself.

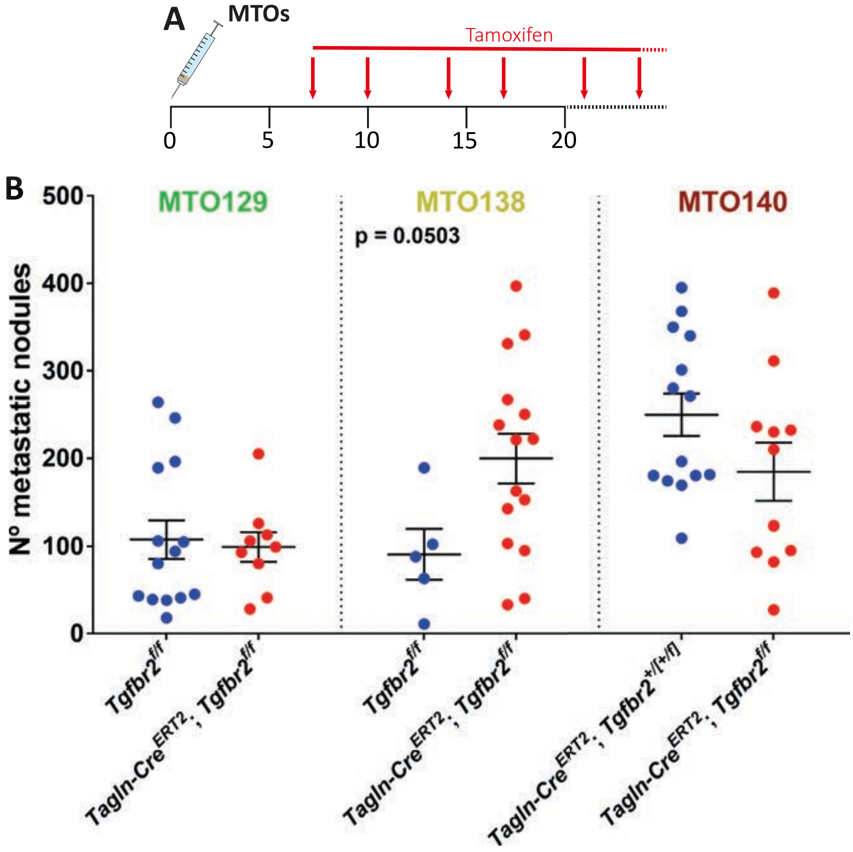

Figure 43. Metastatic burden is not decreased upon deletion of TGFBR2 in CAFs. A. Schematic representation of long-term tamoxifen treatment. **B.** Number of tumour nodules counted from livers *ex vivo* after a long-term tamoxifen treatment. WT (blue) and KO mice (red) are compared in experiments using MTO129, MTO138 or MTO140 as indicated. For MTO140, WT mice expressed CRE, while WT mice for MTO129 and MTO138 did not. N (from left to right) = 14, 9, 5, 15, 14 and 11 mice. Averages and SEM are represented. Unpaired t test was performed.

3.8. KO mice treated with blocking antibodies against PD-L1 have improved survival

In Tauriello et al., 2018, we demonstrated that combinational therapy consisting of Galunisertib and αPD-L1 antibodies induced strong curative effects on mice with established CRC liver metastases (**Tauriello et al., 2018**). Thus, we speculated that TGF-β pathway-deficient CAFs in liver metastasis synergize with anti-PD-L1 immunotherapy in a similar way as systemic pharmacological inhibition of the pathway. We therefore injected WT and KO mice with different MTOs to generate liver metastasis and treated them with tamoxifen and αPD-L1 antibodies or with IgG_2 isotype control (**Figure 44A**).

Administration of αPD-L1 antibodies to tamoxifen-treated KO animals led to fast and strong reductions in bioluminescence (tumour burden) to barely undetectable levels in a large subset of animals (**Figure 44C-E**, purple lines). This therapeutic effect was reminiscent of the dual immunotherapy of Tauriello et al. (**Tauriello et al., 2018**). At the experimental end point, KO mice that were treated with αPD-L1 antibodies presented a reduced number of liver metastases compared to the other groups (**Figure 44B, C-F**). 50% all 24 KO–αPD-L1 animals were free of visible metastasis upon sacrifice. In contrast, only 12.5% of WT animals treated with αPD-L1 had a complete response, and all other animals in the remaining arms presented with overt metastatic disease at experimental endpoint (**Figure 44G**). PDGFRβ+ CAFs sorted from KO + IgG_2 and KO + αPD-L1 mice showed decreased expression of *Tgfbr2* and *Tagln* mRNA (**Figure 44H**), confirming efficient recombination. We tentatively conclude that the curative response of dual blockade using TGFBR1 inhibitor and PD-L1 antibodies can be partially phenocopied by an ablation of the TGF-β pathway in CAFs.

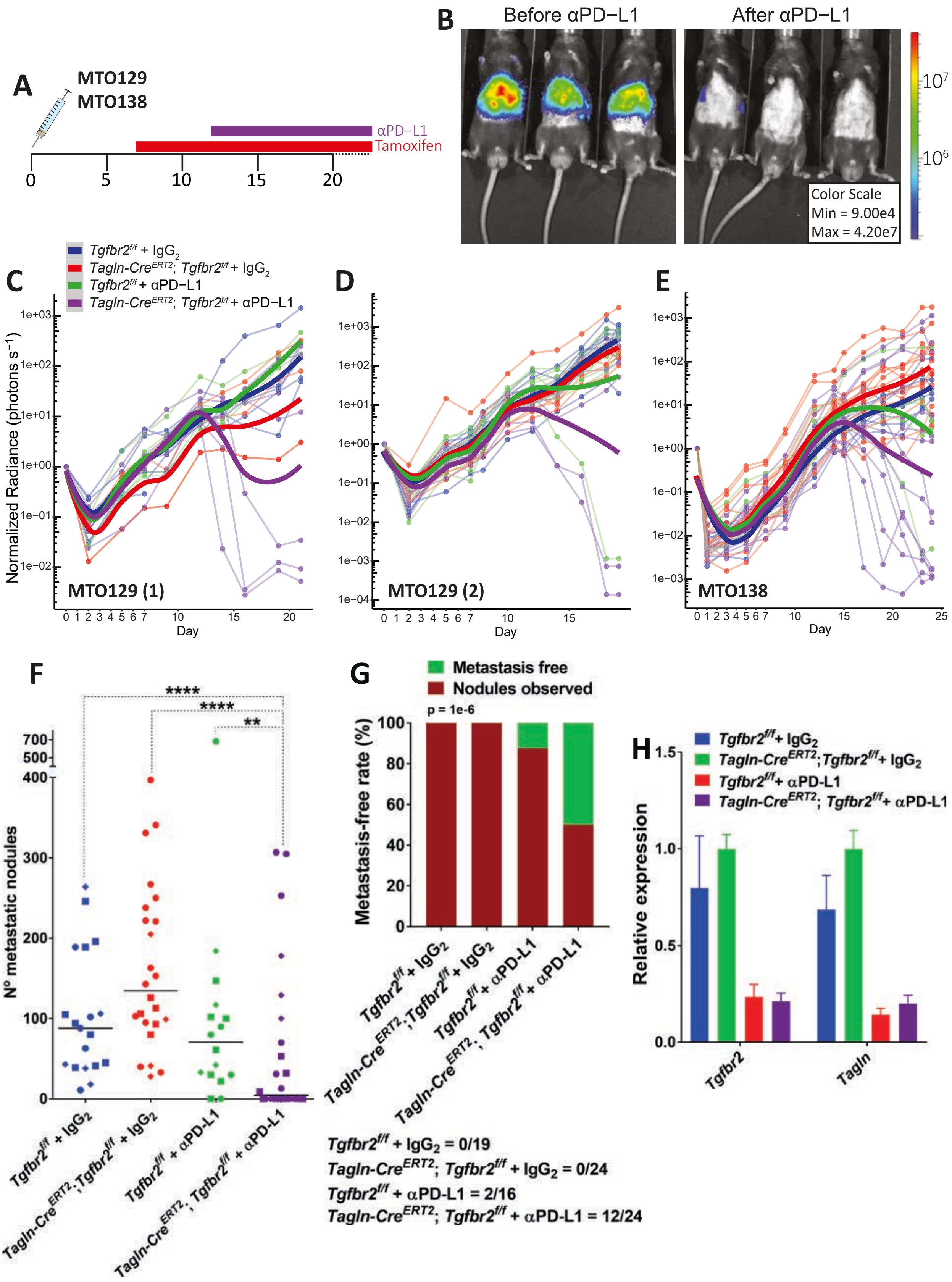

Figure 44. Combination of checkpoint immunotherapy and TGFBR2 deletion in CAFs cures metastasis. A. Schematic representation of dual therapy treatment for *Tagln-Cre*^{ERT2} mice. Tamoxifen was administered in all groups starting at day 7 after tumour transplantation in a long-term regime. αPD-L1 administration started at day 12. Control mice for αPD-L1 received IgG_2. **B.** Bioluminescence from tumours *in vivo* in KO mice before αPD-L1 administration (day 12) and after treatment (day 21). Scale represents radiance values (photons · s^{-1}). **C-E.** Bioluminescence quantification of all three experiments represented, using MTO129 (**C-D**) and MTO138 (**E**). Number of mice used for *Tgfbr2*$^{f/f}$ + IgG_2 (blue), *Tagln-Cre*^{ERT2}; *Tgfbr2*$^{f/f}$ + IgG_2 (red), *Tgfbr2*$^{f/f}$ + αPD-L1 (green) and *Tagln-Cre*^{ERT2}; *Tgfbr2*$^{f/f}$ + αPD-L1 (purple), respectively = **C**: 5, 4, 4, 6; **D**: 9, 5, 7, 5; **E**: 5, 15, 5, 13. **F.** Number of tumour nodules from all three experiments combined. Shapes represent each experiment (**C** = diamonds, **D** = squares, **E** = circles). Medians are represented. A Wald test was performed. **G.** Proportion of metastasis-free mice upon experimental end-points. Absolute numbers of cured mice are shown. A Cocchran-Mantel-Haenszel test was performed. **H.** mRNA expression of *Tgfbr2* and *Tagln* in all four conditions from the experiment represented in **C**. Bars represent upper detection limits.

A caveat of this set of experiments is that, unlike the mice strains described in **3.5** and **3.6** (**Figures 39, 41 and 42, pages 138, 140-141**), WT mice do not carry the *Cre* allele. Therefore, unlike in KO mice, *Tagln*+ CAFs were not recombined to express the GFP reporter in WT mice. This fact poses a possibility that the GFP reporter could represent a source of neoantigens that artificially enhanced immune responses in KO mice. To exclude this possibility, we repeated this experiment using Cre-expressing WT mice with at least one wild-type allele for the *Tgfbr2* as control mice (*Tagln-Cre*^{ERT2}; *Tgfbr2*$^{+/[f/+]}$), which can still express GFP in *Tagln*-expressing CAFs (**Figure 45**). When metastases generated by MTO129 were tested, only one KO mouse treated with αPD-L1 was cured. However, all mice from this group presented an improved survival rate compared to all three remaining groups (**Figure 45B**). Also, the number of liver metastases counted in these mice was reduced in a similar fashion to the previous experiments (**Figure 45C**). Importantly, survival of WT mice treated with αPD-L1 did not differ from WT and KO treated with IgG_2 (**Figure 45B**), arguing against the possibility that GFP is immunogenic in this system.

We verified this result using MTO140 to generate liver metastasis. Similar to MTO129, KO mice treated with αPD-L1 responded to treatment by showing decreased metastasis burden at experimental endpoints. Likewise, metastasis burden in WT mice treated with αPD-L1 was not altered (**Figure 46**).

3.9. Dynamics of T cell infiltration in KO mice

In **chapters 1** and **2**, we reported that immune exclusion in tumours was a dynamic process, and T cell density decreased as metastases expand in size. A simple mechanism to explain this effect is that TGF-β-activated CAFs might be required for an efficient T cell exclusion in tumours. As CAFs accumulate over time, T cell become excluded from metastasis (**Figure 26, page 121**). This effect could be reverted upon inhibition of the TGF-β pathway (Tauriello et al., 2018). We therefore explored if depletion of TGFBR2 in CAFs induces T cell infiltration. To this end, we inoculated WT and KO mice with MTO129 to generate metastasis. Groups of mice were sacrificed at days 7, 13, 21 and 28 after MTO inoculation. Tamoxifen administration started at day 7, after the first group of mice was sacrificed (**Figure 47A**). We then analysed the density of CD3+ T cells in histological sections. T cells were excluded in WT mice with a kinetics similar to what we previously reported (Tauriello et al., 2018). However, T cell infiltration remained unaltered in KO mice for all checked time points (**Figure 47B**).

To verify again that T cell infiltration was not altered by the GFP expression in recombined cells, we compared CD3+ T cell densities of WT *Tagln-Cre*^{ERT2}; *Tgfbr2*$^{+/[f/+]}$ and WT mice without Cre expression used in **3.8** (**Figure 44, page 143**). In line with the results reported

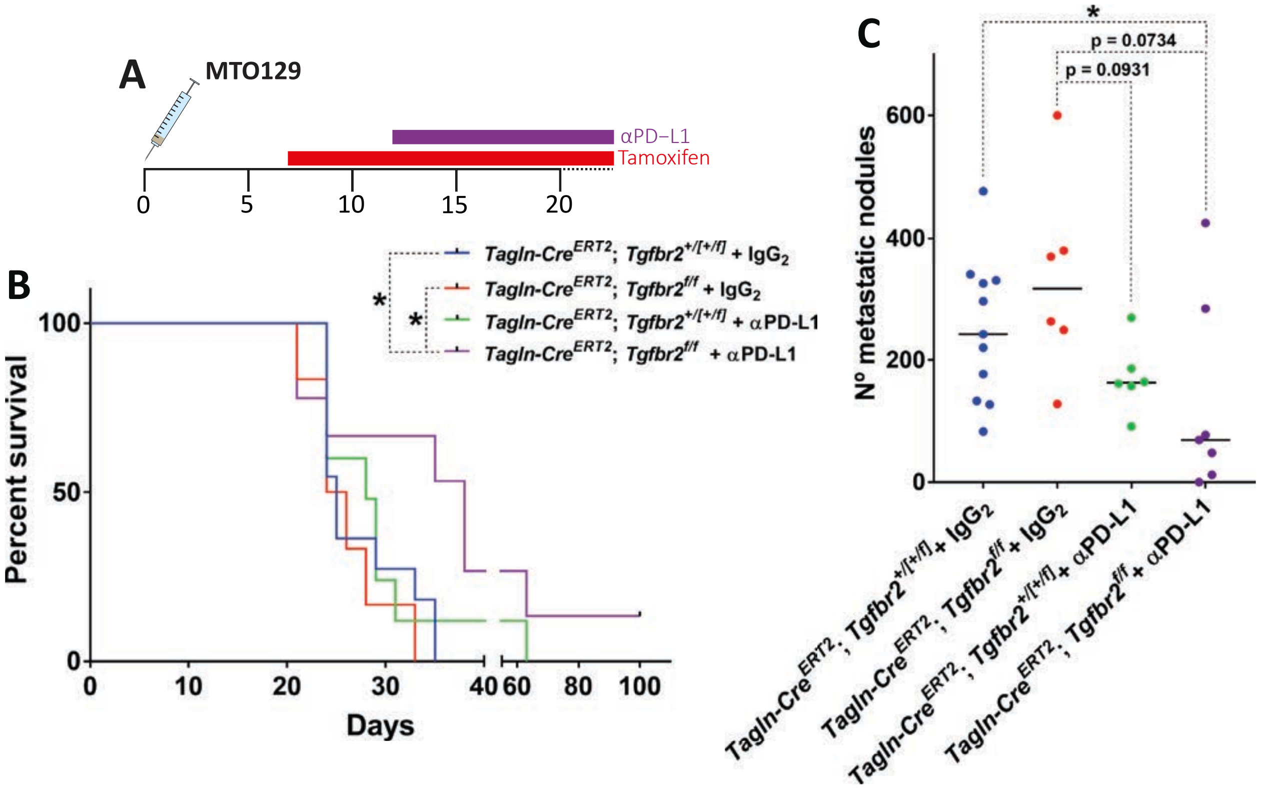

Figure 45. KO mice treated with checkpoint immunotherapy have extended survival. A. Schematic representation of dual therapy treatment for *Tagln-Cre*^{ERT2} mice. **B.** Kaplan-Meier representing disease-free survival rate of mice transplanted with MTO129. 11, 10, 6 and 9 mice were used *Tgfbr2*$^{+/[f/+]}$ + IgG$_2$ (blue), *Tgfbr2*$^{f/f}$ + IgG$_2$ (red), *Tgfbr2*$^{+/[f/+]}$ + αPD-L1 (green) and *Tgfbr2*$^{f/f}$ + αPD-L1 (purple), respectively. A Mantel-Cox test was performed. **C.** Number of tumour nodules in livers from mice after sacrifice. Tumours from 4 *Tgfbr2*$^{+/[f/+]}$ + αPD-L1 mice and 2 *Tgfbr2*$^{f/f}$ + αPD-L1 mice could not be counted after being found dead and were excluded from the analysis. Medians are represented. * = p-value < 0.05. A Mann-Whitney test was performed.

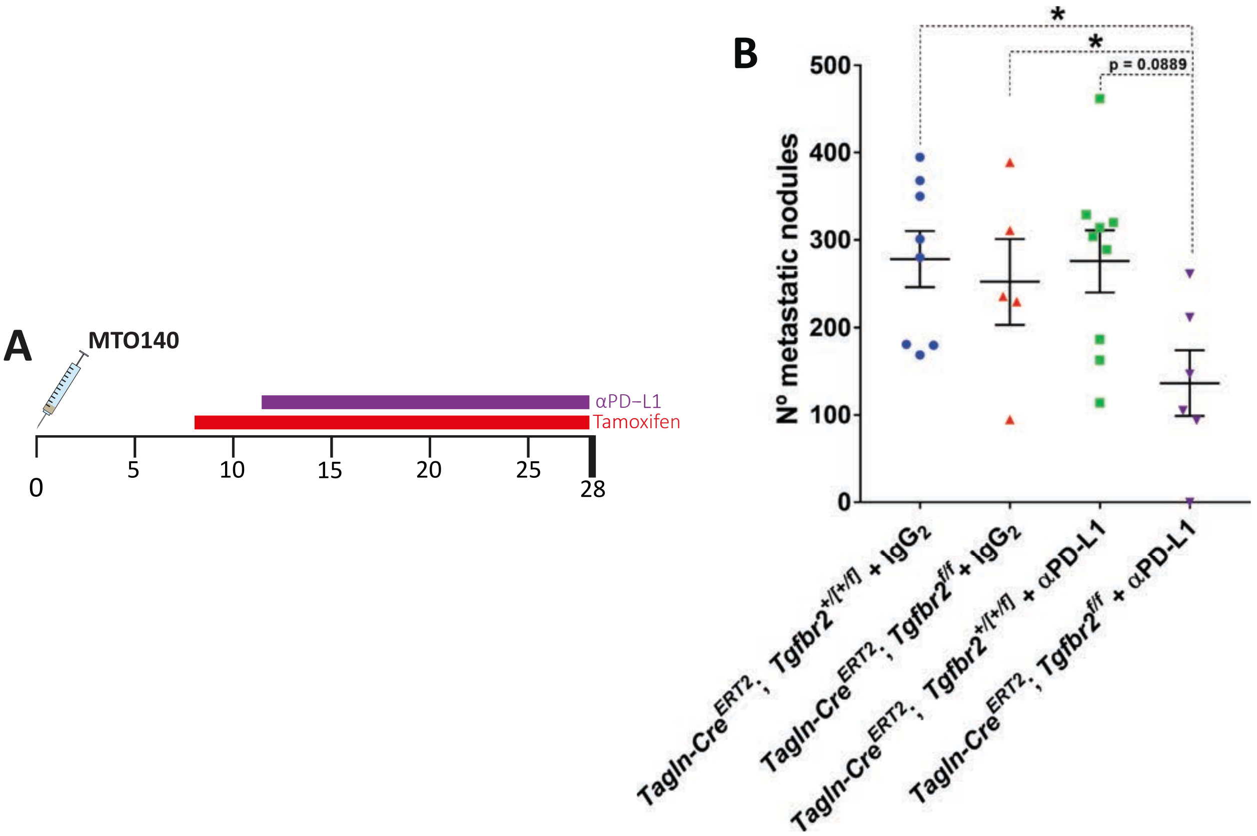

Figure 46. KO mice bearing MTO140-derived metastasis have reduced burden upon treatment with checkpoint immunotherapy. A. Schematic representation of dual therapy treatment for *Tagln-Cre*^{ERT2} mice. **B.** Number of metastatic nodules in mice transplanted with MTO140. 8, 5, 9 and 6 mice were used for *Tgfbr2*$^{+/[f/+]}$ + IgG$_2$ (blue), *Tgfbr2*$^{f/f}$ + IgG$_2$ (red), *Tgfbr2*$^{+/[f/+]}$ + αPD-L1 (green) and *Tgfbr2*$^{f/f}$ + αPD-L1 (purple), respectively. Averages and SEM are represented. * = p-value < 0.05.

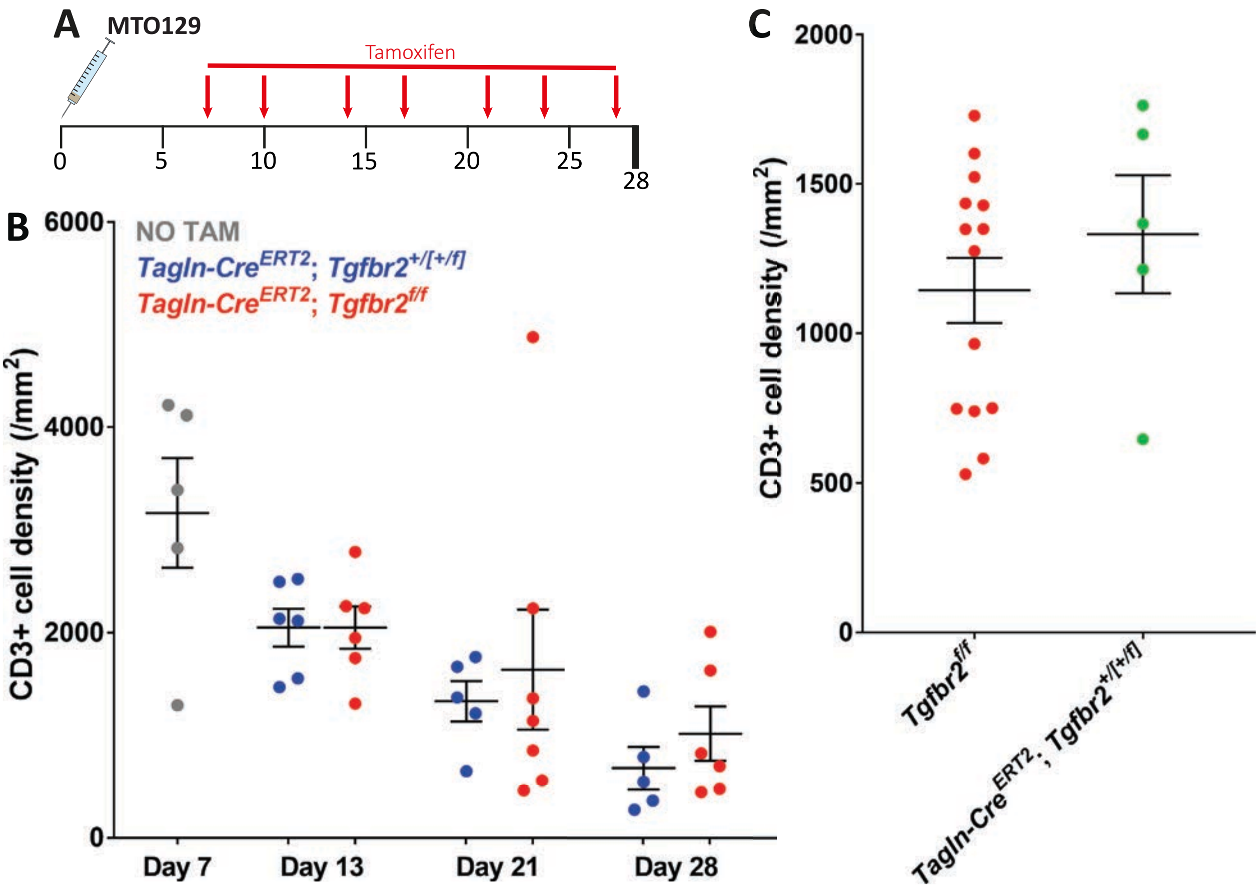

Figure 47. T cell infiltration is not altered upon TGFBR2 deletion in CAFs. A. Schematic representation of long-term tamoxifen administration. **B.** CD3+ T cell densities quantified by IHC in WT and KO mice transplanted with MTO129. Mice from day 7 were sacrificed prior to tamoxifen administration. Values are averages of all metastatic nodules counted in every mouse. 12 nodules on average were quantified from 5, 6, 6, 5, 6, 5 and 6 mice, from left to right. **B.** T cell density comparison between WT mice injected with MTO129 from **Figure 44** (*Tgfbr2*$^{f/f}$) and WT mice from **A** at day 21 (*Tagln-Cre*^{ERT2}; *Tgfbr2*$^{+/[f/+]}$). Averages and SEM are represented.

above, we did not observe major differences in T cell infiltration in tumours from both genotypes (**Figure 47C**). Therefore, TGF-β inhibition in CAFs does not alter the immune exclusion in CRC metastasis.

3.10. Acute TGFBR2 deficiency in CAFs induces T cell responses in CRC metastases.

Our data indicate that whereas the combination of CAF-specific TGFBR2 ablation with αPD-L1 checkpoint blockade offered a curative response (**Figure 44, page 143**), loss of TGFBR2 in CAFs alone does not change T cell density in metastases (**Figure 47B, page 146**). These effects are in opposition to the data shown using Galunisertib, which demonstrates that systemic inhibition of TGF-β signalling triggers T cell infiltration in the same model system (**Tauriello et al., 2018**). We next studied the adaptive immune response upon acute recombination of *Tgfbr2* in CAFs. Mice injected with MTO138 were treated for two consecutive days with tamoxifen, starting at day 13 after tumour transplantation, injected with

PD-L1-blocking antibodies or isotype control on day 14, and sacrificed at day 17 (**Figure 48A**). In these 4 days of treatment, in which a decrease in tumour burden was observed for some KO-aPD-L1 (**Figure 48B**, purple lines), all treatments showed increased T cell density compared to control mice (**Figure 48C, D**). This suggests that a T cell response is produced early after inducing CAF recombination (**Figure 48C**, red points).

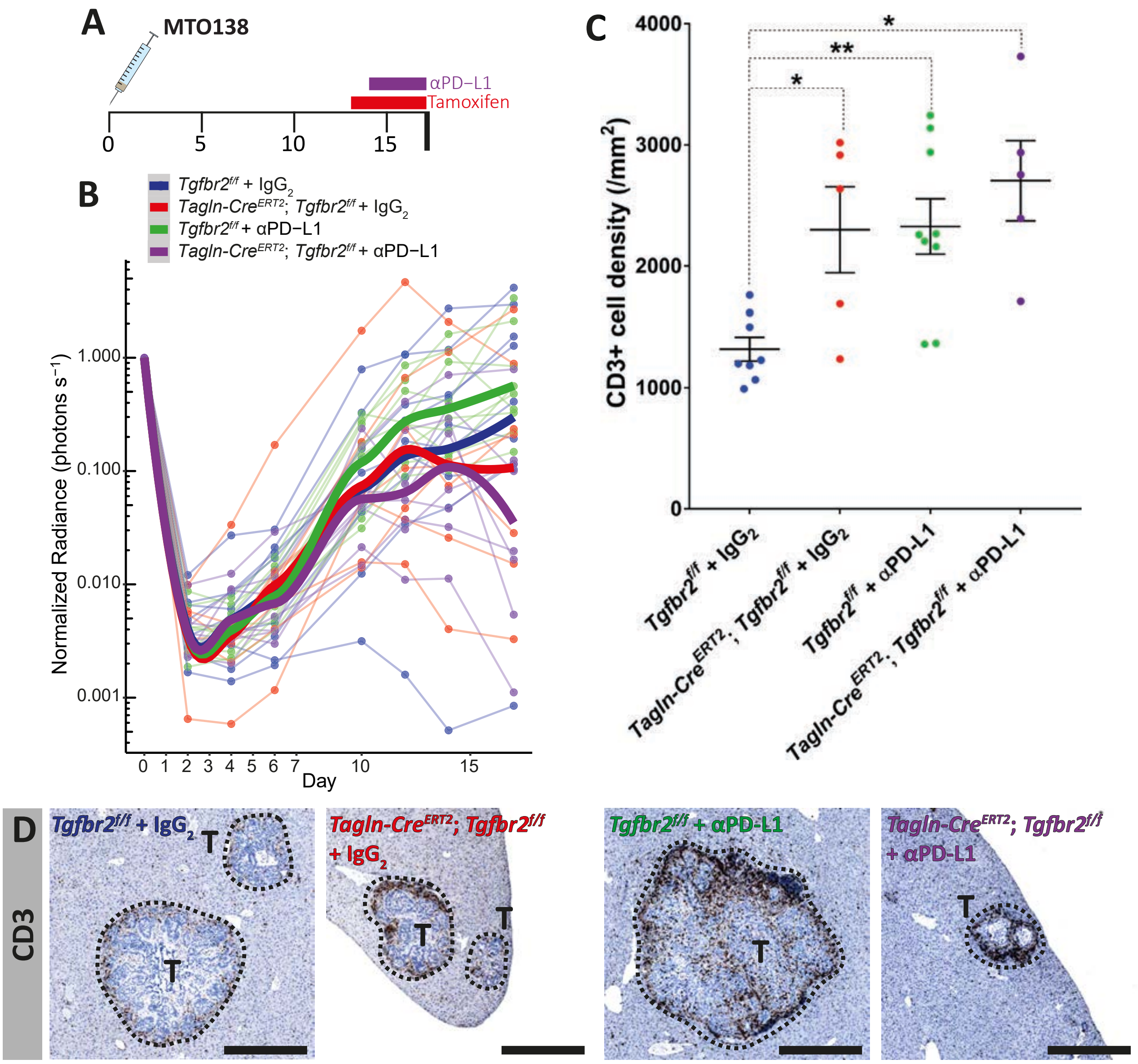

Figure 48. Acute treatment triggers T cell responses in liver metastases. A. Schematic representation of acute treatment of KO mice with αPD-L1 antibodies. Tamoxifen treatment started at day 13. αPD-L1 was administered once at day 14. Control mice received IgG$_2$. 9, 9, 7 and 8 mice were used for *Tgfbr2$^{f/f}$* + IgG$_2$ (blue), *Tagln-Cre^{ERT2}*; *Tgfbr2$^{f/f}$* + IgG$_2$ (red), *Tgfbr2$^{f/f}$* + αPD-L1 (green) and *Tagln-Cre^{ERT2}*; *Tgfbr2$^{f/f}$* + αPD-L1 (purple), respectively. **B.** Bioluminescence quantification of tumours *in vivo*. **C.** CD3+ T cell densities quantified by IHC. Values are averages of all metastatic nodules counted in every mouse. 12 nodules on average were quantified from 8, 5, 9 and 5 mice for *Tgfbr2$^{f/f}$* + IgG$_2$ (blue), *Tagln-Cre^{ERT2}*; *Tgfbr2$^{f/f}$* + IgG$_2$ (red), *Tgfbr2$^{f/f}$* + αPD-L1 (green) and *Tagln-Cre^{ERT2}*; *Tgfbr2$^{f/f}$* + αPD-L1 (purple), respectively. Averages and SEM are represented. Unpaired t test was performed. **D.** Representative IHC stainings of CD3+ T cells from **C**. Dashed lines delineate tumour margins. T = tumour. Scalebars = 500 µm. * = p-value < 0.05, ** = p-value < 0.01.

3.11. Long-term recombination of *Tgfbr2* in CAFs induces a memory response

Our results so far suggest that ablation of the TGF-β pathway in CAFs might trigger an immediate adaptive immune response (**Figure 48, page 147**). However, T cell infiltration was not altered at late time points, implying that the response is sustained over time (**Figure 47, page 146**). We explored whether a short-lived T cell response might result in the generation of memory T cells over the long term.

To verify this possibility, we analysed WT and KO mice bearing MTO140-derived metastases that received a long-term tamoxifen treatment (**Figure 49A**). In agreement with our earlier observations, KO tumours did not show increased CD3+ T cell infiltration compared to WT tumours (**Figure 49B**). However, CD8+ T cells were enriched in T cells that co-express CD44 and CD62L, (**Figure 49C**). CD44+CD62L+ CD8+T cells have been show to include memory T cells (**Krishnan et al., 2007**). Moreover, we found an increase of CD19+ B cells in KO tumours (**Figure 49D**). Based in these preliminary data, we speculate that the lack of CAF-specific TGF-β signalling in the TME generate a memory response, perhaps resulting from the acute T cell response observed in section **3.10**. Nevertheless, these differences did not reach statistical significance and deserve further analyses.

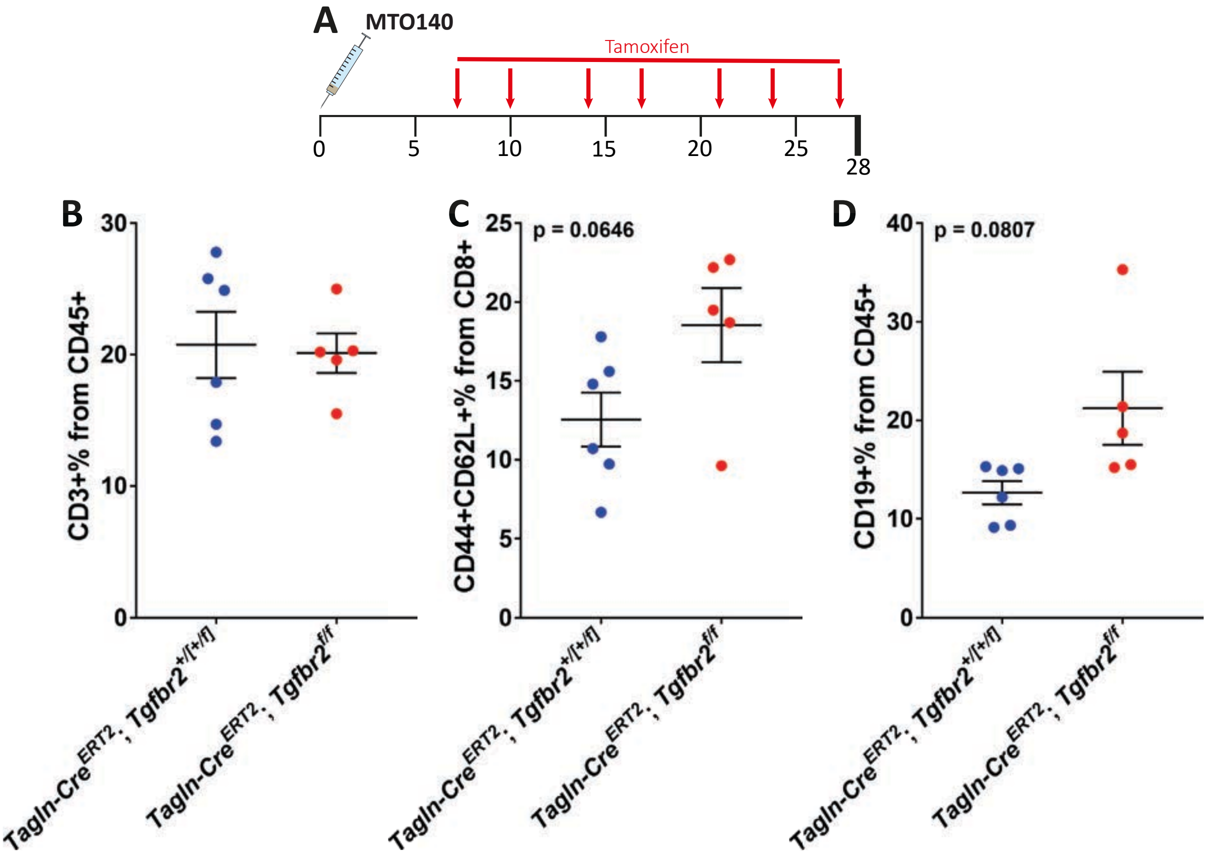

Figure 49. Metastases from KO mice show increased memory T cells and B cells. A. Schematic representation of tamoxifen administration. **B.** Percentage of CD3+ T cells from total CD45+ leukocytes in WT and KO mice transplanted with MTO140 after a long-term tamoxifen treatment, quantified by flow cytometry. **C.** Percentage of CD44+ CD62L+ memory T cells from total CD8+ cytotoxic T cells. **D.** Percentage of CD19+ B cells from total CD45+ leukocytes. N = 6 WT and 5 KO mice (left and right, respectively). Averages and SEM are represented for all plots. Unpaired t test was performed for all plots.

3.12. Ablation of TGFBR2 in CAFs synergizes with αPD-L1 therapy and triggers an adaptive immune reaction

The therapeutic effects triggered in KO mice treated with antibodies against PD-L1 strongly suggest that TGF-*β*-activated CAFs regulate immune responses in the TME. To verify if the blockade of PD-L1 produces synergistic T cell-mediated responses in KO mice, we analysed the CD3+ T cell densities in mice from the experiments detailed in **3.8** (**Figure 44, page 143**). Analysis of CD3 IHC stainings revealed that densities of CD3+ T cells in KO mice were not altered compared to WT mice, nor were those in WT mice treated with αPD-L1 (**Figure 50A, D-E**, red dots). In contrast, those KO mice treated with αPD-L1 antibodies that still had visible tumours, i.e. they had not been yet cured, showed increased T cell infiltration (**Figure 50A, D-E**, purple dots). Therefore, combination of checkpoint immunotherapy with specific inhibition of the TGF-β pathway in CAFs triggers an adaptive immune response.

Furthermore, in mice bearing MTO138-derived tumours, we noted three distinct degrees of therapeutic responses: 1) complete responders (cured mice), 2) mice with stable disease, and 3) mice with progressive disease (**Figure 50B**). The later exhibited a higher number of liver metastases and reduced T cell infiltration (**Figure 50B-E**). On the other hand, mice with stable disease showed the highest T cell densities in metastases, which could represent an ongoing anti-tumoral response (**Figure 50B-E**). Overall, these data indicate that whereas tumour lymphocyte infiltration is not increased when TGF-β pathway is ablated in CAFs, treatment with αPD-L1 synergizes with lack of TGF-β signalling in CAFs. We therefore conclude that TGF-β signalling in CAFs plays a key role in adaptive immune evasion.

Figure 50 (Next page). Combination of TGFBR2 deletion with checkpoint immunotherapy produces synergistic effects. A. Mice averages of CD3+ T cell densities from the two experiments using MTO129 represented in **Figures 44C** and **44D** (**page 143**). An average of 20 tumour were quantified from 14, 9, 10 and 6 mice for *Tgfbr2*$^{f/f}$ + IgG$_2$ (blue), *Tagln-Cre*^{ERT2}; *Tgfbr2*$^{f/f}$ + IgG$_2$ (red), *Tgfbr2*$^{f/f}$ + αPD-L1 (green) and *Tagln-Cre*^{ERT2}; *Tgfbr2*$^{f/f}$ + αPD-L1 (purple), respectively. Unpaired t test was performed. **B.** Bioluminescence from tumours *in vivo* in KO mice treated with αPD-L1 represented in **Figure 44E** (**page 143**). From all mice with overt metastatic disease, three mice presented stable disease (Sta., yellow) and three additional mice presented progressive disease (Prog., orange). **C.** Number of tumour nodules of mice transplanted with MTO138 treated with dual therapy represented in **Figure 44E** (**page 143**). Mice with progressive and stable disease are highlighted. **D.** Mice averages of CD3+ T cell densities from the experiment using MTO138 represented in **Figure 44E** (**page 143**). An average of 29 tumour were quantified from 5, 15, 4, 7 and 6 mice for *Tgfbr2*$^{f/f}$ + IgG$_2$ (blue), *Tagln-Cre*^{ERT2}; *Tgfbr2*$^{f/f}$ + IgG$_2$ (red), *Tgfbr2*$^{f/f}$ + αPD-L1 (green) and *Tagln-Cre*^{ERT2}; *Tgfbr2*$^{f/f}$ + αPD-L1 (purple), respectively. *Tgfbr2*$^{f/f}$ and *Tagln-Cre*^{ERT2}; *Tgfbr2*$^{f/f}$ mice treated with αPD-L1 are separated depending on if they presented stable or progressive disease.* = p-value < 0.05, ** = p-value < 0.01. Unpaired t test was performed. **E.** Representative IHC images showing DAB staining of CD3+ T cells from **D**. Dashed lines delineate tumour margins. Scalebars = 1 mm.

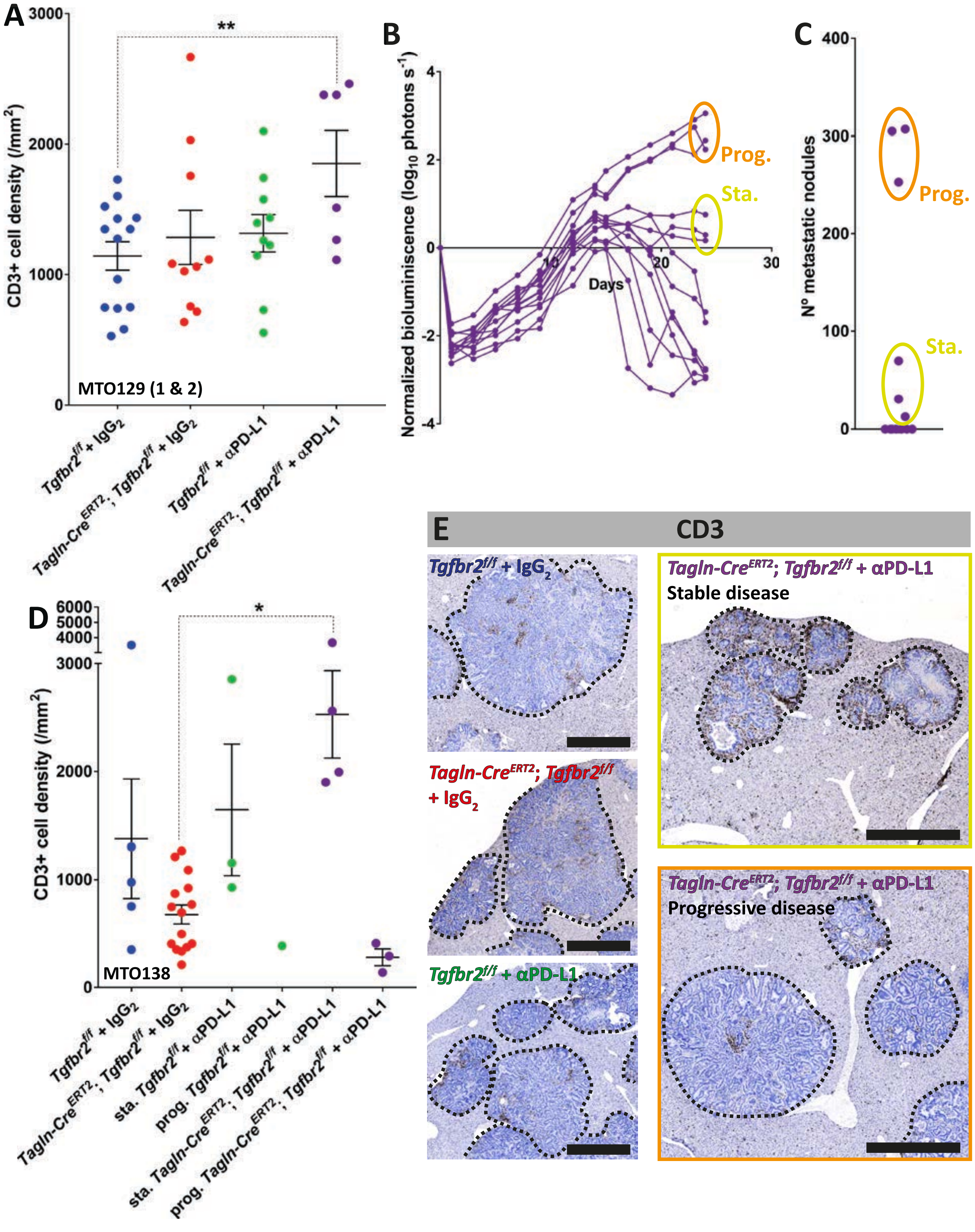
A
CD3+ cell density (/mm²)
3000
2000
1000
0
**
MTO129 (1 & 2)
Tgfbr2f/f + IgG2
Tagln-CreERT2; Tgfbr2f/f + IgG2
Tgfbr2f/f + αPD-L1
Tagln-CreERT2; Tgfbr2f/f + αPD-L1
B
Normalized bioluminiscence (log10 photons s-1)
4
2
0
-2
-4
Days
10
20
30
Prog.
Sta.
C
Nº metastatic nodules
400
300
200
100
0
Prog.
Sta.
D
CD3+ cell density (/mm²)
6000
5000
4000
3000
2000
1000
0
*
MTO138
Tgfbr2f/f + IgG2
Tagln-CreERT2; Tgfbr2f/f + IgG2
sta. Tgfbr2f/f + αPD-L1
prog. Tgfbr2f/f + αPD-L1
sta. Tagln-CreERT2; Tgfbr2f/f + αPD-L1
prog. Tagln-CreERT2; Tgfbr2f/f + αPD-L1
E
CD3
Tgfbr2f/f + IgG2
Tagln-CreERT2; Tgfbr2f/f + IgG2
Tgfbr2f/f + αPD-L1
Tagln-CreERT2; Tgfbr2f/f + αPD-L1
Stable disease
Tagln-CreERT2; Tgfbr2f/f + αPD-L1
Progressive disease

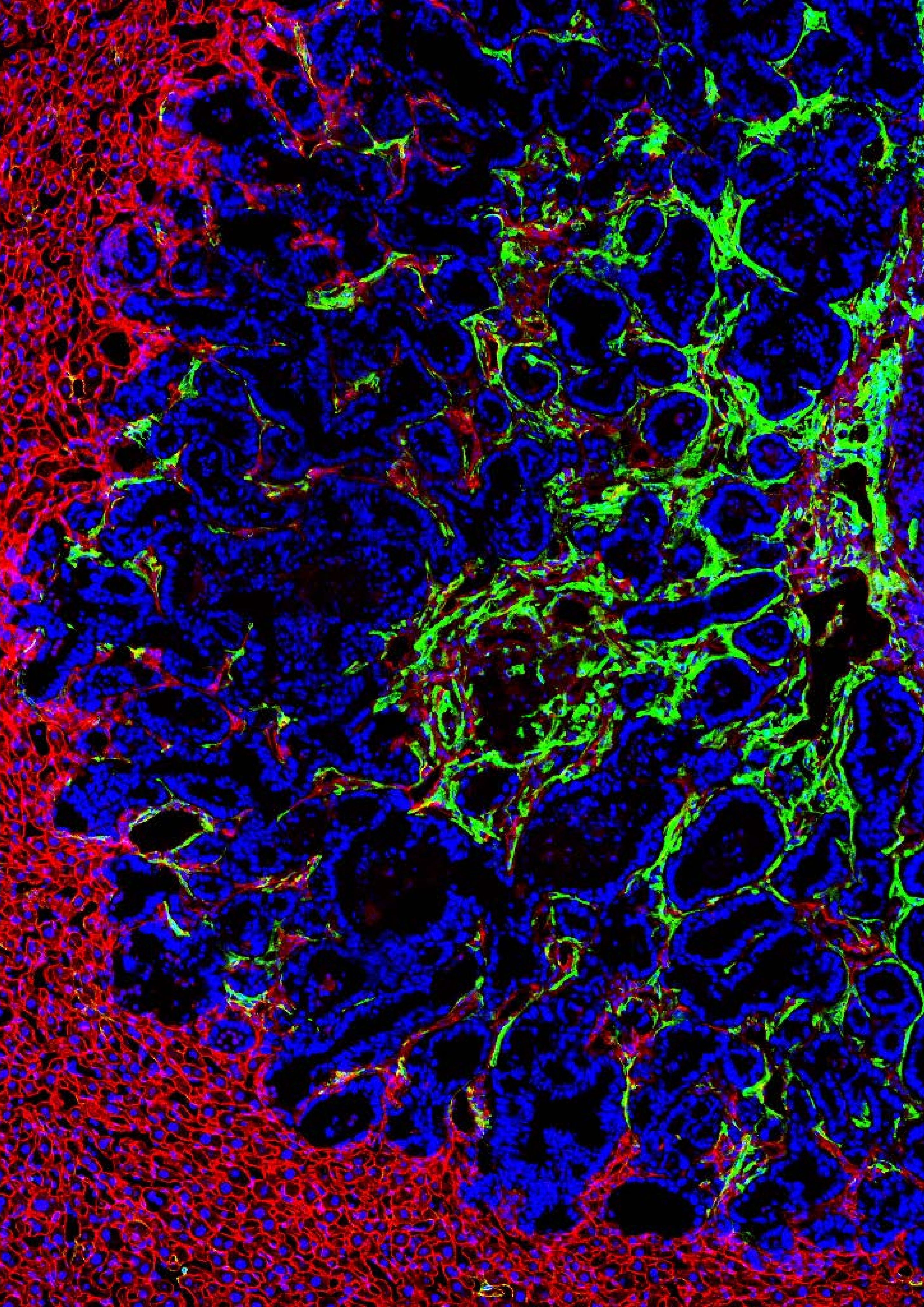

DISCUSSION

> *"Nothing in life is to be feared, it is only to be understood. Now is the time to understand more, so that we may fear less."*
>
> \- Marie Curie

1. Chapter 1: TGF-β drives immune evasion in genetically reconstituted colon cancer metastasis

Chapter 1 identified a prominent immunosuppressive role of TGF-β in CRC metastasis. Using a genetic mouse model for metastatic CRC, our lab found that inhibition of the TGF-β pathway on established tumours allowed T cells to infiltrate. Although this effect alone was not always strong enough to result in significant therapeutic effects, treatment with antibodies anti-PD-L1 synergized with inhibition of the TGF-β pathway to induce profound curative effects and immunization. In this section, I will first discuss the generation of the MTO technology, which has been extensively used for the development of this thesis. Next I will discuss the results published in **Tauriello et al., 2018**, focusing on those to which I have contributed.

1.1. Mouse tumour organoids of CRC: a new tool to study the fully immunocompetent TME of metastasis

Mouse models have been extensively used to study the genetic events leading to formation of colonic adenomas and their progression to aggressive carcinomas. These include genetically engineered mouse models, such as Apc^{min}, p53^{R172H} and PIK3ca^{*+}, (**Leystra et al., 2012; Moser et al., 1995; Ramanathan et al., 2012**) and chemical induction of intestinal tumorigenesis using carcinogens such as azoxymethane (AOM) and dextran sulphate sodium (DSS) (**De Robertis et al., 2011**). Given the fact that transition from colonic adenomas to aggressive carcinomas and metastasis is extremely slow, and because of their relatively short life span, mice typically die from the primary carcinomas before tumour cells can even reach distant organs.

Models of xenograft transplantation of patient-derived CRC cell lines into immunodeficient mice allowed a first approach to comprehend the biology of CRC metastasis. However, two important caveats of this system are the combination of a human sample into a murine host, and the lack of a reactive immune system in the TME of these transplants. The establishment of immortalized murine cell lines of CRC (i.e. CT26 and MC38) bypasses these two problems as they can be transplanted into syngeneic immunocompetent mice (**Karim and Huso, 2013**). However, the high mutational burden of these cell lines generates multiple neoantigens recognized by the immune system. Therefore, results obtained using these cell lines may not represent the majority of CRC tumours, which have much lower mutation rates.

By the time the project of the present thesis was conceived, our lab had generated a new mouse model for metastatic CRC, which resulted from serial crosses of mice bearing mutated alleles affecting the key CRC pathways (*Apc*$^{fl/fl}$, *Kras*$^{LSL\text{-}G12D}$, *Tgfbr2*$^{fl/fl}$ and *Trp53*$^{fl/fl}$, **Fearon, 2011; Fearon and Vogelstein, 1990**). Recombination of these alleles was specific for *Lgr5*+ intestinal stem cells (*Lgr5*$^{eGFP\text{-}creERT2}$, **Barker et al., 2007**) after tamoxifen administration. The combination of these mutations (LAKTP) resulted in the formation of spontaneous, invasive carcinomas that recapitulated key features of human CRC, including the stroma reaction: increased TGF-β signalling and decreased T cell infiltration. Importantly, around a 40% of mutant mice produced metastasis in the peritoneum (carcinomatosis), liver and lungs within their lifespan (**Tauriello et al., 2018**). Tumours and metastases from these mice were brought into 3D-culture to generate a large biobank of MTOs. To study liver metastatic colonization, MTOs were transplanted into syngeneic C57BL/6J immunocompetent mice, either as orthotopic implants in the caecum or focusing on liver metastasis by intrasplenic injection (**Tauriello et al., 2018**).

In parallel, two independent studies proposed new models of CRC that were able to recapitulate the progression of aggressive carcinomas and metastatic dissemination (**Fuma-**

galli et al., 2017; O'Rourke et al., 2017). Both studies took advantage of the CRISP-Cas9 technology to introduce mutations affecting the four key pathways of CRC into intestinal organoids cultured *in vitro*, which can then be transplanted into syngeneic immunocompetent mice (**Fumagalli et al., 2017; O'Rourke et al., 2017**).

The CRC models established by O'Rourke et al., Fumagalli et al. and our lab are able to overcome the above-mentioned caveats from the previous mouse models for metastatic CRC, as they feature non-hypermutated tumours with a complete TME. However, while the former two models rely on genetic manipulation of intestinal organoids *ex vivo*, MTOs are derived from spontaneously developed tumours and acquire a distinct combination of secondary mutations, a phenomenon that is reminiscent of the heterogeneity found in human patients (**Tauriello et al., 2018**).

1.2. TGF-β is required for T cell exclusion in metastatic initiation

It is accepted now that T cell exclusion in CRC is correlated with poor prognosis in patients (**Camus et al., 2009; Galon et al., 2006; Pagès et al., 2005, 2010**). Tumours spontaneously generated in our LAKTP mouse model have low levels of tumoral T cell infiltration. Moreover, we saw a progressive reduction of T cell density in tumours when MTOs were inoculated into spleens to recreate liver metastasis and different time points were analysed. T cells fail to maintain their activity in liver metastases, and therefore liver metastases become immune excluded (**Tauriello et al., 2018**). These findings agree with the fact that many colorectal tumours are immunologically "cold", with a poor adaptive immune reaction due to the low neoantigenic burden that was also determined to apply to quadruple mutant MTOs (**Galon and Bruni, 2019; Tauriello et al., 2018**).

Furthermore, in agreement with the previous observations from our lab (**Calon et al., 2012**), this new study corroborated that inhibition of the TGF-β pathway using Galunisertib in the TME of early metastases abrogates tumour initiation. This pharmacological effect of TGFBR1 inhibition was reproduced when we genetically ablated the TGFBR2 in the stroma (*Ub-Cre^{ERT2}*; *TGFBR2$^{f/f}$*). We concluded that impairment of tumour initiation as a result of TGF-β pathway inhibition was T cell-dependent as a result of the following observations:

- Tumour growth was rescued when T cells were depleted using monoclonal antibodies (**Tauriello et al., 2018**).
- In mice treated with Galunisertib as well as in *Tgfbr2* ubiquitous KO animals, we observed an increased infiltration of CD3+ T cells, which was specially contributed by an increase of CD4+ T cells. Within the CD4+ subset, there was enrichment in TBET+ cells. TBET is the master regulator of a Th1 response, and its expression is inhibited by TGF-β (reviewed in **Batlle and Massagué, 2019**). Therefore, abrogation of TGF-β signalling induced a Th1 activity.
- Both CD4+ and CD8+ T cells in mice treated with Galunisertib showed increased activation (**Tauriello et al., 2018**). Although recombination of the *Tgfbr*2 affected only partially the leukocyte subset (**Tauriello et al., 2018**), KO T cells showed increased activation compared to T cells that resisted recombination (Badia-Ramentol, data not shown). In particular, we saw an increase in expression of IFNγ and GZMB, which are correlated with an effective CTL response and good prognosis in patients, and are directly repressed by TGF-β (**Batlle and Massagué, 2019; Galon et al., 2006; Pagès et al., 2010; Waterhouse et al., 2004**). In line with these findings, previous reports already demonstrated that mice carrying either dominant negative or truncated forms of the TGFBR2 in CD4+ T cells develop autoimmune diseases due to uncontrolled activation (reviewed in **Batlle and Massagué, 2019**).

We confirmed that CAFs were the major source for TGF-β in the TME of liver metastases of the LAKTP-MTO model, at least on the mRNA level. Moreover, both the CAF gene signature and the levels of *TGF-β1*, -β2 and *-β3* were inversely correlated to Th1 responses (**Tauriello et al., 2018**), which links the prognostic potential of TGF-β and CAFs (**Calon et al., 2012, 2015**) to Th1 responses. Consequently, Th1 responses are restablished when the TGF-β pathway in the TME of liver metastases is inhibited.

1.3. Synergism of checkpoint immunotherapy with TGF-β inhibition leads to strong therapeutic effects

Many patients with advanced CRC relapse after surgery in the form of full-blown metastasis at distant organs, especially in the liver. Therefore, while we observed that early treatment with Galunisertib led to a dramatic decrease in liver tumour burden, we decided to explore the effects of TGF-β inhibition in a setting of established metastasis with a mature TME, defined as 2 weeks after implantation of MTOs. This setting was considered to be more relevant in the clinical aspect of advanced disease. At this point, tumour cells have already overcome immune surveillance and grown to visibly detectable sizes (0.5 to 1 mm).

In this scenario, treatment with Galunisertib only yielded a modest reduction in tumour burden, and led to only a modestly extended survival. Nonetheless, even with these incomplete responses, we could observe an increase in T cell infiltration in tumours. This infiltration was accompanied by an increase of PD-1 surface expression on CD4+ and CD8+ T cells (**Tauriello et al., 2018**). PD-1 is typically expressed on the surface of T cells during initial activation and is critical to shape effector responses and the generation of memory T cells (reviewed in **Sharpe and Pauken, 2018**). As antigenic presence persists, PD-1 expression levels of PD-1 on T cells remain high. (**Sharpe and Pauken, 2018**). Conversely, PD-1 expression is crucial to dampen immune responses upon its binding to PD-L1/2 (**Freeman et al., 2000; Rozali et al., 2012**). PD-L1 is the most abundant ligand for PD-1 and can be expressed by a plethora of cells in the TME, including tumour epithelial cells. Thus, blocking antibodies targeting PD-L1 is one of the most attractive strategies for immunotherapy (**Drake et al., 2014; Sharpe and Pauken, 2018**). It is interesting to note that in mouse CRC liver metastases, PD-L1 expression progressively increases over time in the tumour stroma, especially on tumour-associated macrophages (**Tauriello et al., 2018**). PD-L1 expression is triggered mainly by interferons, especially IFNγ, for instance as a result of effector T cell activity (**Garcia-Diaz et al., 2017; Katlinski et al., 2017; Ribas et al., 2017**). We could therefore speculate that T cell-mediated immunosurveillance of liver metastases results in the release of effector cytokines including IFNγ, which triggers PD-L1 expression on the TME.

The expression of stromal PD-L1 gave a hint that established metastases make use of immunological checkpoints as an additional mechanism to evade immune surveillance. Therefore, we tested a combination therapy of Galunisertib with antibodies against PD-L1 in the MTO model (**Tauriello et al., 2018**). Responses after monotherapy with antibodies against PD-L1 were minimal. However, combination of both treatments led to a strong therapeutic response and increased disease-free survival. When analysed, tumours from mice treated with dual therapy showed an enhanced Th1 response. This study demonstrates that treatment with antibodies against PD-L1 further strengthens the T cell responses observed after treatment with Galunisertib, resulting in a synergized response and rapid tumour clearance (**Tauriello et al., 2018**).

Similar to its prognostic power, T cell infiltration can predict patient clinical response to immunotherapy. Indeed, most CRC patients develop tumours with a poor T cell infiltration that are refractory to checkpoint blockade therapy (**Le et al., 2015; Llosa et al., 2015**). In this line, recent work led by Jérôme Galon have shown that the Immunoscore tool can predict patient outcome and can be used in decision-making for targeted therapies for patients with metastatic CRC. In particular, the density of T cells on less-infiltrated metastases correlated with a lower metastatic burden, and consequently with a favourable outcome (**Van den Eynde et al., 2018**). Furthermore, tumour cells that escape the immune editing process create clones that are refractory to immune responses derived from therapy (**Angelova et al., 2018**). The importance on understanding why patients do not respond to immunotherapy lies on the discovery of novel therapeutic strategies. For instance, a recent clinical study show that patients with BRAF mutated melanomas respond to a combination of anti-PD-1 therapy with BRAF and MEK inhibitors (**Ribas et al., 2019**).

The lack of efficacy of checkpoint immunotherapy alone was reflected in the MTO model. Due to this new mouse model for metastatic CRC, we have contributed an explanation to both poor T cell infiltration and the apparent failure of immunotherapy: besides a relatively low immunogenicity of tumours, high levels of TGF-β in the TME are responsible (**Tauriello et al., 2018**). Indeed, abrogation of TGF-β pathway on the TME is sufficient to increase the density of infiltrating T cells and results in an increased susceptibility to immune checkpoint therapy. Therefore, our findings provide a new therapeutic strategy for patients with CRC liver metastasis. In parallel to our research, an independent study on urothelial cancer found a similar mechanism of TGF-β-driven immune evasion (**Mariathasan et al., 2018**). This study showed that a cohort of patients who failed to respond to anti-PD-L1 therapy had tumours enriched in TGF-β and CAF gene signature, and that inhibition of TGF-β pathway reverted T cell exclusion in mouse models for e.g. breast cancer (**Mariathasan et al., 2018**). Moreover, another recent study showed a correlation between a high ECM expression by CAFs and failure to PD-1 blockade immunotherapy (**Chakravarthy et al., 2018**). Therefore, we speculate that TGF-β-mediated T cell exclusion may be a general mechanism driving cancer immune evasion, which should be exploited for more effective immunotherapeutic strategies. Despite a clear implication of CAFs as the source of TGF-β (**Mariathasan et al., 2018; Tauriello et al., 2018**) as well as other predictive biomarkers (**Chakravarthy et al., 2018**), we still have a poor mechanistic understanding of the role these stromal cells have in metastasis and immune evasion.

2. Chapter 2: unravelling the biology of CAFs in liver metastasis

Our lab's previous investigations have demonstrated that TGF-β-activated CAFs are strong predictors of poor prognosis in patients, which are also the major source of TGF-β in the TME (**Calon et al., 2012, 2015; Tauriello et al., 2018**). However, the specific cellular mechanism still remains elusive. Therefore, the question remained whether TGF-β-mediated immune exclusion is directly driven by CAFs. Addressing this question may be relevant in designing more specific (for instance CAF-targeted) treatment strategies.

Chapters 2 and 3 focus on the unpublished and ongoing work which aims to understand the relationship between CAFs and the immune tumour microenvironment as a result of TGF-β. The MTO technology platform (**Tauriello et al., 2018**) allowed us for the first time to dissect the roles of CAFs from liver metastasis by genetically ablating the TGF-β pathway in the activated fibroblasts. Nevertheless, given the existing fibroblast heterogeneity, our first challenge was to comprehend the biology of CAFs in liver metastasis, which would allow us to define markers expressed specifically by CAFs in the MTO model. Therefore, chapter 2 focuses on understanding the biology of CAFs from CRC metastasis.

2.1. At least two distinct CAF subpopulations coexist within CRC liver metastases

Up to 10% of cells in the liver are mesenchymal cells. In particular, they are perivascular cells, or pericytes, and they have been extensively studied (**Friedman, 2008; Lemoinne et al., 2013; Wells, 2014**). In agreement with the literature on liver mesenchymal cells (LMCs), we could detect the twomain populations of LMCs, hepatic stellate cells (HSCs) and portal fibroblasts (PFs), by coexpression of PDGFRα and PDGFRβ (**Friedman, 2008; Wells, 2014**). HSCs are located near the sinusoid capillaries, scattered within the liver parenchyma. PFs are exclusively located in portal areas, which are formed by clusters of a vein, an artery and a bile duct. We also detected a third population of LMCs, a small proportion of perivascular myofibroblasts surrounding the central veins as well as the arteries and veins that compose the portal zone, that do not express PDGFRα. Instead, they coexpress PDGFRβ and αSMA (**Lemoinne et al., 2013; Lepreux and Desmoulière, 2015**).

PDGFRs are common markers used for both resting and activated fibroblasts (**Kalluri, 2016; Kalluri and Zeisberg, 2006**). In fact, several studies have shown that treatments with imatinib, a tyrosine kinase inhibitor that has PDGFRs among its targets, have resulted in impaired tumour growth by blocking fibroblast proliferation and activation (**Kitadai et al., 2006; Shinagawa et al., 2012; Sumida et al., 2011**). We therefore decided to explore the expression pattern of PDGFRα and PDGFRβ on CAFs from full-blown liver metastasis together with αSMA, the classical marker that defines active myofibroblasts (**Kalluri, 2016; Shaw and Martin, 2009**). We found that CAFs are segregated into two mutually exclusive categories of PDGFRα+/PDGFRβ+/αSMA- (α^+/β^+) and PDGFRα-/PDGFRβ+/αSMA+ (α^-/β^+) CAFs (**Figure 51**), which were both TGF-β activated as they did not show differences in expression of TGF-β targets. α^+/β^+ CAFs were a minority population and were found almost exclusively in the periphery of tumours, indicating that PDGRFa expression is lost in CAFs in the tumour centre (**Figure 51**). In agreement with this observation, a study on hepatocellular carcinoma found that PDGFRα expression is lower in tumours than hepatic tissue (**Wallace and Friedman, 2014; Wright et al., 2014**).

One issue that remains unresolved is the origin of CAFs from CRC liver metastasis. The experiments using bone marrow chimeric mice discarded the contribution of bone marrow progenitors to the generation of CAFs in liver metastasis. In line with this observation, previous studies have shown that HSCs and PFs, and not bone marrow-derived mesenchymal cells, are the major sources for myofibroblasts in fibrosis and hepatocellular carcinoma (**Iwaisako et al., 2014; Kramann et al., 2014; Liu et al., 2015; Mederacke et al., 2013; Sekiya et al., 2016**). PDGFRα- liver myofibroblasts do not seem to contribute to liver fibrosis, as reported previously (**Kramann et al., 2014**). It is interesting to note that LMCs and α^+/β^+ CAFs both express PDGFRα/β but not αSMA, and that micrometastases start with a low relative abundance of α^-/β^+ myofibroblasts, while 3-4 week-old metastases are enriched in this particular subpopulation of fibroblasts. Therefore, we hypothesise that α^+/β^+ CAFs arise from LMCs that proliferate and subsequently produce more “mature” α^-/β^+ myofibroblasts. Evidence supporting this hypothesis is that α^+/β^+ CAFs show higher expression of the proliferation marker KI67 compared to α^-/β^+ myofibroblasts (**Figure 51**). However, whether HSCs or PFs are the major contributors to CAF production in liver metastasis remains to be elucidated.

2.2. CAF composition is heterogeneous between metastases with the same driver mutations

The heterogeneity of genetic programs of fibroblasts in different tissues and the multiple potential sources of CAFs lead to the conclusion that CAF composition varies across distinct tumour types (**Cortez et al., 2014; LeBleu and Kalluri, 2018**). In terms of therapy, a different composition of the TME is pivotal to determine the efficiency of responses to immunotherapy (**Salmon et al., 2019**). However, an interesting question is how such heterogeneity affects CRC metastases with a similar set of driver mutations from different patients.

As discussed in chapter 1, the MTO biobank contains organoids that share the same key CRC mutations but were derived from different tumours and mice. In fact, LAKTP murine cancers have acquired various spontaneous mutations in similar rates and patterns as seen in MSS CRCs in patients (**Tauriello et al., 2018**). This genetic heterogeneity among MTOs may be linked to functional heterogeneity, as not all LAKTP MTOs are equally aggressive when implanted in syngeneic mice. To understand these phenomena, we characterized the stromal composition in metastases from different MTOs, which may model differences between patients. Based on what we know of the crucial role of the TME in prognosis and prediction, this could be useful to understand why some patients respond to current therapeutic strategies while others are completely refractory to them.

We used three different LAKTP MTOs -MTO129, MTO140 and MTO138- as an initial approach to tackle this question. It is interesting to note that while all MTO cell types express similar levels of *Tgf-β1*, tumour cells from MTO129 express more *Tgf-β2* and *-β3*, relative to the others. While metastases from all three MTOs show a similar proportion of total CAFs in the TME, metastases derived from MTO129 showed a higher content in α^+/β^+ CAFs. In contrast, the stroma of MTO138- and MTO140-derived metastases was richer in α^-/β^+ myofibroblasts.

Besides TGF-β, PDGF are the main activating factor of fibroblasts (**Kalluri, 2016; Kalluri and Zeisberg, 2006**). We found that tumour cells from MTO129 express increased levels of *Pdgf*, especially *Pdgf-A* and *-C*, compared to cells from MTO138 and MTO140. The biology of PDGF receptors have been extensively studied (**Andrae et al., 2008; Kikuchi and Monga, 2015**). In particular, PDGFRα has a high affinity for PDGF-AA and PDGF-CC homodimers, and their overexpression can lead to fibrosis and CAF generation (**Cortez et al., 2014; Kikuchi and Monga, 2015**). Therefore, the increased expression of PDGF in MTO129 might explain the abundance of the α^+/β^+ subpopulation in MTO129-derived metastases. In contrast, metastases derived from MTO138 and MTO140, which both show reduced expression of PDGF, are enriched in α^-/β^+ myofibroblasts, which may be mostly TGF-β-driven. (**Figure 51**). We could tentatively speculate that such heterogeneity in CAF composition could be that secondary mutations in tumours drive production of different factors affecting CAF activation or differentiation. The differential proportions of CAF subpopulations could be a result of a balance between the relative quantities of such factors found in the TME. However, as fibrosis can also be driven by inflammation (**Fabre et al., 2018; Fielding et al., 2014**), another line of thought could be that tumours have an indirect impact on the CAF composition through the recruitment and activation of different inflammatory cells.

Whole-tumour RNA analysis from liver metastases showed that MTO138- and MTO140-derived metastases, and specially MTO140, have a higher expression of both *Tgf-β1* and -β3 isoforms, which are the best predictors of outcome in CRC patients (**Calon et al., 2012**). Differences in *Tgf-β* expression between these results and RNA sequencing from *in vitro* MTOs, where all *Tgf-β* isoforms were expressed at highest relative levels in MTO129 cells, might therefore be explained by the stromal composition, especially by CAFs (**Calon et al., 2014; Tauriello et al., 2018**). Metastases derived from MTO138 and MTO140 have a higher content in α^-/β^+ myofibroblasts. Therefore, there might be an association between total expression of *Tgf-β1* and *-β3* with a higher content of myofibroblasts in the TME. These preliminary data tentatively suggest that α^-/β^+ myofibroblasts could also acquire predictive potential in CRC liver metastasis. As tumours include phenotipically distinct CAF subpopulations (**Costa et al., 2018; Cremasco et al., 2018; Elyada et al., 2019; Li et al., 2017; Ligorio et al., 2019; Öhlund et al., 2017; Patel et al., 2018; Puram et al., 2018; Su et al., 2018**), an open possibility is the existence of particular subpopulations responsible for poor prognosis stromal signatures in tumours (**Calon et al., 2015; Chakravarthy et al., 2018; Isella et al., 2015; Moffitt et al., 2015**). In this line, it would be interesting to explore if the existing CAF-related poor prognosis signatures in CRC are associated with a particular CAF phenotype.

2.3. Metastases enriched with myofibroblasts are immune excluded

The composition of CAFs and the ECM directly influences the components of the tumour microenvironment, which in turn affects the success of current immunotherapies (reviewed in **Salmon et al., 2019**). Our preliminary data suggests that metastases with the same key mutations orchestrate different combinations of CAF subpopulations in liver metastases. In a next step, we decided to explore how CAF composition in CRC liver metastasis would affect the composition of the TME.

We have reported that exclusion of CD3+ lymphocytes in metastasis increases progressively over time (**Tauriello et al., 2018**). Such progressive exclusion was correlated with an increase in αSMA+ myofibroblasts in the TME. This exclusion is more evident when we compare MTO129- versus MTO140-derived metastases, where in MTO140 there is a higher content of myofibroblasts than MTO129. Indeed, metastases from MTO140 had a lower density of T cells than metastases from MTO129, especially CD8+ CTLs. The spatial distribution of T cells was also affected, as T cells in MTO140-derived metastases were more localized to the tumour margin. In addition to a low abundance of CTLs, CD8+ T cells expressed lower levels of surface PD-1 in MTO140-derived metastases, compared to MTO129, indicating a reduced activation. These metastases also showed a two-fold increase in CD44+CD62L+ memory T cells, which could be an effect of the increased expression of TGF-β (**Ma and Zhang, 2015**).

Data presented in **section 2.5** suggest that metastases with a higher proportion of α^-/β^+ myofibroblasts generates an immune environment deficient in T cells, which is a feature that defines poor prognosis in patients (**Galon et al., 2006; Pagès et al., 2005**). Exploring the immunological properties of α^+/β^+ and α^-/β^+ subtypes further, we found that α^+/β^+ CAFs were especially enriched in *IL-6*, *IL-33*, *Ccl5* and *Ccl9*, which could be related to an enhanced inflammatory phenotype. Indeed, IL-6 can attract monocytes and trigger the expression of T cell chemoattractants (**Scheller et al., 2011**). In addition, secretion of IL-33 and CCL9 is related with recruitment of dendritic cells, monocytes and macrophages (**Raffaghello et al., 2015; Yang et al., 2016**), and CCL9 and CCL5 are strong attractants of T cells (**Raffaghello et al., 2015; Salmon et al., 2012**). The possible role of *Cxcl12*, also upregulated in α^+/β^+ CAFs, is more mysterious, as its expression is associated with repulsion of T cells (**Vianello et al., 2006**), but it can be also critical for the formation of tertiary lymphoid structures (reviewed in **Salmon et al., 2019**).

On the other hand, α-β+ CAFs show enrichment in *Cxcl9*, *Cxcl10*, *Tnf-α*, *Pd-l1* and *Ccl12*. CXCL9 and CXCL10 are also potent T cell chemoattractants (**Chen and Mellman, 2013; Gajewski et al., 2013**). However, increased expression of TNF-α and PD-L1 could impair activation and proliferation of T cells. Furthermore, TNF-α induces apoptosis in T cells (**Joyce and Fearon, 2015**), which could explain the immune exclusion observed in metastases enriched with this particular CAF subpopulation (**Figure 51**). In addition, increased CCL12 has been associated with increased fibrogenesis in tumours (**Moore et al., 2006**).

In the last 3 years, recent advances in single cell RNA sequencing have provided more insights into the heterogeneous composition of CAFs. Several studies have already defined different CAF subpopulations that coexist in breast cancer, PDAC, CRC, melanoma and head and neck cancer (**Costa et al., 2018; Cremasco et al., 2018; Elyada et al., 2019; Li et al., 2017; Ligorio et al., 2019; Öhlund et al., 2017; Patel et al., 2018; Puram et al., 2018; Su et al., 2018**). Although some of them are purely descriptive and arise from a wide analysis from whole tumours (**Li et al., 2017; Puram et al., 2018**), some others already define specific populations that interact with tumour cells to promote stemness, growth and resistance to chemotherapy (**Ligorio et al., 2019; Patel et al., 2018; Su et al., 2018**).

What is more interesting is that most of these studies agree on the idea of the existence of, at least, one subpopulation that acquires immunosuppressive roles. A study led by David Tuveson on PDAC was one of the first to distinguish an inflammatory subpopulation of CAFs different from the αSMA-expressing myofibroblasts (**Öhlund et al., 2017**). A recent follow-up by the same group discovered a third subpopulation that could repress antigen-specific T cell responses through an MHC-II-dependent mechanism (**Elyada et al., 2019**). Independently, studies on melanoma and breast cancer have identified CAF subpopulations with immunosuppressive properties through recruitment of macrophages or Tregs and expression of checkpoint inhibitors such as PD-L2 (**Costa et al., 2018; Cremasco et al., 2018; Lakins et al., 2018**). All these studies are coherent with the hypothesis of a consensus functional class of CAFs with immunosuppressive roles (**Kalluri, 2016**, **Figure 16, page 51**).

While the data presented in chapter 2 are still preliminary, we hypothesize that myofibroblasts in CRC liver metastases are responsible for immune suppression, including T cell exclusion (**Figure 51**). By understanding how CAF heterogeneity affects immune exclusion in metastasis, we may be better able to predict responses to immunotherapies. Moreover, more effective immune-based therapies targeting specific CAF subpopulations could be designed.

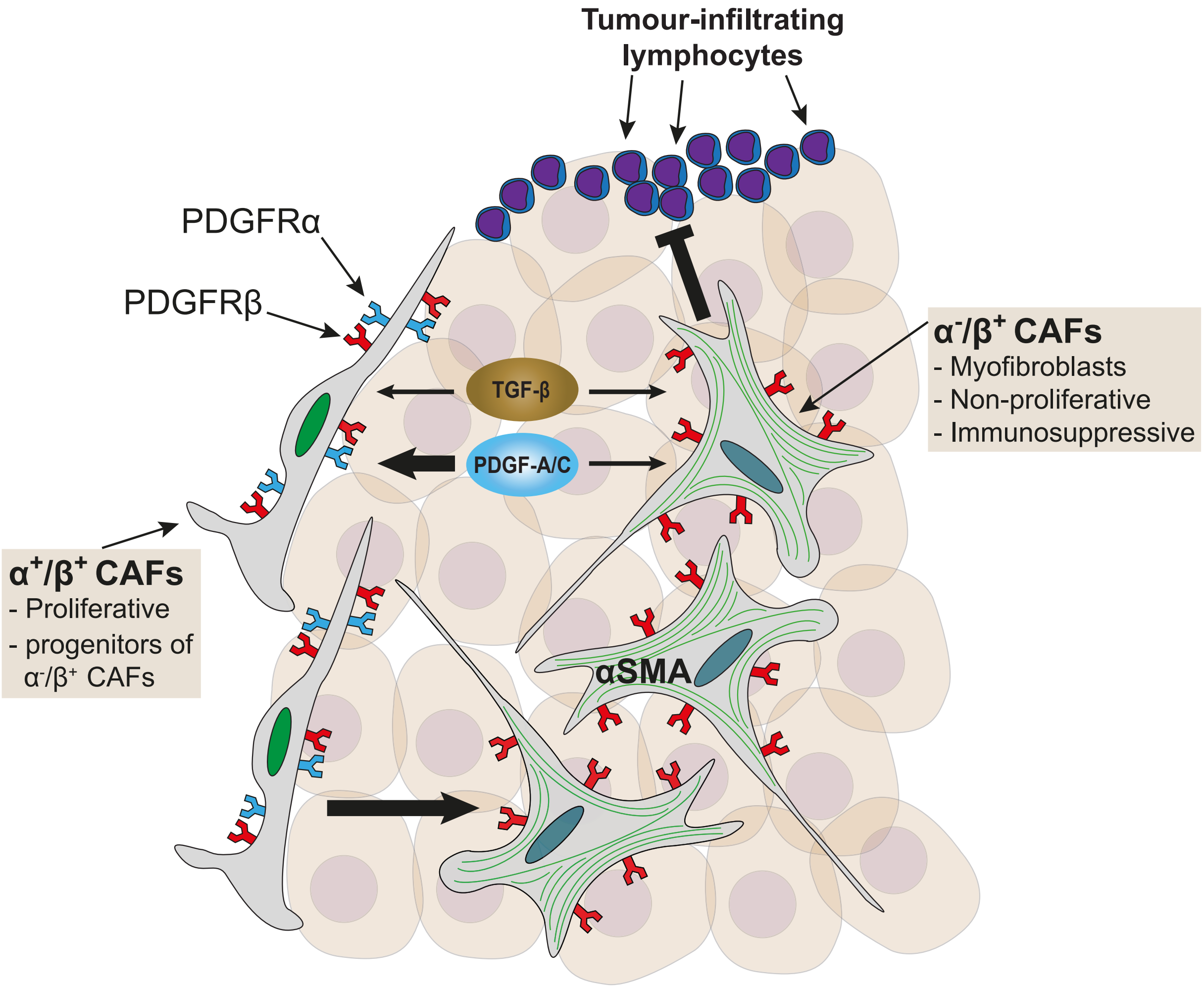

Figure 51. Hypothetical model of CAF subpopulations in CRC liver metastasis. Two CAF subpopulations coexist in CRC liver metastasis: peripheral α^+/β^+ CAFs (PDGFRα+/PDGFRβ+/αSMA-) and α^-/β^+ myofibroblasts (PDGFRα-/PDGFRβ+/ αSMA+). Both CAF subpopulations are activated by TGF-β, while PDGF might contribute to the maintenance of α^+/β^+ progenitor CAF population. We hypothesize that these give rise to the less proliferative α^-/β^+ myofibroblasts. The latter are linked to immunosuppressive roles, i.e. T cell exclusion and may have prognostic and predictive significance in CRC liver metastasis, in the context of immunotherapy.

3. Chapter 3: TGF-β-activated CAFs are pivotal for the lack of responses to checkpoint immunotherapy in CRC

After discovering that TGF-β mediates immune suppression in CRC liver metastasis (**Chapter 1**, **Tauriello et al., 2018**), our main question for this project was to understand the contribution of TGF-β-activated CAFs to this phenomenon. To tackle this question, we chose to ablate the TGF-β pathway by genetic recombination of the *Tgfbr2* in CAFs. To this end, we chose *Tagln* to target TGF-β-activated CAFs of liver metastasis. In this chapter we will discuss the main findings on this subject.

3.1. Tagln is a specific marker for TGF-β-activated CAFs in liver metastases

Previous studies conducted in our lab on CAFs established a TGF-β response signature in fibroblasts (F-TBRS) that correlated with poor prognosis in patients (**Calon et al., 2015**). One of the top upregulated genes is *TAGLN*. TAGLN is an actin-binding protein expressed in the smooth muscle and myofibroblasts (**Assinder et al., 2009**). TGF-β-activated, TAGLN-expressing myofibroblasts are crucial for a correct embryonic development and TGF-β ablation in these cells leads to malformations and congenital anomalies (**Aldeiri et al., 2017, 2018**). Importantly, *TAGLN* expression have been reported in CAFs in several malignancies and its overexpression promotes tumorigenesis (**Calon et al., 2015; Chen et al., 2014a; Elyada et al., 2019; Li et al., 2017; Wu et al., 2014**). Indeed, our analyses have revealed that *TAGLN*, together with other CAF-specific genes (**Calon et al., 2015**), can predict clinical outcome. Moreover, its expression is enriched in tumours classified as CMS4, which is the category with worse overall survival according to Guinney and colleagues (**Guinney et al., 2015**). In agreement with its nature as a TGF-β target, *Tagln* is upregulated in CAFs compared to LMCs, and treatment with Galunisertib abrogated TAGLN expression (**Figure 52**). Moreover, GFP expression of *Tagln*-expressing cells from the *Tagln-Cre*^{ERT2} genetic model overlapped with that of CALD1, another TGF-β target gene expressed in CAFs (**Calon et al., 2015**).

The majority of markers used for CAFs are not fibroblast-specific (**Kalluri, 2016**). As TAGLN is not only expressed by myofibroblasts in healthy tissues, we needed to validate that the *Tagln-Cre*^{ERT2} mouse model was only targeting CAFs in liver metastases. Luckily, we found that GFP expression was specific for PDGFRβ+ CAFs and not immune cells nor endothelial cells, and *Cre* was exclusively expressed in GFP+ CAFs. A reduced proportion of PDGFRβ+ GFP+ cells stained also for CD45 in flow cytometry analyses. A possibility could be that these PDGFRβ+CD45+GFP+ cells are fibrocytes (**Abe et al., 2001**). However, we did not find any event with overlapped expression between GFP and CD11b, a marker of myeloid cells also expressed by fibrocytes (**Abe et al., 2001**), and the proportion of GFP+ events over total CD45+ cells was negligible (below 0.01%). Moreover, in chapter 2 we found that CAFs are not generated by bone marrow-derived progenitors, which is supported by previous lineage tracing studies indicating more local sources for myofibroblasts in liver fibrosis and cancer (**Iwaisako et al., 2014; Kramann et al., 2014; Liu et al., 2015; Mederacke et al., 2013; Sekiya et al., 2016**). Instead, PDGFRβ+CD45+GFP+ cells may be false positives for CD45 expression and *Tagln-Cre*^{ERT2} targets specifically CAFs and activated LMCs.

3.2. The recombination efficiency of Tagln+ CAFs is MTO-dependent

In chapter 2, we concluded that CAF composition depends on the injected MTO. This finding is reflected in the overall expression of *Tagln*, which is correlated to the overall expression of *Tgf-β1* and *–β3* in the TME (**Figure 52**). In particular, MTO140-derived metastases showed a higher RNA expression of *Tagln*. Differences in *Tagln* expression likely affect the efficiency of recombination in the *Tagln-Cre*^{ERT2} mouse strain. Indeed, CAFs from

MTO140-derived metastases show an increased proportion of GFP+ PDGFRβ+ events compared to MTO129.

The recombination efficiency may also have an impact on the deletion of the receptor and subsequent downregulation of the TGF-β targets. We show a clear dowregulation not only on the *Tgfbr2* but also in targets of the TGF-β pathway such as *IL-11* and *Serpine1* in CAFs derived from MTO140 metastases, yet we could not see dowregulation of *Tagln* expression in CAFs from MTO129 metastases. Nevertheless, in both MTO types, the reported downregulation of *Tgfbr2* is rather poor (only a 4-fold decrease). Since the recombination of the reporter gene and the gene of interest are independent events, we cannot be certain that GFP expression equals the full recombination of the *Tgfbr2*. In fact, a report from Owen Sansom's lab has shown that in a similar setting, recombination of the reporting gene occurred at a higher frequency than their gene of interest (**Huels et al., 2018**). Therefore, a possibility could be that we are capturing false positives for recombination, adding to the biological noise in our experiments.

Another caveat of this model is that the GFP does not report the entire population of *Tagln*-expressing CAFs. In WT mice with MTO129 metastases, we saw no differences in *Tagln* expression between GFP+ and GFP- CAFs, and we only observed a 2.5-fold upregulation in GFP+ CAFs from MTO140 metastases. A possibility could be that the CRE has a low penetrance in liver metastases from this model. On the other hand, the distance between both LoxP sites flanking the *tdTomato* cassette is around 3kbp (**Muzumdar et al., 2007**), which reduces substantially the probability of recombination. The use of an alternative reporter strain expressing a reporting fluorescent protein with a shorter recombination distance could validate this possibility and perhaps improve the targeting of *Tagln*+ CAFs.

3.3. Abrogation of the TGF-β pathway in CAFs results in a reduction of total CAFs in the TME

In our lab, we demonstrated that pharmacological inhibition of TGF-β pathway using Galunisertib results in a strong reduction of the CAF-specific TGF-β response signature (**Calon et al., 2015; Tauriello et al., 2018**). However, we never took into account the possible effect on CAF behaviour. We now report we saw that the total amount of PDGFRβ CAFs is diminished upon treatment with Galunisertib. This observation might change our perception on how the TGF-β pathway is downregulatded: is it because the inhibition of TGF-β *per se*, or is it a result of a loss of CAFs? In our data, when TAGLN expression is normalized to that of PDGFRβ the total decrease that we observed in treated mice becomes attenuated, suggesting that the total loss of CAFs highly contributes to the reported shut-down of the TGF-β program in fibroblasts. In agreement with this observation, when the TGF-β pathway is inhibited specifically in CAFs by genetic deletion of the TGFBR2 the amount of observed GFP+ PDGFRβ+ events is reduced compared to mice bearing a WT allele of the *Tgfbr2*. This reduction is translated into a global loss of TAGLN expression in the TME (**Figure 52**).

To explain this apparent loss of CAFs. We suggest two possibilities which are currently under investigation:

1) As TGF-β induces proliferation in fibroblasts (**Kalluri, 2016**), we could suspect that CAFs become arrested upon inhibition of the TGF-β pathway. Given that tumours are "addicted" to the presence of CAFs to ensure their progression survival (**Calon et al., 2012; Lisanti et al., 2013**), a *de novo* generation of *Tagln*+ CAFs from newly activated LMCs or unrecombined CAFs could compensate the arrest of KO CAFs. This could result in the reduction in the proportion of GFP+ KO CAFs, but not necessarily of the overall numbers of CAFs.
2) The chronic activation of CAFs by TGF-β in the TME could create a "TGF-β addiction

status" in CAFs. Several reports point to an irreversible activation of CAFs through epigenetic changes in their genetic program (**Albrengues et al., 2015; Bechtel et al., 2010; Hu et al., 2005; Mrazek et al., 2014**), and TGF-β could mediate this epigenetic switch (**Cardenas et al., 2014; Chan et al., 2008**). One of the effects of this epigenetic activation is the inhibition of apoptosis in CAFs (**Huang et al., 2013**). We could speculate that TGF-β inhibition reverts the epigenetic status in CAFs, resulting in a total loss of CAFs by apoptosis. A possible outcome for this phenomenon is that the numbers of GFP+ events we detect are those CAFs that are resilient to the recombination of the *Tgfbr2* or have undergone incomplete recombination.

3.4. Long-term T cell infiltration is not affected by the loss of TGF-β pathway in CAFs

Given the fact that recombination in our model affects TGF-β-activated CAFs, this brings the genetic ablation experiments close to the setting of established metastases, rather than the stage of initiation (**Tauriello et al., 2018**). Although treatment of established metastases with Galunisertib did not yield a major curative response, metastases became highly infiltrated with T cells (**Tauriello et al., 2018**). Upon deletion of the TGFBR2, metastatic burden is unaltered when either MTO129 or MTO140 are used. In KO mice injected with MTO138, metastatic burden was mildly increased. Such an effect was already reported (**Özdemir et al., 2014**), which seems to agree with the discussed CAF loss. However, we cannot explain why such an increase in metastatic burden happens only when MTO138 is used.

Our analyses on T cell infiltration in mice treated with Galunisertib showed that metastases had an increased T cell density upon TGF-β inhibition (**Tauriello et al., 2018**). To our surprise, specific ablation of the TGF-β pathway in CAFs in further experiments did not affect T cell exclusion. The density of T cells in metastases from KO mice remained unaltered by the experimental end point, and this was consistent for every analysed experiment. Moreover, the dynamics of T cell infiltration in KO mice remained invariable compared to the dynamics we reported in control mice (**Tauriello et al., 2018**).

Nevertheless, CD3+ T cells were highly infiltrating metastases in KO mice immediately four days after an acute treatment with tamoxifen. This effect was not manifested in the T cell dynamics, probably because the first analysed time-point was later than four days (treatment started at day 7 after inoculation of MTOs, first time-point was at day 13). This could suggest that genetic ablation of the TGF-β induces a short-lived adaptive response that stabilizes back to basal values days later. After a long-term treatment, metastases from KO mice show enrichment in CD44+CD62L+ memory T cells and CD19+ B cells. In agreement with our observations, a consequence of the acute T cell-mediated response could be the generation of immunologic memory (**Figure 52**). Previous investigations have demonstrated that the abundance of memory T cells and B cells is correlated with favourable outcome (reviewed in **Pagès et al., 2010**).

3.5. Immune checkpoint therapy synergises with TGF-β pathway inhibition in CAFs to produce curative effects

In **Tauriello et al., 2018**, we showed that mice with overt metastatic disease strongly responded to a combinational therapy of TGF-β inhibitors with checkpoint immunotherapy. Despite the fact that ablation of TGFBR2 in CAFs did not result in a long-term increase in T cell infiltration, we found striking responses when KO mice were treated with antibodies against PD-L1, which were comparable to what we previously reported (**Tauriello et al., 2018**, **Figure 52**). One possibility could be that treatment with αPD-L1 takes advantage from the early responses observed after acute treatment with tamoxifen. In addition, a recent study has reported that checkpoint therapy does not only trigger proliferation and activation of effector CTLs, but also converts memory T cells into effector memory T cells, which consequently contribute to the anti-tumour cytotoxic response (**Kurtulus et al., 2019**). Therefore, our reported increase in memory T cells could also take part in the favourable responses obtained with checkpoint therapy.

For the experiments represented in **Figure 44**, a 50% of KO mice treated with αPD-L1 experienced complete remissions. A 12.5% of control mice treated with αPD-L1 responded to monotherapy as well, which reproduces the previously reported responses (**Tauriello et al., 2018**). However, the response rate in KO + αPD-L1 was below the effect of dual therapy using galuniertib (**Tauriello et al., 2018**). This is likely to happen because of the variability in the recombination efficiency and the low penetrance of the Cre discussed earlier. On the other hand, this cure rate was not observed for the experiments represented in **Figures 45 and 46**, although mice experienced a reduction in metastatic burden and improved survival.

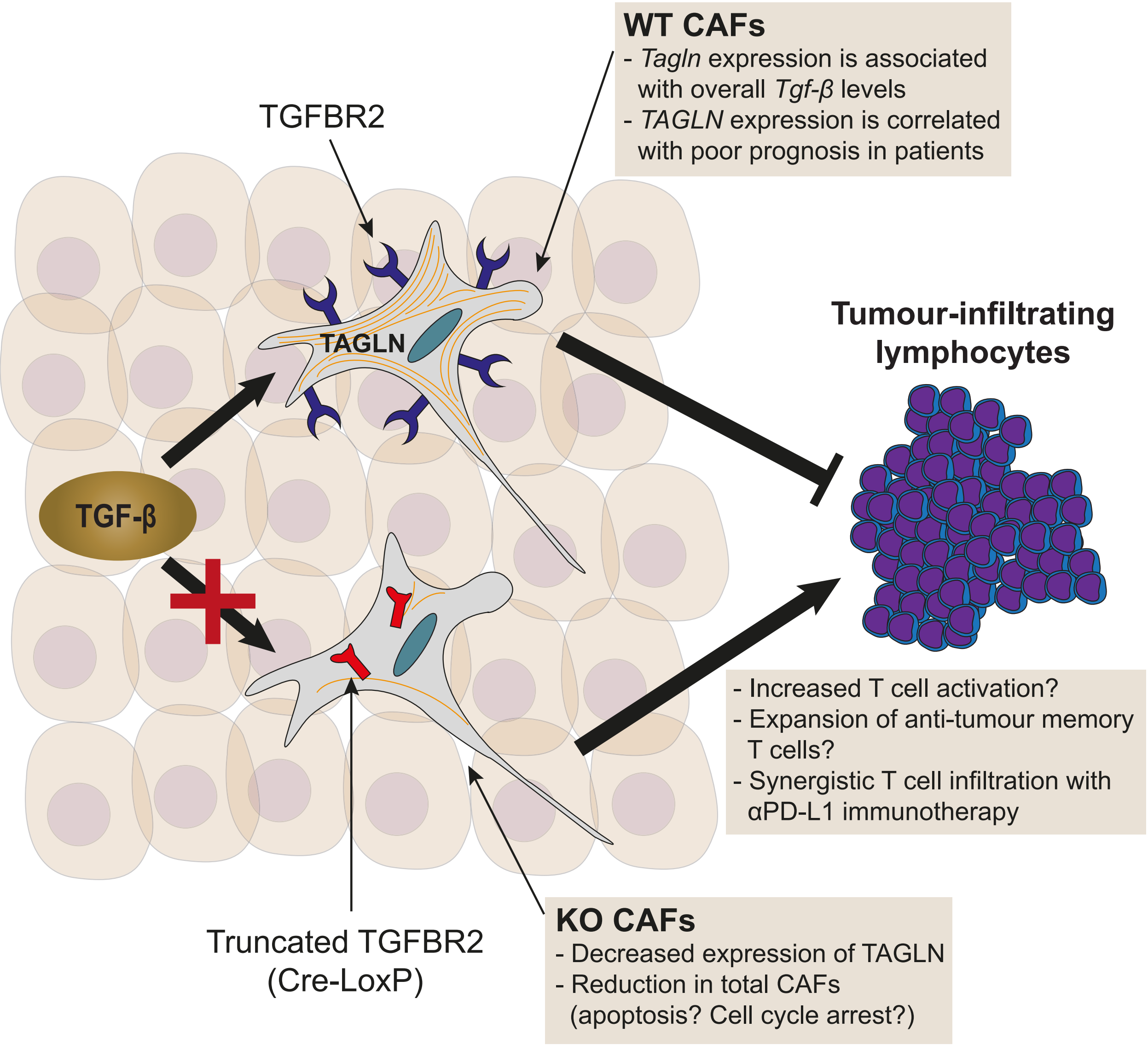
WT CAFs
- *Tagln* expression is associated with overall *Tgf-β* levels
- *TAGLN* expression is correlated with poor prognosis in patients
TGFBR2
TAGLN
Tumour-infiltrating lymphocytes
TGF-β
- Increased T cell activation?
- Expansion of anti-tumour memory T cells?
- Synergistic T cell infiltration with αPD-L1 immunotherapy
Truncated TGFBR2 (Cre-LoxP)
KO CAFs
- Decreased expression of TAGLN
- Reduction in total CAFs (apoptosis? Cell cycle arrest?)

Figure 52. Hypothetical model of the immune-derived effects of TGFBR2 ablation in CAFs. CAFs from CRC liver metastases express *Tagln*, a TGF-β target that is associated with poor prognosis in patients. When the TGFBR2 is genetically ablated in CAFs, there is an overall reduction of activated fibroblasts in liver metastasis. Whether if such reduction is due to apoptosis or cell cycle arrest remains to be elucidated. When genetic recombination is combined with immunotherapy using antibodies against PD-L1, a strong adaptive immune response is achieved, prolonging and synergizing with a short-lived acute T cell infiltration increase upon CAF recombination alone. Thus, we can hypothesise that TGF-β-activated, TAGLN+ CAFs contribute to resistance to immunotherapy.

In these particular cases, metastatic burden in control mice with IgG was higher compared to the previous experiments (average of 250-300 counted nodules versus 90), which make the complete remission upon treatment much more difficult.

Mice treated with αPD-L1 showed three different responses: 1) complete remissions, 2) stable disease and 3) progressive disease. While in the first group no tumour material remained to analyse, somewhat surprisingly, KO mice with stable disease showed an increased T cell infiltration compared to their counterparts. This indicates a synergistic effect between TGFBR2 ablation in CAFs and the checkpoint blockade therapy. This effect was also observed when mice were treated with an acute dosage, which resulted in noticeable early responses in three KO mice treated with αPD-L1. For the mice with progressive disease, we speculate that most (if not all) metastases were refractory to genetic recombination of the *Tgfbr2* in CAFs. Given the fact that cured mice cannot be included into the analysis, it is of special relevance to gain more insight into the early responses after an acute treatment in future experiments.

4. Final remarks and future directions

The presented data suggest that CAFs are important contributors to immune exclusion through TGF-β signalling. With this work, we establish a connection between all three clinical predictors of the TME in CRC –TGF-β expression, the fibroblast TGF-β response gene signature and T cell infiltration- beyond the correlative data (**Calon et al., 2012, 2015; Chakravarthy et al., 2018; Galon et al., 2006; Mariathasan et al., 2018; Pagès et al., 2005; Tauriello et al., 2018**). Mechanistically speaking, we still lack conclusive evidence on the specific effects of TGF-β inhibition in CAFs on the tumour immune microenvironment. Nevertheless, we suggest three hypothesis that are currently under investigation:

1) As the main sources of TGF-β, the possible depletion of CAFs as a result of TGF-β inhibition could consequently dampen the global levels of extracellular TGF-β in the TME. Consequently, this reduction would phenocopy the effects reported previously using Galunisertib (**Tauriello et al., 2018**).
2) *Tagln* expression could define a novel CAF subpopulation with a role in immune suppression. Taking this hypothesis, the effects of TGFBR2 depletion could be subdivided into two alternatives, which depend on the fate of recombined CAFs. Therefore, inhibition of the TGF-β pawthway in CAFs could a) deplete the TAGLN+ immunosuppressive CAF subpopulation or b) induce changes into the transcriptional program related to immune-related cytokines and chemokines. Either way, it is of particular interest to improve the conditions for genetic recombination to genetically characterize the TAGLN-expressing CAFs.
3) According to what has been reported (**Salmon et al., 2012**), TGF-β inhibition could result in changes in the ECM composition that ultimately alter the immune landscape.

Our analyses on T cell responses started as a parallelism with our previous investigations in **Tauriello et al., 2018**. Although combined treatment of Galunisertib with PD-L1 antibodies leads to noticeable T cell responses, it seems that T cell infiltration is not stably improved by genetic recombination of the *Tgfbr2* in CAFs alone. Thus, our current partial phenocopy indicates that global stromal TGF-β inhibition with Galunisertib may have additional relevant therapeutic targets besides CAFs alone. Nevertheless, these results indicate a critical immune evasive role for TGF-β signalling in CAFs. TGF-β inhibition in CAFs could actually result into subtle changes into the activation status of T cells. To tackle this possibility, we are making use of the RNA sequencing of single cells to unravel how T cell activation is altered upon recombination in CAFs. Alternatively, we will also explore additional responses in distinct subsets of immune cells that could also converge into the reported responses.

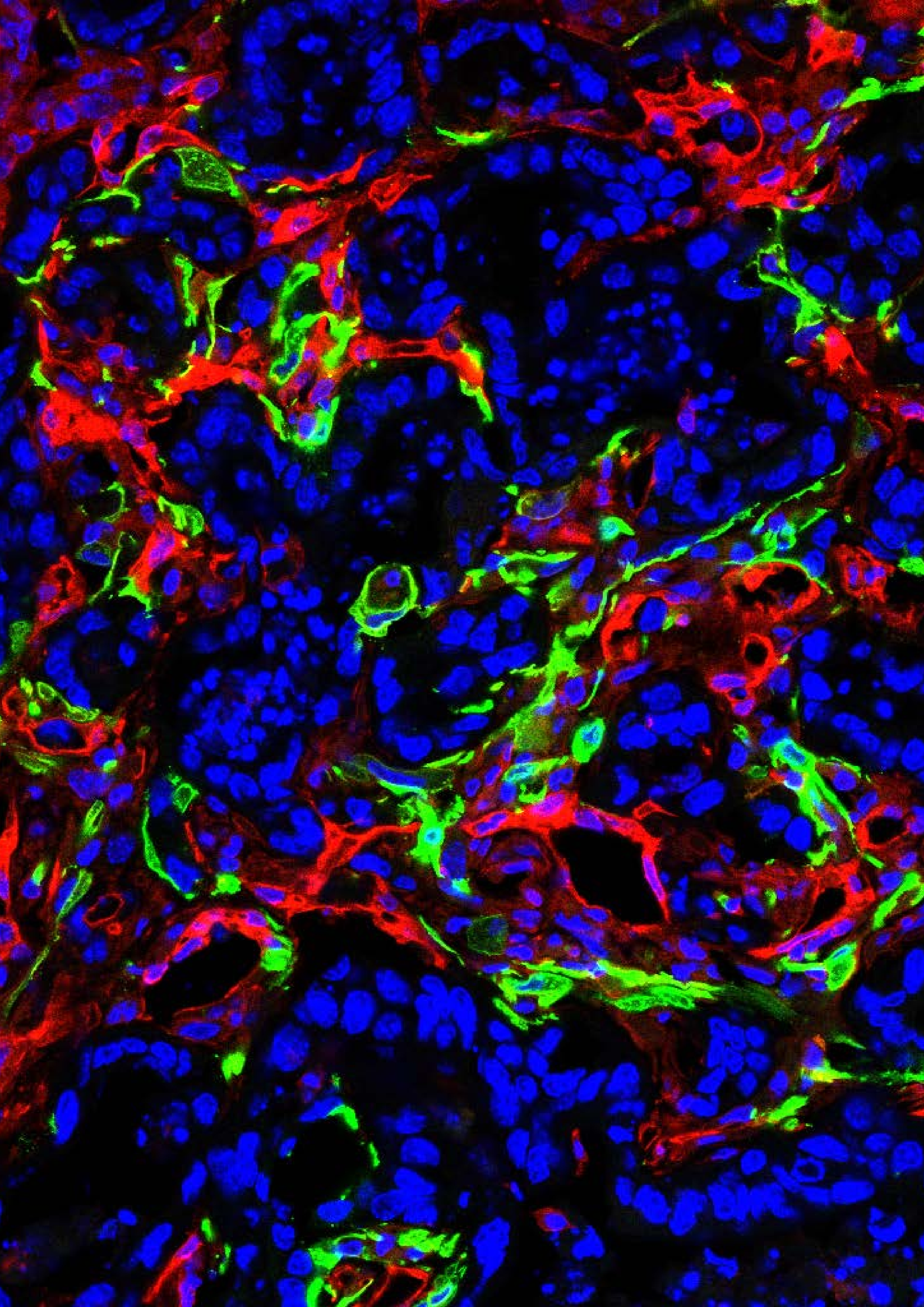

CONCLUSIONS

"Science, for me, gives a partial explanation for life. In so far as it goes, it is based on fact, experience and experiment."

- Rosalind Franklin

Chapter 1: TGF-β drives immune evasion in genetically reconstituted colon cancer metastasis

1. For a successful growth, liver metastases from MSS CRC avoid T cell infiltration.

2. TGF-β is critical for blocking an anti-tumour adaptive immunity during liver colonization and metastatic initiation. When the TGF-β pathway is blocked in the TME with Galunisertib, T cell responses are restablished, thus impairing metastatic growth.

3. Ubiquitous genetic recombination of the TGFBR2 also leads to a decrease of metastatic burden by allowing T cell activation and infiltration into metastases.

4. TGF-β inhibition alone in the TME of established metastases does not completely block metastatic growth, although T cell infiltration and activation is increased upon treatment.

5. Upon activation, T cells upregulate surface expression of PD-1, which blocks T cell-mediated tumour cell killing after binding PD-L1 expressed in the TME.

6. Dual inhibition of TGF-β and PD-1/PD-L1 pathways produce synergistic effects on T cell infiltration and activation, which ultimately leads to dramatic curative responses in mice.

Chapter 2: Unravelling the biology of CAFs in liver metastasis

7. At least two distinct subpopulations coexist within liver metastases from CRC: α^{+}/β^{+} CAFs that coexpress PDGFRα and PDGFRβ, and α^{-}/β^{+} myofibroblasts that express PDGFRβ and αSMA, but not PDGFRα.

8. α^{+}/β^{+} CAFs are enriched in the periphery of metastases, while α^{-}/β^{+} myofibroblasts occupy most of the CAF compartment in the centre of metastases.

9. α^{+}/β^{+} CAFs retain enhanced proliferative capabilities, as they expressed increased levels of KI67 compared to α^{-}/β^{+} myofibroblasts.

10. CAFs from CRC liver metastases are likely to arise from local precursors, and not from bone marrow-derived progenitors.

11. Metastases arisen from different MTOs produce a stroma with distinct proportions of α^{+}/β^{+} and α^{-}/β^{+} CAFs.

12. The relative abundance of α^{-}/β^{+} myofibroblasts is correlated with the phenomenon of T cell exclusion in liver metastases.

13. α^{+}/β^{+} and α^{-}/β^{+} CAFs differ in production of immune cytokines. Consequently, the relative proportions of both subpopulations impact on the TME generated in liver metastases.

Chapter 3: TGF-β-activated CAFs are pivotal for the lack of responses to checkpoint immunotherapy in CRC

14. *TAGLN* is a TGF-β target gene expressed in CAFs in from CRC in human patients. Its expression is enriched in CMS4 CRC tumours and can predict patient prognosis.

15. In the liver, TAGLN is specific for CAFs in liver metastases generated from MTOs. Treatment with Galunisertib abrogates *Tagln* expression in CAFs.

16. *Tagln-Cre*^{ERT2} mice target specifically CAFs and activated LMCs from livers with overt metastatic disease.

17. Recombination efficiency is subjected to the overall expression of *Tagln* in metastases, which differs depending on the MTO of origin.

18. Genetic recombination of the TGFBR2 in CAFs leads to the loss of CAFs, which consequently decreases the overall *Tagln* expression in the TME.

19. Metastatic burden is not decreased upon ablation of the TGFBR2 in CAFs.

20. Acute recombination of the TGFBR2 in CAFs leads to an increased T cell infiltration.

21. Genetic recombination of the TGFBR2 in CAFs does not affect long-term T cell infiltration in liver metastases, but KO mice show increased proportions of B cells and memory T cells.

22. Treatment with monoclonal antibodies against PD-L1 in KO mice leads to a decrease in metastatic burden. Genetic recombination of the TGFR2 synergises with PD-L1 inhibition, resulting in an increase of T cell infiltration in liver metastases.

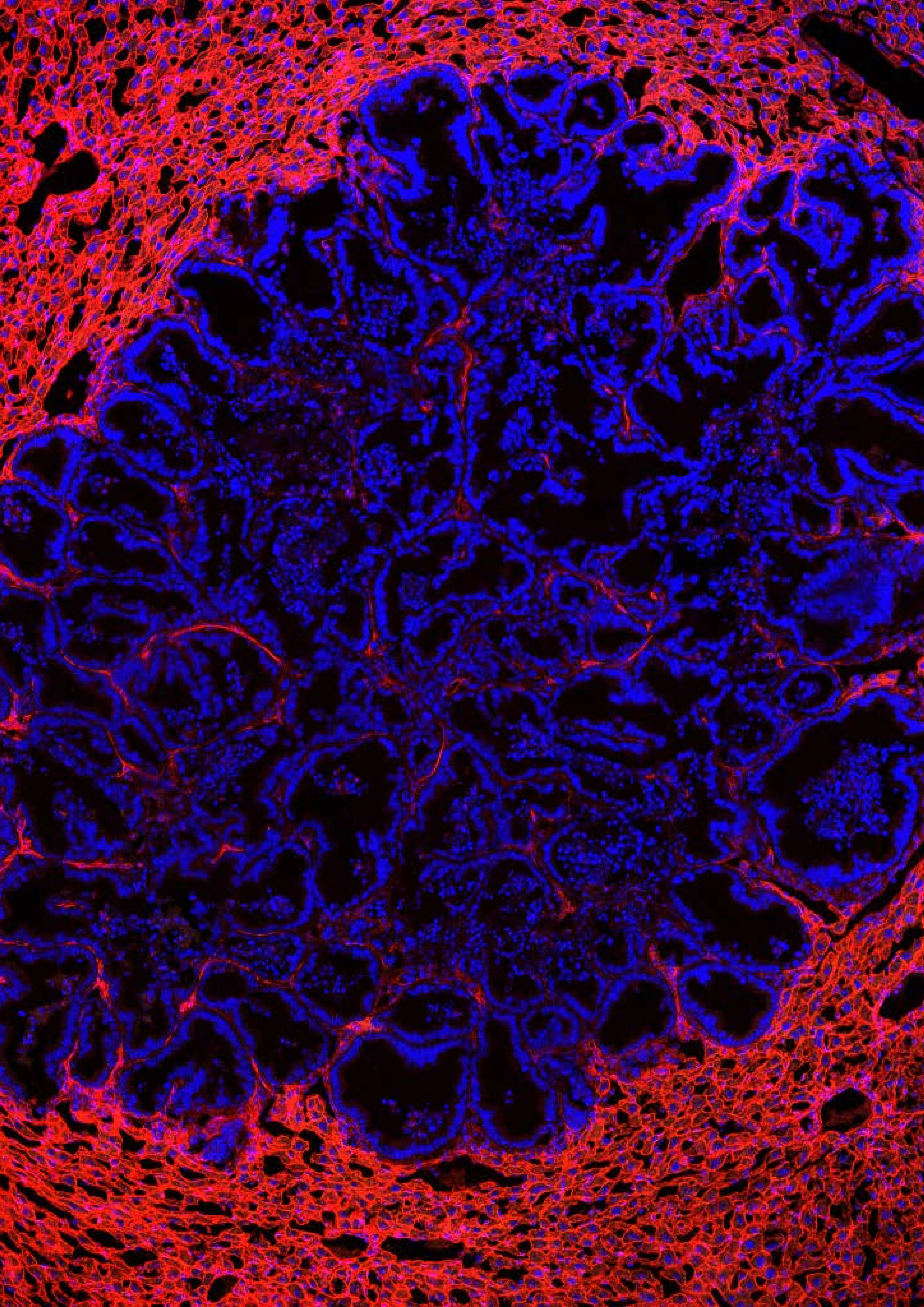

METHODOLOGIES

“I was taught that the way of progress was neither swift nor easy.”

- Marie Curie

Ethics and mice maintenance

All experiments using mouse models were approved by the Animal Care and Use Committee of Barcelona Science Park (CEEA-PCB) and the Catalan Government. Mice were maintained in a specific-pathogen free facility (SPF) with a 12-hour light-dark cycle and being given *ad libitum* access to a standard diet and water. Mice welfare was monitored by an expert team in the animal house and by Sergio Palomo-Ponce. Crosses and weanings were performed by Sergio Palomo-Ponce.

Mice models and genotyping

6-week old C57BL/6J mice were purchased from Janvier Labs. Col1a2-CRE^{ERT} (Tg(Col1a2-cre/ERT,-ALPP)7Cpd/J; stock 029235), GFAP-CRE^{ERT2} (B6.Cg-Tg(GFAP-cre/ERT2)505Fmv/J; stock 012849), Tgfbr2^{loxP} (B6.129-*Tgfbr2*^{tm1Karl}/J; stock 012603) and ROSA^{mTmG} (B6.129(Cg)-Gt(ROSA)26Sortm4 (ACTB-*tdTomato-eGFP*)Luo/J; stock 007676) mouse strains (**Ganat et al., 2006; Levéen et al., 2002; Muzumdar et al., 2007; Zheng et al., 2002**) were obtained from the Jackson Laboratory. *Pdgfrα-CRE*^{ERT2} (**Rivers et al., 2008**) were a kind gift from Salvador Aznar's laboratory in IRB. *Tagln-Cre*^{ERT2} (**Kühbandner et al., 2000**) were a kind gift from Robert Feil's laboratory.

For gDNA extraction, tail fragments were obtained from mice after weaning. Tails were digested using a tail lysis buffer solution (1 M Tris/HCl, 5 M NaCl, 10% SDS, 0.5 M EDTA) and 2% proteinase K (Life Technologies, ref: 10407583) O/N at 55ºC. Fragments were precipitated by centrifugation at 13.200 rpm for 15 minutes and DNA was extracted by mixing the supernatant with isopropanol. DNA was washed with 70% ethanol and resuspended in distilled water. All mice were genotype using standard PCR protocols using primers detailed in **Table 2**.

Intrasplenic injection

Intrasplenic transplantation of MTOs was performed by Sergio Palomo-Ponce or Xavier Hernando-Momblona as described in **Tauriello et al., 2018**. Mice were randomized in order to decrease technical bias. For the *Tagln-Cre*^{ERT2} genetic model, mice with different genotypes were randomized unbiased to avoid technical artefacts.

Mice treatments and genetic recombination

Galunisertib (LY2157299) was synthesised in house and prepared as previously described (**Calon et al., 2012**). Galunisertib and vehicle were administered twice a day by oral gavage in a volume of 150 µl, starting at day 13 after MTO transplantation. A total dose of 1.44 g/kg of galunisertib a day was administered per mice. For immunotherapy, rat PD-L1 (10F.9G2; BioXCell BE0101) or control rat IgG2b (LTF-2; BioXCell BE0090) were administered as described in **chapter 1** (**Tauriello et al., 2018**).

Recombination for all genetic models was achieved by administration of 200 mg/kg of tamoxifen (sigma, ref: T5648). For each administration, 200 µl were injected intraperitoneally. For acute treatment, one daily shot was administered for three consecutive days, starting at day 18 after MTO transplantation. For long-term treatment, one shot was administered every 3-4 days, starting at day 7 after MTO transplantation until the experimental end point. For the survival analysis in **Section 3.9** (**Figure 46**), tamoxifen treatment was interrupted at day 29 after tumour transplantation.

In vivo imaging

For *in vivo* monitoring of tumour growth, MTO129 and MTO138 were previously engineered to express the luciferase enzyme (**Tauriello et al., 2018**). Transplanted mice received 50 µl of a luciferin solution (D-luciferin K-salt, Resem) by retroorbital injection. The

Table 2. Primers used for mice genotyping. For *Tagln-Cre^{ERT2}* and *mT/mG*, the size of WT and KI bands is indicated.

PRIMER	SEQUENCE	
Pdgfra-Cre_F	CAGGTCTCAGGAGCTATGTCCAATTTACTGAACGTA	
Pdgfra-Cre_R	GGTGTTATAAGCAATCCCCAGAA	
Col1a2-Cre_F	TCCAATTTACTGACCGTACACCAA	
Col1a2-Cre_R	CCTGATCCTGGCAATTTCGGCTA	
Gfap-Cre_F	GCAACGAGTGATGAGGTTCGCAAG	
Gfap-Cre_R	TCCGCCGCATAACCAGTGAAACAG	
Tagln-Cre_F	CTCAGAGTGGAAGGCCTGCTT	
Tagln-Cre_R1 (WT)	CACACCATTCTTCAGCCACA	WT band = 276 bp
Tagln-Cre_R2 (KI)	GGCGATCCCTGAACATGTCC	KI band = 220 bp
mT/mG_F	CTCTGCTGCCTCCTGGCTTCT	
mT/mG_R1 (WT)	CGAGGCGGATCACAAGCAATA	WT band = 330 bp
mT/mG_R2 (KI)	TCAATGGGCGGGGGTCGTT	KI band = 250 bp
Tgfbr2-flox_F	TATGGACTGGCTGCTTTTGTATTC	
Tgfbr2-flox_R	TGGGGATAGAGGTAGAAAGACATA	

administered luciferin acted as a substrate for the luciferase, and emmited photons as a product of the enzymatic reaction. Emitted photons were quantified using the IVIS Spectrum In Vivo Imaging System (Perkin Elmer) and Living Image® software (v4.5.2, Perkin Elmer).

Bone marrow transplantation

C57BL/6J mice were irradiated with sub-lethal doses of 2x 4 Gray. GFP+ donor bone marrow was extracted from femurs from recombined *Sox2-Cre^{ERT2}*; *mTmG* mice and cleaned of erythrocytes using red blood lysis buffer. 1 million cells per recipient were injected by retro-orbital injection into irradiated C57BL/6J. Mice irradiation and bone marrow reconstitution was performed by a professional team from the Parc de Recèrca Biomèdica de Barcelona (PRBB) animal facility.

Single cell suspension preparation for flow cytometry

Dissected tumours from livers *ex vivo* were minced with blades until pieces were not bigger than 1 mm^3. The tissue was enzymatically digested in 2 ml of DMEM supplemented with 2% fetal bovine serum (FBS, Gibco, ref: 10270-106) and containing 0.2 mg/ml Collagenase IV (Sigma, ref: C5138), 0.2 mg/ml Dispase II (Sigma, ref: D4693) and 0.04 mg/ml DNase I (Sigma, ref: 10104159001). Enzymatic digestion followed 4 cycles of 20 minutes each at 37ºC, which included three steps of mechanical disaggregation every 5 minutes. Mechanical forces consisted on vortexing for cycles 1 and 2, pipetting with widened tips for cycle 3 and pipetting with normal 1 ml tips for cycle 4. After the third round of mechanical disaggregation, pieces were left to precipitate and the supernatant was recollected and kept in FACS buffer (PBS + 2% FBS + 5mM EDTA + 5% bovine serum albumin [BSA, Roche, ref: 10735086001]) on ice. Then, remaining pieces were resuspended in 2 ml of fresh digestion medium, to start a new cycle of 20 minutes. After cycle 4, complete disaggregation could be observed. The cell suspension in FACS buffer was filtered using 100 µm strainers (Corning) and erythrocytes were removed using a red cell lysis buffer (NH_4CL 150 mM, potassium bicarbonate 10 mM, EDTA 0.1 mM). Single cells were resuspended in FACS buffer and counted.

1-2 million cells were used per staining reaction. Cells were incubated with FACS buffer containing blocking antibodies against CD16/CD32 at 4ºC for 20 minutes to block the Fc receptor. Mix of conjugated antibodies were added to the cell suspension in the presence of anti-CD16/CD32 and cells were stained for 20 minutes at 4ºC. Conjugated antibodies are described in **Table 3**. When cells were to be sorted, viability was determined by nuclear staining with DAPI (Sigma). For analysis panels, cells were washed with PBS and labelled for viability using the Yellow LIVE/DEAD Fixable Cell Dead stain kit (Life technologies) for 8 minutes at RT.

Table 3. Antibodies used for cytometry.

ANTIBODY	CLONE	COMPANY	REFERENCE
CD103-BV421	2E7	BioLegend	121421
CD11b-BV711	141/70	BioLegend	101241
CD140a-PE (PDGFRa)	APA5	BD Biosciences	562776
CD140b-APC (PDGFRb)	APB5	Invitrogen	17-1402-82
CD16/32	2.4G2	Tonbo Biosciences	70-0161-U500
CD19-BV711	ID3	BD Biosciences	563157
CD3e-PerCP-Cy5.5	145-2C11	BD Biosciences	561108
CD31-PeCy7	390	Abcam	ab46733
CD4-FITC	GK1.5	eBiosciences	11-0041-81
CD44-BV421	IM7	BD Biosciences	563970
CD45-APCef780	30-F11	eBiosciences	47-0451-82
CD62L-APC	MEL-14	BD Biosciences	553152
CD8a-APC	53-6.7	eBiosciences	17-0081-81
CD8a-BV711	53-6.7	BioLegend	100759
Epcam-BV605	G8.8	BD Biosciences	740389
NK1.1-PE-Cy7	PK 136	BioLegend	108714

Flow cytometry analysis and sorting

Mice with unresectable liver metastases were excluded from the analysis. To select CAFs and LMCs, the gating strategy described in **Figure 2** was followed. An initial negative selection of tumour epithelial cells was performed by selecting Cells/Single cells/Live cells/ EPCAM-. Tumour epithelial cells were selected by EPCAM+ staining. Triple Negative (TN) population was selected from EPCAM- cells by excluding endothelial cells (CD31+/CD45-) and leukocytes (CD31-/CD45+). From the TN population, PDGFRβ+ was used to select CAFs. Further selection using PDGFRα was used to select α^{+}/β^{+} CAFs (PDGFRα+) or α^{-}/β^{+} myofibroblasts (PDGFRα-). This gating strategy was used to analyse and sort CAFs. For the genetic model, GFP+ events were selected from Cells/Single cells/Live cells/EPCAM-/ CD31-/CD45-/ PDGFRβ+.

For immunophenotyping, total leukocytes were selected by size and shape. From Cells/ Single cells/Live cells, dendritic cells were detected with CD103+/CD11b- and the rest of the myeloid compartment by CD103-/CD11b+. From Cells/Single cells/Live cells/CD103-/CD11b-, B cells were detected by CD19+. NK cells were selected by NK1.1+/CD3-, and T cells by NK1.1-/CD3+. CD3+ T cells were further segregated to helper T cells (CD4+/CD8-) and cytotoxic T cells (CD4-/CD8+). For both CD4+ and CD8+ cells, activation status was determined by CD44+/CD62L-, while naive T cells were determined by CD44-/CD62L+. Memory T cells were determined within CD3+/CD8+ T cells by CD44+/CD62L+. Data were analysed using FlowJo v10.

Isolation, culture and treatment of LMCs

Livers from naive mice were digested following the protocol for tissue enzymatic disaggregation detailed in **Single cell suspension preparation for flow cytometry**. Single cells were seeded in 175 cm^2 cell culture flasks (Corning) and cultured with DMEM (Gibco, ref: 41966-029) + 10% FBS and Normocin (InvivoGen, ref: ant-nr1) until confluence was reached. Medium was changed every 2 days. Confluent cells were then harvested after incubation with Trypsin-EDTA (Gibco, ref: 25300-054) for 10 minutes at 37ºC, and stained for EPCAM, CD31, CD45 and PDGFRβ (see antibody references in **Table 3**). EPCAM-/CD31-/CD45-/PDGFRβ+ cells were sorted by FACS and cultured *in vitro* with DMEM + 10% FBS. FACS purification procedure was repeated twice. For passaging of LMCs, confluent cells were washed with PBS (Gibco, ref: 14190-094) and incubated with Trypsin-EDTA for 5 minutes at 37ºC. FBS was used to quench trypsin reaction. Cells were passaged in a 1:10 ratio.

For treatments with TGF-β and Galunisertib, 500.000 cells were plated in petri dishes and cultured with DMEM + 0.5% FBS. After 1 day, cells become attached to the plate and were treated with recombinant TGF-β (Peprotech, ref: 100-21-10UG) or Galunisertib (in-house) for 24 hours. Cells were then washed with PBS (Gibco), recovered using cell lifters (Corning) and resuspended in Trizol (Life Technologies, ref: 15596018) for further RNA extraction.

In vitro culture of MTOs

Isolation of tumour cells for generation of MTOs was described previously (**Tauriello et al., 2018**). For organoid growth, single cells were embedded into a 70% solution of cold BME (Cultrex, ref: 3533-005-02) in PBS (Gibco, ref: 14190-094). 5-10 μl drops of the single cell suspension were placed in pre-heated 6-well culture plates (Costar, ref: 3506) and left 5 minutes at 37ºC to ensure BME polymerisation. MTOs were then maintained in Advanced DMEM F12 supplemented with B27 (Gibco, ref: 12587-010), EGF (Peprotech, ref: AF-100-15), Noggin (in-house, **Tauriello et al., 2018**) and galunisertib (in-house, **Tauriello et al., 2018**) for 3-4 days. Medium was changed every 2 days, and was tested for mycoplasma contamination.

For MTO passaging, drops were washed once with PBS (Gibco) and incubated with Trypsin-EDTA (Gibco, ref: 25300-054) for 20 minutes at 37ºC, followed by mechanical disaggregation by vigorous pipetting until a single cell suspension was obtained. FBS was used to quench trypsin reaction. For passaging, cells were resuspended in a cold solution of 70% BME as described above. Cells were passaged in a 1:6 ratio.

Cell preparation for IS injection

For mouse intrasplenic transplantation, single cells were obtained following the procedure described in ***In vitro* culture of MTOs**. Total number of viable cells was counted using Tripan blue 0.4% (Gibco, ref: 15250-061) and a TC20 Automated cell counter (BIO-RAD). Cells were resuspended in sterile PBS. Cell concentration was adjusted for a 70 μl volume for injection per mouse. For MTO129 and MTO140, 300.000 viable cells were injected per mouse. For MTO138, 500.000 viable cells were injected per mouse.

Immunohistochemistry and immunofluorescence

Organs extracted from mice were fixed in a 10% formalin solution (Sigma, ref: HT501128) O/N at RT, and washed with PBS. Fixed tissues were embedded in paraffin blocks and used to obtain 4 µm sections by an expert team from the histopathology facility in the IRB.

Sections were deparaffinised by serial washes on solutions with a decreasing percentage of alcohol. For antigen recovery, deparaffinised sections were either boiled in a TRIS-EDTA solution (Sigma, ref TRIS: T6066, ref EDTA: E5134) for 20 minutes or autoclaved for 20 minutes at 1 atm of pressure in a citrate buffer at pH 6 (see **Table 4** for specific antigen recovery protocol used for every antibody). Sections were washed using a wash buffer solution from DAKO (ref: K800721) and endogenous peroxidise was blocked using a Peroxidase-Blocking solution from DAKO (ref: S202386) at RT for 10 minutes. For immunofluorescence staining, unspecific unions were blocked using 10% normal donkey serum (Jackson Immunoresearch, ref: 017-00-121) for 20 minutes at RT. Sections were then incubated with the primary antibody (see **Table 4** for antibodies, references and specific incubation protocols)-

For immunohistochemistry staining, after incubation with the primary antibody, sections were incubated with a peroxidase-conjugated secondary antibody (HRP) for 30 minutes at RT, and revealed using a DAB solution (DAKO, ref: K346811) at RT (see **Table 4** for incubation time). Sections were then washed with distilled water and stained with haematoxylin (Panreac, ref: 254766.1611) for 2 minutes at RT. Finally, stained sections were dehydrated by serial washes with alcohol solutions of increasing percentages and mounted with DPX (Panreac, ref: 255254.1608).

For immunofluorescence staining, sections incubated with the primary antibody were incubated with a 1/400 dilution of a fluorescent-conjugated antibody in DAKO diluent (DAKO, ref: K8006) for 1 hour at RT, and next were incubated with secondary antibodies conjugated to Alexa-488, Alexa-568 and Alexa-647 (Life Technologies). After incubation with the sec-

Table 4. Antibodies and specific conditions for IHC. CD11b was only used for IF. D.D = Dako Diluent (DAKO, ref: K8006). BSA = bovine serum albumin (Roche). 1% BSA was diluted in wash buffer.

ANTIBODY	ANTIGEN RETR.	REF	DILUTION	IHQ CONDITIONS	DAB
αSMA	Citrate	BIOGENEX, MU128-UC	1/400 D.D.	2 h RT	1 min
CALD1	Citrate	Sigma, HPA008066	1/250 BSA 1%	O/N 4ºC	30 s
CD11b	N/A	Abcam, ab133357	N/A	N/A	N/A
CD3	TRIS-EDTA	Dako, IS50330	1/10 BSA 1%	1 h RT	1 min
GFP	Citrate	Life Tech., S202386	1/1000 D.D.	40 min RT	2 min
IGFBP7	Citrate	Sigma, HPA002196	1/200 BSA 1%	O/N 4ºC	2 min
KI67	Citrate	Novocastra Clone MM1	1/1000 D.D.	1 h RT	2 min
PDGFRα	Citrate	RD Systems, AF1062	1/200 BSA 1%	O/N 4ºC	40 s
PDGFRβ	Citrate	Ther. Scient. MA5-14851	1/100 D.D.	O/N 4ºC	5 min
TAGLN	TRIS-EDTA	Proteintech, 10493-1-AP	1/100 D.D.	O/N RT	5 min
tdTOMATO	TRIS-EDTA	Sicgen, AB8181-200	1/250 D.D.	O/N 4ºC	1 min

PEROXIDASE SECONDARY ANTIBODY	HOST AFFINITY
Immunoresearch, DPVR-110HRP	Rabbit
Dako, PO447	Mouse
Immunoresearch, DPVG55HRP	Goat

ondary antibody, nuclei were stained with a 1/2500 DAPI solution (Sigma) in DAKO wash buffer for 10 minutes at RT. Finally, stained sections were mounted using a fluorescent mounting medium (DAKO, ref: S3023-80).

Histological analyses

Images for IHC were taken with a Nikon DS-Ri1 camera or with a Hamamatsu NanoZoomer Digital Slide Scanner (20X magnification). Images for IF were taken with a Leica TCS SP5 spectral confocal multiphoton microscope or with a Hamamatsu NanoZoomer Digital Slide Scanner (20X magnification).

Positive staining from NanoZoomer images was quantified using Qupath (v0.2.0-m2, **Bankhead et al., 2017**). Several ROIs delimiting tumours were taken per section. Tumours with faulty staining or damaged areas due to technical errors were excluded from analysis. Necrotic areas were excluded from the ROIs. For CD3 staining, positive cells were counted using the “positive cell detection” feature with empirical parameters. For PDGFRβ, αSMA and TAGLN, total positive pixels per area were quantified using the “positive pixel count” feature. Data was analysed using Graphpad Prism (v7.03).

RNA extraction from whole tumours

Whole individual tumours were excised from livers *ex vivo* and mechanically disaggregated in 1 ml of Trizol (Life Technologies, ref: 15596018) using a tissue disruptor. Disaggregated tissues in Trizol were stored in -80ºC until processing. For RNA extraction, samples in Trizol were thawed. 200 µl of chloroform (Sigma, ref: 372978) were then added and samples were vigorously mixed for 15 seconds. Mixed samples were centrifuged at 12.000 g for 15 minutes at 4ºC, after which a colourless upper phase containing the RNA was separated from the mix. The upper phase was extracted, placed in new tubes and mixed with one volume of 70% ethanol. The mix was then processed using a PureLink® RNA Mini Kit (Life technologies, ref: 12183025) following the manufacturer’s specifications.

mRNA was eluted using distilled water (Invitrogen, ref: 10977-035) and the concentration was determined using the Nanodrop 1000 spectrophotometer (Thermofisher). For cDNA synthesis, 2000 ng of RNA were used for the cDNA conversion using the High Capacity cDNA reverse transcription kit (Life Technologies, ref: 4368813) following the manufacturer’s specifications. After cDNA was synthesised, distilled water was added to reach a final concentration of 10 ng/µl of cDNA.

RNAsequencing of MTOs

mRNA harvesting from MTOs and sequencing was described in chapter 1 (**Tauriello et al., 2018**).

mRNA extraction and cDNA synthesis for reduced number of cells (picoprofling)

For mRNA extraction from a reduced number of cell, 1000 cells were sorted and processed by a professional team in the functional genomics facility of IRB as previously reported (**Gonzalez-Roca et al., 2010**). The cDNA concentration was determined using the Nanodrop 1000 spectrophotometer. A volume of the final cDNA solution was diluted in distilled water (Invitrogen, ref: 10977-035) to reach a concentration of 10 ng/µl of cDNA.

Gene expression analysis

To assess mRNA expression levels, qRT-PCR was performed with triplicate reactions, each containing 10 ng of cDNA, using a StepOne instrument (Thermo Fisher) and Taqman probes. See **Table 5** for used probes. *Ppia* and *Actb* were used as normalisers for gene expression.

Table 5. Taqman probes used for gene expression analysis.

GENE	TAQMAN PROBE
Acta2	Mm_00728412_s1
Actb	Mm_00607939_s1
Cald1	Mm_01129541_m1
Ccl5	Mm_01302427_m1
Ccl9	Mm_00432087_m1
Ccl12	Mm_01617100_m1
Col1a1	Mm_08801666_g1
Col1a2	Mm_00483888_m1
Cre enzyme	1535842
Csf2	Mm_01290062_m1
Cxcl9	Mm_00434946_m1
Cxcl10	Mm_00445265_m1
Cxcl12	Mm_00445553_m1
Epcam	Mm_00493214_m1
Igfbp7	Mm_03807886_m1
IL-6	Mm_00446190_m1
IL-10	Mm_01288386_m1
IL-11	Mm_00434159_m1
IL-33	Mm_00505403_m1
mki67	Mm_01278671_m1
Pdgfra	Mm_00440701_m1
Pdgfrb	Mm_00435546_m1
Pecam1 (*Cd31*)	Mm_00476702_m1
Postn	Mm_00450111_m1
Ppia	Mm_02342430_g1
Ptprc (*Cd45*)	Mm_01293577_m1
Serpin	Mm_04335860_m1
Tagln	Mm_00441661_g1
Tgfb1	Mm_01178819_m1
Tgfb2	Mm_00436955_m1
Tgfbr2	Mm_03024091_m1
Tgfb3	Mm_03024091_m1
Tnfa	Mm_00443258_m1

Statistical analysis for mouse samples.

Column analyses were performed using the statistical package included in GraphPad Prism. For all comparisons, a Fisher's F test was performed to compare variances. When null hypothesis was accepted, an unpaired t student test was performed to compare two groups. Alternatively, when null hypothesis for variance comparison was rejected, a Welch's correction was applied to the t test. For **Figure 45C**, a Mann-Whitney test was used to compare medians between groups.

Correlation analyses from **Figure 26A-C** were performed using the Pearson correlation test with a 95% of confidence interval. For analyses in **Figure 37B-D**, the nonparametric Spearman correlation was computed. To validate consistence of the obtained results, analysis was also performed omitting the outlier with *Tagln Relative Expression* = 9.076.

Pair-wise analysis of Kaplan-Meier survival plot in **Figure 45B** was performed using a Mantel-Cox Log-rank test.

To assess differences in metastatic burden between the four mice groups in **Figure 44F**, a linear model was fitted to the number of grown modules in which experiment run was included as a covariate. The outcome in this model (number of nodules) was previously quadratic-root transformed (x^1/4) in order to fulfil the assumptions of the linear model. A Wald test was used to assess statistical significance, and adjusted group means and corresponding 95% confidence intervals were derived from the linear model. Within each analysis, p-values were adjusted by multiple comparisons using the Westfall method (**Westfall, 1997**). The threshold for statistical significance was set at 5%. To compare the proportions of metastasis-free mice in **Figure 44G**, a Cocchran-Mantel-Haenszel test was used to determine the overall significance stratifying by experiment run using the Montecarlo simulation (**Hothorn et al., 2006**).

Patient data analysis: CRC human meta-cohort

Seven public high-throughput datasets were used for transcriptomic analyses in human tumors (**Table 6**), including five Affymetrix microarray series publicly available in the NCBI GEO repository (**Barrett et al., 2013**) and the TCGA RNAseq datasets for Colon and Rectum tumors (**TCGA**). Consensus Molecular Subtypes (CMS) information was available for most of these samples and was retrieved from (**Guinney et al., 2015**).

Patient data analysis: Pre-processing of TCGA CRC data

RNA-Seq (version 2) data from the The Cancer Genome Atlas (TCGA) project was retrieved from the legacy version of the GDC commons repository (**Grossman et al., 2016**). Clinical and follow-up information was retrieved from the TCGA-Clinical Data Resource (CDR) (**Liu et al., 2018**). Expression measures were expressed in RSEM in the legacy ver-

Table 6. Databases used for transcriptomic analyses in CRC human patients. N = number of patients analysed per database.

DATABASE	N	LINK
GSE14333	290	https://www.ncbi.nlm.nih.gov/pubmed/19996206
GSE33113	90	https://www.ncbi.nlm.nih.gov/pubmed/22496204
GSE39582	562	https://www.ncbi.nlm.nih.gov/pubmed/23700391
GSE38832	122	https://www.ncbi.nlm.nih.gov/pubmed/25320007
GSE44076	98	https://www.ncbi.nlm.nih.gov/pubmed/25253512
TCGA-COAD	393	https://www.cancer.gov/about-nci/organization/ccg/research/structural-genomics/tcga
TCGA-READ	150	https://www.cancer.gov/about-nci/organization/ccg/research/structural-genomics/tcga

sion, which were log2-transformed and quantile normalized. Samples from different tumours (colon and rectum) and from different platforms (Genome Analyzer and HiSeq) were processed separately. Non-primary tumour samples were filtered out and duplicated samples measured in different platforms were excluded from the HiSeq subset. Only primary tumours from patients with no previous cancer diagnosis were kept for analyses. An exploratory analysis was carried out using Principal Component Analyses in order to identify samples with abnormal expression values in each dataset. Samples TCGA-A6-2679-01A and TCGA-AA-A004-01A were excluded as their gene expression showed an anomalous distribution compared to the rest of samples in their dataset, even after quantile normalization. Finally, each dataset was corrected by technical variation using a mixed-effect linear model, in which sample's centre of origin and plate identifiers were modelled as a fixed and a random effect, respectively. Coefficients from the fixed effects and random effects' imputations provided by the models were then used to correct these technical effects.

Patient data analysis: Pre-processing of microarray CRC datasets

Microarray datasets were separately processed using R packages affy (**Gautier et al., 2004**) and affyPLM (**Bolstad et al., 2005**) from Bioconductor (**Gentleman et al., 2004**). Raw cel files data were processed using RMA (**Irizarry et al., 2003**) and annotated using the information available in the Affymetrix web page (**Affymetrix – Thermofisher web page**).

Standard quality controls were performed in order to identify abnormal samples (**Gentleman et al., 2005**) regarding: a) spatial artefacts in the hybridization process (scan images and pseudo-images from probe level models); b) intensity dependences of differences between chips (MvA plots); c) RNA quality (RNA digest plot); d) global intensity levels (boxplot of perfect match log-intensity distributions before and after normalization and RLE plots); e) anomalous intensity profile compared to the rest of samples (NUSE plots, Principal Component Analyses). Technical information concerning samples processing and hybridization was retrieved from the original CEL files: date of scanning were collected in order to define scan batches in each dataset separately; technical metrics described by Eklund and Szallasi (**Eklund and Szallasi, 2008**) were computed and recorded as additional features for each sample. Microarray expression values were summarized at the gene level (entrez) using the first principal component of the probesets mapping to the same gene. This component was centered and scaled to the weighted mean of the means and standard deviations of the probesets using the corresponding contribution to the component as weight. The sign of this gene-based expression summary was imputed so that it was congruent to the sign of the probeset contributing the most to the original first component.

Previously to gene-level summarization, each microarray dataset was corrected a priori by Eklund metrics (**Eklund and Szallasi, 2008**) effects estimated from a standard linear model. In addition, mixed-effect linear models were used to correct microarray expression by the sample's centre of origin (if more than one) and date of scanning (microarrays). Expression values were corrected using the coefficients from the fixed effects and the imputations of the random effects provided by the models.

Patient data analysis: Final CRC transcriptomic pooled cohort (TCGA + GEO)

Datasets were merged after gene-wise standardization (median and median absolute deviation) to the GSE39582 dataset according to their distribution of gender, age, tumour site, MSI and stage, when available. Such standardization was carried out by inverse probability weighting using a logistic regression (LogReg) model. For doing so and for each dataset D, a LogReg model was carried out on D and GSE39582 that included the aforementioned clinical parameters as predictors of the dataset affiliation. Clinical parameters were included in the model as they were informative according to the Akaike Information Criterion (AIC) after running a forward step-wise algorithm for variables selection. Next, conditional probabilities of belonging to datasets D and GSE39582 (Pd and Pr, respectively) were retrieved from the model; then, weights were computed as the ratio of Pd/Pr; finally, weights were truncated to value "five", in order to avoid the overrepresentation of any sample in the standardization process. Expression values were truncated to the maximum and minimum values observed in this reference dataset. As a result, this CRC pooled cohort (TCGA + GEO) included a total of 1.705 primary tumour samples.

Patient data analysis: MSI imputation in transcriptomic CRC samples

When not available in the published clinical information, MSI status was imputed in each dataset separately based on the expression of genes included in a published transcriptomic signature (**Jorissen et al., 2008**). For doing so, Pearson's correlation coefficients were computed between each sample's profile and an artificial MSI profile consisting on "one" values for genes included in the signature that were over-expressed in MSI samples and a "zero" values for genes over-expressed in MSS samples in (**Jorissen et al., 2008**). Assignation to MSI or MSS was performed according to results of a cluster analysis based on non-parametric density estimation (**Azzalini and Menardi, 2014; Azzalini and Torelli, 2007**) on these correlation coefficients. This imputation procedure was performed at the gene level using the entrez identifier and Affymetrix annotation (**Affymetrix – Thermofisher web page**) before correction by technical effects (see **section Pre-processing of microarray CRC datasets**); for doing so, not-corrected microarray datasets were summarized at the gene level by the most variable probeset mapping to the same gene as measured by the median absolute deviation. In each case, the same number of top MSI and MSS over-expressed genes were used in order to avoid biases towards the group that included more genes (MSI). Accuracy of this imputation was evaluated in dataset GSE39582 and TCGA colon dataset, which included annotation of microsatellite-stable (MSS) and -instable (MSI) samples in their clinical information (GSE39582: 97% and 77% accuracy for MSS and MSI samples, respectively; TCGA colon: 97% and 92% accuracy for MSS and MSI, respectively).

Patient data analysis: Cell Population datasets

Two data sets publicly available in the NCBI GEO repository (**Barrett et al., 2013**)http://www. ncbi.nlm.nih.gov/geo/ were used to characterize gene expression in tumour cell subpopulations: GSE39395 and GSE39396 (**Calon et al., 2012**). In these datasets, FACS was used to separate the following populations from 14 fresh CRC samples: CD45+EpCAM−CD31−FAP−, CD45−EpCAM+CD31−FAP−, CD45−EpCAM−CD31+FAP− and CD45−EpCAM− CD31−FAP+. Expression matrices were processed using RMA (**Irizarry et al., 2003**), as described in **section Pre-processing of microarray CRC datasets**.

Patient data analysis: Association analyses with clinical outcome in human CRC datasets

Association with relapse was evaluated using a Cox proportional hazards model, while linear models were used for group comparisons of gene expression levels. In all cases, sample's dataset or origin was included in the models for statistical adjustment.

Statistical significance was assessed by means of a Log-likelihood Ratio Test (LRT, survival analyses) and F-tests (linear models), while Wald tests were used for pair-wise comparisons. Sample groups of low, medium and high expression levels were defined using the tertiles of its distribution as cut-offs. Hazard Ratios (HR) were computed as measures of association. For visualization purposes, Kaplan-Meier survival curves and boxplots were estimated for groups of samples showing low, medium and high gene expression levels.

Also, local Cox proportional hazard ratios estimates by gene expression levels were graphically represented using smoothing splines with a p-spline basis (**Eilers and Marx, 1996**) as implemented in the R package phenoTest (**Planet, 2018**).

Only samples from patients diagnosed in stages I, II and III were taken into consideration for analyses of time to relapse, for a total of 955 CRC samples; out of them 768 samples were Microsatellite Stable tumours (MSS) while 186 were Microsatellite Instable (MSI); TCGA's rectum samples were excluded from prognosis analyses accordingly to recommendations of the TCGA-Clinical Data Resource (CDR) (**Liu et al., 2018**)The Cancer Genome Atlas (TCGA. The threshold for statistical significance was set at 5%. All analyses were carried out using R (**Team, 2018**).

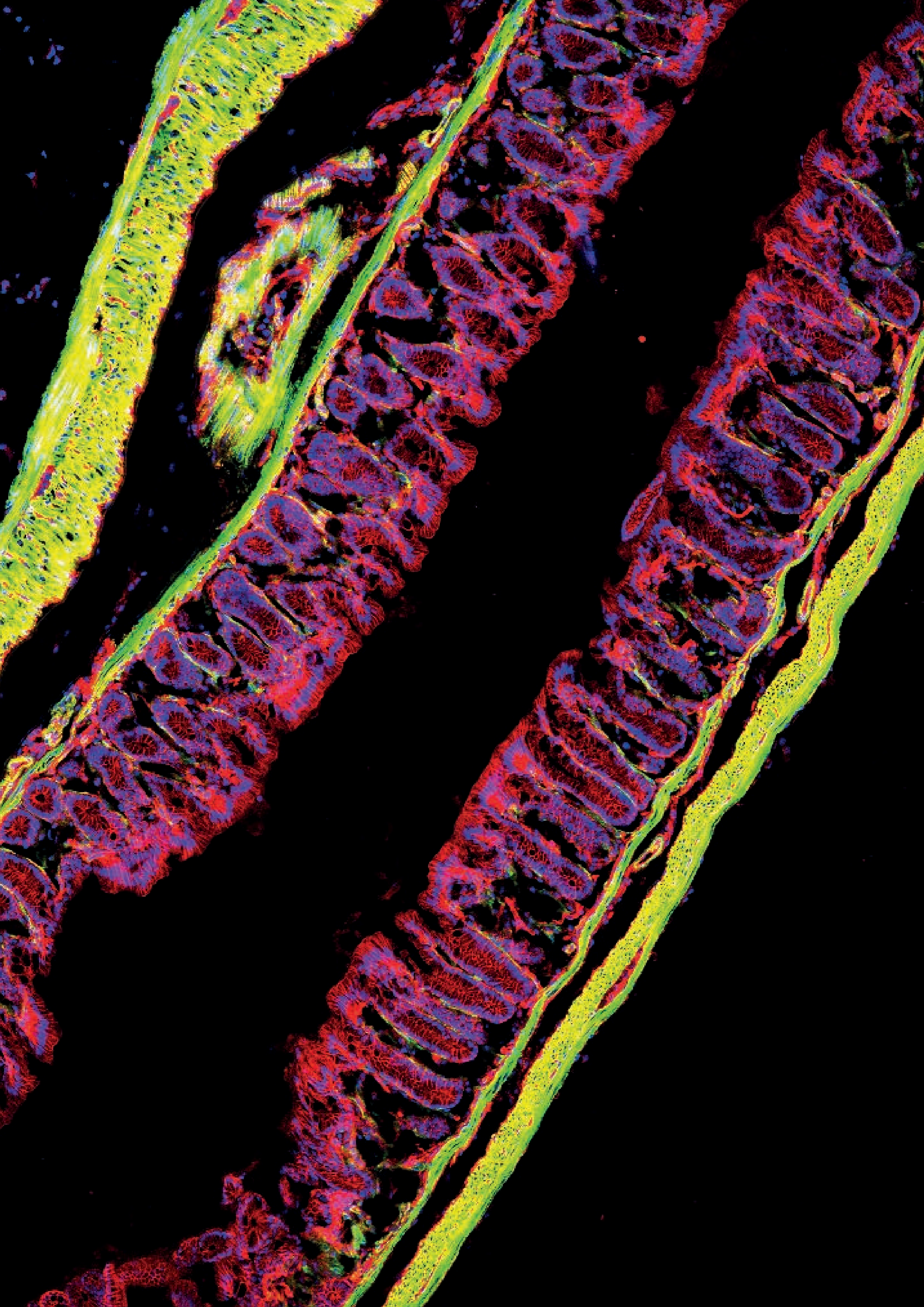

REFERENCES

> *"Science knows no country, because knowledge belongs to humanity, and is the torch which illuminates the world."*
>
> \- Louis Pasteur

Abe, R., Donnelly, S.C., Peng, T., Bucala, R., and Metz, C.N. (2001). Peripheral Blood Fibrocytes: Differentiation Pathway and Migration to Wound Sites. J. Immunol. *166*, 7556–7562.

AECC (2018). Incidencia y mortalidad de cáncer colorrectal en España en la población entre 50 y 69 años. Asociación Española Contra El Cáncer.

Affymetrix – Thermofisher web page. URL: https://www.thermofisher.com/es/en/home/life-science/microarray-analysis/affymetrix.html

Agudo, J., Park, E.S., Rose, S.A., Alibo, E., Sweeney, R., Dhainaut, M., Kobayashi, K.S., Sachidanandam, R., Baccarini, A., Merad, M., et al. (2018). Quiescent Tissue Stem Cells Evade Immune Surveillance. Immunity *48*, 271–285.

AJCC (2009). Colon and Rectum Cancer Staging. Am. Cancer Soc. 1.

Aklilu, M., and Eng, C. (2011). The current landscape of locally advanced rectal cancer. Nat. Rev. Clin. Oncol. *8*, 649–659.

Albrengues, J., Bertero, T., Grasset, E., Bonan, S., Maiel, M., Bourget, I., Philippe, C., Herraiz Serrano, C., Benamar, S., Croce, O., et al. (2015). Epigenetic switch drives the conversion of fibroblasts into proinvasive cancer-associated fibroblasts. Nat. Commun. *6*, 1–15.

Aldeiri, B., Roostalu, U., Albertini, A., Wong, J., Morabito, A., and Cossu, G. (2017). Transgelin-expressing myofibroblasts orchestrate ventral midline closure through TGFβ signalling. Development *144*, 3336–3348.

Aldeiri, B., Roostalu, U., Albertini, A., Behnsen, J., Wong, J., Morabito, A., and Cossu, G. (2018). Abrogation of TGF-beta signalling in TAGLN expressing cells recapitulates Pentalogy of Cantrell in the mouse. Sci. Rep. *8*, 1–13.

Alkasalias, T., Moyano-Galceran, L., Arsenian-Henriksson, M., and Lehti, K. (2018). Fibroblasts in the tumor microenvironment: Shield or spear? Int. J. Mol. Sci. *19*, 1–21.

Allaoui, R., Bergenfelz, C., Mohlin, S., Hagerling, C., Salari, K., Werb, Z., Anderson, R.L., Ethier, S.P., Jirström, K., Påhlman, S., et al. (2016). Cancer-associated fibroblast-secreted CXCL16 attracts monocytes to promote stroma activation in triple-negative breast cancers. Nat. Commun. *7*, 1–14.

Anderson, K.G., Stromnes, I.M., and Greenberg, P.D. (2017). Obstacles Posed by the Tumor Microenvironment to T cell Activity: A Case for Synergistic Therapies. Cancer Cell *31*, 311–325.

Andrae, J., Gallini, R., and Betsholtz, C. (2008). Role of platelet-derived growth factors in physiology and medicine. Genes Dev. *22*, 1276–1312.

André, P., Denis, C., Soulas, C., Bourbon-Caillet, C., Lopez, J., Arnoux, T., Bléry, M., Bonnafous, C., Gauthier, L., Morel, A., et al. (2018). Anti-NKG2A mAb Is a Checkpoint Inhibitor that Promotes Anti-tumor Immunity by Unleashing Both T and NK Cells. Cell *175*, 1731–1743.

Angelova, M., Mlecnik, B., Vasaturo, A., Bindea, G., Fredriksen, T., Lafontaine, L., Buttard, B., Morgand, E., Bruni, D., Jouret-Mourin, A., et al. (2018). Evolution of Metastases in Space and Time under Immune Selection. Cell *175* 751–765.

Arina, A., Idel, C., Hyjek, E.M., Alegre, M.-L., Wang, Y., Bindokas, V.P., Weichselbaum, R.R., and Schreiber, H. (2016). Tumor-associated fibroblasts predominantly come from local and not circulating precursors. Proc. Natl. Acad. Sci. U. S. A. *113*, 7551–7556.

Assinder, S.J., Stanton, J.-A.L., and Prasad, P.D. (2009). Transgelin: an actin-binding protein and tumour suppressor. Int. J. Biochem. Cell Biol. *41*, 482–486.

Ayob, A.Z., and Ramasamy, T.S. (2018). Cancer stem cells as key drivers of tumour progression. J. Biomed. Sci. *25*, 1–18.

Azzalini, A., Torelli, N. (2007). Clustering via nonparametric density estimation. Statistics and Computing. 17, 71-80.

Azzalini, A., and Menardi, G. (2014). Clustering via nonparametric density estimation: The R package pdfCluster. J. Stat. Softw. *57*, 1–26.

Bai, J., Gao, Z., Li, X., Dong, L., Han, W., and Nie, J. (2017). Regulation of PD-1/PD-L1 pathway and resistance to PD-1/PDL1 blockade. Oncotarget *8*, 110693–110707.

Balkwill, F., and Mantovani, A. (2001). Inflammation and cancer: Back to Virchow? Lancet *357*, 539–545.

Bankhead, P., Loughrey, M.B., Fernández, J.A., Dombrowski, Y., McArt, D.G., Dunne, P.D., McQuaid, S., Gray, R.T., Murray, L.J., Coleman, H.G., et al. (2017). QuPath: Open source software for digital pathology image analysis. Sci. Rep. *7*, 1–7.

Barker, N., van Es, J.H., Kuipers, J., Kujala, P., van den Born, M., Cozijnsen, M., Haegebarth, A., Korving, J., Begthel, H., Peters, P.J., et al. (2007). Identification of stem cells in small intestine and colon by marker gene Lgr5. Nature *449*, 1003–1007.

Barnes, T.A., and Amir, E. (2017). HYPE or HOPE: The prognostic value of infiltrating immune cells in cancer. Br. J. Cancer *117*, 451–460.

Barrett, T., Wilhite, S.E., Ledoux, P., Evangelista, C., Kim, I.F., Tomashevsky, M., Marshall, K.A., Phillippy, K.H., Sherman, P.M., Holko, M., et al. (2013). NCBI GEO: Archive for functional genomics data sets - Update. Nucleic Acids Res. *41*, 991–995.

Barron, L., Gharib, S.A., and Duffield, J.S. (2016). Lung Pericytes and Resident Fibroblasts: Busy Multitaskers. Am. J. Pathol. *186*, 2519–2531.

Batlle, E., and Massagué, J. (2019). Transforming Growth Factor-β Signaling in Immunity and Cancer. Immunity *50*, 924–940.

Bechtel, W., McGoohan, S., Zeisberg, E.M., Müller, G.A., Kalbacher, H., Salant, D.J., Müller, C.A., Kalluri, R., and Zeisberg, M. (2010). Methylation determines fibroblast activation and fibrogenesis in the kidney. Nat. Med. *16*, 544–550.

Bhowmick, N.A., Chytil, A., Plieth, D., Gorska, A.E., Dumont, N., Shappell, S., Washington, M.K., Neilson, E.G., and Moses, H.L. (2004). TGF-b signaling in fibroblasts modulates the oncogenic potential of adjacent epithelia. Science *303*, 848–851.

Bolstad, B.M., Collin, F., Brettschneider, J., Simpson, K., Cope, L., Irizarry, R.A., Speed, T.P. (2005) Quality Assessment of Affymetrix GeneChip Data. In: Gentleman R., Carey V.J., Huber W., Irizarry R.A., Dudoit S. (eds) Bioinformatics and Computational Biology Solutions Using R and Bioconductor. Statistics for Biology and Health. Springer, New York, NY

Bonaventura, P., Shekarian, T., Alcazer, V., Valladeau-Guilemond, J., Valsesia-Wittmann, S., Amigorena, S., Caux, C., and Depil, S. (2019). Cold tumors: A therapeutic challenge for immunotherapy. Front. Immunol. *10*, 1–10.

Bray, F., Ferlay, J., Soerjomataram, I., Siegel, R.L., Torre, L.A., and Jemal, A. (2018). Global cancer statistics 2018: GLOBOCAN estimates of incidence and mortality worldwide for 36 cancers in 185 countries. CA. Cancer J. Clin. *68*, 394–424.

Calon, A., Espinet, E., Palomo-Ponce, S., Tauriello, D.V.F., Iglesias, M., Céspedes, M.V., Sevillano, M., Nadal, C., Jung, P., Zhang, X.H.-F., et al. (2012). Dependency of colorectal cancer on a TGF-β-driven program in stromal cells for metastasis initiation. Cancer Cell *22*, 571–584.

Calon, A., Tauriello, D.V.F., and Batlle, E. (2014). TGF-beta in CAF-mediated tumor growth and metastasis. Semin. Cancer Biol. *25*, 15–22.

Calon, A., Lonardo, E., Berenguer-Llergo, A., Espinet, E., Hernando-Momblona, X., Iglesias, M., Sevillano, M., Palomo-Ponce, S., Tauriello, D.V.F., Byrom, D., et al. (2015). Stromal gene expression defines poor-prognosis subtypes in colorectal cancer. Nat. Genet. *47*, 320–329.

Camus, M., Tosolini, M., Mlecnik, B., Pagès, F., Kirilovsky, A., Berger, A., Costes, A., Bindea, G., Charoentong, P., Bruneval, P., et al. (2009). Coordination of intratumoral immune reaction and human colorectal cancer recurrence. Cancer Res. *69*, 2685–2693.

Cardenas, H., Vieth, E., Lee, J., Segar, M., Liu, Y., Nephew, K.P., and Matei, D. (2014). TGF-β induces global changes in DNA methylation during the epithelial-to-mesenchymal transition in ovarian cancer cells. Epigenetics *9*, 1461–1472.

Carstens, J.L., De Sampaio, P.C., Yang, D., Barua, S., Wang, H., Rao, A., Allison, J.P., Le Bleu, V.S., and Kalluri, R. (2017). Spatial computation of intratumoral T cells correlates with survival of patients with pancreatic cancer. Nat. Commun. *8*, 1–13.

Chakravarthy, A., Khan, L., Bensler, N.P., Bose, P., and De Carvalho, D.D. (2018). TGF-β-associated extracellular matrix genes link cancer-associated fibroblasts to immune evasion and immunotherapy failure. Nat. Commun. *9*, 1–10.

Chan, M.W.Y., Huang, Y.W., Hartman-Frey, C., Kuo, C.T., Deatherage, D., Qin, H., Cheng, A.S.L., Yan, P.S., Davuluri, R. V., Huang, T.H.M., et al. (2008). Aberrant transforming growth factor β1 signaling and SMAD4 nuclear translocation confer epigenetic repression of ADAM19 in ovarian cancer. Neoplasia *10*, 908–919.

Chang, H.Y., Chi, J.T., Dudoit, S., Bondre, C., Van De Rijn, M., Botstein, D., and Brown, P.O. (2002). Diversity, topographic differentiation, and positional memory in human fibroblasts. Proc. Natl. Acad. Sci. U. S. A. *99*, 12877–12882.

Chen, D.S., and Mellman, I. (2013). Oncology meets immunology: the cancer-immunity cycle. Immunity *39*, 1–10.

Chen, W., and Ten Dijke, P. (2016). Immunoregulation by members of the TGFβ superfamily. Nat. Rev. Immunol. *16*, 723–740.

Chen, S.-X., Xu, X.-E., Wang, X.-Q., Cui, S.-J., Xu, L.-L., Jiang, Y.-H., Zhang, Y., Yan, H.-B., Zhang, Q., Qiao, J., et al. (2014a). Identification of colonic fibroblast secretomes reveals secretory factors regulating colon cancer cell proliferation. J. Proteomics *110*, 155–171.

Chen, Y.-T., Chang, Y.-T., Pan, S.-Y., Chou, Y.-H., Chang, F.-C., Yeh, P.-Y., Liu, Y.-H., Chiang, W.-C., Chen, Y.-M., Wu, K.-D., et al. (2014b). Lineage tracing reveals distinctive fates for mesothelial cells and submesothelial fibroblasts during peritoneal injury. J. Am. Soc. Nephrol. *25*, 2847–2858.

Cheng, N., Chytil, A., Shyr, Y., Joly, A., and Moses, H.L. (2008). Transforming Growth Factor- Signaling-Deficient Fibroblasts Enhance Hepatocyte Growth Factor Signaling in Mammary Carcinoma Cells to Promote Scattering and Invasion. Mol. Cancer Res. *6*, 1521–1533.

Cirri, P., and Chiarugi, P. (2012). Cancer-associated-fibroblasts and tumour cells: a diabolic liaison driving cancer progression. Cancer Metastasis Rev. *31*, 195–208.

Cortez, E., Roswall, P., and Pietras, K. (2014). Functional subsets of mesenchymal cell types in the tumor microenvironment. Semin. Cancer Biol. *25*, 3–9.

Costa, A., Kieffer, Y., Scholer-Dahirel, A., Pelon, F., Bourachot, B., Cardon, M., Sirven, P., Magagna, I., Fuhrmann, L., Bernard, C., et al. (2018). Fibroblast Heterogeneity and Immunosuppressive Environment in Human Breast Cancer. Cancer Cell *33*, 463–479.

Cremasco, V., Astarita, J.L., Grauel, A.L., Keerthivasan, S., MacIsaac, K., Woodruff, M.C., Wu, M., Spel, L., Santoro, S., Amoozgar, Z., et al. (2018). FAP Delineates Heterogeneous and Functionally Divergent Stromal Cells in Immune-Excluded Breast Tumors. Cancer Immunol. Res. *6*, 1472–1485.

Dalerba, P., Dylla, S.J., Park, I.K., Liu, R., Wang, X., Cho, R.W., Hoey, T., Gurney, A., Huang, E.H., Simeone, D.M., et al. (2007). Phenotypic characterization of human colorectal cancer stem cells. Proc. Natl. Acad. Sci. U. S. A. *104*, 10158–10163.

Dieter, S.M., Ball, C.R., Hoffmann, C.M., Nowrouzi, A., Herbst, F., Zavidij, O., Abel, U., Arens, A., Weichert, W., Brand, K., et al. (2011). Distinct types of tumor-initiating cells form human colon cancer tumors and metastases. Cell Stem Cell *9*, 357–365.

Drake, C.G., Lipson, E.J., and Brahmer, J.R. (2014). Breathing new life into immunotherapy: review of melanoma, lung and kidney cancer. Nat. Rev. Clin. Oncol. *11*, 24–37.

Driskell, R.R., and Watt, F.M. (2015). Understanding fibroblast heterogeneity in the skin. Trends Cell Biol. *25*, 92–99.

Driskell, R.R., Lichtenberger, B.M., Hoste, E., Kretzschmar, K., Simons, B.D., Charalambous, M., Ferron, S.R., Herault, Y., Pavlovic, G., Ferguson-Smith, A.C., et al. (2013). Distinct fibroblast lineages determine dermal architecture in skin development and repair. Nature *504*, 277–281.

Droeser, R. a, Hirt, C., Viehl, C.T., Frey, D.M., Nebiker, C., Huber, X., Zlobec, I., Eppenberger-Castori, S., Tzankov, A., Rosso, R., et al. (2013). Clinical impact of programmed cell death ligand 1 expression in colorectal cancer. Eur. J. Cancer *49*, 2233–2242.

Dunn, G.P., Old, L.J., and Schreiber, R.D. (2004). The three Es of cancer immunoediting. Annu. Rev. Immunol. *22*, 329–360.

Dunn, G.P., Koebel, C.M., and Schreiber, R.D. (2006). Interferons, immunity and cancer immunoediting. Nat. Rev. Immunol. *6*, 836–848.

Dvorak, H.F. (1986). Tumors: wounds that do not heal. Similarities between stroma generation and wound healing. N. Engl. J. Med. *315*, 1650–1659.

Eilers, P.H.C., and Marx, B.D. (1996). Flexible smoothing with B-splines and penalties. Stat. Sci. *11*, 89–102.

Eklund, A.C., and Szallasi, Z. (2008). Correction of technical bias in clinical microarray data improves concordance with known biological information. Genome Biol. *9*, 1-8.

Elyada, E., Bolisetty, M., Laise, P., Flynn, W.F., Courtois, E.T., Burkhart, R.A., Teinor, J.A., Belleau, P., Biffi, G., Lucito, M.S., et al. (2019). Cross-Species Single-Cell Analysis of Pancreatic Ductal Adenocarcinoma Reveals Antigen-Presenting Cancer-Associated Fibroblasts. Cancer Discov. *9*, 1102–1123.

Erreni, M., Mantovani, A., and Allavena, P. (2011). Tumor-associated Macrophages (TAM) and Inflammation in Colorectal Cancer. Cancer Microenviron. *4*, 141–154.

Van den Eynde, M., Mlecnik, B., Bindea, G., Fredriksen, T., Church, S.E., Lafontaine, L., Haicheur, N., Marliot, F., Angelova, M., Vasaturo, A., et al. (2018). The Link between the Multiverse of Immune Microenvironments in Metastases and the Survival of Colorectal Cancer Patients. Cancer Cell *34*, 1012–1026.

Fabre, T., Molina, M.F., Soucy, G., Goulet, J.-P., Willems, B., Villeneuve, J.-P., Bilodeau, M., and Shoukry, N.H. (2018). Type 3 cytokines IL-17A and IL-22 drive TGF-β-dependent liver fibrosis. Sci. Immunol. *3*. eaar7754

Fearon, E.R. (2011). Molecular genetics of colorectal cancer. Annu. Rev. Pathol. Mech. Dis. *6*, 479–507.

Fearon, E.R., and Vogelstein, B. (1990). A genetic model for colorectal tumorogenesis. Cell *61*, 759–767.

Feil, R., Brocard, J., Mascrez, B., Lemeur, M., Metzger, D., and Chambon, P. (1996). Ligand-activated site-specific recombination in mice. Proc. Natl. Acad. Sci. U. S. A. *93*, 10887–10890.

Fessler, E., and Medema, J.P. (2016). Colorectal Cancer Subtypes: Developmental Origin and Microenvironmental Regulation. Trends in Cancer *2*, 505–518.

Fielding, C.A., Jones, G.W., McLoughlin, R.M., McLeod, L., Hammond, V.J., Uceda, J., Williams, A.S., Lambie, M., Foster, T.L., Liao, C. Te, et al. (2014). Interleukin-6 signaling drives fibrosis in unresolved inflammation. Immunity *40*, 40–50.

Fontana, E., Eason, K., Cervantes, A., Salazar, R., and Sadanandam, A. (2019). Context matters-consensus molecular subtypes of colorectal cancer as biomarkers for clinical trials. Ann. Oncol. *30*, 520–527.

Franco, O.E., Jiang, M., Strand, D.W., Peacock, J., Fernandez, S., Jackson, R.S., Revelo, M.P., Bhowmick, N.A., and Hayward, S.W. (2011). Altered TGF-β signaling in a subpopulation of human stromal cells promotes prostatic carcinogenesis. Cancer Res. *71*, 1272–1281.

Freeman, G.J., Long, A.J., Iwai, Y., Bourque, K., Chernova, T., Nishimura, H., Fitz, L.J., Malenkovich, N., Okazaki, T., Byrne, M.C., et al. (2000). Engagement of the PD-1 immunoinhibitory receptor by a novel B7 family member leads to negative regulation of lymphocyte activation. J. Exp. Med. *192*, 1027–1034.

Friedman, S.L. (2008). Hepatic stellate cells: protean, multifunctional, and enigmatic cells of the liver. Physiol. Rev. *88*, 125–172.

Fumagalli, A., Drost, J., Suijkerbuijk, S.J.E., Van Boxtel, R., De Ligt, J., Offerhaus, G.J., Begthel, H., Beerling, E., Tan, E.H., Sansom, O.J., et al. (2017). Genetic dissection of colorectal cancer progression by orthotopic transplantation of engineered cancer organoids. Proc. Natl. Acad. Sci. U. S. A. *114*, E2357–E2364.

Gajewski, T.F., Schreiber, H., and Fu, Y.X. (2013). Innate and adaptive immune cells in the tumor microenvironment. Nat. Immunol. *14*, 1014–1022.

Galdiero, M.R., Bonavita, E., Barajon, I., Garlanda, C., Mantovani, A., and Jaillon, S. (2013). Tumor associated macrophages and neutrophils in cancer. Immunobiology *218*, 1402–1410.

Galiatsatos, P., and Foulkes, W.D. (2006). Familial Adenomatous Polyposis. Am. J. Gastroenterol. *101*, 385–398.

Galon, J., and Bruni, D. (2019). Approaches to treat immune hot, altered and cold tumours with combination immunotherapies. Nat. Rev. Drug Discov. *18*, 197–218.

Galon, J., Costes, A., Sanchez-Cabo, F., Kirilovsky, A., Mlecnik, B., Lagorce-Pagès, C., Tosolini, M., Camus, M., Berger, A., Wind, P., et al. (2006). Type, density, and location of immune cells within human colorectal tumors predict clinical outcome. Science *313*, 1960–1964.

Ganat, Y.M., Silbereis, J., Cave, C., Ngu, H., Anderson, G.M., Ohkubo, Y., Ment, L.R., and Vaccarino, F.M. (2006). Early postnatal astroglial cells produce multilineage precursors and neural stem cells In Vivo. J. Neurosci. *26*, 8609–8621.

Garcia-Diaz, A., Shin, D.S., Moreno, B.H., Saco, J., Escuin-Ordinas, H., Rodriguez, G.A., Zaretsky, J.M., Sun, L., Hugo, W., Wang, X., et al. (2017). Interferon Receptor Signaling

Pathways Regulating PD-L1 and PD-L2 Expression. Cell Rep. *19*, 1189–1201.

Gautier, L., Cope, L., Bolstad, B.M., and Irizarry, R.A. (2004). Affy - Analysis of Affymetrix GeneChip data at the probe level. Bioinformatics *20*, 307–315.

Gentleman, R.C., Carey, V.J., Bates, D.M., Bolstad, B., Dettling, M., Dudoit, S., Ellis, B., Gautier, L., Ge, Y., Gentry, J., et al. (2004). Bioconductor: open software development for computational biology and bioinformatics. Genome Biol. *5*, 1-16.

Gentleman, R., Carey,V., Huber, W., Irizarry, R., Dudoit, S. (2005). Bioinformatics and Computational Biology Solutions Using R and Bioconductor (Springer, New York).

Gieseck, R.L., Wilson, M.S., and Wynn, T.A. (2018). Type 2 immunity in tissue repair and fibrosis. Nat. Rev. Immunol. *18*, 62–76.

Gonzalez-Roca, E., Garcia-Albéniz, X., Rodriguez-Mulero, S., Gomis, R.R., Kornacker, K., and Auer, H. (2010). Accurate expression profiling of very small cell populations. PLoS One *5*.

Gonzalez-Zubeldia, I., Dotor, J., Redrado, M., Bleau, A.-M., Manrique, I., de Aberasturi, A.L., Villalba, M., and Calvo, A. (2015). Co-migration of colon cancer cells and CAFs induced by TGFβ1 enhances liver metastasis. Cell Tissue Res. *359*, 829–839.

Grossman, R.L., Heath, A.P., Ferretti, V., Varmus, H.E., Lowy, D.R., Kibbe, W.A., and Staudt, L.M. (2016). Toward a Shared Vision for Cancer Genomic Data Robert. N. Engl. J. Med. *375*, 1109–1112.

Gubin, M.M., Zhang, X., Schuster, H., Caron, E., Ward, J.P., Noguchi, T., Ivanova, Y., Hundal, J., Arthur, C.D., Krebber, W.-J., et al. (2014). Checkpoint blockade cancer immunotherapy targets tumour-specific mutant antigens. Nature *515*, 577–581.

Guinney, J., Dienstmann, R., Wang, X., De Reyniès, A., Schlicker, A., Soneson, C., Marisa, L., Roepman, P., Nyamundanda, G., Angelino, P., et al. (2015). The consensus molecular subtypes of colorectal cancer. Nat. Med. *21*, 1350–1356.

Hanahan, D., and Weinberg, R. a (2011). Hallmarks of cancer: the next generation. Cell *144*, 646–674.

Hanahan, D., Weinberg, R.A., and Francisco, S. (2000). The Hallmarks of Cancer. Cell *100*, 57–70.

Hayes, B.J., Riehle, K.J., Shimizu-Albergine, M., Bauer, R.L., Hudkins, K.L., Johansson, F., Yeh, M.M., Mahoney, W.M., Yeung, R.S., and Campbell, J.S. (2014). Activation of platelet-derived growth factor receptor alpha contributes to liver fibrosis. PLoS One *9*, 1–10.

Hiraoka, N., Ino, Y., and Yamazaki-Itoh, R. (2016). Tertiary lymphoid organs in cancer tissues. Front. Immunol. *7*.

Hisatomi, K., Sakamoto, N., Ishimatsu, Y., Kakugawa, T., Hara, S., Fujita, H., Kohno, S., Mukae, H., Nakamichi, S., Oku, H., et al. (2012). Pirfenidone inhibits TGF-β1-induced over-expression of collagen type I and heat shock protein 47 in A549 cells. BMC Pulm. Med. *12*, 1–9.

Hodi, F.S., Mihm, M.C., Soiffer, R.J., Haluska, F.G., Butler, M., Seiden, M. V., Davis, T., Henry-Spires, R., MacRae, S., Willman, A., et al. (2003). Biologic activity of cytotoxic T lymphocyte-associated antigen 4 antibody blockade in previously vaccinated metastatic melanoma and ovarian carcinoma patients. Proc. Natl. Acad. Sci. U. S. A. *100*, 4712–4717.

Hothorn, T., Hornik, K., Van De Wiel, M.A., and Zeileis, A. (2006). A lego system for conditional inference. Am. Stat. *60*, 257–263.

Hu, M., Yao, J., Cai, L., Bachman, K.E., Van Den Brûle, F., Velculescu, V., and Polyak, K. (2005). Distinct epigenetic changes in the stromal cells of breast cancers. Nat. Genet. *37*, 899–905.

Huang, S.K., Scruggs, A.M., Donaghy, J., Horowitz, J.C., Zaslona, Z., Przybranowski, S., White, E.S., and Peters-Golden, M. (2013). Histone modifications are responsible for decreased Fas expression and apoptosis resistance in fibrotic lung fibroblasts. Cell Death Dis. *4*, e621-8.

Huels, D.J., Bruens, L., Hodder, M.C., Cammareri, P., Campbell, A.D., Ridgway, R.A., Gay, D.M., Solar-Abboud, M., Faller, W.J., Nixon, C., et al. (2018). Wnt ligands influence tumour initiation by controlling the number of intestinal stem cells. Nat. Commun. *9*, 1–10.

Irizarry, R.A., Hobbs, B., Collin, F., Beazer-Barclay, Y.D., Antonellis, K.J., Scherf, U., and Speed, T.P. (2003). Exploration, normalization, and summaries of high density oligonucleotide array probe level data. Biostatistics *4*, 601–616.

Isella, C., Terrasi, A., Bellomo, S.E., Petti, C., Galatola, G., Muratore, A., Mellano, A., Senetta, R., Cassenti, A., Sonetto, C., et al. (2015). Stromal contribution to the colorectal cancer transcriptome. Nat. Genet. *47*, 312–319.

Iwai, Y., Terawaki, S., and Honjo, T. (2005). PD-1 blockade inhibits hematogenous spread of poorly immunogenic tumor cells by enhanced recruitment of effector T cells. Int. Immunol. *17*, 133–144.

Iwaisako, K., Jiang, C., Zhang, M., Cong, M., Moore-Morris, T.J., Park, T.J., Liu, X., Xu, J., Wang, P., Paik, Y.-H., et al. (2014). Origin of myofibroblasts in the fibrotic liver in mice. Proc. Natl. Acad. Sci. U.S.A. *111*, E3297–E3305.

Jacobs, J., Smits, E., Lardon, F., Pauwels, P., and Deschoolmeester, V. (2015). Immune Checkpoint Modulation in Colorectal Cancer: What's New and What to Expect. J. Immunol. Res. *2015*.

Jess, T., Rungoe, C., and Peyrin-Biroulet, L. (2012). Risk of Colorectal Cancer in Patients With Ulcerative Colitis: A Meta-analysis of Population-Based Cohort Studies. Clin. Gastroenterol. Hepatol. *10*, 639–645.

Van Der Jeught, K., Xu, H.C., Li, Y.J., Lu, X. Bin, and Ji, G. (2018). Drug resistance and new therapies in colorectal cancer. World J. Gastroenterol. *24*, 3834–3848.

Jiménez-Sánchez, A., Memon, D., Pourpe, S., Veeraraghavan, H., Li, Y., Vargas, H.A., Gill, M.B., Park, K.J., Zivanovic, O., Konner, J., et al. (2017). Heterogeneous Tumor-Immune Microenvironments among Differentially Growing Metastases in an Ovarian Cancer Patient. Cell *170*, 927–938.

Jorissen, R.N., Lipton, L., Gibbs, P., Chapman, M., Desai, J., Ian, T., Yeatman, T.J., East, P., Tomlinson, I.P.M., Verspaget, H.W., et al. (2008). DNA copy-number alterations underlie gene expression differences between microsatellite stable and unstable colorectal cancers. Clin. Cancer Res. *14*, 8061–8069.

Joyce, J.A., and Fearon, D.T. (2015). T cell exclusion, immune privilege, and the tumor microenvironment. Science (80-.). *348*, 74–79.

Kalluri, R. (2016). The biology and function of fibroblasts in cancer. Nat. Rev. Cancer *16*, 582–598.

Kalluri, R., and Zeisberg, M. (2006). Fibroblasts in cancer. Nat. Rev. Cancer *6*, 392–401.

Kalos, M., and June, C.H. (2013). Adoptive T Cell Transfer for Cancer Immunotherapy in the Era of Synthetic Biology. Immunity *39*, 49–60.

Karim, B.O., and Huso, D.L. (2013). Mouse models for colorectal cancer. Am. J. Cancer Res. *3*, 240–250.

Katlinski, K. V., Gui, J., Katlinskaya, Y. V., Ortiz, A., Chakraborty, R., Bhattacharya, S., Carbone, C.J., Beiting, D.P., Girondo, M.A., Peck, A.R., et al. (2017). Inactivation of Interferon Receptor Promotes the Establishment of Immune Privileged Tumor Microenvironment. Cancer Cell *31*, 194–207.

Kikuchi, A., and Monga, S.P. (2015). PDGFRα in liver pathophysiology: Emerging roles in development, regeneration, fibrosis, and cancer. Gene Expr. *16*, 109–127.

Kitadai, Y., Sasaki, T., Kuwai, T., Nakamura, T., Bucana, C.D., and Fidler, I.J. (2006). Targeting the expression of platelet-derived growth factor receptor by reactive stroma inhibits growth and metastasis of human colon carcinoma. Am. J. Pathol. *169*, 2054–2065.

Kozono, S., Ohuchida, K., Eguchi, D., Ikenaga, N., Fujiwara, K., Cui, L., Mizumoto, K., and Tanaka, M. (2013). Pirfenidone inhibits pancreatic cancer desmoplasia by regulating stellate cells. Cancer Res. *73*, 2345–2356.

Kramann, R., Schneider, R.K., DiRocco, D.P., Machado, F., Fleig, S., Bondzie, P.A., Henderson, J.M., Ebert, B.L., and Humphreys, B.D. (2014). Perivascular Gli1+ Progenitors Are Key Contributors to Injury-Induced Organ Fibrosis. Cell Stem Cell *16*, 51–66.

Krishnan, L., Gurnani, K., Dicaire, C.J., van Faassen, H., Zafer, A., Kirschning, C.J., Sad, S., and Sprott, G.D. (2007). Rapid Clonal Expansion and Prolonged Maintenance of Memory CD8 + T Cells of the Effector (CD44 high CD62L low) and Central (CD44 high CD62L high) Phenotype by an Archaeosome Adjuvant Independent of TLR2 . J. Immunol. *178*, 2396–2406.

Kühbandner, S., Brummer, S., Metzger, D., Chambon, P., Hofmann, F., and Feil, R. (2000). Temporally controlled somatic mutagenesis in smooth muscle. Genesis *28*, 15–22.

Kuipers, E.J., Grady, W.M., Lieberman, D., Seufferlein, T., Sung, J.J., Boelens, P.G., van de Velde, C.J.H., and Watanabe, T. (2015). Colorectal cancer. Nat. Rev. Dis. Prim. *1*, 1–25.

Kurahashi, M., Nakano, Y., Peri, L.E., Townsend, J.B., Ward, S.M., and Sanders, K.M. (2013). A novel population of subepithelial platelet-derived growth factor receptor α-positive cells in the mouse and human colon. Am. J. Physiol. Gastrointest. Liver Physiol. *304*, 823-834.

Kurtulus, S., Madi, A., Escobar, G., Klapholz, M., Nyman, J., Christian, E., Pawlak, M., Dionne, D., Xia, J., Rozenblatt-Rosen, O., et al. (2019). Checkpoint Blockade Immunotherapy Induces Dynamic Changes in PD-1 − CD8 + Tumor-Infiltrating T Cells. Immunity *50*, 181–194.

Labernadie, A., Kato, T., Brugués, A., Serra-Picamal, X., Derzsi, S., Arwert, E., Weston, A., González-Tarragó, V., Elosegui-Artola, A., Albertazzi, L., et al. (2017). A mechanically active heterotypic E-cadherin/N-cadherin adhesion enables fibroblasts to drive cancer cell invasion. Nat. Cell Biol. *19*, 224–237.

Lakins, M.A., Ghorani, E., Munir, H., Martins, C.P., and Shields, J.D. (2018). Cancer-associated fibroblasts induce antigen-specific deletion of CD8+T Cells to protect tumour cells. Nat. Commun. *9*, 1–9.

Langley, R.R., and Fidler, I.J. (2011). The seed and soil hypothesis revisited--the role of tumor-stroma interactions in metastasis to different organs. Int. J. Cancer *128*, 2527–2535.

Le, D.T., Uram, J.N., Wang, H., Bartlett, B.R., Kemberling, H., Eyring, A.D., Skora, A.D., Luber, B.S., Azad, N.S., Laheru, D., et al. (2015). PD-1 Blockade in Tumors with Mismatch-Repair Deficiency. N. Engl. J. Med. *372*, 2509–2520.

Leach, D.R., Krummel, M.F., and Allison, J.P. (1996). Enhancement of antitumor immunity by CTLA-4 blockade. Science *271*, 1734–1736.

LeBleu, V.S., and Kalluri, R. (2018). A peek into cancer-associated fibroblasts: Origins, functions and translational impact. Dis. Model. Mech. *11*, 1–9.

Lemoinne, S., Cadoret, A., El Mourabit, H., Thabut, D., and Housset, C. (2013). Origins and functions of liver myofibroblasts. Biochim. Biophys. Acta - Mol. Basis Dis. *1832*, 948–954.

Lepreux, S., and Desmoulière, A. (2015). Human liver myofibroblasts during development and diseases with a focus on portal (myo)fibroblasts. Front. Physiol. *6*, 1-8.

Levéen, P., Larsson, J., Ehinger, M., Cilio, C.M., Sundler, M., Sjöstrand, L.J., Holmdahl, R., and Karlsson, S. (2002). Induced disruption of the transforming growth factor beta type II receptor gene in mice causes a lethal inflammatory disorder that is transplantable. Blood *100*, 560–568.

Leystra, A.A., Deming, D.A., Zahm, C.D., Farhoud, M., Paul Olson, T.J., Hadac, J.N., Nettekoven, L.A., Albrecht, D.M., Clipson, L., Sullivan, R., et al. (2012). Mice expressing activated PI3K rapidly develop advanced colon cancer. Cancer Res. *72*, 2931–2936.

Li, H., Courtois, E.T., Sengupta, D., Tan, Y., Chen, K.H., Goh, J.J.L., Kong, S.L., Chua, C., Hon, L.K., Tan, W.S., et al. (2017). Reference component analysis of single-cell transcriptomes elucidates cellular heterogeneity in human colorectal tumors. Nat. Genet. *49*, 708–718.

Ligorio, M., Sil, S., Malagon-Lopez, J., Nieman, L.T., Misale, S., Di Pilato, M., Ebright, R.Y., Karabacak, M.N., Kulkarni, A.S., Liu, A., et al. (2019). Stromal Microenvironment Shapes the Intratumoral Architecture of Pancreatic Cancer. Cell *178*, 160–175.

Linde, N., Casanova-Acebes, M., Sosa, M.S., Mortha, A., Rahman, A., Farias, E., Harper, K., Tardio, E., Reyes Torres, I., Jones, J., et al. (2018). Macrophages orchestrate breast cancer early dissemination and metastasis. Nat. Commun. *9*, 1–14.

Lisanti, M.P., Martinez-Outschoorn, U.E., and Sotgia, F. (2013). Oncogenes induce the cancer-associated fibroblast phenotype: Metabolic symbiosis and “fibroblast addiction” are new therapeutic targets for drug discovery. Cell Cycle *12*, 2723–2732.

Liu, J., Lichtenberg, T., Hoadley, K.A., Poisson, L.M., Lazar, A.J., Cherniack, A.D., Kovatich, A.J., Benz, C.C., Levine, D.A., Lee, A. V., et al. (2018). An Integrated TCGA Pan-Cancer Clinical Data Resource to Drive High-Quality Survival Outcome Analytics. Cell *173*, 400–416.e11.

Liu, Y., Yang, X., Jing, Y., Zhang, S., Zong, C., Jiang, J., Sun, K., Li, R., Gao, L., Zhao, X., et al. (2015). Contribution and Mobilization of Mesenchymal Stem Cells in a mouse model of carbon tetrachloride-induced liver fibrosis. Sci. Rep. *5*, 1–10.

Llosa, N.J., Cruise, M., Tam, A., Wicks, E.C., Hechenbleikner, E.M., Taube, J.M., Blosser, R.L., Fan, H., Wang, H., Luber, B.S., et al. (2015). The vigorous immune microenvironment of microsatellite instable colon cancer is balanced by multiple counter-inhibitory checkpoints. Cancer Discov. *5*, 43–51.

Lopez-de la Mora, D.A., Sanchez-Roque, C., Montoya-Buelna, M., Sanchez-Enriquez, S., Lucano-Landeros, S., Macias-Barragan, J., and Armendariz-Borunda, J. (2015). Role and New Insights of Pirfenidone in Fibrotic Diseases. Int. J. Med. Sci. *12*, 840–847.

Lynch, H.T., and de la Chapelle, A. (2003). Hereditary Colorectal Cancer Syndromes. N. Engl. J. Med. *348*, 919–932.

Lynch, H.T., Lynch, P.M., Lanspa, S.J., Snyder, C.L., Lynch, J.F., and Boland, C.R. (2009). Review of the Lynch syndrome: History, molecular genetics, screening, differential diagnosis, and medicolegal ramifications. Clin. Genet. *76*, 1–18.

Ma, C., and Zhang, N. (2015). Transforming growth factor-β signaling is constantly shaping memory T-cell population. Proc. Natl. Acad. Sci. U. S. A. *112*, 11013–11017.

Malladi, S., MacAlinao, D.G., Jin, X., He, L., Basnet, H., Zou, Y., De Stanchina, E., and Massagué, J. (2016). Metastatic Latency and Immune Evasion through Autocrine Inhibition of WNT. Cell *165*, 45–60.

Mannavola, F., Salerno, T., Passarelli, A., Tucci, M., Internò, V., and Silvestris, F. (2019). Revisiting the role of exosomes in colorectal cancer: Where are we now? Front. Oncol. *9*, 1–9.

Mantovani, A., Allavena, P., Sica, A., and Balkwill, F. (2008). Cancer-related inflammation. Nature *454*, 436–444.

Mariathasan, S., Turley, S.J., Nickles, D., Castiglioni, A., Yuen, K., Wang, Y., Kadel, E.E., Koeppen, H., Astarita, J.L., Cubas, R., et al. (2018). TGFβ attenuates tumour response to PD-L1 blockade by contributing to exclusion of T cells. Nature *554*, 544–548.

Marisa, L., de Reyniès, A., Duval, A., Selves, J., Gaub, M.P., Vescovo, L., Etienne-Grimaldi, M.-C., Schiappa, R., Guenot, D., Ayadi, M., et al. (2013). Gene expression classification of colon cancer into molecular subtypes: characterization, validation, and prognostic value. PLoS Med. *10*, e1001453.

Massagué, J. (2012). TGFβ signalling in context. Nat. Rev. Mol. Cell Biol. *13*, 616–630.

Massagué, J., and Gomis, R.R. (2006). The logic of TGFβ signaling. FEBS Lett. *580*, 2811–2820.

Mccarthy, E.F. (2006). The toxins of William B. Coley and the treatment of bone and soft-tissue sarcomas. Iowa Orthop. J. *26*, 154–158.

Mederacke, I., Hsu, C.C., Troeger, J.S., Huebener, P., Mu, X., Dapito, D.H., Pradere, J.-P., and Schwabe, R.F. (2013). Fate tracing reveals hepatic stellate cells as dominant contributors to liver fibrosis independent of its aetiology. Nat. Commun. *4*, 2823.

Merlos-Suárez, A., Barriga, F.M., Jung, P., Iglesias, M., Céspedes, M.V., Rossell, D., Sevillano, M., Hernando-Momblona, X., da Silva-Diz, V., Muñoz, P., et al. (2011). The intestinal stem cell signature identifies colorectal cancer stem cells and predicts disease relapse. Cell Stem Cell *8*, 511–524.

Modest, D.P., Pant, S., and Sartore-Bianchi, A. (2019). Treatment sequencing in metastatic colorectal cancer. Eur. J. Cancer *109*, 70–83.

Moffitt, R.A., Marayati, R., Flate, E.L., Volmar, K.E., Loeza, S.G.H., Hoadley, K.A., Rashid, N.U., Williams, L.A., Eaton, S.C., Chung, A.H., et al. (2015). Virtual microdissection identifies distinct tumor- and stroma-specific subtypes of pancreatic ductal adenocarcinoma. Nat. Genet. *47*, 1168–1178.

van Montfoort, N., Borst, L., Korrer, M.J., Sluijter, M., Marijt, K.A., Santegoets, S.J., van Ham, V.J., Ehsan, I., Charoentong, P., André, P., et al. (2018). NKG2A Blockade Potentiates CD8 T Cell Immunity Induced by Cancer Vaccines. Cell *175*, 1744–1755.e15.

Moore, B.B., Murray, L., Das, A., Wilke, C.A., Herrygers, A.B., and Toews, G.B. (2006). The role of CCL12 in the recruitment of fibrocytes and lung fibrosis. Am. J. Respir. Cell Mol. Biol. *35*, 175–181.

Moser, A., Luongo, C., Gould, K., McNeley, M., Shoemaker, A., and Dove, W. (1995). ApcMin: a mouse model for intestinal and mammary tumorigenesis. Eur. J. Cancer *31A*, 1061–1064.

Mrazek, A.A., Carmical, J.R., Wood, T.G., Hellmich, M.R., Eltorky, M., Bohanon, F.J., and Chao, C. (2014). Colorectal Cancer-Associated Fibroblasts are Genotypically Distinct. Curr. Cancer Ther. Rev. *10*, 97–218.

Muñoz, N.M., Upton, M., Rojas, A., Washington, M.K., Lin, L., Chytil, A., Sozmen, E.G., Madison, B.B., Pozzi, A., Moon, R.T., et al. (2006). Transforming growth factor β receptor type II inactivation induces the malignant transformation of intestinal neoplasms initiated by Apc mutation. Cancer Res. *66*, 9837–9844.

Murcia, O., Juárez, M., Hernández-Illán, E., Egoavil, C., Giner-Calabuig, M., Rodríguez-Soler, M., and Jover, R. (2016). Serrated colorectal cancer: Molecular classification, prognosis, and response to chemotherapy. World J. Gastroenterol. *22*, 3516–3530.

Muzumdar, M.D., Tasic, B., Miyamichi, K., Li, L., and Luo, L. (2007). A Global Double-Fluorescent Cre Reporter Mouse. Genesis *605*, 593–605.

NCRAS Colorectal cancer survival by stage - NCIN Data briefing.

Nielsen, S.R., Quaranta, V., Linford, A., Emeagi, P., Rainer, C., Santos, A., Ireland, L., Sakai, T., Sakai, K., Kim, Y.S., et al. (2016). Macrophage-secreted granulin supports pancreatic cancer metastasis by inducing liver fibrosis. Nat. Cell Biol. *18*, 549–560.

Nishimura, H., Okazaki, T., Tanaka, Y., Nakatani, K., Hara, M., Matsumori, A., Sasayama, S., Mizoguchi, A., Hiai, H., Minato, N., et al. (2001). Autoimmune dilated cardiomyopathy in PD-1 receptor-deficient mice. Science (80-.). *291*, 319–322.

Nojadeh, J.N., Sharif, S.B., and Sakhinia, E. (2018). Review article : Microsatellite instability in colorectal cancer. EXCLI J. *17*, 159–168.

Nowacki, T.M., Kuerten, S., Zhang, W., Shive, C.L., Kreher, C.R., Boehm, B.O., Lehmann, P. V., and Tary-Lehmann, M. (2007). Granzyme B production distinguishes recently activated CD8+ memory cells from resting memory cells. Cell. Immunol. *247*, 36–48.

O'Brien, C.A., Pollett, A., Gallinger, S., and Dick, J.E. (2007). A human colon cancer cell capable of initiating tumour growth in immunodeficient mice. Nature *445*, 106–110.

O'Donnell, J.S., Teng, M.W.L., and Smyth, M.J. (2019). Cancer immunoediting and resistance to T cell-based immunotherapy. Nat. Rev. Clin. Oncol. *16*, 151–167.

O'Rourke, K.P., Loizou, E., Livshits, G., Schatoff, E.M., Baslan, T., Manchado, E., Simon, J., Romesser, P.B., Leach, B., Han, T., et al. (2017). Transplantation of engineered organoids enables rapid generation of metastatic mouse models of colorectal cancer. Nat. Biotechnol. *35*, 577–582.

Öhlund, D., Elyada, E., and Tuveson, D. (2014). Fibroblast heterogeneity in the cancer wound. J. Exp. Med. *211*, 1503–1523.

Öhlund, D., Handly-Santana, A., Biffi, G., Elyada, E., Almeida, A.S., Ponz-Sarvise, M., Corbo, V., Oni, T.E., Hearn, S.A., Lee, E.J., et al. (2017). Distinct populations of inflammatory fibroblasts and myofibroblasts in pancreatic cancer. J. Exp. Med. *214*, 579–596.

Orimo, A., Gupta, P.B., Sgroi, D.C., Arenzana-Seisdedos, F., Delaunay, T., Naeem, R., Carey, V.J., Richardson, A.L., and Weinberg, R.A. (2005). Stromal fibroblasts present in invasive human breast carcinomas promote tumor growth and angiogenesis through elevated SDF-1/CXCL12 secretion. Cell *121*, 335–348.

Özdemir, B.C., Pentcheva-Hoang, T., Carstens, J.L., Zheng, X., Wu, C.C., Simpson, T.R., Laklai, H., Sugimoto, H., Kahlert, C., Novitskiy, S. V., et al. (2014). Depletion of carcinoma-associated fibroblasts and fibrosis induces immunosuppression and accelerates pancreas cancer with reduced survival. Cancer Cell *25*, 719–734.

Padua, D., and Massagué, J. (2009). Roles of TGFbeta in metastasis. Cell Res. *19*, 89–102.

Pagès, F., Berger, A., Camus, M., Sanchez-Cabo, F., Costes, A., Molidor, R., Mlecnik, B., Kirilovsky, A., Nilsson, M., Damotte, D., et al. (2005). Effector Memory T Cells, Early Metastasis, and Survival in Colorectal Cancer. N. Engl. J. Med. *353*, 2654–2666.

Pagès, F., Galon, J., Dieu-Nosjean, M.-C., Tartour, E., Sautès-Fridman, C., and Fridman, W.-H. (2010). Immune infiltration in human tumors: a prognostic factor that should not be ignored. Oncogene *29*, 1093–1102.

Palucka, K., and Banchereau, J. (2013). Dendritic-cell-based therapeutic cancer vaccines. Immunity *39*, 38–48.

Patel, A.K., Vipparthi, K., Thatikonda, V., Arun, I., Bhattacharjee, S., Sharan, R., Arun, P., and Singh, S. (2018). A subtype of cancer-associated fibroblasts with lower expression of alpha-smooth muscle actin suppresses stemness through BMP4 in oral carcinoma. Oncogenesis *7* 1-15.

Phillips, R.J., Burdick, M.D., Hong, K., Lutz, M.A., Murray, L.A., Xue, Y.Y., Belperio, J.A., Keane, M.P., and Strieter, R.M. (2004). Circulating fibrocytes traffic to the lungs in response to CXCL12 and mediate fibrosis. J. Clin. Invest. *114*, 438–446.

Planet, E. (2018). phenoTest: Tools to test association between gene expression and phenotype in a way that is efficient, structured, fast and scalable. R package version1.30.0.

Powell, D.W., Pinchuk, I.V., Saada, J.I., Chen, X., and Mifflin, R.C. (2011). Mesenchymal Cells of the Intestinal Lamina Propria. Annu. Rev. Physiol. *73*, 213–237.

Puram, S. V., Tirosh, I., Parikh, A.S., Patel, A.P., Yizhak, K., Gillespie, S., Rodman, C., Luo, C.L., Mroz, E.A., Emerick, K.S., et al. (2018). Single-Cell Transcriptomic Analysis of Primary and Metastatic Tumor Ecosystems in Head and Neck Cancer. Cell *172*, 1–14.

Raffaghello, L., Vacca, A., Pistoia, V., and Ribatti, D. (2015). Cancer associated fibroblasts in hematological malignancies. Oncotarget *6*, 2589–2603.

Ramanathan, V., Jin, G., Westphalen, C.B., Dubeykovskiy, A., Takaishi, S., and Wang, T.C. (2012). P53 gene mutation increases progastrin dependent colonic proliferation and colon cancer formation in mice. Cancer Invest. *30*, 275–286.

Ribas, A. (2015). Adaptive immune resistance: How cancer protects from immune attack. Cancer Discov. *5*, 915–919.

Ribas, A., Dummer, R., Puzanov, I., VanderWalde, A., Andtbacka, R.H.I., Michielin, O., Olszanski, A.J., Malvehy, J., Cebon, J., Fernandez, E., et al. (2017). Oncolytic Virotherapy Promotes Intratumoral T Cell Infiltration and Improves Anti-PD-1 Immunotherapy. Cell *170*, 1109–1119.

Ribas, A., Lawrence, D., Atkinson, V., Agarwal, S., Miller, W.H., Carlino, M.S., Fisher, R., Long, G. V., Hodi, F.S., Tsoi, J., et al. (2019). Combined BRAF and MEK inhibition with PD-1 blockade immunotherapy in BRAF-mutant melanoma. Nat. Med. *25*, 936–940.

Ricci-Vitiani, L., Lombardi, D.G., Pilozzi, E., Biffoni, M., Todaro, M., Peschle, C., and De Maria, R. (2007). Identification and expansion of human colon-cancer-initiating cells. Nature *445*, 111–115.

Rivers, L.E., Young, K.M., Rizzi, M., Jamen, F., Psachoulia, K., Wade, A., Kessaris, N., and Richardson, W.D. (2008). PDGFRA/NG2 glia generate myelinating oligodendrocytes and piriform projection neurons in adult mice. Nat. Neurosci. *11*, 1392–1401.

De Robertis, M., Massi, E., Poeta, M.L., Carotti, S., Morini, S., Cecchetelli, L., Signori, E., and Fazio, V.M. (2011). The AOM/DSS murine model for the study of colon carcinogenesis: From pathways to diagnosis and therapy studies. J. Carcinog. *10*.

De Rosa, M., Pace, U., Rega, D., Costabile, V., Duraturo, F., Izzo, P., and Delrio, P. (2015). Genetics, diagnosis and management of colorectal cancer (Review). Oncol. Rep. *34*, 1087–1096.

Rozali, E.N., Hato, S. V., Robinson, B.W., Lake, R.A., and Lesterhuis, W.J. (2012). Programmed death ligand 2 in cancer-induced immune suppression. Clin. Dev. Immunol. *2012*, 1–8.

Sadanandam, A., Lyssiotis, C. a, Homicsko, K., Collisson, E. a, Gibb, W.J., Wullschleger, S., Ostos, L.C.G., Lannon, W. a, Grotzinger, C., Del Rio, M., et al. (2013). A colorectal cancer classification system that associates cellular phenotype and responses to therapy. Nat. Med. *19*, 619–625.

Sadanandam, A., Wang, X., Melo, F.D.S.E., Gray, J.W., Vermeulen, L., Hanahan, D., and Medema, J.P. (2014). Reconciliation of classification systems defining molecular subtypes of colorectal cancer. Cell Cycle *13*, 353–357.

Saijo, A., Goto, H., Nakano, M., Mitsuhashi, A., Aono, Y., Hanibuchi, M., Ogawa, H., Uehara, H., Kondo, K., and Nishioka, Y. (2018). Bone marrow-derived fibrocytes promote stem cell-like properties of lung cancer cells. Cancer Lett. *421*, 17–27.

Salmon, H., Franciszkiewicz, K., Damotte, D., Dieu-Nosjean, M.C., Validire, P., Trautmann, A., Mami-Chouaib, F., and Donnadieu, E. (2012). Matrix architecture defines the preferential localization and migration of T cells into the stroma of human lung tumors. J. Clin. Invest. *122*, 899–910.

Salmon, H., Remark, R., Gnjatic, S., and Merad, M. (2019). Host tissue determinants of tumour immunity. Nat. Rev. Cancer *19*, 215–227.

Van Schaeybroeck, S., Allen, W.L., Turkington, R.C., and Johnston, P.G. (2011). Implementing prognostic and predictive biomarkers in CRC clinical trials. Nat. Rev. Clin. Oncol. *8*, 222–232.

Scheller, J., Chalaris, A., Schmidt-Arras, D., and Rose-John, S. (2011). The pro- and anti-inflammatory properties of the cytokine interleukin-6. Biochim. Biophys. Acta *1813*, 878–888.

Scholten, D., Österreicher, C.H., Scholten, A., Iwaisako, K., Gu, G., Brenner, D.A., and Kisseleva, T. (2010). Genetic labeling does not detect epithelial-to-mesenchymal transition of cholangiocytes in liver fibrosis in mice. Gastroenterology *139*, 987–998.

Segditsas, S., and Tomlinson, I. (2006). Colorectal cancer and genetic alterations in the Wnt pathway. Oncogene *25*, 7531–7537.

Sekiya, S., Miura, S., Matsuda-Ito, K., and Suzuki, A. (2016). Myofibroblasts Derived from Hepatic Progenitor Cells Create the Tumor Microenvironment. Stem Cell Reports *7*, 1130–1139.

SEOM (2019). Las Cifras del Cáncer en España. Sociedad Española de Oncología Médica 2–12.

Sharpe, A.H., and Pauken, K.E. (2018). The diverse functions of the PD1 inhibitory pathway. Nat. Rev. Immunol. *18*, 153–167.

Shaw, T.J., and Martin, P. (2009). Wound repair at a glance. J. Cell Sci. *122*, 3209–3213.

Shinagawa, K., Kitadai, Y., Tanaka, M., Sumida, T., Onoyama, M., Ohnishi, M., Ohara, E., Higashi, Y., Tanaka, S., Yasui, W., et al. (2012). Stroma-directed imatinib therapy impairs the tumor-promoting effect of bone marrow-derived mesenchymal stem cells in an orthotopic transplantation model of colon cancer. Int. J. Cancer *132*, 813–823.

American Cancer Society. Colorrectal cancer stages. 01/08/2019. URL: https://www.cancer.org/cancer/colon-rectal-cancer/detection-diagnosis-staging/staged.html

De Sousa E Melo, F., Wang, X., Jansen, M., Fessler, E., Trinh, A., de Rooij, L.P.M.H., de Jong, J.H., de Boer, O.J., van Leersum, R., Bijlsma, M.F., et al. (2013). Poor-prognosis colon cancer is defined by a molecularly distinct subtype and develops from serrated precursor lesions. Nat. Med. *19*, 614–618.

Spranger, S. (2016). Mechanisms of tumor escape in the context of the T-cell-inflamed and the non-T-cell-inflamed tumor microenvironment. Int. Immunol. *28*, 383–391.

Su, S., Chen, J., Yao, H., Liu, J., Yu, S., Lao, L., Wang, M., Luo, M., Xing, Y., Chen, F., et al. (2018). CD10+GPR77+Cancer-Associated Fibroblasts Promote Cancer Formation and Chemoresistance by Sustaining Cancer Stemness. Cell *172*, 841–856.

Sugimoto, H., Mundel, T.M., Kieran, M.W., and Kalluri, R. (2006). Identification of fibroblast heterogeneity in the tumor microenvironment. Cancer Biol. Ther. *5*, 1640–1646.

Sumida, T., Kitadai, Y., Shinagawa, K., Tanaka, M., Kodama, M., Ohnishi, M., Ohara, E., Tanaka, S., Yasui, W., and Chayama, K. (2011). Anti-stromal therapy with imatinib inhibits growth and metastasis of gastric carcinoma in an orthotopic nude mouse model. Int. J. Cancer *128*, 2050–2062.

Swann, J.B., and Smyth, M.J. (2007). Immune surveillance of tumors. J. Clin. Invest. *117*, 1137–1146.

Takai, K., Le, A., Weaver, V.M., and Werb, Z. (2016). Targeting the cancer-associated fibroblasts as a treatment in triple-negative breast cancer. Oncotarget *7*, 82889–82901.

Tauriello, D.V.F., and Batlle, E. (2016). Targeting the Microenvironment in Advanced Colorectal Cancer. Trends in Cancer *2*, 495–504.

Tauriello, D.V.F., Calon, A., Lonardo, E., and Batlle, E. (2017). Determinants of metastatic competency in colorectal cancer. Mol. Oncol. *11*, 97–119.

Tauriello, D.V.F., Palomo-Ponce, S., Stork, D., Berenguer-Llergo, A., Badia-Ramentol, J., Iglesias, M., Sevillano, M., Ibiza, S., Cañellas, A., Hernando-Momblona, X., et al. (2018). TGFβ drives immune evasion in genetically reconstituted colon cancer metastasis. Nature *554*, 538–543.

TCGA (2012). Comprehensive molecular characterization of human colon and rectal cancer. Nature *487*, 330–337.

TCGA Research Network. URL: http://cancergenome.nih.gov/.

Team, R. C. R: A language and environment for statistical computing. R Foundation for Statistical Computing, Vienna, Austria (2018). URL: http://www.r-project.org

Tivol, E.A., Borriello, F., Schweitzer, A.N., Lynch, W.P., Bluestone, J.A., and Sharpe, A.H. (1995). Loss of CTLA-4 leads to massive lymphoproliferation and fatal multiorgan tissue destruction, revealing a critical negative regulatory role of CTLA-4. Immunity *3*, 541–547.

Tsushima, H., Ito, N., Tamura, S., Matsuda, Y., Inada, M., Yabuuchi, I., Imai, Y., Nagashima, R., Misawa, H., Takeda, H., et al. (2001). Circulating transforming growth factor β1 as a predictor of liver metastasis after resection in colorectal cancer. Clin. Cancer Res. *7*, 1258–1262.

Tu, J.F., Ding, Y.H., Ying, X.H., Wu, F.Z., Zhou, X.M., Zhang, D.K., Zou, H., and Ji, J.S. (2016). Regulatory T cells, especially ICOS+ FOXP3+ regulatory T cells, are increased in the hepatocellular carcinoma microenvironment and predict reduced survival. Sci. Rep. *6*, 2–9.

Turley, S.J., Cremasco, V., and Astarita, J.L. (2015). Immunological hallmarks of stromal cells in the tumour microenvironment. Nat. Rev. Immunol. *15*, 669–682.

Ursem, C., Atreya, C.E., and Van Loon, K. (2018). Emerging treatment options for BRAF-mutant colorectal cancer. Gastrointest. Cancer *8*, 13–23.

Uryvaev, A., Passhak, M., Hershkovits, D., Sabo, E., and Bar-Sela, G. (2018). The role of tumor-infiltrating lymphocytes (TILs) as a predictive biomarker of response to anti-PD1 therapy in patients with metastatic non-small cell lung cancer or metastatic melanoma. Med. Oncol. *35*, 1–9.

Veglia, F., Perego, M., and Gabrilovich, D. (2018). Myeloid-derived suppressor cells coming of age. Nat. Immunol. *19*, 108–119.

Verhoef, C., de Wilt, J.H., Burger, J.W.A., Verheul, H.M.W., and Koopman, M. (2011). Surgery of the primary tumour in stage IV colorectal cancer with unresectable metastases. Eur. J. Cancer *47*, 61–66.

Vermeulen, L., De Sousa E Melo, F., van der Heijden, M., Cameron, K., de Jong, J.H., Borovski, T., Tuynman, J.B., Todaro, M., Merz, C., Rodermond, H., et al. (2010). Wnt activity defines colon cancer stem cells and is regulated by the microenvironment. Nat. Cell Biol. *12*, 468–476.

Vianello, F., Papeta, N., Chen, T., Kraft, P., White, N., Hart, W.K., Kircher, M.F., Swart, E., Rhee, S., Palù, G., et al. (2006). Murine B16 melanomas expressing high levels of the chemokine stromal-derived factor-1/CXCL12 induce tumor-specific T cell chemorepulsion and escape from immune control. J. Immunol. *176*, 2902-2914.

Wallace, M.C., and Friedman, S.L. (2014). Hepatic Fibrosis and the Microenvironment : Fertile Soil for Hepatocellular Carcinoma Development. Gene Expr. *16*, 77–84.

Waterhouse, N.J., Sedelies, K.A., and Clarke, C.J.P. (2004). Granzyme B; the chalk-mark of a cytotoxic lymphocyte. J. Transl. Med. *2*, 1–3.

Weiser, M.R. (2018). AJCC 8th Edition: Colorectal Cancer. Ann. Surg. Oncol. *25*, 1454–1455.

Wells, R.G. (2014). The portal fibroblast: not just a poor man's stellate cell. Gastroenterology *147*, 41–47.

Westfall, P.H. (1997). Multiple Testing of General Contrasts Using Logical Constraints and Correlations. J. Am. Stat. Assoc. *92*, 299–306.

Wherry, E.J. (2011). T cell exhaustion. Nat. Immunol. *12*, 492–499.

Wortzel, I., Dror, S., Kenific, C.M., and Lyden, D. (2019). Exosome-Mediated Metastasis: Communication from a Distance. Dev. Cell *49*, 347–360.

Wright, J.H., Johnson, M.M., Shimizu-Albergine, M., Bauer, R.L., Hayes, B.J., Surapisitchat, J., Hudkins, K.L., Riehle, K.J., Johnson, S.C., Yeh, M.M., et al. (2014). Paracrine activation of hepatic stellate cells in platelet-derived growth factor C transgenic mice: evidence for stromal induction of hepatocellular carcinoma. Int. J. Cancer *134*, 778–788.

Wu, X., Dong, L., Zhang, R., Ying, K., and Shen, H. (2014). Transgelin overexpression in lung adenocarcinoma is associated with tumor progression. Int. J. Mol. Med. *34*, 585–591.

Xouri, G., and Christian, S. (2010). Origin and function of tumor stroma fibroblasts. Semin. Cell Dev. Biol. *21*, 40–46.

Xu, J., Lamouille, S., and Derynck, R. (2009). TGF-B-induced epithelial to mesenchymal transition. Cell Res. *19*, 156–172.

Yaffee, P., Osipov, A., Tan, C., Tuli, R., and Hendifar, A. (2015). Review of systemic therapies for locally advanced and metastatic rectal cancer. J. Gastrointest. Oncol. *6*, 185–200.

Yang, J., Guo, X., Wang, M., Ma, X., Ye, X., and Lin, P. (2017). Pre-treatment inflammatory indexes as predictors of survival and cetuximab efficacy in metastatic colorectal cancer patients with wild-type RAS. Sci. Rep. *7*, 1–9.

Yang, Y., Andersson, P., Hosaka, K., Zhang, Y., Cao, R., Iwamoto, H., Yang, X., Nakamura, M., Wang, J., Zhuang, R., et al. (2016). The PDGF-BB-SOX7 axis-modulated IL-33 in pericytes and stromal cells promotes metastasis through tumour-associated macrophages. Nat. Commun. *7*, 1–18.

Yu, I.S., and Cheung, W.Y. (2018). Metastatic colorectal cancer in the era of personalized medicine: A more tailored approach to systemic therapy. Can. J. Gastroenterol. Hepatol. *2018*. 1-11.

Yu, B., Chen, X., Li, J., Qu, Y., Su, L., Peng, Y., Huang, J., Yan, J., Yu, Y., Gu, Q., et al. (2013). Stromal fibroblasts in the microenvironment of gastric carcinomas promote tumor metastasis via upregulating TAGLN expression. BMC Cell Biol. *14*, 1-10

Zheng, B., Zhang, Z., Black, C.M., de Crombrugghe, B., and Denton, C.P. (2002). Ligand-dependent genetic recombination in fibroblasts : a potentially powerful technique for investigating gene function in fibrosis. Am. J. Pathol. *160*, 1609–1617.

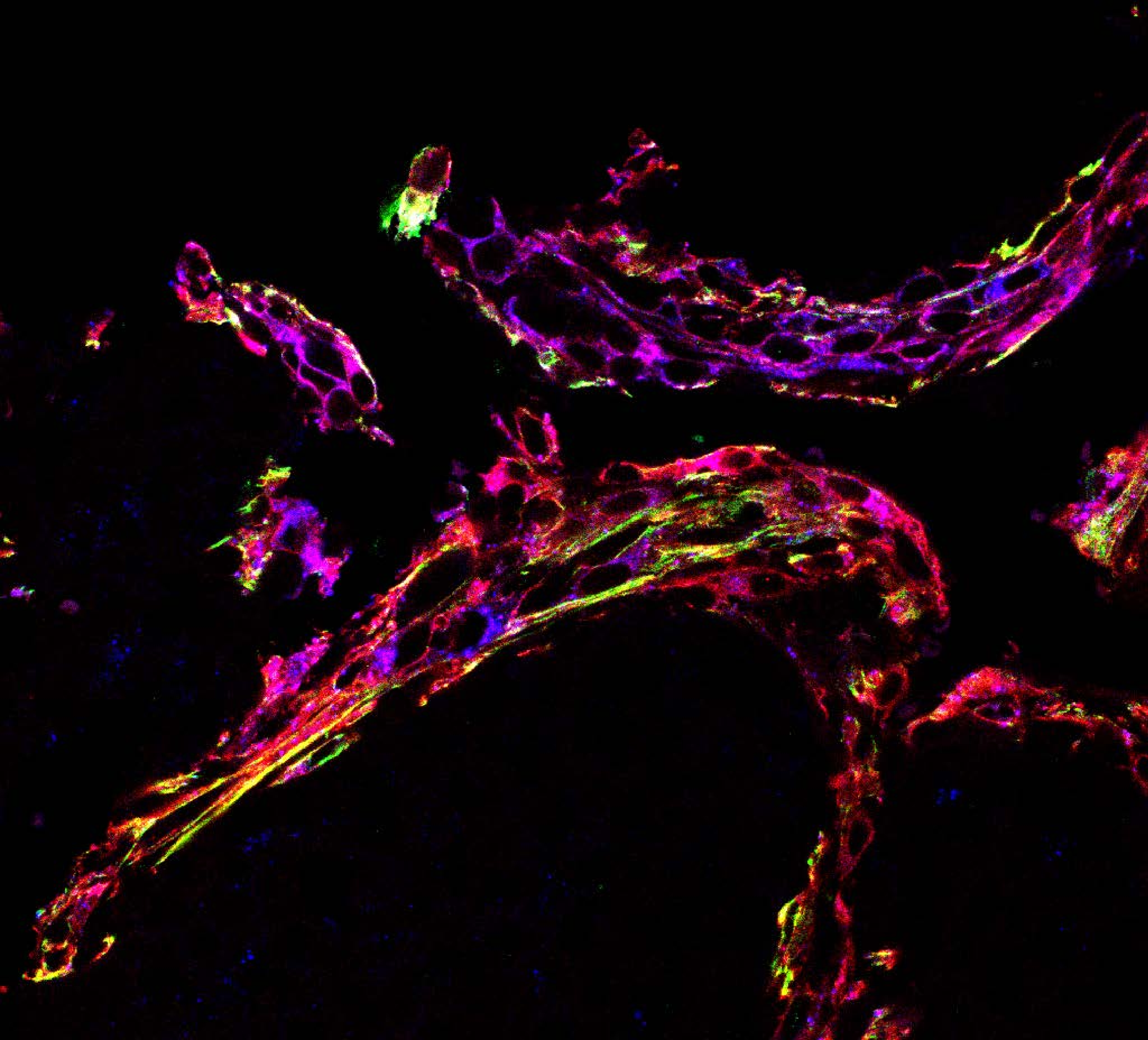Zhu, L., Cheng, X., Shi, J., Lin, J., Chen, G., Jin, H., Liu, A.B., Pyo, H., Ye, J., Zhu, Y., et al. (2016). Crosstalk between bone marrow-derived myofibroblasts and gastric cancer cells regulates cancer stemness and promotes tumorigenesis. Oncogene *35*, 5388–5399.